CRYSTAL MORPHOLOGY AND SURFACE REACTIVITY STUDIES OF CALCIUM HYDROXIDE

A Thesis submitted for the degree of Doctor of Philosophy

by

ADRIAN CHARLES GRAY

Department of Chemistry, Brunel University

February 1990

ABSTRACT

Calcium hydroxide samples, obtained as a precipitate from the mixing of solutions of sodium hydroxide with a variety of calcium salts in the optional presence of ethanol and a silylating agent, have been characterised by the techniques of nitrogen adsorption, water vapour adsorption , thermogravimetric analysis, Fourier-transform infra-red spectroscopy, ultra-violet spectroscopy and electron microscopy.

The morphology of the samples varied from octahedral crystals to hexagonal prisms to sheets. The individual morphology depends on the conditions of precipitation, the nature and concentration of the calcium salt(s) and the nature of the precipitation medium. It has been shown that a large excess of sodium hydroxide results in octahedral forms, calcium salt(s) in approximate equimolar amount or in large excess to the sodium hydroxide results in hexagonal forms, and sheets are formed in the presence of ethanolic precipitation medium. A poisoning mechanism has been suggested in terms of the morphological properties of the samples. It has been found that the sheet forms of calcium hydroxide can be stabilised by reaction with a silylating agent, resulting in greater thermal stability and chemical stability of the surface. Silylation was found not to occur by direct contact between the precipitated calcium hydroxide samples and silylating agents. Silylation only occurred when precipitation was carried out in the presence of a solution of the silylating agent in absolute ethanol. The silylation of the surface of calcium hydroxide has been found to stabilise the material. Reaction of this with 3-aminopropyltriethoxysilane formed an intermediate which subsequently reacted with *p*-nitrobenzoyl chloride to form an inorganic - organic composite. The technique of thermogravimetric analysis has been employed to measure the thermal stability of the samples. It has been found that the samples exhibit major weight losses at around 688K for the non-silylated samples and around 918K for the silylated samples. The BET-nitrogen and the BET-H_2O surface areas of the samples range typically from ~1 to 43 m^2g^{-1}, and from 9 to 798 m^2g^{-1} respectively. On the basis of this evidence, taken together with the isotherm shapes it has been shown that: the samples are non-porous; non-silylated calcium hydroxide samples are more hydrophobic than the silylated samples, but upon heat-treatment in air below the decomposition temperature the silylated samples became more hydrophobic, whereas the non-silylated samples became more hydrophilic; samples heated in air at above the decomposition temperature exhibit a dramatic increase in hydrophilicity, the H_2O-BET surface areas becoming ~800 m^2g^{-1} for non-silylated samples, compared to 368 - 600 m^2g^{-1} for silylated samples, indicative of chemisorption following decomposition of the calcium hydroxide to form calcium oxide.

ACKNOWLEDGEMENTS

I wish to express my gratitude to my supervisors Dr. C Theocharis and Prof. K S W Sing for their help and guidance over the past three years.

Thanks must also go to all the technical staff at Brunel, in particular Bob, Alan, Steve, Nita and Brenda in ETC for their invaluable training and assistance in electron microscopy.

Thanks go to Prof. J D Birchall, Mr. R N Rothon and Mr. R J Ashley, all of ICI New Science Division, for their valuable discussions and technical help during my visits to Runcorn.

ICI New Science Division and the SERC are thanked for the provision of grants and awards under which this work was carried out.

And last, but not least, I am grateful to my fiancé, Jennifer, for her support and encouragement.

For

Jennifer

With Love

Our investigations have always contributed more to our amusement than they have to knowledge.

Will Rogers

CONTENTS

FIGURES

TABLES

LIST OF PLATES

SYMBOLS AND ABBREVIATIONS

A	Affinity or differential free energy of adsorption
Å	Angstrom unit
A_{BET}	BET surface area
a_m	Cross-sectional area of adsorbate molecule (nm^2)
a_s	Lattice spacing
b	Similarity coefficient
B	Structural constant
BCF	Burton, Cabrera and Frank
B.E.	Electron binding energy
BDDT	Brunauer, Deming, Deming and Teller
BET	Brunauer Emmett and Teller
C	Constant for the system
c	is a BET equation constant
c_o	Fraction of crystal surface occupied by separate growth units
d	Density of the adsorbate in the liquid phase
ΔH_f	Heat of fusion
DR	Dubinin-Radushkevitch
DRK	Dubinin-Radushkevitch-Kaganer
D_s	Surface diffusion coefficient
DTA	Differential thermal analysis
e	Potential energy change per solid fluid bond
$E^f(k)$	Total energy of the final state with a hole in the kth subshell
E^i	Total energy of the initial state
E_{kin}	Kinetic energy of the photoelectron expelled from the kth subshell
ESCA	Electron spectroscopy for chemical analysis
ϕ_{ff} ϕ_{ss} ϕ_{sf}	Represent the bond energies for nearest neighbour bonds
FHH	Frenkel-Halsey-Hill
FTIR	Fourier transform infra red
γ	Surface tension

γ_e	Edge energy
$h\nu$	Energy of the incident photon
k	Gas constant
KeV	Kiloelectron volts
K_r	Rate constant
kV	Kilovolts
L	Avogadro's number
l_s	Mean diffusion distance of adsorbed growth units on surface
M	Molecular weight of the adsorbate
mA	Milliamps
M_{sample}	Weight of sample (g)
NIR	Near infra red
n_{so}	Equilibrium value of surface solute density
p^o	Saturated vapour pressure
p_{ox}	Pressure read from the oxygen manometer
r	FHH exponent
R	Linear growth rate
r	Liquid density of adsorbate
r'	Actual pore radius
s	Number of cooperating spirals or strength of the step source
σ	Supersaturation
σ^*	Angle of contact between the liquid and the wall of the pore
S_a	External surface area
S_{BET}	BET surface area
S_{DR}	DR plot surface area
SEM	Scanning electron microscopy
S_{He}	Helium surface area (m^2)
S_N	Nitrogen surface area (m^2)
S_o	Area covered by 1ml of adsorbate
S_s	Specific surface

S_{SP}	Single point surface area
T	Temperature
t	Time in seconds
T(Å)	Coating thickness in Angstroms
TEM	Transmission electron microscopy
TGA	Thermogravimetric analysis
T_{LN}	Temperature of liquid nitrogen
UV	Ultraviolet
V	Volume
V/V_m	Surface coverage
V_{DR}	Volume required to fill the micropores
VIS	Visible
V_L	Molar volume of the adsorbate in liquid form

1. INTRODUCTION

The crystal structure of calcium hydroxide has been determined by means of X-ray methods, among others [1-13]. These measurements showed that calcium hydroxide in the solid state forms ditrigonal - scalenohedral crystals belonging to the hexagonal - rhombohedral system D^3_{3d} ($c\bar{3}m$) The unit cell, as shown in Figure 1.1, is a rectangular prism with a rhombic base The edge of the base has a length of a_o = 3.5918(3) Å; the height of the prism c_o = 4.9063(7) Å [1-14]. The unit cell contains one molecule of $Ca(OH)_2$; Ca:(000);O:($^1/_3$,$^2/_3$,u); ($^2/_3$,$^1/_3$,$\bar{u}$), where u = 0.2330(4) [8-10]. The position of the proton cannot be determined by X-ray diffraction methods, but they may very well be used to determine the corresponding electron density maximum, which is situated in such a way that the OH bond is parallel to the c-axis: ($^1/_3$,$^2/_3$,v'), ($^2/_3$,$^1/_3$,$\bar{v}'$), where v'=0.395(8) [8-10]. Hence the length of the bond is obtained, 0.79(4) Å. The position of the proton has been investigated with the help of infra red [15-16] and determined by means of neutron diffraction [14]: H:($^1/_3$,$^2/_3$,v), ($^2/_3$,$^1/_3$,$\bar{v}$), where v = 0.4248(6). The OH bond is found to be 0.936(3) Å.

Well developed calcium hydroxide crystals have the shape of hexagonal tablets or prisms with perfect basal cleavage. Every second face of the tablet is most frequently longer, and every alternate face is shorter. In most cases, three rhombohedral surfaces are formed between the bases and the faces at the ends of the prism. Several facets can also be met with.

By shaking loosely burnt lime with water, calcium hydroxide in microcrystalline, colloidal, and possibly also amorphous forms [17-19] is obtained. This is likewise the case when calcium hydroxide is precipitated with alkali from calcium salt solutions. The colloidal variety has a marked tendency to form aggregates or agglomerates differing in size and in density.

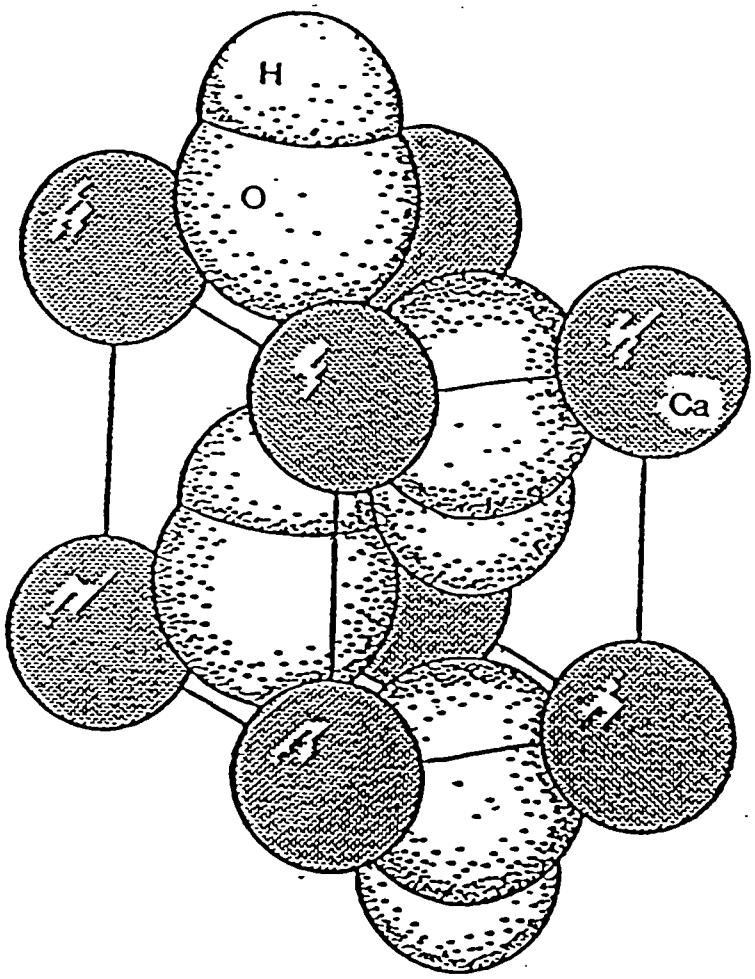

Figure 1.1 Unit Cell of Calcium Hydroxide.

Coarse crystalline calcium hydroxide can be prepared by slow crystallisation from supersaturated solutions. Hexagonal prisms and hexagonal plate - like crystals of calcium hydroxide have been synthesised by hydrating calcium oxide under differing conditions and differing additives in the reaction mixture [20].

Rapid crystallisation from highly concentrated solutions sometimes yields hemispherical, spherulitic shapes, which some researchers have confused with calcium hydroxide. These shapes originate from unintentional formation of calcium carbonate.

This investigation was undertaken to study the morphology of calcium hydroxide precipitated from solutions of sodium hydroxide and calcium salts, with the aim of developing a process for the preparation of large, thin, sheet - like crystals of calcium hydroxide

Our knowledge of the nucleation and crystal growth of calcium hydroxide is surprisingly limited [21-24], even though these processes have many important industrial applications, especially in Portland cement production.

Previous work has concentrated on the precipitation of calcium hydroxide crystals from saturated calcium hydroxide solutions in the presence of sodium (potassium) chloride. Little, if any work has studied the morphology of calcium hydroxide crystals precipitated from alkali metal hydroxide solutions with a strong or weak acid salt of calcium.

Recent work of the ICI New Science Group [25] has shown that very thin crystals (thickness < 10nm) of certain clay minerals can be deposited in the forms of films and coatings. Such films have been studied and found to have remarkably high tensile strengths and to act as very effective thermal barriers when deposited on the surface of metal, glass, or organic polymers.

At present the thin plate - like crystals are produced by a two - stage process of delamination and dispersion. The first stage involves the exchange, of interlamellar Mg^{2+} ions by Na^{+} ions and replacement of the latter by n - butylammonium ions; this allows expansion of the lattice to occur as water enters the interlayer space. Deaggregation of the chemically expanded mineral is then achieved by high shear mixing. So far the lamellar crystals have been prepared from natural clay minerals, but for a number of reasons it would be advantageous to use manufactured inorganic material. In principle, it should be possible to control the dimensions and degree of dispersion of plate - like particles.

It is well known that the alkaline earth metal hydroxides possess layer structures and that calcium hydroxide in particular can be precipitated in a platy form. In the present context, plate - like crystals of calcium hydroxide would not be attractive because any thermal decomposition or carbonate formation would result in departure from the layer morphology. A much more promising system for commercial exploitation would appear to be calcium silicate hydrate, which is produced as one of the hydration products of Portland cement or by the reaction between calcium hydroxide and sodium silicate.

Taylor [26] has pointed out that such order as exists in the calcium silicate hydrate structure is likely to reside in the CaO part and therefore to resemble the structure of calcium hydroxide. Such an arrangement is consistent with the X-ray diffraction pattern of calcium silicate hydrate. The model of a sheet like core of CaO sandwiched between two silicate layers [27] could also account for the range of stoichiometry reported for calcium silicate hydrate and for particular features of its adsorptive properties [28]. The recent work of Wu and Young [29] indicates that silicate can retard the growth of calcium hydroxide, and these findinggs appear to support the suggestion[27] that calcium silicate hydrate is produced by the deposition of silicate anions on a preformed calcium hydroxide nucleus.

2.CRYSTAL GROWTH

Over the past 10 - 15 years the advances that have been made in modelling crystal size distributions in crystallisers have tended to dominate the chemical engineering view of crystallisation. This same period has also seen significant advances in our understanding of crystal growth mechanisms. Many of these advances have taken place outside the mainstream of industrial crystallisation research and by their nature are rooted in physical chemistry and applied physics.

Many aspects of the production of crystalline materials are rooted in problems of crystal growth. Most obviously crystal size and shape (habit) and the effect of process variables such as supersaturation, temperature, solvent, impurity content and crystal - solution slip velocities are defined by the crystal growth mechanism and the corresponding kinetic reaction for a particular system. A number of other factors are less obviously related to crystal growth. Crystal purity has received surprisingly little attention, this in spite of the classical view that crystallisation is primarily a purification process, and the interactions of growth mechanisms with the incorporation of impurities within the crystal lattice as solution inclusions or as surface deposits during solid - liquid separation have been largely unexplored. Crystal perfection has also been generally ignored in the chemical industry although it is of paramount importance in the production of crystals for solid state electronic device applications.

Crystal growth theory cannot at present predict, *a priori*, crystal growth rates except under conditions of simple geometry where growth is controlled by bulk diffusion rates. Crystal growth theory can however tell us the form of relation we might expect between the growth rate and the variables above. It can frequently predict the effect of changes in process parameters and, in the same way as reaction kinetics, guide our judgments as to the possibilities open to us when specific changes in rates or habit are required.

The mechanism by which a crystal grows is determined by the nature of the crystal - solution interface. When a growth unit reaches the crystal surface it either integrates into the lattice at a kink site or returns to the fluid phase. The chance of reaching such a site depends on the concentration of kinks, the mechanism and the rate of growth so depending on the structure of the crystal surface.

If the interface is rough on the molecular scale there are many potential kink sites and in the limit of maximum roughness any impact site is also an integration site. Fine details of the surface topography are then unimportant, considerations related to surface diffusion do not arise and continuous or normal growth models apply.

On the other hand when the interface is smooth, growth is more difficult. Kink sites are only found in the edges of two-dimensional nuclei or of steps, the surface topography must be defined and surface diffusion of growth units must be taken into account. Layer growth models are applicable under such conditions.

The interface structure can be characterised in terms of the surface entropy factor, α, first introduced by Jackson [30]. Jackson's treatment for a simple one-component system was later extended to two-component systems by Tempkin [31], so that the concept could be applied directly to solution growth [32-37].

The nature of a specific surface imposes constraints on the mechanism by which that crystal can grow. Consequently there are a range of growth theories covering various sets of assumptions.

Layer growth models consider the case for a two-dimensional nucleus to form on a surface, wherein sufficient growth units must cluster together to form a stable critical nucleus (surface nucleation). When this has been achieved other growth units can attach themselves to the edge of the nucleus and growth takes place across the face. A number of two-dimensional nucleation growth theories have been proposed which differ mainly

in their assumptions concerning the relative rates at which critical nuclei form and at which they spread across the surface.

Ohara and Reid [38] and Hillig [39] discuss three models which all result in the relation between growth rate and supersaturation. At low supersaturations all such models are dominated by the exponential term which determines that there is a range of supersaturation where the growth rate is negligibly small.

Continuous step models relate to crystal surfaces with $\alpha > 4$, which are so smooth that a high energy barrier to nucleation exist at low supersaturations. Frank [40] suggested that the presence of screw dislocations provides a self perpetuating source of steps on the surface and hence a ready source of kink sites at which growth can occur. Subsequently Burton, Cabrera and Frank (BCF) [41] developed a step model of crystal growth which describes how an otherwise flat crystal surface grows by the addition of growth units to kink sites in an infinite sequence of equidistant steps. The source of these steps is assumed to be a screw dislocation, the steps are considered parallel and equidistant and the steps are fed by a surface diffusion flux governed by Fick's law [42].

The driving force for the crystallisation process has, up to this point, been described as the supersaturation, but no specific definition of this term has been given. The difficulty in doing so is that the supersaturation ratio, S, evaluated from the ratio of the bulk solution concentration to the equilibrium concentration could take on widely differing values.

Growth rate models of the type discussed above predict specific relations between growth rate and supersaturation. In addition to the difficulty of defining the appropriate value of the supersaturation it can also be extremely difficult to distinguish between the different growth models solely on the basis of experimental growth rate supersaturation data.

In discussing crystal growth theories it has been assumed that the solute concentration at the crystal - solution interface which determines the surface integration kinetics is known. This concentration is less than that in the bulk solution and is determined by the convective resistance to transport of solute to the crystal surface. Considering that such mass transfer processes are at the heart of chemical engineering it is surprising that so much confusion has been generated on this topic in the crystal growth literature.

The interaction between diffusion and surface integration has traditionally formulated in terms of the "stagnant film" concept. There is of course no stagnant film more than a few atomic dimensions in extent, but the idealisation of a stagnant film has frequently been taken literally by workers in crystal growth. This has led to two problems; a lack of appreciation of the value of boundary layer theory in describing crystal growth and, indirectly, to errors in formulating the diffusion equations applicable to crystal growth.

Jagannathan and Wey [43,44] have drawn attention to the effect of diffusion on crystal growth rates in a "crowded environment". When small crystals, the growth rate of which are controlled by diffusion, are present at high concentrations such that interparticle distances are comparable with the diffusion layer thickness, significant increases in growth rate for a given supersaturation can be obtained. Calculations showed that such effects could explain the observed effect of crystal number concentration on the growth rates of AgBr crystals. In a wider context the results are likely to be of significance for analysing precipitation of most sparingly soluble salts.

Analogies between aspects of reaction engineering and crystallisation can be very fruitful and most recent approaches to crystalliser design and characterisation are based on such an approach. One such analogy can be drawn between heterogeneous solid - fluid reactions and crystal growth in both of which diffusion and reaction take place in series, the validity of the in-series approach to crystal growth having been shown as generally valid [45].

There is substantial experimental evidence that, when exposed to constant external conditions of supersaturation, temperature and hydrodynamics, different crystals of the same material grow at different rates. This phenomenon has become known as growth rate dispersion and it is important for at least three reasons. First it complicates the interpretation of nucleation rates estimated from the steady state size distribution in mixed suspension mixed product removal (MSMPR) crystallisers. Second, its occurrence affects the crystal size distribution, and hence the product quality, produced in industrial crystallisers. Third, and perhaps most important in the present context, it is a reflection of the growth processes taking place at the crystal surface and so the nature and magnitude of this dispersion may give information about the growth mechanism.

At least two mechanisms will contribute to size - dependent growth. The effect of crystal size on solubility (the Gibbs - Thomson effect) is such as to increase the solubility with decreasing size. The driving force for growth, and hence the growth rate, of small crystals is therefore less than that for larger crystals. The size at which this effect becomes significant depends on the interfacial tension for the material in question. Although this is a quantity that is difficult to measure or predict with any accuracy, calculations using typical values (10 - 40 mJ/m^2) indicate that the effect is unlikely to be significant for crystals larger than 1μm. The second mechanism that could result in size - dependent growth arise from diffusion effects. The causes of both growth rate dispersion and possible size - dependent growth rates must therefore be sought in the integration process taking place at the crystal surface. Continuous step models, and in particular the BCF theory, provide a framework for such explanations.

The link between dislocations and growth rates has been demonstrated experimentally. Changes in the point of emergence of a screw dislocation from one face to another result in a step change in the growth rate of both faces. Similarly the absence of a dislocation greatly reduces the corresponding growth rate particularly at low supersaturations where a layer growth mechanism dominates.

The origin of dislocations and the random way in which these can occur clearly provide a link with observed dispersions in growth rate. Dislocations may be initiated by the basic defect structure of any seed crystal, by damage caused by crystal collisions and by damage induced by rapid growth and the incorporation of impurity and solvent inclusions. The extent to which dislocations form depends in turn on the plasticity of the material. In general terms plastic materials allow easy generation , motion and multiplication of dislocations whereas in brittle materials dislocations do not easily form even as a consequence of crystal fracture.

There are therefore a number of factors, some related to material properties, others to growth conditions, make it difficult to predict the magnitude of this dispersion, but the phenomenon appears to be inherent in the growth process.

Our understanding of crystal growth has increased significantly over the past decade and in consequence it is becoming more realistic to think in terms of tailoring the growth process to meet specific requirements of size, shape and purity.

The morphological quality of crystalline precipitates is dependent upon many variables, such as supersaturation, the chemical composition of the solution, including impurities, and the method used to induce precipitation. The latter refers to the alternative methods; introduction of solute crystal seeds to a metastable supersaturated solution, or to spontaneous nucleation and precipitation due to excessive supersaturation. Tomazic et al [46] found that plots of initial seed size versus growth rate for several supersaturations as determined from the two independent sources of data show that the growth rate increases with increased initial seeds' size. That is, even though the growth rate is constant for a group of seeds of given initial size, it is different from the growth rate of seeds of different initial size seeds throughout the growth period. This peculiar size dependence of growth rate is a restricted form of growth dispersion.

A similar conclusion was reached by Larson and Berglund [47] who also found that the growth rate was constant for an individual crystal and that the relationship between growth rate and initial size can be approximated by a straight line through data points on a plot of particle diameter versus time, although the data were scattered.

During an actual precipitation reaction, the size distribution may change continuously for reasons other than growth, *i.e.* as a consequence of agglomeration and morphological breakdown or secondary nucleation. These phenomena limit the direct application of acceptable growth mechanisms.

Tomazic et al [48] have shown the development of crystals in time leads to a rather sudden appearance of small crystals at some intermediate time. There is also some evidence that this coincides with a change in crystal product morphology for intermediate seeds. Growth form changes from nearly one - dimensional to nearly three - dimensional at about the same time as the appearance of small product crystals. It appears that morphological changes accompanying secondary nucleation are more evident in intermediate and large seeds than in small seeds. This is further supported by studies of the level of agitation which is effective in bringing about an abrupt change in overall precipitation rate. The abrupt change in solute uptake, as observed with an increase in agitation level, occurs in the same period as nucleation and / or morphological change occur.

The nucleation behaviour described above could well be due to initial breeding (*i.e.* nuclei introduced with the introduction of the seeds).

Another characteristic supporting secondary nucleation occurrence is the difference in behaviour of the small seeds (0.5 μm) from the intermediate (6 μm) and large (10 μm) seeds. The latter appear to effect nucleation, the former do not; in fact the small seeds agglomerate very noticeably. These traits, together with the agitation effect observed,

and the size independence of intermediate and large seeds, all suggest that mechanical force fields contributed significantly to the observed nucleation.

The ideas of Shinnar [49] may be applied to the observations above. These involve consideration of the breakage and coalescence of neutrally suspended droplets in a turbulently agitated environment. Estimation of appropriate fluid mechanical parameters suggested that the size of an effective turbulent eddy was much larger than even the largest crystals, so that breakage of particles due to turbulence *per se* was unlikely. Agglomeration (coalescence) is not discounted by the method of Shinnar and may in fact account for the agglomeration occurrences of the small seeds. That is, the larger crystals acquire kinetic energies which easily overcome the forces of adhesion, and this is not the case for smaller entities (say < 2 μm). From consideration of the above, nucleation and possibly morphological changes were due to mechanical influences.

3. EXPERIMENTAL

3.1 Materials

Analytical grade sodium hydroxide, calcium chloride, calcium propionate, zinc chloride, zinc acetate, and tetraethyl silicate (obtained from BDH Chemicals), analytical grade ethanol (obtained from James Burrough plc) and 1,1,1,3,3,3-hexamethyldisiloxane ($(Me_3Si)_2O$) and 1,1,1,3,3,3-hexamethyldisilazane ($(Me_3Si)_2NH$) (obtained from Aldrich Chemical Co. Ltd.) were used for the work.

3.2 Calcium Hydroxide Precipitation

Precipitation was carried out using a 250 ml or 1000 ml pyrex glass beaker as a reaction vessel, using high shear stirring or ultrasonics as a means of agitation.

The calcium salts were used as 1M solutions in distilled water and were used either alone or in mixtures.

The precipitants were mixed in one of the following ways:

(1) Calcium salt(s) added to sodium hydroxide in the reaction vessel;

(2) Sodium hydroxide added to calcium salt(s) in the reaction vessel; and

(3) Precipitants added simultaneously to the reaction vessel.

Transfer of the precipitants to the reaction vessel was accomplished using a 50 ml burette, or a Watson-Marlow 101/S/R peristaltic pump at a rate of 0.2 - 53 ml/min; rapid transfer was accomplished by pouring the precipitants from measuring cylinders.

Initially the reaction vessel may contain 25-100 ml of water and /or 5-50 ml of ethanol; these liquids being referred to as the reaction medium.

The precipitated material was separated from the reaction medium by centrifuging at 4000 rpm in a MSE Centaur 1 centrifuge. The material was subsequently dried in an air oven at 358K for 15 minutes.

3.3 Silylation of Calcium Hydroxide

Silylation was attempted by the following two processes:

(1) The material precipitated by the processes as described in 3.2, but excluding the drying step, is suspended in acetone containing a molar excess of silylating agent, and agitated by refluxing or by use of mechanical agitation for a time of 15 minutes. to 2 hours. The product is separated from the reaction liquor by centrifuging at 4000 rpm, and subsequently dried at 358K in an air oven; or

(2) The process as described in 3.2 is followed with a modification that the liquid initially contained in the reaction vessel is an ethanolic solution of a molar excess of silylating agent. Following completion of the addition of the precipitants the mixture is mechanically agitated for 30 minutes. The product is separated from the reaction liquor by centrifuging at 4000 rpm, and subsequently dried in an air oven at 358K.

3.4 Solid State Organic Reactions with Calcium Hydroxide Materials

A 20% m/v solution of 3-aminopropyltriethoxysilane was made up in sodium-dried toluene and 50 ml was added to 1 g of the calcium hydroxide material in a 100 ml round bottomed flask and the mixture refluxed for 4 hours. Reasonable dryness was maintained since significant amounts of water will lead to siloxane polymer formation.

The solid aminopropylated product was vacuum filtered and washed with dry toluene, and then placed in a vacuum oven at ca. 343K for 1 hour.

The dried aminopropylated product was placed in a 100 ml round bottomed flask, a solution of 2.5 g of para-nitrobenzoyl chloride and 2.5 g of triethylamine in 50 ml of chloroform was added, and the mixture gently refluxed for 48 hours. The product was vacuum filtered, washed with chloroform and dried under vacuum.

3.5 Low Temperature Nitrogen Adsorption

3.5.1 Nitrogen Isotherm Determination

The isotherms were determined by two types of volumetric apparatus:

(1) The type designed by Harris and Sing [50] (Figure 3.1) and discussed in some detail by Baker [51] and Carrott [52]. The system essentially comprises:

(a) A pumping system consisting of a mercury diffusion pump and a double stage rotary pump through a liquid nitrogen cold trap to produce a vacuum of 8×10^{-4} Torr or less;

(b) The dosing system consists of a series of calibrated thermostatted gas bulbs in combination with a mercury manometer whose level is measured by a cathetometer to 1×10^{-5} m;

(c) The sample bulb fitted with a copper collar is joined to the apparatus by a greased cone;

(d) The nitrogen storage vessel is connected to the dosing volume via taps;

(e) The temperature of the liquid nitrogen bath is monitored using an oxygen vapour pressure thermometer.

The whole apparatus is housed in a temperature-controlled room, and the temperature in the region of the dosing volume recorded from a thermometer.

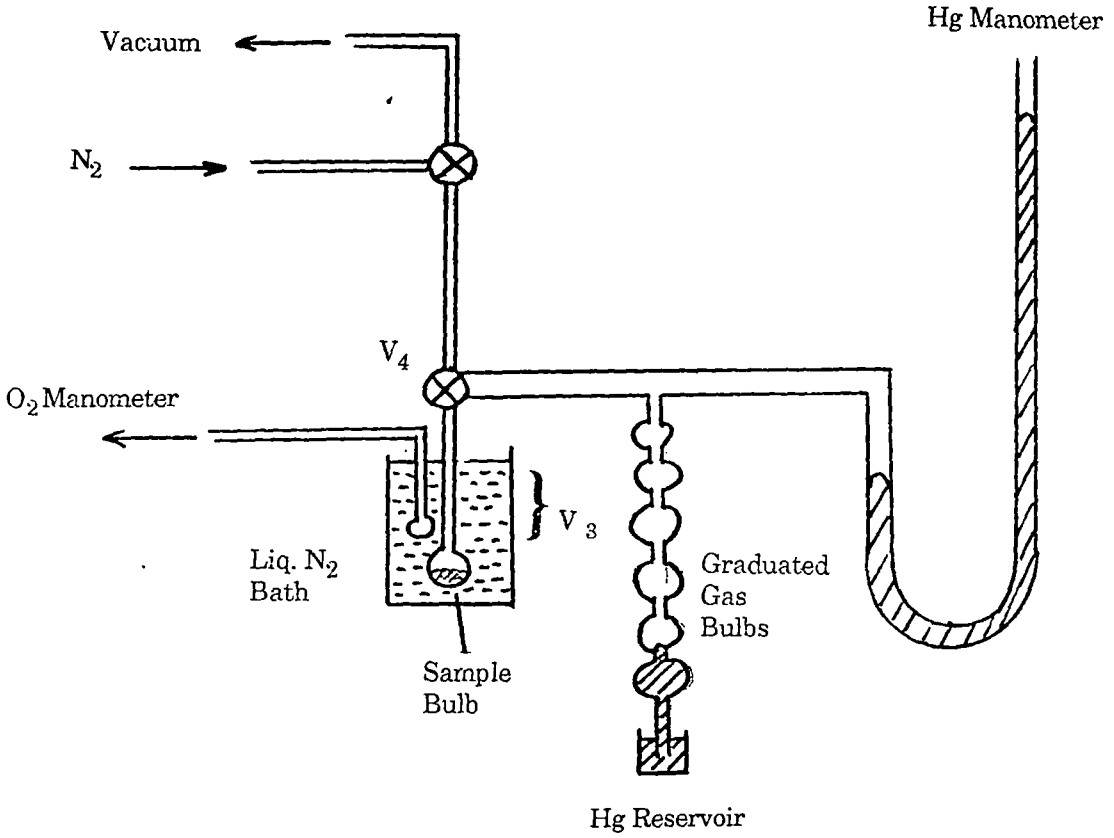

Figure 3.1 Nitrogen Adsorption Apparatus.

The temperature (T_{LN}) of the liquid nitrogen sample bath is calculated from [53]

$$\log p_{ox} = -419.3/T_{LN} + 7.1173 - 0.00648T_{LN} \qquad \textbf{Equation 3.1}$$

where p_{ox}(cm) is the pressure read from the oxygen manometer. The saturated vapour pressure (p^o, cm) of the liquid nitrogen is related to T_{LN} by

$$\log p^o = -339.8/T_{LN} + 6.7106 - 0.005630T_{LN} \qquad \textbf{Equation 3.2}$$

The liquid nitrogen was maintained at a constant level using an automatic levelling device [54]. The effects of small variations in liquid nitrogen level were minimised by the copper collar around the sample bulb.

It was assumed that the entire apparatus was at room temperature except for volume V_3, which was at liquid nitrogen temperature. The calibrated volume for V_3 was corrected for the volume of the sample using 2.0 g cm^{-3} for the density of the sample [52], and the pressure in this volume was corrected for non-ideality using the factor $(1 + 0.000658p)$ [53].

Gas bulb volumes and the tap volume V_4 have previously been measured by repeatedly filling with mercury and weighing. Dead-space calibrations were made by admitting a series of doses of nitrogen to the outgassed, empty sample bulb immersed to a constant level in liquid nitrogen, and then repeating the procedure with the sample bulb at room temperature as described by Baker [51]. A calibration plot was drawn using the equilibrium pressures.

All measurements involved outgassing for a minimum of 16 hours at a temperature of 333 +/- 5K to a residual pressure of 10^{-3} Torr or less. Oxygen-free nitrogen (purity 99.99%) was used as the absorptive.

3.5.2 Surface Area Determination

Surface areas of the samples were determined using a Carlo Erba Sorpty 1750 single point nitrogen adsorption rig, the operation of which is based on the Brunauer, Emmett and Teller equation (BET equation). This is a semi-automatic volumetric instrument of stainless steel construction (Figure 3.2) having the following essential features:

(a) An analytical unit comprising two independent outgassing positions with manual solenoid valves V_6 and V_7, two furnaces to thermostat the sample within the temperature range of 313 - 723K and a measurement circuit inlet (6);

(b) A pneumatic circuit comprising inlet fittings for adsorptive gases, a gas selection valve (V), a high precision metal diaphragm pressure controller (V_2) (for up to 5 kg cm^{-2}), a pressure gauge (P_1) (0 - 5 kg cm^{-2}), a calibrated restrictor, a pressure sensor (PS_1) (max. pressure 795 Torr), a variable volume chamber (CIL) (piston pump), a burette connector, a pressure sensor (PS_2) (set to 135 Torr), a pirani vacuum pressure transducer (TR), a vacuum meter (VG) (min. reading 10^{-3} mbar), and a rotary vacuum pump (VP) (efficiency 1.3 $m^3\ h^{-1}$);

(c) A control panel on the top front panel and the right hand side panel.

The Sorpty 1750 works on a static-volumetric principle, the volume of adsorbed gas is calculated by measuring the pressure change resulting from adsorption of known volume of gas. The gas is introduced into the variable volume chamber until it reaches a pre-set pressure. The chamber is then connected to a burette under vacuum containing the outgassed sample. The burette is maintained at liquid nitrogen temperature.

A solenoid valve, between burette and the variable volume chamber, is triggered by a pressure censor calibrated within the linearity range of BET. The pressure sensor regulates the adsorption cycle, which is considered finished when the sample no longer adsorbs gas during a pre-set time.

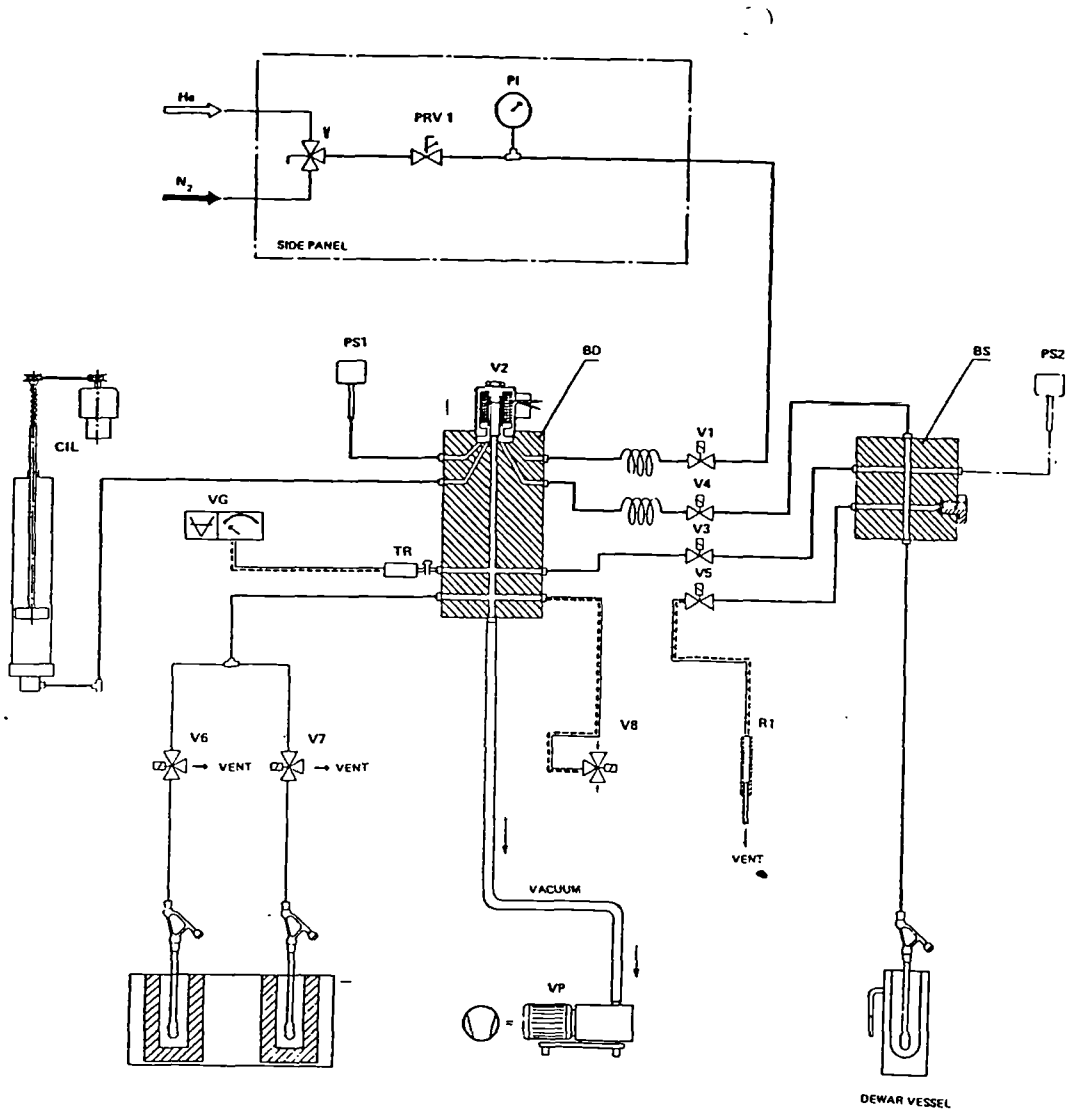

Figure 3.2 Carlo Erba Single-Point Nitrogen Adsorption Rig

When no further pressure change occurs within the interval the burette is cut off from the chamber, and the piston of the variable chamber compresses the residual gas to the original pressure.

Since the displacement of the piston is automatically detected, the surface area (in m^2) is directly displayed on the front panel of the instrument.

A surface area is determined by weighing the sample into a burette (Figure 3.3), outgassing the sample on the Sorpty at either ambient or elevated temperature, running a blank by adsorbing helium gas at liquid nitrogen temperature, re-outgassing the sample at ambient temperature, followed by adsorbing nitrogen gas at liquid nitrogen temperature. The surface area is calculated from $(S_N - S_{He})/M_{sample}$, where S_N is the nitrogen surface area (m^2), S_{He} is the helium surface area (m^2), and M_{sample} is the weight of sample (g)..

3.6 Water Vapour Adsorption

The adsorption of water vapour on the calcium hydroxide samples and the calcium hydroxide based silylated materials were studied by a gravimetric technique using a McBain-Bakr [55] type balance as shown in Figure 3.4., having a fused quartz spring (sensitivity ca. 10.78 mg cm^{-1}). The apparatus has been designed and constructed by Baker [51], and consists essentially of the following:

(a) A four-stage silicone oil diffusion pump, backed by a double stage rotary pump , pumping the high vacuum (<10 Torr) line through a liquid nitrogen trap;

(b) A fused quartz spring suspended in a balance case and thermostatted (299.65 +/- 0.02 K) by a water jacket fed from a Townsen and Mercer thermostat bath;

(c) A silica sample bucket suspended from the spring by means of a fine silica rod;

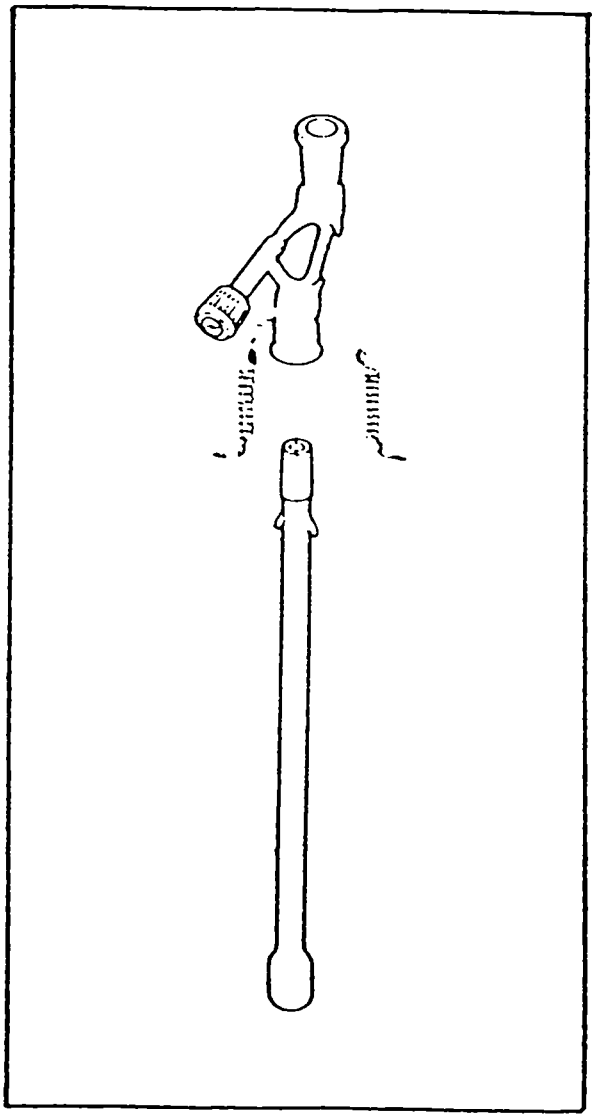

Figure 3.3 Sample Burette for the Carlo Erba Rig.

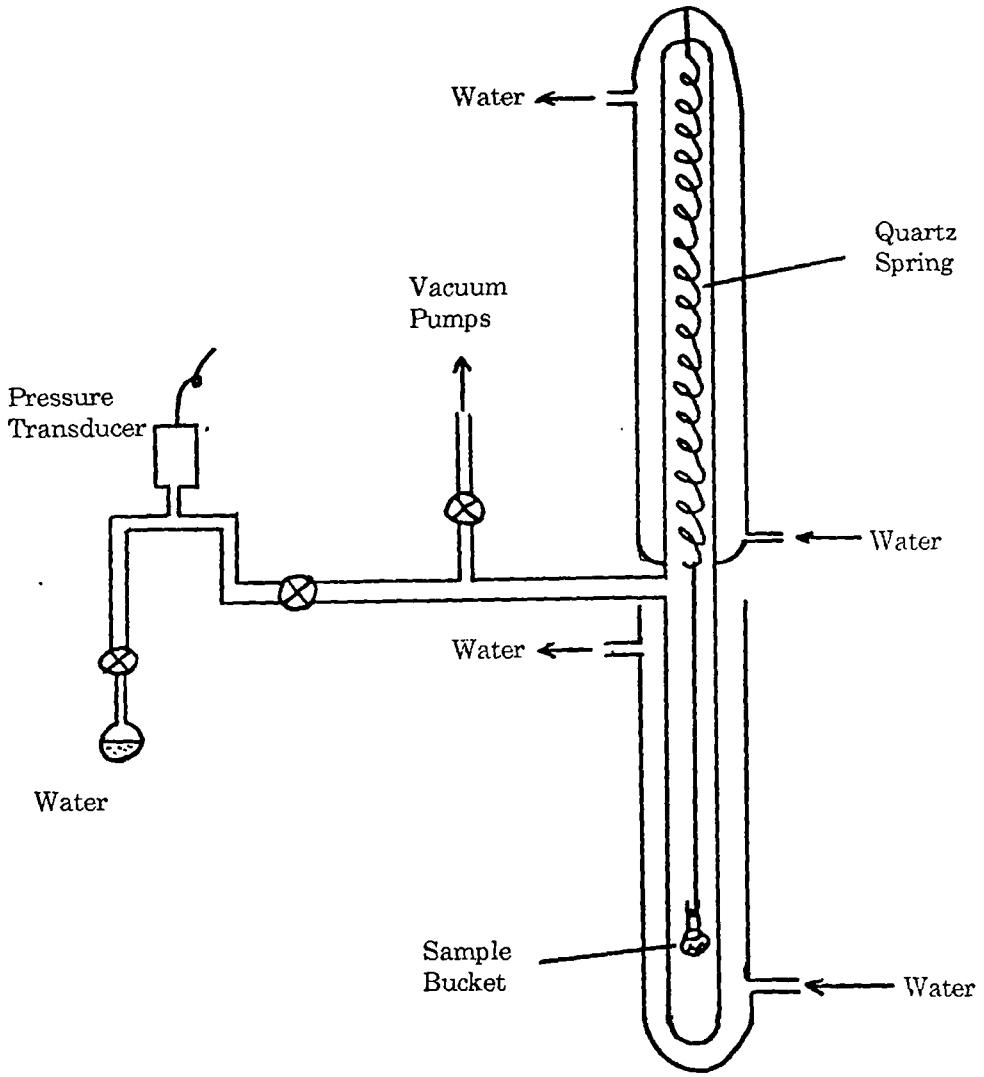

Figure 3.4 Water Adsorption Apparatus.

(d) A silica detachable hang-down tube;

(e) A removable water jacket fed from a Townsen and Mercer thermostat bath and used to thermostat the hang-down tube (307.30 +/- 0.10 K);

(f) A water reservoir and a pressure transducer.

Greaseless stopcocks (G. Springham & Co. Ltd.) were used throughout the apparatus.

Water vapour was provided from a reservoir containing triply distilled water [54] which was subjected to repeated freeze thaw cycles before use (ultimate vacuum $1x10^{-4}$ Torr). The saturated vapour pressure was taken as 34.082 mmHg [56] at 303K.

The pressure transducer (Consolidated Electrodynamics, California, type 4-353-0001) was an electronic type having a range of 0 - 0.5 psia. The transducer was used in conjunction with a digital multimeter (Thurlly Electronics Ltd., type 1503-HA). The response of the transducer/digital multimeter was linear and reversible over the pressure range used.

The extension of the spring was determined, with reference to a fixed point on the balance case using a cathetometer (precision $1x10^{-5}$ m). The spring was calibrated in air by hanging weights (Cahn Instrument Co. calibration weights) to cover a range of extension greater than that in normal usage. The spring was found to behave both linearly and elastically over this range.

All outgassing prior to the isotherm measurements was carried out for a minimum of 24 hours and to a residual pressure of $<10^{-3}$ Torr. For the measurement of the isotherm the samples were outgassed for 24 hours at temperatures of ambient to 773K, or were heated in air in situ at 423 - 773K for 24 hours prior to outgassing at 423K for 24 hours to a residual pressure of under $8x10^{-4}$ Torr. Temperature control was to +/- 2K using a Stanton Redcroft LVP-C.

Buoyancy corrections were negligible. The adsorptions were expressed in terms of micro-grammes of water adsorbed per gramme of sample, and in terms of micro-grammes of water adsorbed per unit of external area of the sample.

3.7 Fourier Transform Infra Red Spectroscopy

The cells used for infra red studies of calcium hydroxide samples were:

(1) A reflectance cell consisting of a sample holder, in which the pure sample is placed, positioned in an array of mirrors which directs the laser beam onto the sample surface and a second array of mirrors to transmit the reflected and refracted light into the detector;

(2) A variable temperature cell consisting of a cell holder supported within a vacuum jacket by a screw threaded retaining ring at the top of the chamber. The cell was connected to an outgassing rig consisting of a rotary pump, a liquid nitrogen trap and two connections for the attachment of flasks containing desired adsorptive; and

(3) A KBr disc holder consisting of a steel plate having a 1 cm well in the centre into which the disc was secured by a push-fit holding ring.

All spectra were recorded on a Perkin Elmer Model 1710 Infrared Fourier Transform spectrometer. The instrument had the following essential features:

(a) an optical unit;

(b) a visual display unit with a keyboard;

(c) a microprocessor control and data processing system;

(d) a model PP1 plotter printer.

Spectra were computed from interferograms by Fourier Transformation. The instrument had a single beam and sample spectra were obtained from the ratio of spectra with a

sample in the beam against background spectra obtained without a sample. Each spectrum obtained was stored in the instrument, displayed on the visual display unit and subsequently stored on floppy disc. The displayed spectra were plotted on the plotter printer. The displayed spectra could be manipulated by the use of a range of data processing facilities which were controlled from the keyboard.

For measurement of reflectance infra red spectra the samples were placed in the sample "cup" and the surface of the sample smoothed by pressing down with, and moving in a circular fashion, a microscope slide. The cup was then placed in the reflectance attachment.

For measurement of transmission infra red spectra at room temperature and elevated temperatures KBr discs containing calcium hydroxide material in a weight ratio of ca. 100:1, favouring the KBr, were prepared by pressing the powdered mixture (ca. 0.3 g) at 10 tons in^{-2} for 1 minute in a steel die.

3.8 Ultra Violet Spectroscopy

The cell used for ultra violet studies of calcium hydroxide samples was a reflectance type which consisted of a holder which held a disc of sample prepared by pressing ca. 0.5 g of sample in a 1" die at a pressure of 1 ton.

All spectra were recorded on a Perkin-Elmer Lambda 9 UV/VIS/NIR spectrophotometer. The instrument had the following essential features:

(a) an optical unit;

(b) a visual display unit with a keyboard;

(c) a microprocessor control and data processing system; and

(d) a printer plotter.

The instrument had a single beam and sample spectra were obtained from the ratio of spectra with a sample in the beam against a spectrum of a blank. Each spectrum obtained was plotted on the printer plotter as the sample was being scanned.
Sample spectra were obtained by running a background sample comprising a calcium hydroxide free from ultra violet absorbing species, then running the sample spectrum. The microprocessor in the spectrophotometer subtracted the background spectrum from the sample spectrum and printed the result on a printer plotter attachment.

3.9 Scanning Electron Microscopy

Morphological studies were carried out using a Cambridge Stereoscan 250 electron microscope. A schematic diagram of a scanning electron microscope is shown in Figure 3.5. The samples were prepared for the microscope by preparing a suspension in acetone (ca. 0.05 g ml^{-1}), placing a few drops of the suspension onto a 1 cm aluminium stub, allowing the acetone to evaporate off to leave a layer of dispersed particles, and coating the particulate layer with a layer of gold (ca. 4500 Å thick) by use of a sputter coater. The images were produced by scanning the sample in the microscope with a 10 keV or 20 keV electron beam and the images were recorded by photographic means.

Sputter coating was accomplished using a SEM Coating Unit E5000 (Polaron Equipment Ltd.) sputter coater which has the following essential features:

(a) A bell jar attached to a base connected to a rotary vacuum pump;

(b) A "target" of the material to be deposited at the top of the bell jar, and connected to an electrical lead;

(c) A water cooled block as the specimen stand;

(d) A device for leaking argon into the bell jar; and

(e) A vacuum gauge (range 0 - 1 Torr).

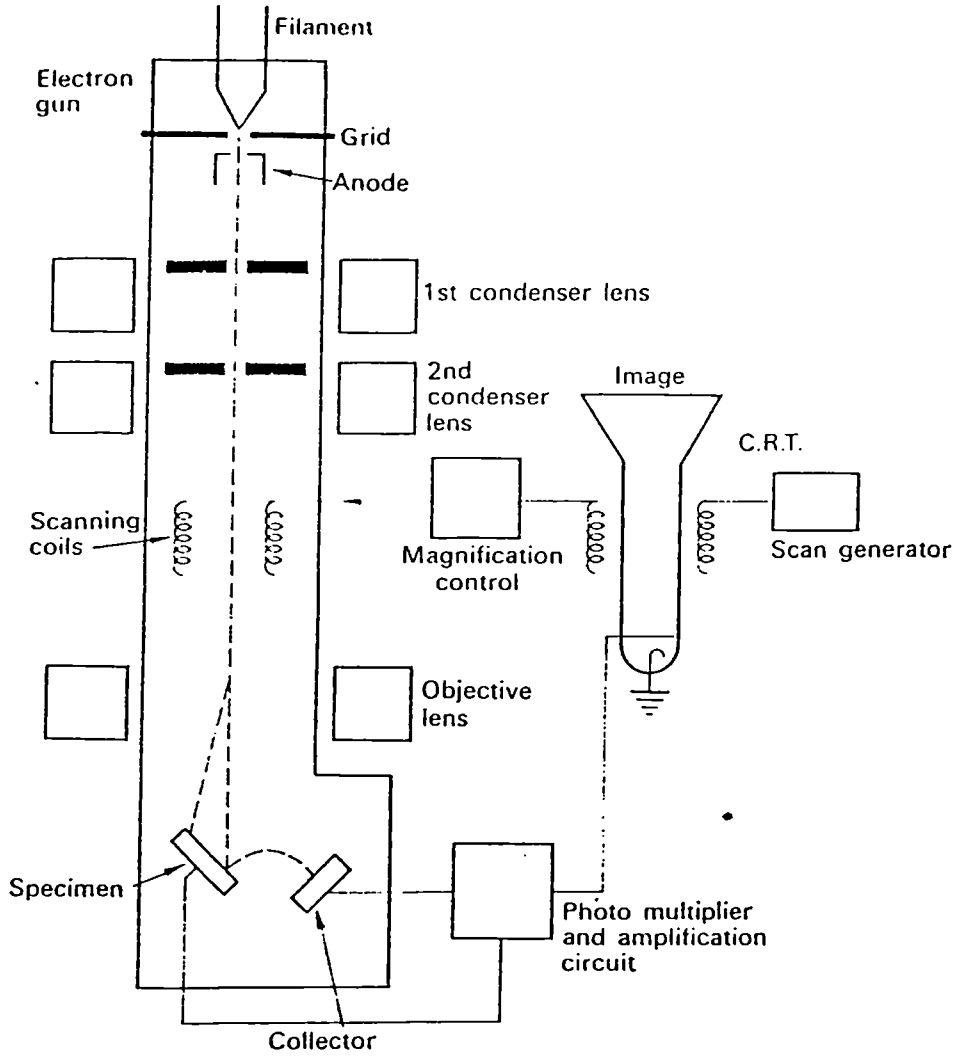

Figure 3.5 Schematic of a Scanning Electron Microscope.

Sputter coating is a low pressure coating technique which allows the specimen to be bombarded with metal particles from all sides. It is only used with gold, gold-palladium and aluminium as other materials are difficult to sputter. A relatively high pressure is used for this technique of the order of 10^{-2} torr and great care must be taken to eliminate all likely sources of contamination such as solvents, oil vapour, water vapour, etc.

The coating thickness is derived by use of the following equation:

$$T(Å) = mA \times kV \times t \times k \qquad \textbf{Equation 3.3}$$

where, T(Å) is the coating thickness in Angstroms;

mA is the dial reading in milliamps;

kV is the high tension setting in kilovolts;

t is the sputter time in seconds; and

k is the constant for the gas (5 for argon).

The argon gas is ionised and the positive gas ions etch the surface of the cathodic target to produce small particles of metal. The metal particles are deposited onto the cooled anode, where the specimen is placed, in random order due to collisions between the metal and gas ions. In this way the whole of the surface of the specimen is coated and a conducting layer is formed. The graininess of the coating is dependent on the conditions used.

3.10 Transmission Electron Microscopy

Samples were prepared for electron diffraction and crystal thickness determination by suspending the sample material in acetone (ca. 0.05 g ml^{-1}), placing one drop of the suspension on to a carbon coated copper grid (ca. 3 mm diam.) and allowing the acetone to evaporate, leaving a few particles of sample on the grid.

All samples were examined using a JEOL 100CX transmission electron microscope. A schematic diagram is shown in Figure 3.6 . The electron beam in the microscope is a monochromatic beam operated at 100 keV.

3.10.1 Crystal Thickness Determination

Thicknesses of crystals are determined by imaging an isolated crystal and "spotting" the surface of the crystal by concentrating the electron beam on the surface of the crystal for 15 - 30 seconds. This has the effect of depositing "contaminants" onto the upper and lower crystal surfaces. By rotation of the microscope stage and using a high magnification (up to 300,000x) the upper and lower contaminant spots can be viewed, and the image photographed. Knowing the degree of tilt of the microscope stage, the magnification used and the degree of enlargement of the photographic positive, the crystal thickness can be determined (Figure 3.7).

3.10.2 Electron Diffraction

Electron diffraction patterns of the calcium hydroxide materials were obtained using the JEOL 100CX electron microscope, by withdrawing the objective apertures from, and inserting a field defining aperture into the imaging system.

3.10.3 Freeze-Etch Microscopy

Freeze-etch microscopy, also known as freeze-fracture microscopy, was carried out on calcium hydroxide material samples.

The freeze-etch method involved:

(1) Taking freshly precipitated calcium hydroxide material samples and, before the drying step, preparing an ethanolic suspension thereof;

(2) Crash freezing the ethanolic dispersion to liquid nitrogen temperature in copper rivets;

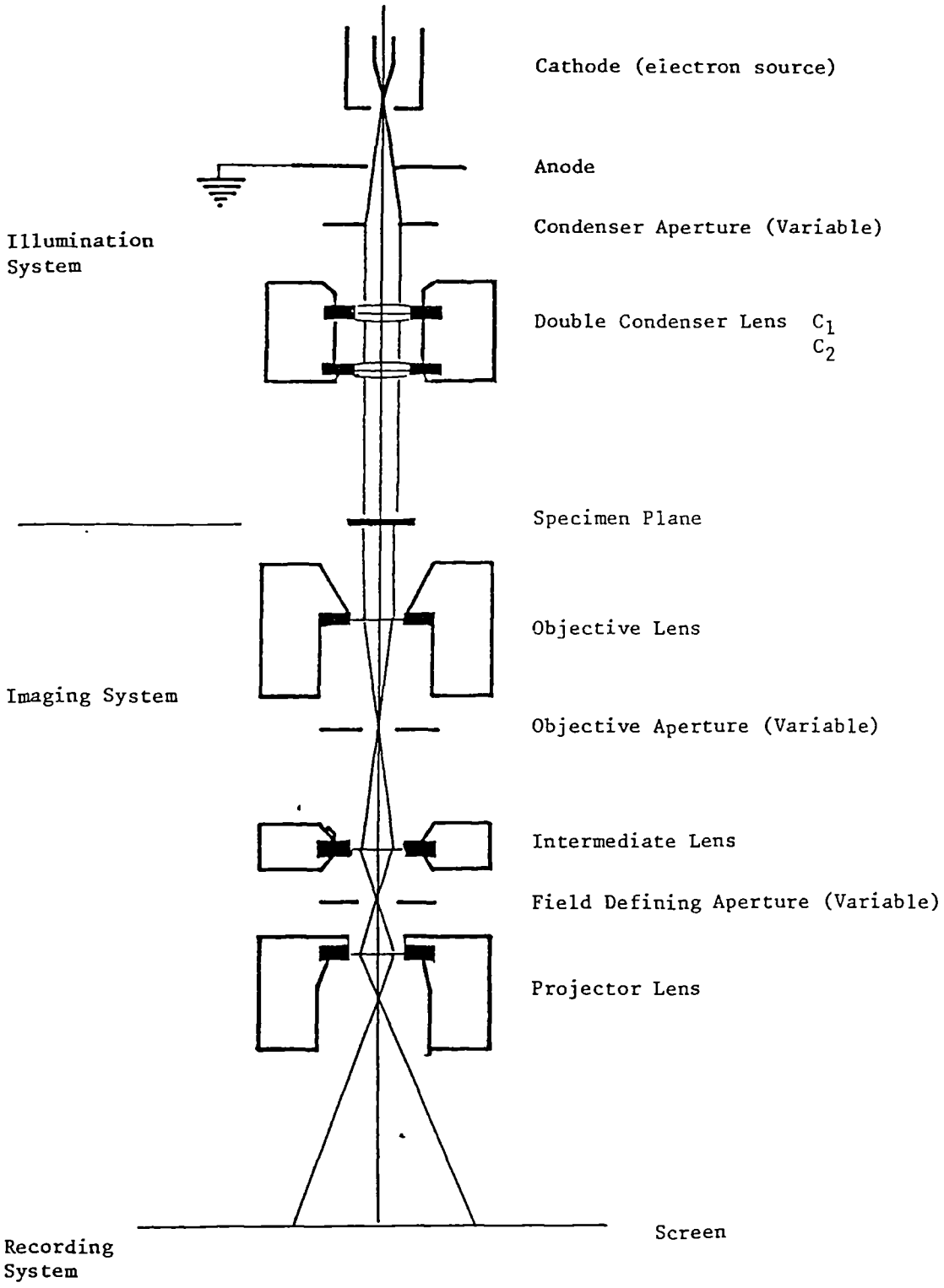

Figure 3.6 Schematic of a Transmission Electron Microscope.

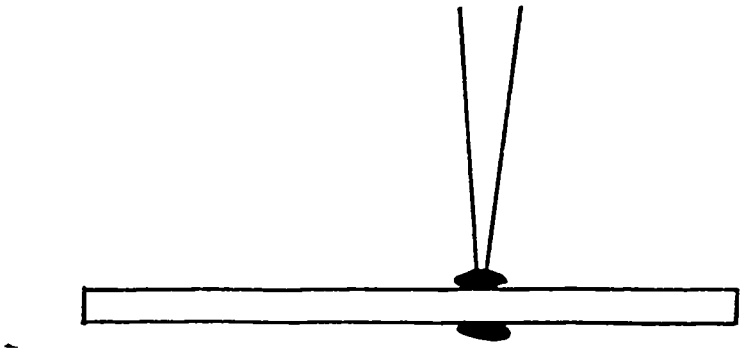

(a) Focussing the electron beam on the surface of the sample causes condensation of organic matter onto the upper and lower surfaces.

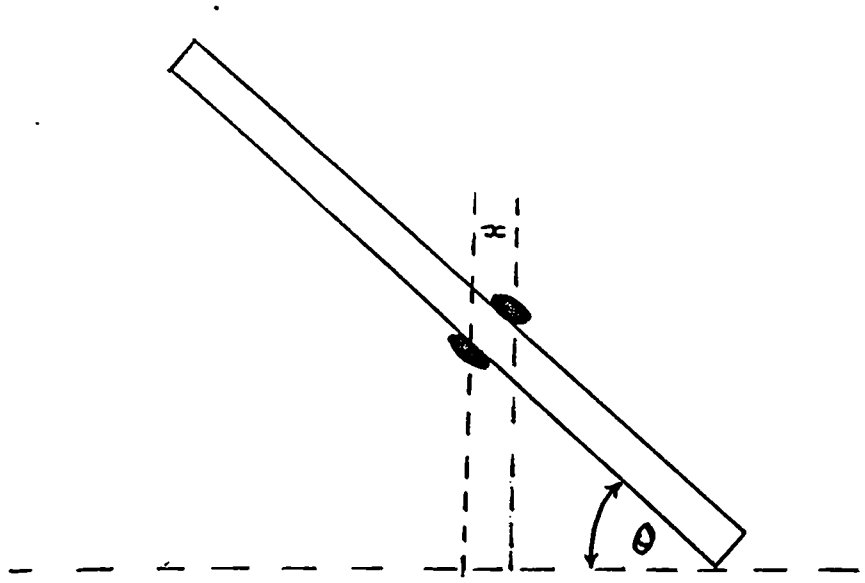

(b) Tilting the sample stage permits viewing of the condensate on both the upper and lower surfaces. The apparent distance between the two deposits (x) is then measured. The sample thickness is then given by x cos θ

Figure 3.7 Thickness Determination by Transmission Electron Microscopy.

(3) Production of a fracture face under a vacuum of ca. 10^{-6} Torr;

(4) Replication of the fracture surface with platinum/carbon and carbon; and

(5) Examination of the platinum/carbon replica in a JEOL 100CX transmission electron microscope.

3.11 X - Ray Photoelectron Spectroscopy

X - ray photoelectron spectroscopy (XPS), also known as electron spectroscopy for chemical analysis (ESCA), was carried out on prepared calcium hydroxide, silylated calcium hydroxide and the calcium hydroxide - organo-silicon composite using a Kratos ES 300 X-ray photoelectron spectrometer (Figure 3.8).

The spectrometer basic unit consists of a support bench on which is mounted a sample analysis chamber pumped to a vacuum of $< 10^{-7}$ torr by a trapped diffusion pump, with a dual anode X - ray source (ion sublimation pumped) variable source slit and various accessory ports. Above this is mounted a 127 mm radius, 180° deflection hemispherical analyser (Figure 3.9) enclosed by a mu - metal screen. Electrons are directed to the analyser by a retarding lens and pass through a collector slit into the electron multiplier, from which pulses are fed into the data handling system. Control electronics for the analyser, X - ray source, vacuum gauges etc., are rack mounted alongside the spectrometer. Sample insertion is achieved in less than 5 minutes via a rotary pumped fast insertion lock. The sample is located on the end of a sample probe which can be heated or cooled as required.

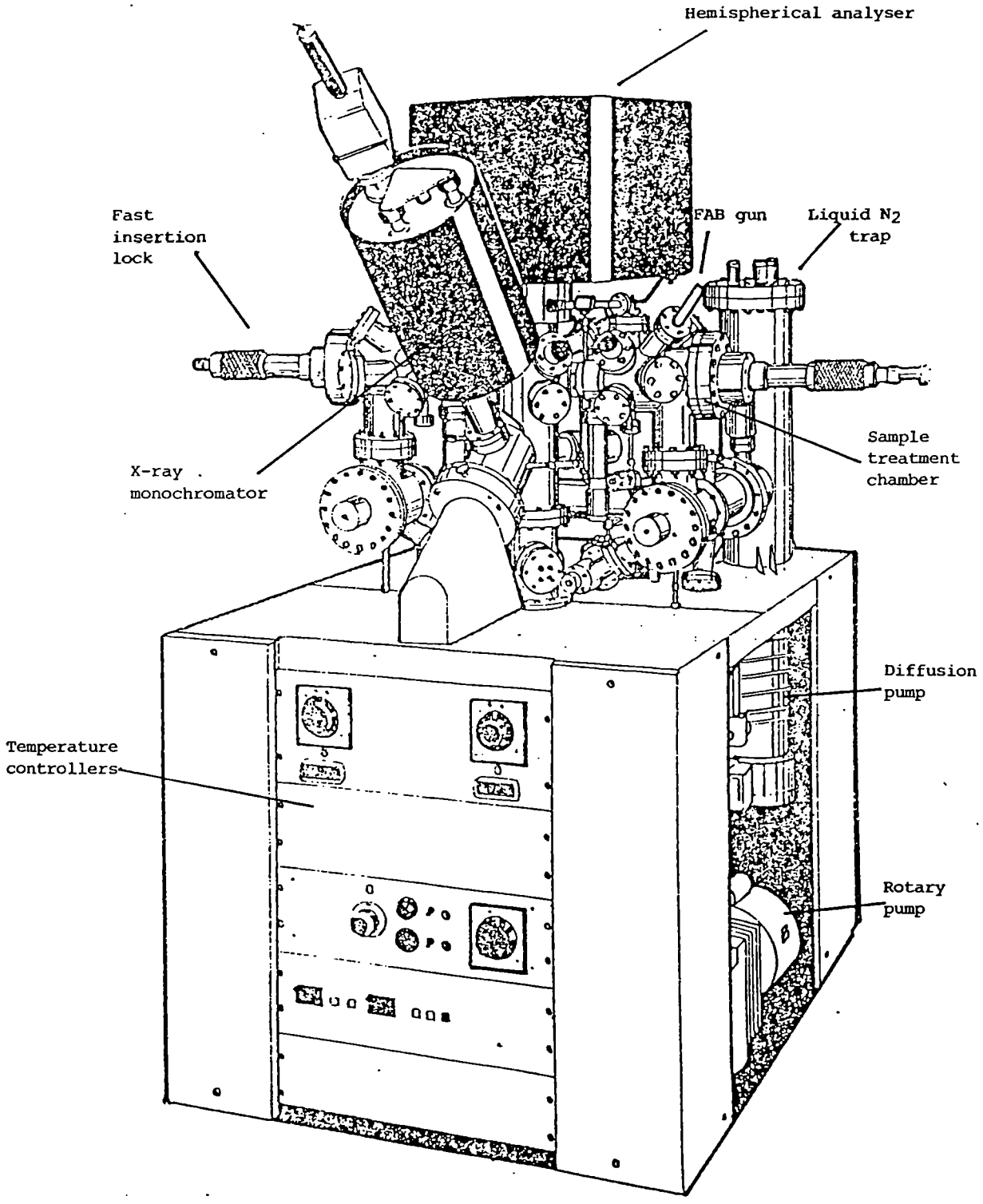

Figure 3.8 X-Ray Photoelectron Spectrometer.

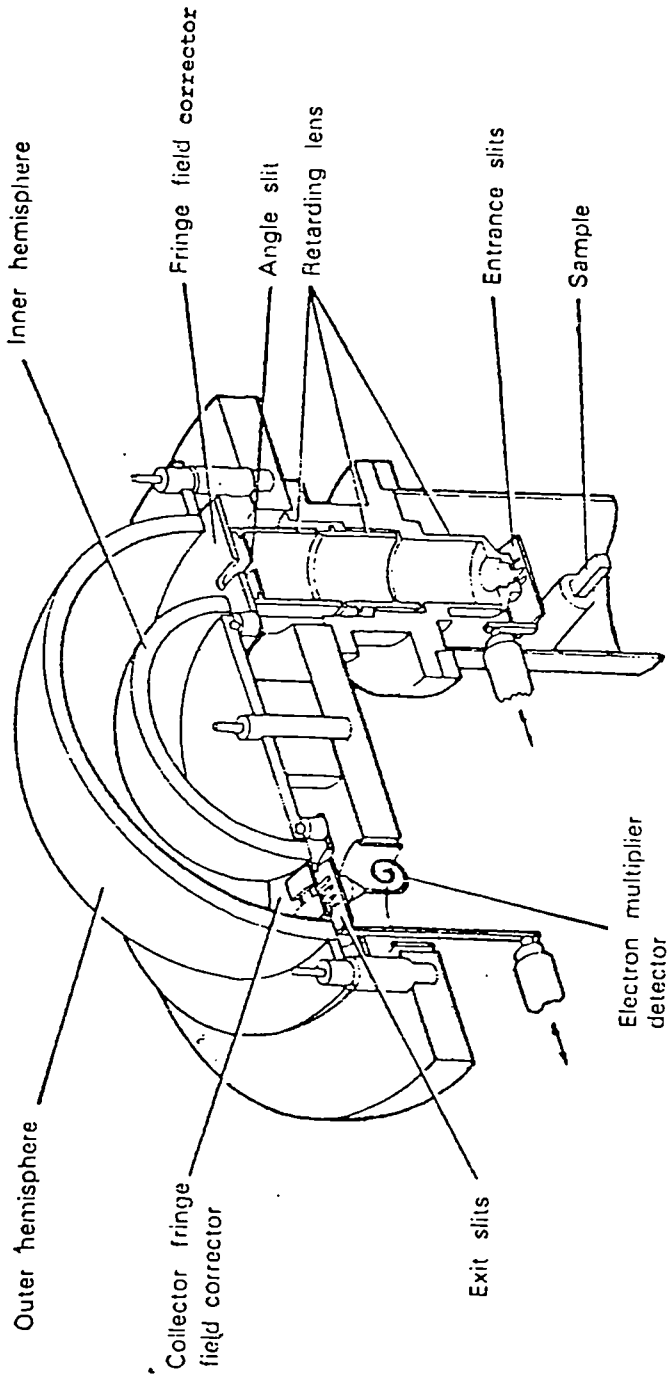

Figure 3.9 Hemispherical Analyser for XPS.

4. PRINCIPLES

4.1 Gas Adsorption

4.1.1 Introduction

Adsorption [57] in the context of the gas-solid interface denotes the enrichment (or depletion) of one or more components in a surface layer between the two bulk phases. The forces may be chemical and give rise to chemical adsorption (chemisorption) or they may be physical and give rise to physical adsorption (physisorption). Chemisorption involves the sharing or transferring of electrons between the adsorbed species and the surface atoms or ions in the solid. Physisorption is dependent on intermolecular attractive and repulsive forces.

The adsorbed species make up the "adsorbate" while the gas phase is termed the "adsorptive". The solid is the "adsorbent". Where penetration of gas into the solid phase is thought to occur it mat be appropriate to use the term "sorption". The related terms are sorbate, sorptive and sorbent [53].

4.1.2 Physisorption

When a gas comes into contact with an adsorbent, the molecules of the gas reach an equilibrium between the gaseous and the solid phase.

The atoms, or atomic groups on the surface of a solid do not completely exchange their own valence electrons with those nearby (gas molecules), there are some residual valences (Van der Waals type) which can combine labilely with liquid or gas molecules in forming their interaction field. This occurs particularly when the structure of the solid is rich in interstices and ultramicroscopic pores, forming a highly developed irregular surface.

An equilibrium is always achieved during adsorption, the quantity of gas adsorbed is a function of temperature, pressure and characteristics of the adsorbate and adsorbent. At constant pressure and temperature adsorption depends entirely on the nature of the adsorbate and adsorbent.

Physisorption involves the interaction between the potential field of the adsorbent and the electronic configuration of the adsorbate molecules. In the simplest case the interaction will only involve nonspecific forces known as London forces [58] and short range repulsion forces. Where specific adsorbate-adsorbent interactions also contribute to the adsorption energy, the total energy of physisorption can be expressed [59] as:-

$$\Phi = \Psi_D + \Psi_R + \Psi_{F\mu} + \Psi_{FQ} + \Psi_p \qquad \textbf{Equation 4.1}$$

where ($\Psi_D + \Psi_R$) is the non-specific contribution (dispersion and repulsion) and ($\Psi_{F\mu} + \Psi_{FQ} + \Psi_p$) is the specific contribution. Ψ_p, the polarisation term, is usually insignificant but both $\Psi_{F\mu}$, the field-dipole and Ψ_{FQ}, the field gradient-quadrupole term may be significant when the adsorbate molecules possess permanent dipole or quadrupole moments [60].

4.1.3 Adsorption Isotherms

For a gas-solid system maintained at a constant temperature (T) below the critical temperature of the gas, the volume (V) adsorbed by a unit mass of adsorbent is dependent on the gas concentration which is expressed in terms of relative pressure.

$$V = f(p/p^o)_{T,gas,solid} \qquad \textbf{Equation 4.2}$$

where p^o is the saturated vapour pressure of the adsorptive.

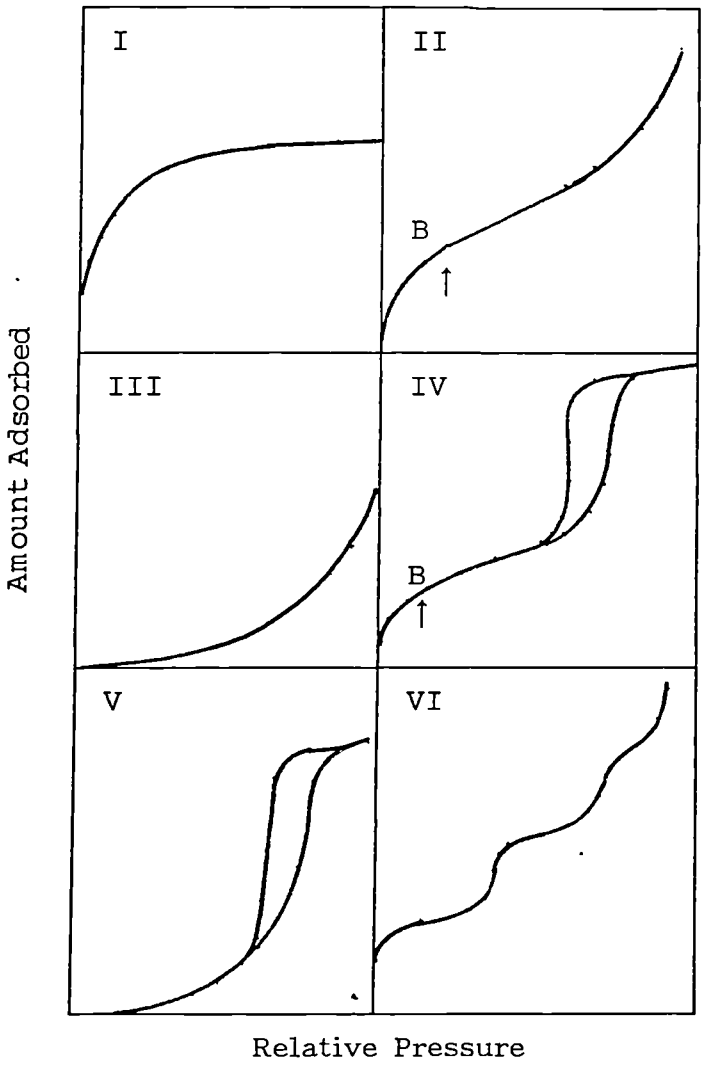

Figure 4.1 IUPAC Classification of Adsorption Isotherms.

Most of the tens of thousands of isotherms reported in the literature fall into one of six classes (Figure 4.1). Types I to V were originally the Brunauer, Deming, Deming and Teller (BDDT) [61] classification. Type VI was added subsequently. This classification has been approved by the IUPAC [57].

The differences in shapes of the six types of isotherms reflect differences not only in the interaction energies involved but also in the porosities of the solids. Within this context pores can be classified according to their width (d).

The Type I adsorption isotherm is identified by a steep initial region at low pressure followed by a plateau which extends to high relative pressures.

For many years Type I isotherms were interpreted in terms of the Langmuir Theory of monolayer adsorption [62,63]. It is now widely accepted that this mechanism is not applicable in the case of physical adsorption. The adsorption process is considered to be one of volume filling rather than surface coverage [64]. The adsorbate molecules are thus envisaged as forming a liquid-like phase within the pores as distinct from the layer-by-layer formation on the pore walls, hence the concept of micropore filling [53,65].

The width of a micropore is of molecular dimensions. As a result the adsorption fields of opposite walls will overlap leading to a much deeper potential energy well. Everett [66] has considered a range of models, including a slit-shape pore with walls one molecule thick, a cylinder tunnelled from an infinite slab of solid and a slit formed from parallel slabs of solid. The extent of enhancement of the interaction potential was shown to be dependent upon the collision radius, r_o, of the adsorbed molecule and the pore radius, r, the enhancement being considerably greater in cylindrical pores than in slit-shaped pores.

A different mechanism of micropore filling [53] is thought to operate in wider micropores where the enhancement of the interaction energy and enthalpy of adsorption is relatively

small and the adsorption is now thought to be the result of a secondary process, the co-operative effect. Where a monolayer is initially formed on the walls of the pore; if molecules 1 and 2 then happen to condense opposite one another there is an increased probability that 3 will condense. This in turn will promote the condensation of 4 and further molecules. Because the co-operative mechanism occurs rapidly the process can be considered as a form of multilayer formation within wider micropores, without the formation of a liquid meniscus.

Type II isotherms are obtained with non-porous or macroporous adsorbents and represent unrestricted monolayer-multilayer adsorption. The adsorption mechanism involved can be inferred from the sharpness of the "knee". A sharp "knee" indicates that the net heat of adsorption is relatively high and that molecules are therefore initially adsorbed in a layer one molecule thick until a large proportion of the surface is covered. The position known as "point B" at the beginning of the linear portion of the isotherm has been identified as the stage at which the "statistical" monolayer is complete.

With a reduction in the net heat of adsorption the "B point" becomes less well defined until a Type III isotherm is evident. There is a change in adsorption mechanism from one based on monolayer-multilayer formation to one based on adsorbate-adsorbate cooperative adsorption without a well defined monolayer being formed.

When the adsorbents have pores that are mesoporous instead of a Type II isotherm a Type IV is obtained, and similarly Type V instead of Type III. The characteristic feature of these isotherms is the hysteresis loop, which is associated with capillary condensation taking place in mesopores, and a limiting uptake over a range of high p/p^{o}.

The Type VI isotherm represents a stepwise multilayer adsorption on an energetically uniform non-porous surface. The step represents the monolayer capacity for each adsorbed layer.

A number of isotherms do not fit the IUPAC classification easily. These include isotherms with characteristics of more than one type such as mixed Type I / Type IV isotherms.

4.1.4 Monolayer Capacity and Surface Area

The use of gas adsorption is most widely used as the standard procedure for the determination of the surface area of finely divided and porous materials. The parameter which the isotherm yields is the monolayer capacity, V_m, expressed as a gas volume at STP. The multiplication of V_m by the area occupied by an individual molecule gives the calculation of the surface area. The equation to use is

$$A_{BET} = V_m \cdot \frac{a_m L \times 10^{-18}}{22414} \qquad \textbf{Equation 4.3}$$

where V_m is expressed in cm^3g^{-1}.

In the equation a_m is the cross-sectional area of the adsorbate molecule in nm^2, L is Avogadro's number, 22414 cm^3 is the molar volume of an ideal gas at STP and the surface area A_{BET}, is given in m^2g^{-1}.

The surface area can be calculated directly from Type II or Type IV isotherms from the B point.Type III and Type V isotherms do not have a knee and consequently the monolayer volume cannot be calculated directly from these isotherms.

When considering Type I isotherms where micropore filling occurs, rather than surface coverage by monolayer and multilayer formation, the values of surface area calculated are found to be unrealistically high. It remains useful, however to retain the apparent surface area as a "finger print parameter" [67]. It is useful to distinguish between the "internal" and "external" surface area. The external area is the area remaining after all

the micropores have been filled and the internal area is the surface area inside the pores. Neither the external nor internal area can be calculated directly from the isotherm.

4.1.5 The BET Theory

The most common method for the calculation of surface area is from the Brunauer-Emmett-Teller (BET) [68] theory. Their theory was based on the earlier theory of Langmuir [62] with the extension of the theory beyond a single monolayer model to multilayer adsorption. The assumptions made are that dynamic equilibrium exists within each layer and the rates of evaporation and condensation are equal in all layers except the first. The heat of adsorption is equal to the molar heat of condensation in all layers but the first. The theory also assumes that at a relative pressure of unity the adsorbate condenses to a liquid like film. The resulting equation is:

$$\frac{p}{v(p^o - p)} = \frac{1}{V_m c} + \frac{(c-1)}{V_m c} \cdot \frac{p}{p^o} \qquad \textbf{Equation 4.4}$$

where V_m is the monolayer capacity and "c" is a constant. Both V_m and "c" can be obtained from a plot of p/p^o against $p/V(p^o - p)$, where V is the volume of gas adsorbed at a given relative pressure, expressed in $cm^{-3}g^{-1}$ at STP. The plot has a linear region over a limited range of relative pressure (Figure 4.2). The slope "s" and intercept "i" from this linear portion may be used to calculate the monolayer capacity V_m and the BET constant "c" as follows:

$$V_m = \frac{1}{s+i} \qquad \textbf{Equation 4.5}$$

$$c = \frac{s+1}{i} \qquad \textbf{Equation 4.6}$$

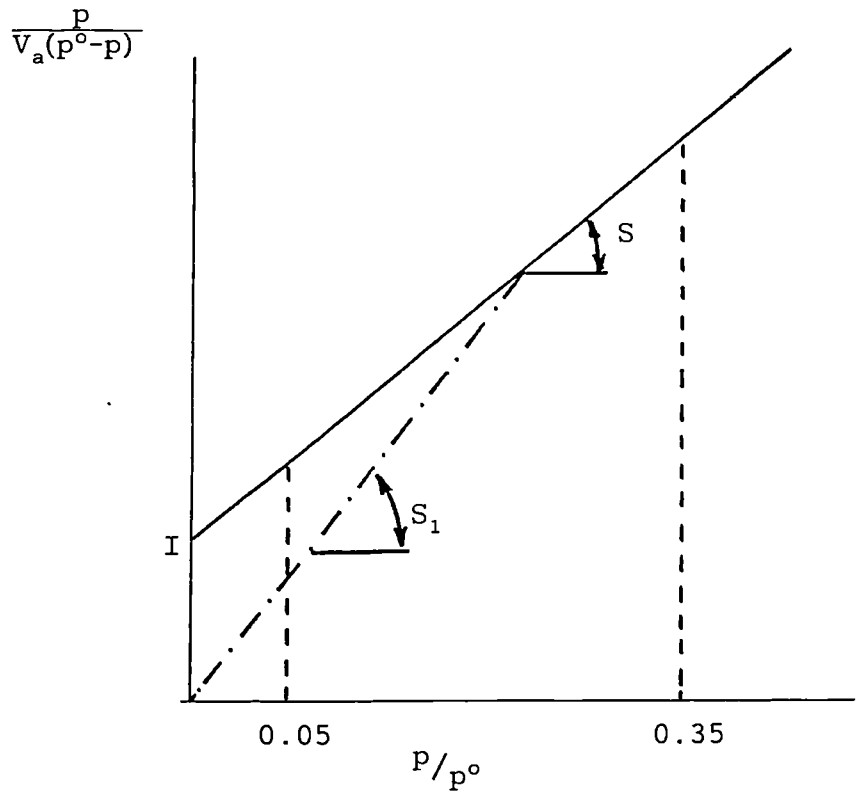

slope $S = \frac{c-1}{V_m.c}$, intercept $I = \frac{1}{V_m.c}$, $V_m = \frac{1}{S+I}$

The equation used in the calculations, according to the Brunauer-Emmet-Teller (BET) method, is as follows:

$$\frac{p}{V_a(p^\circ-p)} = \frac{1}{V_m.c} + \frac{(c-1)}{V_m.c} \cdot \frac{p}{p^\circ}$$

p = equilibrium pressure
p° = saturation pressure
V_a = volume of gas adsorbed at p
V_m = volume of gas adsorbed corresponding to monolayer coverage
c = constant expressing the adsorption energy
p/p° = relative pressure of the adsorbed gas

Single point ignores the intercept I, thus $V_m = \frac{1}{S_1}$

Figure 4.2 Calculation of Surface Area from the BET Equation.

The range of linearity of the BET plot varies considerably according to the chemical nature of both the adsorptive and the adsorbent. According to the original work of Brunauer et al [68], for Type II and Type IV isotherms the linear range should be between relative pressures 0.05 and 0.35. In the case of a Type I isotherm the range of linearity is found to be shorter and displaced to lower relative pressures between $p/p^o = 0.1 - 0.1$ [60].

The "c" constant, which is a free energy term related to both the enthalpy and entropy of adsorption [69], gives an indication of the sharpness of the "knee". High "c" values (>100) indicate a sharp "knee", while low "c" values (<10) correspond to a poorly defined "knee". If the "c" value is less than 2 the isotherm is either Type III or Type V.

Deviations between the BET theory and experimental results have been emphasised [53]. They include:

(1) The degree of heterogeneity has been neglected. This is especially important at sub monolayer coverages;

(2) The theory is restricted to the forces between the adsorbent and the adsorbate molecules neglecting the forces between an adsorbate molecule and its neighbour in the same layer;

(3) The assumption that all molecules in all layers after the first should be treated as equivalent: one would expect the interaction to diminish significantly as distance from the surface increases corresponding to an equivalent decrease in adsorptive potential;

(4) The assumption that condensation to a liquid like film occurs at a relative pressure of unity: there are several cases in which the number of molecular layers remains finite even when the solid is exposed to saturated vapour [70].

4.1.6 Molecular Cross Sectional Areas

The technique of nitrogen adsorption is now a recognised procedure for the determination of surface area and porosity. The nitrogen adsorbate is convenient to use, as liquid nitrogen baths are readily available and there is no difficulty in measuring the saturated vapour pressure.

The cross-sectional area of a nitrogen molecule, a_m, can be calculated from the liquid density as 0.162 nm^2. This value has been confirmed by use of transmission electron micrographs [71] with agreement within +/- 5% for a wide range of nonporous materials. The exceptions have been attributed to localisation in the monolayer [72]. The localisation is due to the quadrupole moment of the N_2 molecule which gives ride to specific Ψ_{FQ} contribution to the interaction energy. This has lead to criticism of the use of N_2 and the suggestion that non-polar adsorbates might be more appropriate. The disadvantage of using a non-polar adsorbate is that the interaction is not strong enough to give a sharp "knee" to the isotherm and the precision with which Point B can be located is less than when N_2 is used.

In some cases a high degree of specificity is involved in the interaction. In water isotherms the areas calculated are often very different from the corresponding N_2 areas. The explanation for these variations when carbon is the adsorbent is that the adsorption mechanism is different.

Nucleation of water molecules occurs on polar sites followed by "cluster" growth by a hydrogen bonded network which leaves areas of surface uncovered until high pressures. The monolayer is therefore a very open structure and therefore the monolayer capacity cannot be determined as a total surface area.

Where appropriate it is best to calculate an apparent molecular cross-sectional area from the N_2 BET surface area. This will give an indication of the distribution of adsorption sites and hence the chemical nature of the surface.

4.1.7 Capillary Condensation and Hysteresis.

In the multilayer region of a Type IV isotherm the adsorption at a particular relative pressure is determined not only by the adsorbate-adsorbent interactions but also by capillary effects. The Kelvin equation [73] is used as an aid to calculate mesopore size from the capillary condensation effect. For a spherical meniscus the equation can be written as [74]:

$$\ln(P/p^{o}) = -(2\gamma V_L/rRT)\cos\sigma^* \qquad \textbf{Equation 4.7}$$

where gamma and V_L are the surface tension and molar volume of the adsorbate in liquid form, R is the gas constant and σ^* is the angle of contact between the liquid and the wall of the pore.

The Kelvin equation gives the relative pressure at which liquid adsorbate begins to evaporate from a "pore" of radius $r = r' - t$, where r' is the actual pore radius and t is the thickness of the multilayer adsorbed on the walls of the pore. The process is referred to as capillary evaporation and forms the basis for the conventional explanation for the desorption branch of the hysteresis loop of a Type IV isotherm. The adsorption branch is generally explained in terms either build up of a multilayer which increases in thickness as the pore is filled, or in terms of capillary condensation. The latter occurs in all pores of radius r as soon as the relative pressure reaches the valve given by insertion of r in the Kelvin equation.

The IUPAC [57] has given a classification of four types of hysteresis loop (Figure 4.3). The hysteresis loops exhibit a wide variety of shapes. The two extremes are H1 and H4, the former shows branches which are vertical whilst the latter remains almost horizontal over a range of relative pressure. H2 and H3 may be considered as intermediate between two extremes.

A common feature of many hysteresis loops is the steep region of the desorption branch leading to a lower closure point which is independent of the nature of the porous adsorptive (e.g. for nitrogen at 77K $^{p}/_{p^o}$ ~ 0.42 and for benzene at 298K $^{p}/_{p^o}$ ~ 0.17).

The shapes of hysteresis loops have often been identified with specific pore structures. Type H1 is often associated with porous materials known to consist of agglomerates or compacts of regular shape with narrow distribution of pores. Type H2 hysteresis loop is found with adsorbents with narrow necks and wide body pores (ink bottle pores). The Type H3 loop, which does not exhibit any limiting adsorption at high $^{p}/_{p^o}$ is observed with aggregates of plate-like particles giving rise to slit-shaped pores. Similarly, the Type H4 loop is often associated with narrow slit-like pores, but in this case the Type I isotherm character is indicative of microporosity. With many systems especially those containing micropores, low pressure hysteresis (indicated by dashed lines in Figure 4.3) may be observed extending to the lowest pressure attainable.

4.1.8 Low Pressure Hysteresis

When hysteresis in nitrogen isotherms is associated with capillary condensation the lower point of closure of the hysteresis loop is frequently found to be 0.42 p^o(the Harris point) [75]. With certain systems however hysteresis is observed even in the monolayer region of the isotherm. The phenomenon is known as low pressure hysteresis (LPH). The hysteresis may extend all the way down the isotherm and it may be accompanied by a small residual adsorption after re-outgassing at the end of the desorption branch.

4.2 Surface Area Measurement

Accurate measurement of the amount of gas adsorbed by the solid allows the determination of the adsorbent surface area. The method is based on the experimental determination of the adsorption and desorption isotherms for different gases such as nitrogen, argon, krypton, butane and others.

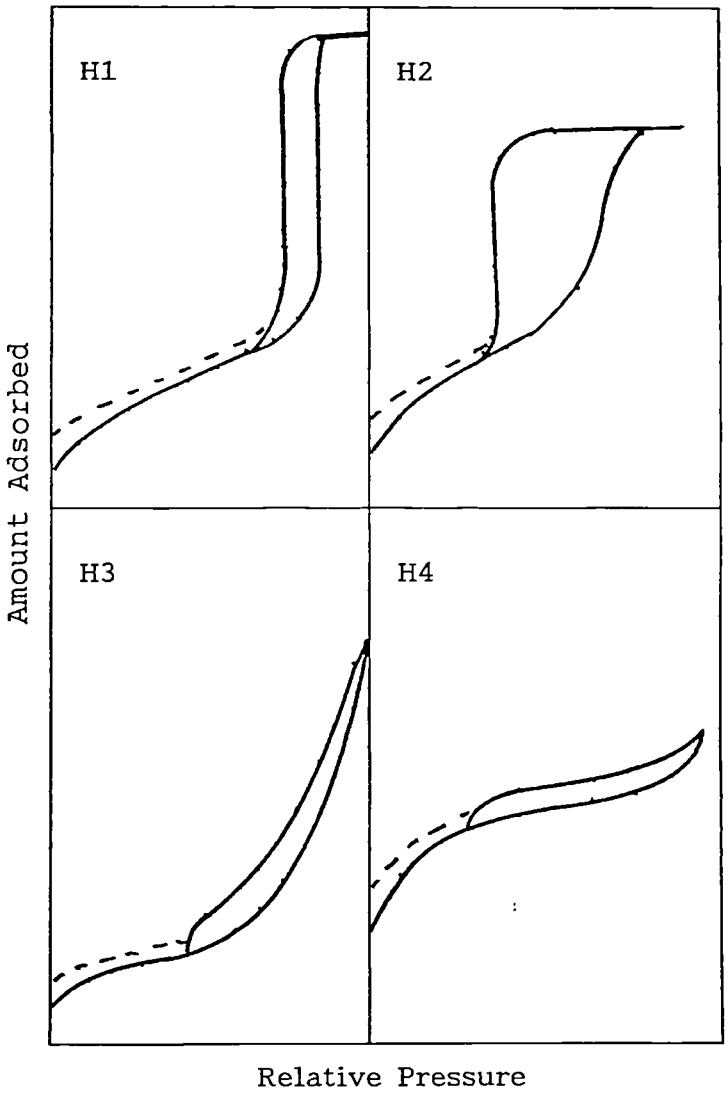

Figure 4.3 IUPAC Classification of Hysteresis Loops.

Emmett and Brunauer stated that if Van der Waals gas adsorption is measured at the boiling point of the gas and at relatively high pressures, the result represents either multimolecular adsorption or capillary condensation.

In fact, a surface area covered with a complete layer of molecules may sometimes adsorb a second layer of molecules if the forces of interaction between the adsorbed molecules and those in the gaseous phase are sufficiently strong.

It is difficult to decide with precision when adsorption of the first layer is complete and subsequent layers start to form. However, to calculate the surface area of the adsorbent, the volume of gas required to form a monolayer must be determined, and the fraction of molecules of the adsorbed gas must also be known; this requires special techniques.

The technique most widely used today is based on the theory of Brunauer, Emmett and Teller equation (B.E.T. equation).

In a given system "V_m" (volume of gas required to cover a surface with a monomolecular layer) and c are constant, so that the BET equation (Equation 4.4) can be expressed as:

$$\frac{p}{V_a(p^o - p)} = \frac{mp}{p^o} + b \qquad \textbf{Equation 4.8}$$

where m and b are constants:

$$m = \frac{c - 1}{V_m c} \qquad \textbf{Equation 4.9}$$

$$b = \frac{1}{V_m c} \qquad \textbf{Equation 4.10}$$

Equation 4.8 may be transformed into a linear relationship of the type

$$y = mx + b$$

where "m" is the slope of the straight line and "b" is the intercept of the ordinate. Plotting $p/V_a(p^o - p)$ against p/p^o a straight line is obtained. Further studies have shown that the BET linearity is fulfilled in a relative pressure range of $p/p^o = 0.05$ to 0.35 .

Determination of V_m, by plotting Equation 4.8, is essential for calculating the surface area.

Consequently, when the slope "m" and intercept "b" are known, "V_m" may be calculated and the surface area of the sample may be determined. It has been found experimentally that elimination of intercept b gives no more than 7% deviation in determining the specific surface area. The design of the Sorpty is based on this experimental fact.

In order to calculate the specific surface area, V_m must be converted into surface units. The conversion may be carried out as follows:

The number of molecules adsorbed that come from 1 ml of vapour (Z) is determined by using the Avogadro's number:

$$Z = \frac{6.0323}{22414} \times 10^{23} \quad \text{molecules}$$

The area covered by 1 ml of adsorbate (S_o) in the monomolecular layer is given by:

$$S_o = Z \times a \qquad \textbf{Equation 4.11}$$

where "a" is the area of the adsorbed molecules defined as:

$$a = A \times 0.866 \times \left(\frac{M}{4Nd\sqrt{2}}\right)^{2/3} \qquad \textbf{Equation 4.12}$$

where

M is the molecular weight of the adsorbate;

N is the Avogadro number;

d is the density of the adsorbate in the liquid phase.

If "S_o" represents the area covered by 1 ml of adsorbate, V_m corresponds to an area given by:

$$S = S_o \times V_m \qquad \textbf{Equation 4.13}$$

If "W" is the weight of the adsorbent, the specific surface, S_s, will be:

$$S_s = S/W \qquad \textbf{Equation 4.14}$$

For nitrogen at 77K, the molecular cross-section is 16.2 Å^2 therefore the S_o value is 4.375 m^2/ml.

4.2.1 The Frenkel - Halsey - Hill Equation

Frenkel [76], Halsey [77] and Hill [78] independently arrived theoretically at the multilayer isotherm equation (the FHH equation):

$$-\log(p/p^o) = k/(V/V_m)^r \qquad \textbf{Equation 4.15}$$

where V/V_m is the surface coverage, sometimes referred to as the number of statistical layers and r is an exponent based on the decay of the surface forces with distance. The equation can be rearranged to give:

$$\log V = (1/r) \log (kV_m^r) - (1/r) \log [\log(p^o/p)] \qquad \textbf{Equation 4.16}$$

and r can therefore be obtained from the slope of a plot of $\log[\log(p^o/p)]$ against log V.

Interest in the application of the FHH equation for analysis of isotherms was stimulated by the work of Pierce [79,80] who came to the conclusion that r = 2.75 for adsorption of nitrogen on graphitised carbon black. Over the last decade several different adsorbents have been adopted [52,81] as non-porous reference materials and these have been further studied to find how the range of applicability for a value of r depends on the nature of the adsorbent surface. The findings show [82] that for a range of non-porous oxides the value of the index r, is nearly constant ($r = 2.7 \pm 0.2$). If r is found to be low (*e.g.* r ~ 2.1) the decrease is likely to be due to the effect of capillary condensation. When r is high (*e.g.* r ~ 3) this may be due to the presence of microporosity. The value of r may also vary with some adsorbents for example organic polymers which have low energy surfaces.

The linear range of FHH plots often begins at a coverage of 1 - 1.5 layers and extends to a coverage of only 2 - 3 statistical layers. By the time 4 or 5 layers have been adsorbed the plot has frequently deviated upwards due to capillary condensation.

In the absence of porosity, experimental r values are determined by the nature of the interaction between the adsorbate and adsorbent, strong interactions giving high r values and weak interactions low values. For H_2O adsorption, reported r values vary from 2.5 for hydrophilic surfaces to 1.3 - 1.9 for hydrophobic surfaces [83,84].

The effect of porosity on the r value has been acknowledged but not always given due consideration. Within this context pores can be classified into three categories depending on whether they fill at high, medium or low relative pressures:

(a) High p/p^o : At high relative pressure capillary condensation occurs and gives rise to an upward swing of the plot;

(b) Medium p/p^o : Either a curved plot is produced or a linear plot with reduced r value. In considering linear plots, it is very important when dealing with plots which swing upward at high relative pressure to consider to what extent the effects of capillary condensation are felt in the linear range of the plot; and

(c) Low p/p^o : Micropore filling which is complete before the linear range begins will lead to an r value which is high.

4.2.2 The α_s - Method

In order to obtain a reliable value for the surface area from an isotherm with only a poorly defined knee or from a Type III or Type IV isotherm it is necessary to use a comparative method in which the isotherm is compared with that of a non-porous reference adsorbent of known surface area.

In the α_s - method [85-87] the comparison is achieved by plotting the adsorption at a particular relative pressure against α_s, which is defined as the ratio of the adsorption x, by the reference adsorbent at the same relative pressure to its adsorption x_s, at an arbitrary standard state. Invariably α_s is put equal to unity at $p/p^o = 0.4$ as, with N_2 adsorption at 77K, monolayer coverage and micropore filling occur below this while any hysteresis loop (associated with capillary condensation) is located at higher pressures. Also the isotherm is quite flat at 0.4 p^o and x_s can therefore be interpolated from the standard isotherm with some degree of accuracy.

Ideal α_s plots corresponding to the isotherms of the BDDT classification are shown in Figure 4.4 . The surface area S_α, can be obtained from the slope of the linear portions of the plots as :

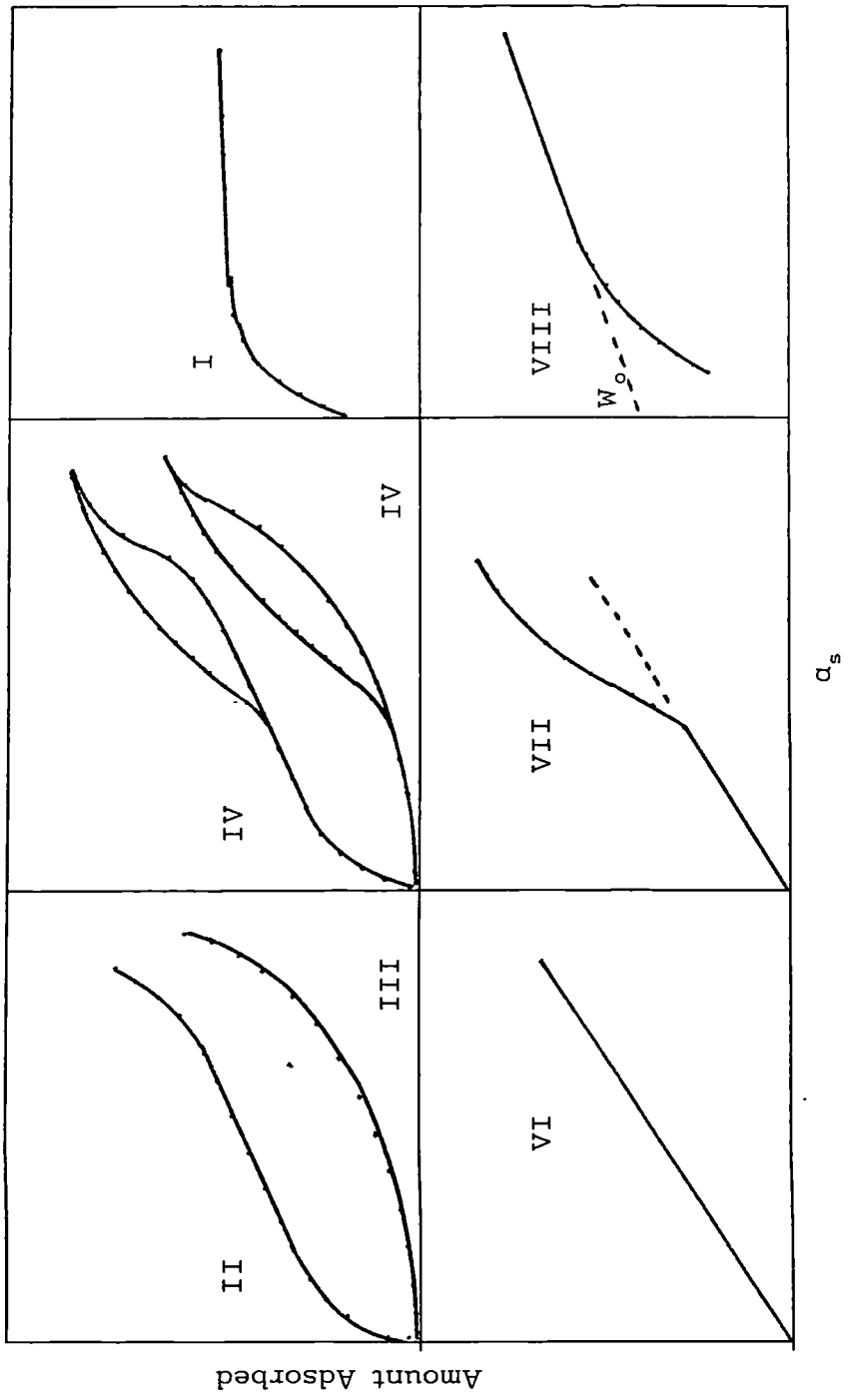

Figure 4.4 Standard Alpha-s Plots.

$$S_\alpha = (S_{ref} \,.\, slope)/x_s \qquad \textbf{Equation 4.17}$$

where,

S_{ref} = surface area of the reference

For a plot obtained from a Type I isotherm S_α corresponds to the external surface area. The intercept of such plots is proportional to the micropore volume, $W_o(cm^3\ g^{-1})$:

$$W_o = (M \,.\, intercept)/(V_N \,.\, \rho) \qquad \textbf{Equation 4.18}$$

where,

M = molecular weight of the adsorbate

ρ = liquid density of adsorbate

V_N = molar volume of an ideal gas at STP

For N_2 at 77K, $W_o = 0.00156$. intercept.

Deviations of the plots from linearity at high relative pressures are attributed to capillary condensation.

Deviations of α_s plots from the ideal shapes can lead to useful information concerning the monolayer and multilayer structure and the porosity.

Microporosity generally results in a positive intercept which often enables microporosity to be detected in adsorbents which do not give a Type I isotherm. However the influence of micropore filling on the α_s plot may be obscured by a compensating effect between restrictive adsorption in micropores and capillary condensation in mesopores. Bhambhani et al [88] have invoked this effect to explain why N_2 adsorption on two silica gels gave α_s plots which were linear to 0.5 p^o and 0.4 p^o and which back-extrapolated through the origin (indicative of no microporosity) yet gave high BET c constants and high isoteric heats of adsorption at low coverage (both indicative of microporosity).

Carruthers et al [89] have reported argon α_s plots on low area α - alumina samples which had a linear multilayer section which back-extrapolated through the origin, but a non-linear monolayer section. The non-linearity was attributed to localisation in the monolayer. N_2 α_s plots on the same samples were found to have poorer linearity and it was suggested that the formation of the localised N_2 monolayer influenced the structure of the multilayer due to the effects of quadrupole interactions.

The choice of an appropriate reference adsorbent is very important if correct conclusions are to be drawn from the α_s plots. The reference must be non-porous. Its surface should also be of a similar chemical nature to that of the sample being studied; this is particularly important if specific interactions are involved. According to Brunauer and co-workers [90] the reference should have the same c constant (calculated from the uncorrected raw data) as the sample. Parfitt et al [91] on the other hand have demonstrated that for microporous rutiles the c constant of the reference should match that of the external surface of the sample.

4.2.3 Comparison Plots & f - Plots

In the absence of standard data on a well characterised reference adsorbent the Comparison plot of Brown & Hall [92] may be adopted, in which the amount adsorbed on one solid is plotted against the amount adsorbed at the same relative pressure on another solid which is taken as an arbitrary reference adsorbent. Departures from linearity of the plot can be interpreted in terms of differences in the porosity and surface structure of the samples.

An alternative approach [93] is to plot f, the ratio of the amounts adsorbed, against relative pressure. The resulting f - plot will be horizontal in the absence of differences in the porosity or surface structure of the samples.

4.2.4 DR Plots

Dubinin and his co-workers [94] were largely responsible for the early work on the theory of volume filling of micropores. Their approach was to combine the characteristic curve principle of Polanyi [95] with the concept of micropore filling. The equation for the characteristic curve proposed by Dubinin and Astakhov [96] for the adsorption of gases by microporous carbons and zeolites can be expressed in the form :

$$V/V^{DR} = \exp(-A/\beta E_o)^n \qquad \textbf{Equation 4.19}$$

where,

V = amount of gas adsorbed at p/p^o;

V^{DR} = amount required to fill the micropores;

and

A = the affinity or differential free energy of adsorption.

and

$$A = RT \ln(p/p^o) \qquad \textbf{Equation 4.20}$$

and n, β and E_o are empirical parameters for a given system. For a microporous carbon containing a fairly narrow distribution of pore size, n = 2, and Equation 4.18 is then transformed to the Dubinin - Radushkevich equation which in linear form is :

$$\log(V) = \log(V^{DR}) - B(T/\beta)\log^2(p/p^o) \qquad \textbf{Equation 4.21}$$

where,

B = the structural constant;

and

β = a scaling factor (similarity coefficient).

The DR plot has been widely used with many reported cases of non-linearity [97-99]. These deviations have been due to several possible factors:

(1) Change in the adsorption mechanism;

(2) Change in adsorption potential with pore size;

(3) Active surface groups; and

(4) Constrictions in the micropores.

When such deviations occur the position of the V_{DR} value becomes uncertain. With many microporous carbons, linearity of the DR plot (i.e. log(V) against $\log^2(P/P_o)$) is obtained only at $P/P_o < 0.01$ and if the micropore size distribution is wide the linear range may be restricted to $P/P_o < 0.005$.

The linearity of the DR plot is not sufficient in itself to establish the existence of micropore filling. Kaganert [100] constructed linear DR plots from adsorption data of non-porous adsorbents. Reasonable agreement between monolayer volume calculated from the intercept of the DR plot and the BET method was established. Therefore Kaganer's findings are based on a process of surface coverage rather than micropore filling.

4.3 X-Ray Photoelectron Spectroscopy

X - ray photoelectron spectroscopy (XPS) involves irradiating a sample in vacuum with monoenergetic soft X-rays (typically Al Kα; 1486.6 eV or Mg Kα; 1253.6 eV) and measuring the energy of the emitted electrons. The X - ray photons interact with the atoms of the sample, causing electrons to be emitted by the photoelectric effect.

The fundamental equation for the photoelectric process is based on the energy - conservation principle, being:

$$h\nu = E^f(k) - E^i + E_{kin} \qquad \textbf{Equation 4.22}$$

where,

$h\nu$ = energy of the incident photon

$E^f(k)$ = the total energy of the final state with a hole in the *k*th subshell

E^i = the total energy of the initial state

and

E_{kin} = the kinetic energy of the photoelectron expelled from the *k*th subshell

X-ray photoelectron spectroscopy can be used to study both core- and valence - electron states. The technique is often referred to as electron spectroscopy for chemical analysis (ESCA), therefore emphasising its important chemical applications.

Referring to Equation 4.22 we note that the energy of the final state $E^f(k)$ will be reflected in the photoelectron spectrum. In the case of the final state being simply a hole left in the *k*th electron energy level, $E^f(k) - E^i$ is equal to the electron binding energy (B.E.) of the *k*th electron referred to the vacuum level of the sample:

$$(B.E.)_v = E^f(k) - E^i \qquad \textbf{Equation 4.23}$$

For solid samples, the Fermi level is a more convenient reference level, and the work function of the sample becomes involved in the energy equation. If the definition of E_{kin} is changed slightly to mean the kinetic energy as measured in the electron spectrometer, then we must account for the fact that the photoelectron will have adjusted to the work function of the spectrometer material ϕ_{sp}. The energy equation therefore becomes:

$$h\nu = (B.E.)_F + \phi_{sp} + E_{kin} \qquad \textbf{Equation 4.24}$$

A binding energy is defined as the energy required to remove an electron from the bound state to infinity. However, the binding energy of a core electron has a single, uniquely defined value only for a closed - shell element in the form of a monatomic gas. In all other cases either the final state is not fully defined or the core levels are perturbed by the environment. In the former case the corresponding photoelectron

spectrum will exhibit multi - component lines, and in the latter case the lines will be shifted in energy. The two effects may also occur together. The core - level energies of an atom are dependent on the total environment of the atom. This gives rise to chemical shifts in recorded photoelectron peaks. Additional structure, due to multiplet splittings of electron binding energies, can be described in terms of a one - electron - transition model of the photoemission process. On the other hand, multielectron processes involve the excitation of two or more electrons during photoemission and represent a fundamentally different effect. Both these effects have the potential of adding considerably to the information inherent in a photoelectron spectrum.

There is a different probability (or cross - section) of electron emission for each orbital. This is reflected in the relative intensities of the different spectral lines (1s, 2s, 2p, etc.). The spectrum obtained is a plot of the number of electrons versus their kinetic energy. Each element has a unique spectrum, the spectral peaks from a mixture are approximately the sum of the elemental peaks from the individual constituents.

Quantitative data can be obtained from the peak heights or areas, and identification of chemical states can often be made from the exact peak position or separation, as well as from other spectral parameters.

Those electrons which are detected originate from only the top few atomic layers (~30 to 100), because the electrons generated have a very large probability of losing energy by inelastic scattering as they leave the sample. These scattered electrons form the rising spectral background in front of each peak.

4.4 Electron Microscopy.

4.4.1 Basic Principles of Transmission Electron Microscopy

Electron microscopes have been developed to exploit fully the analytical capability which results from the many different interactions between electrons and materials.

The interaction of electrons with solids results in:

(1) Electron scattering by (a) elastic, and (b) inelastic mechanisms; and

(2) Electron excitation of radiation in the form of (a) characteristic X-rays; (b) continuous X-radiation; (c) visible light emission; and (d) photoelectron emission.

The information gained from these effects includes:

(1) Crystallographic information via diffraction data from regions ~1 μm in diameter;

(2) Chemical identification by X-ray analysis from volumes of the sample ~1 μm in diameter;

(3) Morphological information at resolutions approaching 0.5 nm separation from internal structures;

(4) Photoelectron characterisation of surfaces;

(5) Cathodoluminescence data from solids;

(6) X-ray micro-radiography from the continuous and characteristic X-radiation emitted from a small source; and

(7) Characterisation of surfaces by electron reflection microscopy.

The resolution (R) of a microscope is given by:

$$R = \lambda/2 \sin \alpha \qquad \textbf{Equation 4.25}$$

Using this relationship we can see that as λ becomes smaller (0.04 Å for 100 kV electrons) so the resolvable distance becomes smaller.

Unlike the optical microscope, electron microscopes operate under high vacuum using a magnetic lens rather than a glass lens. The basic construction (Figure 3.6) consists of an electron gun, a condenser lens system, a specimen stage, objective lens, projector lens system, a viewing screen and an image recording facility.

Apertures are inserted below the condenser lens and above the objective lens to minimise lens defects (spherical aberration). Other lens defects such as astigmatism are corrected by a set of charged pins set to correct the distorted beam. Chromatic aberration is avoided by using a monochromatic beam of electrons, *i.e.* maintaining a stable high-voltage supply.

The alignment of the electron beam is critical to the performance of the microscope. The illumination section must be aligned with the magnification section, along the axis of the microscope, otherwise a distorted image or, in the case of gross misalignment, no image is seen on the fluorescent screen. Mechanical alignment is carried out periodically. Electronic alignment is performed by charging deflector plates (electrostatic plates) placed above the specimen chamber.

The specimen is moved by micro-controls for translation of the specimen across the incident electron beam.

4.4.2 Basic Principles of Scanning Electron Microscopy

The scanning electron microscope (S.E.M.) is designed as an analytical tool capable of studying surfaces. Nearly 60% of all TEM micrographs are recorded at magnifications of $\leq$ x40,000, which does not utilise the high resolution capability of the system. The SEM *does* fully use the microscope properties of:

(1) resolution in the X - Y plane;

(2) depth of field (Z direction);

(3) larger specimen size; and

(4) chemical data collection.

The essential features of the design are:

(a) an electron source, using conventional tungsten filaments, lanthanum hexaboride or field emission types;

(b) a condenser system to focus a fine beam (probe) of electrons on the specimen surface;

(c) a scanning system to translate the electron beam over a selected area of the specimen;

(d) a detection facility to image the emitted signals from the specimen, and to control image contrast; and

(e) a display and recording system to view the image.

The interaction of electrons with solids by four principal mechanisms forms an image in the SEM:

(1) Elastic scattering of primary (high energy) electrons from a surface layer.

(2) The emission of secondary electrons from within the surface layers as a result of primary electron inelastic scattering and collision effects.

(3) The absorption and leakage to earth of electron charges within the material.

(4) The generation of X-rays within the irradiated volume of the specimen.

4.5 Fourier Transform Infra Red Spectroscopy

4.5.1 The Michelson Interferometer

The Michelson interferometer is a device that can split a beam of radiation into two paths and then recombine them so that the intensity variations of the exit beam can be measured by a detector as a function of path difference. The simplest form of the interferometer is shown in Figure 4.5. It consists of two mutually perpendicular plane mirrors, one of which can move along the axis shown. The movable mirror is either moved at a constant velocity or is held at equidistant points for fixed short time periods and rapidly stepped between these points. Between the fixed mirror and the movable mirror is a beamsplitter, where a beam of radiation from an external source can be partially reflected to the fixed mirror (at point F) and partially transmitted to the movable mirror (at point M). After each beam has been reflected back to the beam splitter, they are again partially reflected and partially transmitted. Thus, a portion of

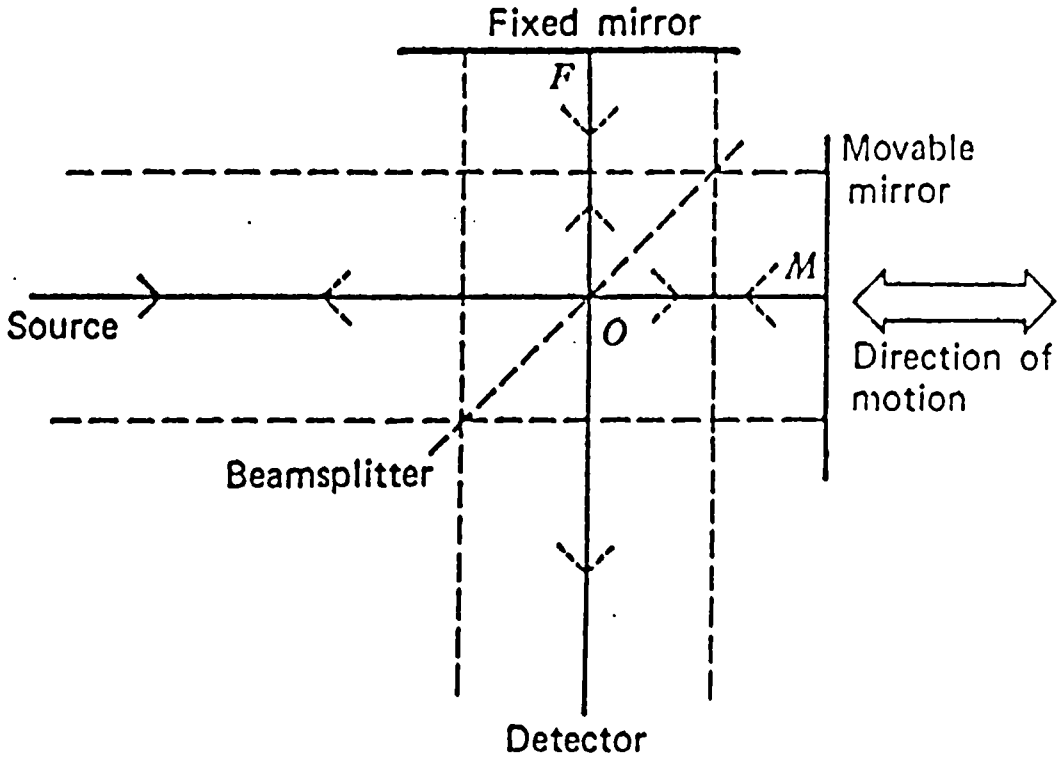

Figure 4.5 Schematic Diagram of Michelson Interferometer.

the beams which have travelled in the path to both the fixed and movable mirrors reach the detector, while portions of each beam also travel back toward the source.

The beam that returns to the source is only occasionally of interest for spectroscopy and only the output beam passing in the direction perpendicular to that of the input beam is usually measured. However, it is important to remember that both the output beams contain equivalent information. The main reason for measuring only one of the output beams is the difficulty in separating the second output beam from the input beam if the beamsplitter is at 45° to each mirror. In some measurements, both output beams are measured using one or two detectors; in others separate input beams can be passed into each arm of the interferometer and the resultant signal measured using one or two detectors. The data obtained is interpreted using a fast Fourier transform [101].

5. RESULTS AND DISCUSSION I

SAMPLE PRECIPITATION AND MORPHOLOGY

5.1 Introduction

In this chapter the morphology obtained in the precipitation process is discussed in relation to the nature of the precipitants, the nature of the precipitation medium, and the precipitation conditions. A typical range of morphologies is considered in detail. The precipitation details are summarised in Table 5.1 , and electron micrographs of the precipitated crystals are shown in Plates 1 - 14. Precipitation details for all samples prepared are shown in Appendix A.

5.1.1 Effects of Precipitants

Mole ratios of sodium hydroxide to the calcium salt(s) are important in determining the morphology of the calcium hydroxide. Addition of 0.05M calcium chloride solution to 1M sodium hydroxide solution, to produce an ultimate mole ratio $CaCl_2$:NaOH of 0.05:1, results in an octahedral form, shown in Plate 1 A. Addition of 0.75M calcium chloride solution to 0.75M sodium hydroxide solution, to produce on ultimate mole ratio $CaCl_2$:NaOH of 1:1, giving an excess of chloride, results in formation of large hexagonal prisms, shown in Plate 1 B. With a stoichiometric precipitation reaction, *i.e.* a mole ratio NaOH:$CaCl_2$ of 2:1, the crystals formed are smaller, Plate 9 A, and have a very irregular crystal morphology, *cf* Plate 4 A.

Maintaining the molar ratio of the precipitants, but varying the molarity of the calcium salt solution causes morphological changes. Precipitation using 0.15M calcium chloride solution produces large hexagonal prisms, shown in Plate 1 B, whereas using 0.375M calcium chloride solution a morphologically heterogeneous precipitate is produced, shown in Plate 2 A.

Precipitation involving the use of a weak acid salt results in similar morphologies to those obtained using strong acid salts. Plate 3 B shows a hexagonal prism prepared in

the precipitation reaction of calcium acetate ($Ca(OAc)_2$) solution and sodium hydroxide solution, with mole ratios $Ca(OAc)_2$:NaOH of 1:1, giving an excess of acetate, and Plate 5 A shows hexagonal prisms prepared by the precipitation of a stoichiometric mixture of sodium hydroxide and calcium acetate. The non-stoichiometric precipitation reaction results in the prisms being formed with slit-shaped "pores" up to a size of 1μm x 0.5μm, compared to the stoichiometric precipitation which results in hexagonal prisms having "defect-free" faces.

Calcium hydroxide precipitation using a mixed calcium salt solution, with mole ratios NaOH:$CaCl_2$:$Ca(OAc)_2$ of 5:1:4, also results in formation of large hexagonal prisms, shown in Plate 4 A, of size range 2 x 4μm to 4 x 10μm, some of which exhibit a layer structure, shown in Plate 4 B.

There is no significant difference in the morphology of the crystals precipitated by either the addition of sodium hydroxide solution to the mixed calcium salt solution, with mole ratios NaOH:$CaCl_2$:$Ca(OAc)_2$ of 2:1:1, shown in Plate 8 B, or the addition of the mixed calcium salt solution to sodium hydroxide solution, shown in Plate 9 B.

The nature of the weak acid salt of calcium may have an effect on the morphology. Calcium acetate, Plate 10 A & B, and calcium propionate, Plate 11 A & B, produce, on cursory examination, precipitates of a similar nature; but measurement of the crystal thicknesses shows a significant difference between the two products. Calcium acetate produces crystals approximately 40nm thick, compared to approximately 20nm thick when produced by calcium propionate ($Ca(OPr)_2$). This result may be due to the nature of the calcium salt used, or to the rate of mixing of the precipitants which was approximately 10 times faster for the calcium propionate precipitation.

5.1.2 Effect of Precipitation Medium

The presence of ethanol in the precipitation medium has marked effects on the morphology of the crystalline precipitate. Hexagonal plates of calcium hydroxide of varying thicknesses were produced in the precipitation reaction of sodium hydroxide solution and mixed calcium salt solution, with mole ratios $NaOH:CaCl_2:Ca(OAc)_2$ of 2:1:1, in the presence of 50 ml of an ethanolic medium. For this the ethanolic medium was added to the solution of the sodium hydroxide solution in the reaction vessel prior to addition of the calcium salt solution. It was found that the higher the final concentration of ethanol in the precipitation mixture, the thinner the hexagonal platelets of calcium hydroxide become (thicknesses vary from 300nm to 40nm), as are shown in Plates 6 A, 6 B, 7 A, 7 B, and 8 A, which relate to a final ethanol concentration of 5 vol%, 10 vol%, 20 vol%, 30 vol% and 50 vol% respectively.

Simultaneous addition of sodium hydroxide solution and a mixture of calcium chloride and calcium acetate solutions, with mole ratios $NaOH:CaCl_2:Ca(OAc)_2$ of 2:1:1, to absolute ethanol contained in the reaction vessel, results in formation of sheets, as shown in Plate 10 A & B. Repeating the simultaneous addition, but replacing the calcium acetate with calcium propionate, again produces sheets, as shown in Plate 11 A, but also thin, very large hexagonal plates, 20nm x 6,000nm, as shown in Plate 11 B.

Precipitation of calcium hydroxide from sodium hydroxide and calcium chloride as a 1M solutions in absolute ethanol, with mole ratios $NaOH:CaCl_2$: of 1:2.26, results in the formation of a heterogeneous crystalline product, shown in Plate 3 A, which upon analysis by FTIR spectroscopy, Figure 8.3, was found to be calcium carbonate.

5.1.3 Silylation of Calcium Hydroxide

Calcium hydroxide was precipitated by the simultaneous addition of 1M solutions of sodium hydroxide and calcium hydroxide, with mole ratios $NaOH:CaCl_2$ of 2:1, to absolute ethanol. After washing with acetone, ca. 1 g of the product was suspended in

50 ml of acetone containing 5 ml of either dimethylsulphoxide or 1,1,1,3,3,3-hexamethyldisilazane, and agitated in an ultrasonic bath for 2 hours. Both silylating agents introduced ca. 0.02% Si w/w (measured by atomic absorption) into the sample.

Calcium hydroxide precipitated by simultaneous addition of 1M solutions of sodium hydroxide, calcium chloride and calcium propionate, with mole ratios $NaOH:CaCl_2:Ca(OPr)_2$ of 2:1:1, to absolute ethanol. After washing in acetone, ca. 1 g of the product was refluxed in acetone containing 5 ml 1,1,1,3,3,3-hexamethyldisilazane for 2 hours, this resulting in the introduction of 0.02% Si w/w (measured by atomic absorption).

Attempts to silylate precipitated calcium hydroxide failed. No silicon could be detected using atomic absorption.

Simultaneous addition of sodium hydroxide solution and mixed calcium salt solution, with mole ratios $NaOH:CaCl_2:Ca(OPr)_2$ of 2:1:1, to 100 ml of absolute ethanol containing 10 ml of 1,1,1,3,3,3-hexamethyldisilazane, and agitated for 30 minutes in an ultrasonic bath. A silylated calcium hydroxide material was produced containing 3.4% Si w/w (measured by atomic absorption). This silylated product has a sheet-type morphology, shown in Plate 12 A.

Precipitation of calcium hydroxide by the simultaneous addition of 1M sodium hydroxide solution and 1M calcium chloride solution to absolute ethanol, in volume ratios $NaOH:CaCl_2:EtOH$ of 2:1:2, results in formation of a particulate product comprising particles of size ca. 0.25 μm, some of which have hexagonal character, shown in Plate 13 B.

Preparation of a silylated calcium hydroxide from 1M sodium hydroxide solution and 1M mixed calcium salt solution added to absolute ethanol containing a molar excess of

1,1,1,3,3,3-hexamethyldisilazane, in volume ratios NaOH:$CaCl_2$:$Ca(OPr)_2$:EtOH of 20:10:1:20 or of 2:1:1:2 results in the formation of hexagonal platelets, shown in Plates 12 B and 13 A respectively.

5.1.4 Effect of the Rate of Addition of Precipitants

The rate of mixing of the precipitants in the reaction vessel causes a marked change in morphology of the precipitated calcium hydroxide.

Slow addition, ca. 10 ml/min, of one precipitant to the other, in aqueous medium, results in formation of large crystals, shown in Plates 1 B, 3 B, 4 A & B, 5 A and 9 A.

Mixing one precipitant with another, at a rate of ca. 53 ml/min, in ethanolic medium, results in the formation of hexagonal plates of calcium hydroxide, shown in Plates 8 B and 9 B, whereas rapid mixing of the precipitants, at ca. 3750 ml/min, results in the formation of thin sheet-like crystals of calcium hydroxide, shown in Plates 10 A and B, and 11 A and B.

A possible explanation for these results is obtained by considering the mechanisms involved in crystal growth. Slow mixing of the precipitants allows time for growth of crystals, where the crystals obtained from the first instant of mixing of the precipitants grow at the expense of crystals formed as each drop of precipitant enters the reaction medium, as the surface energy of small crystals is larger, hence the solubility is greater, than for large crystals, >1μm, the small crystals being "sacrificed" in favour of the growth of the large crystals. Mixing the precipitants at ca. 53 ml/min in ethanolic medium results in the formation of hexagonal plates probably because of poisoning of the surface. But, when the precipitants are very rapidly mixed, at ca. 3750 ml/min, thin sheet-like crystals are formed. This is most likely due to a combination of surface poisoning by acetate/propionate groups and/or ethanol molecules. The rapid rate of mixing, and thus a rapid increase in supersaturation, will not allow time for calcium

hydroxide molecules to work their way through the surface poisoning groups to produce growth on the (0001) face. Therefore, growth can only occur at the edges of the crystals, where there is no substantial poisoning, resulting in sheet-type crystal formation.

Table 5.1 Precipitation Data for Examined Samples

Sample	Sodium Hydroxide Vol/ml	Sodium Hydroxide Concn/M	Calcium Chloride Vol/ml	Calcium Chloride Concn/M	Calcium Acetate Vol/ml	Calcium Acetate Concn/M	Rate of addn of .Ca salts ml/min	Vol. of water placed in reaction vessel /ml	Vol. of EtOH placed in reaction vessel /ml	Agitation
19	25.0	1.5	25.0	0.75	-	-	6.0	100	-	Y
40	50.0	1.0	-	-	25.0	1.0	6.0	75	-	Y
51	25.0	1.0.	12.5	1.0	12.5	1.0	6.0	30	20	Y
67	25.0	1.0	12.5	1.0	12.5	1.0	*53.0	-	50	Y
68	250.0	1.0	125.0	1.0	125.0	1.0	*500.0	-	250	Y
69	250.0	1.0	125.0	1.0	125.0	1.0	*500.0	-	250	Y
#74	50.0	1.0	25.0	1.0	+25.0	1.0	*500.0	-	100	Y
#79	100.0	1.0	50.0	1.0	+5.0	1.0	*500.0	-	100	Y
#80	100.0	1.0	50.0	1.0	+50.0	1.0	*500.0	-	100	Y
#82	100.0	1.0	50.0	1.0	-	-	*500.0	-	100	Y

= Prepared in the presence of a silylating agent

+ = Calcium propionate used in place of calcium acetate

* = Precipitants added simultaneously

6. RESULTS AND DISCUSSION II

Nitrogen Adsorption

6.1 Introduction

In this chapter the nitrogen isotherms are presented. The BET surface areas, DR plots and FHH exponents will be discussed. The results are summarised in Tables 6.1 and 6.2, and the raw data has been collected in Appendix B.

6.1.1Nitrogen Adsorption Isotherms

The nitrogen isotherms of vermiculite, and samples 19, 40, 51, 67, 68, and 69 outgassed at room temperature are shown in Figures 6.1 - 6.7 (solid symbols represent desorption branch) respectively. The isotherm of sample 80 outgassed at 423K is shown in Figure 6.8.

Vermiculite and samples 51, 67, 68, 69 and 80 all exhibit isotherms of Type II in character in the BDDT Classification [102], but it is evident that their precise location and shape varies significantly from one sample to another, whereas sample 19, shown in Plate 9 A, exhibits an isotherm having characteristics of *the stepped isotherm*, designated asType VI, and sample 40, shown in Plate 5 A, exhibits an isotherm having characteristics of a Type V isotherm. With the exception of the isotherm of sample 51 which is reversible, all the Type II characteristic isotherms exhibit hysteresis loops which occur at medium to high relative pressures ($P/P_o \sim 0.4 - 0.9$), with the exception of sample 69 which exhibits non-closing hysteresis. Sample 40 exhibits an unusual hysteresis loop at medium to high relative pressure ($P/P_o \sim 0.4 - 0.95$).

The Type II isotherms show that the sample is non-porous and that there is some heterogeneity in the sample related to the face size of the crystals. Sample 51, shown in Plate 7 A, exhibits a fully reversible Type II isotherm, Figure 6.4, but samples 67 and 68, shown in Plates 10 A and 10 B, and 11 A respectively, exhibit Type II isotherms with hysteresis loops, shown in Figures 6.5 and 6.6 respectively, which may be

Table 6.1 Summary of Results Obtained from Nitrogen Adsorption.

Sample	DR Surface Area	BET Surface Area	c value	FHH exponent	Morphology
Vermiculite	4	4	16.3	0.99	Layered structure
19	2.5	1	-1577	2.55	Irregular hexagonal prisms
40	1.5	1	15.8	2.74	Hexagonal & octagonal prisms
51	13	10.4	29.5	2.5	Hexagonal plates
67	14	10.1	49.6	2.32	Continuous sheets
68	13	13.7	53.1	2.26	Continuous sheets
69	26	21.7	38.8	2.83	Hexagonal plates
69*		23.4	24.7	2.48	Hexagonal plates

* = results of a consecutive isotherm

Table 6.2 Summary of Results Obtained from Single Point Nitrogen Surface Area Determination

Sample	Room Temp.	473K	553K	603K	623K	703K
68	15				19	16(15)
69	14	16	27	21		
74	61(35)	69(44)	68		59	
80	43			33		
81	38	39	39		37	
82	25[25]	29[29]	29[29]		28[48]	

( ) = Surface area after water adsorption

[ ] = Heated under vacuum

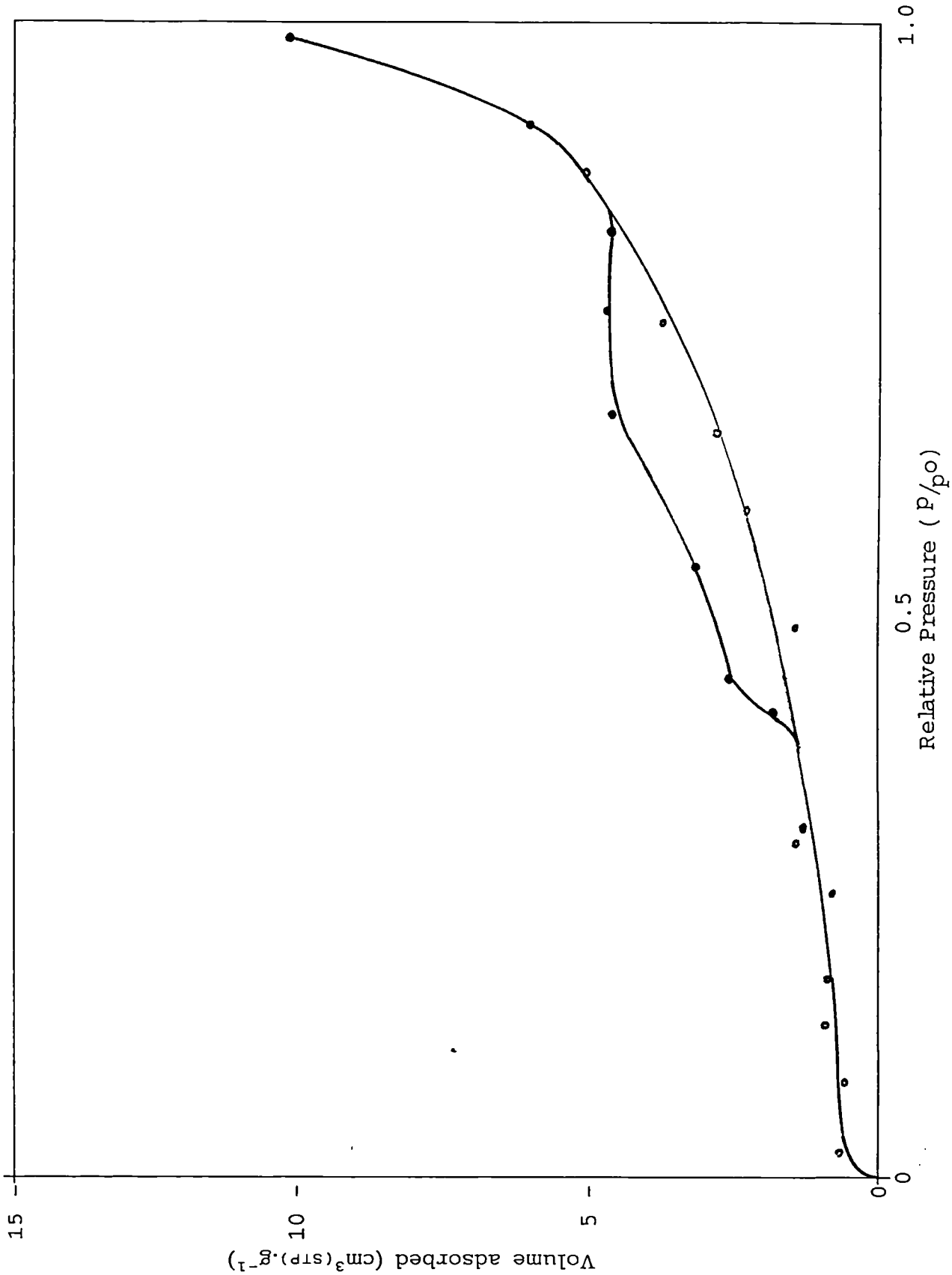

Figure 6.1 Nitrogen adsorption isotherm at 77K for vermiculite.

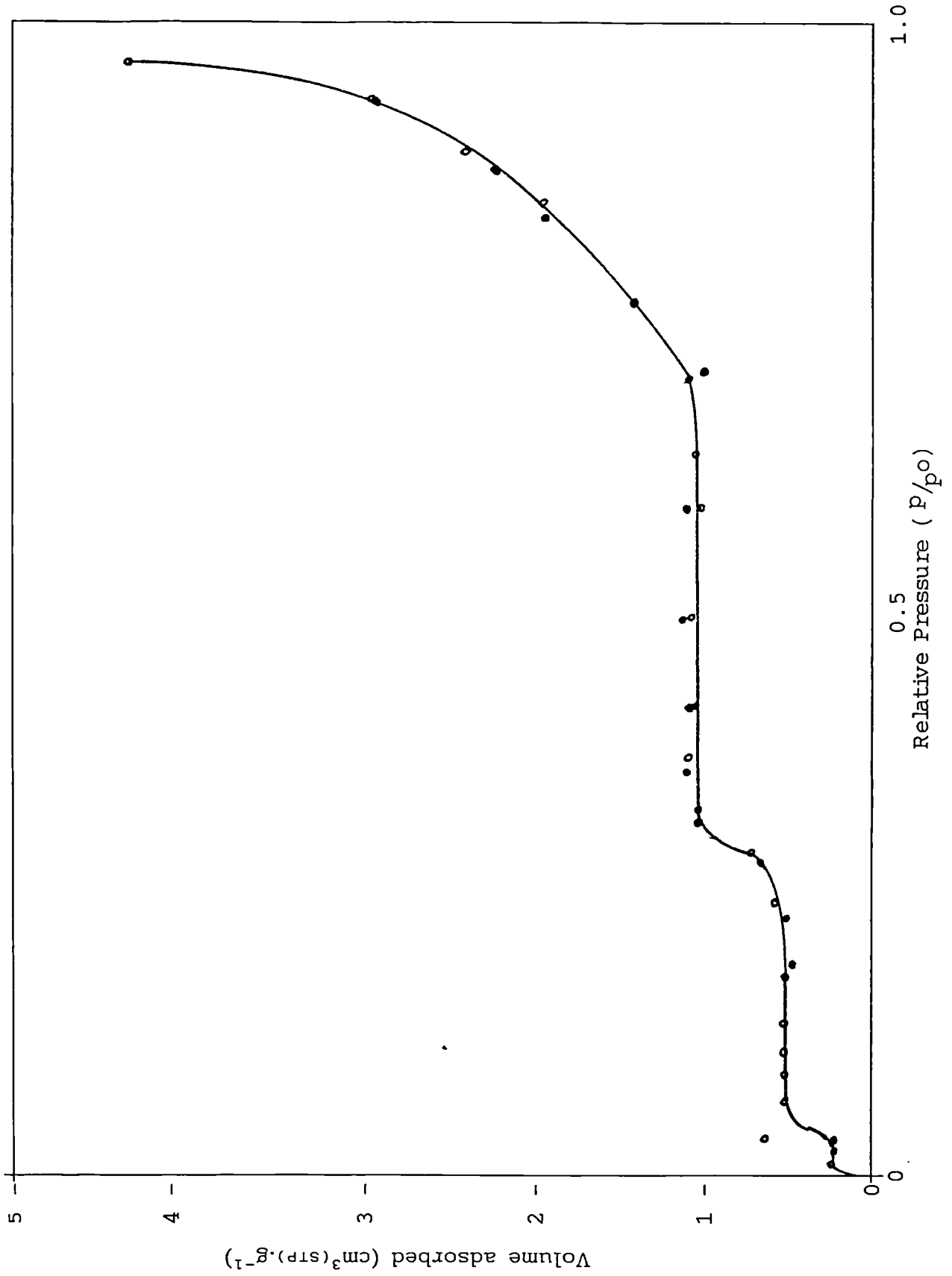

Figure 6.2 Nitrogen adsorption isotherm at 77K for sample 19.

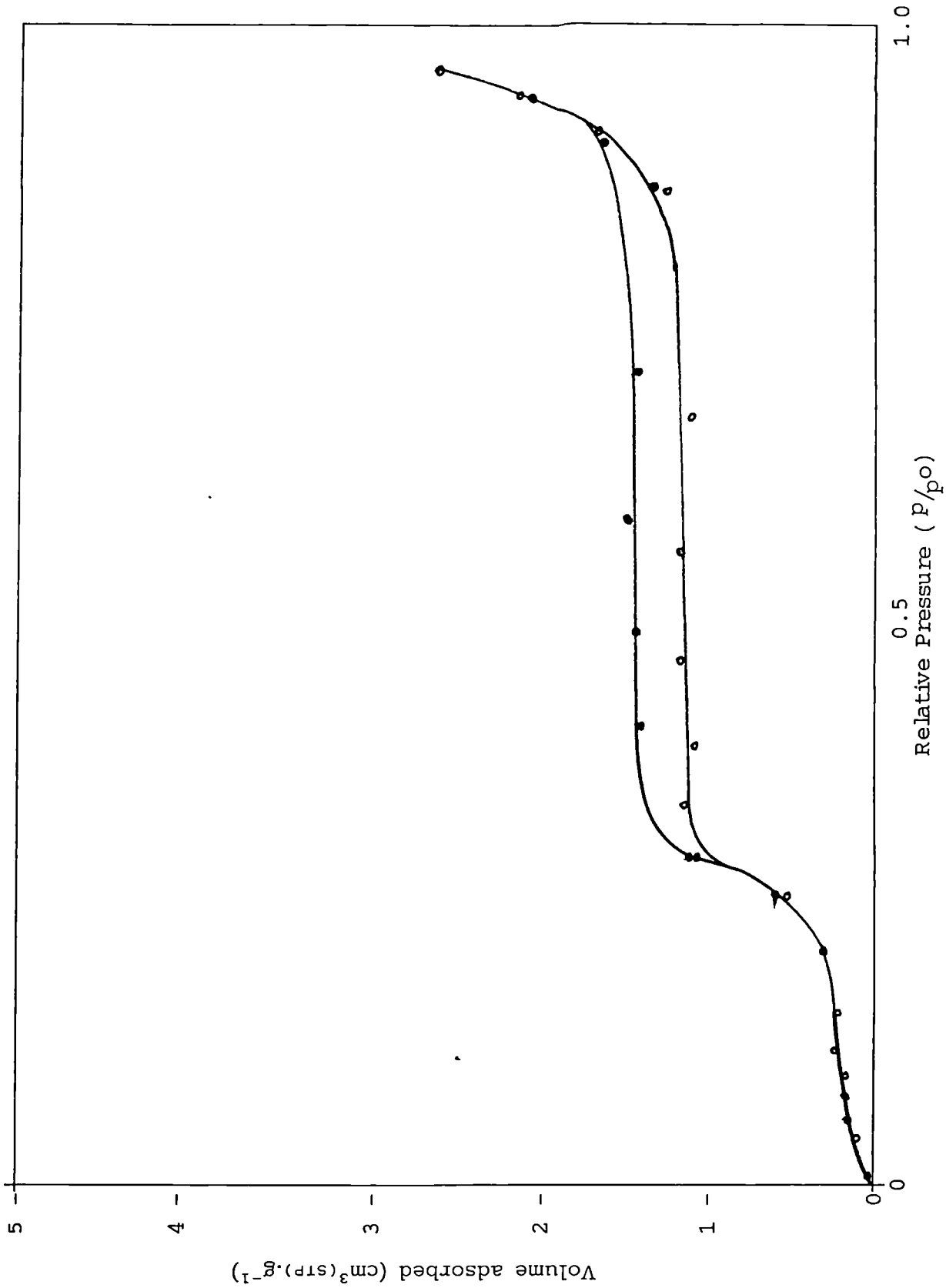

Figure 6.3 Nitrogen adsorption isotherm at 77K for sample 40.

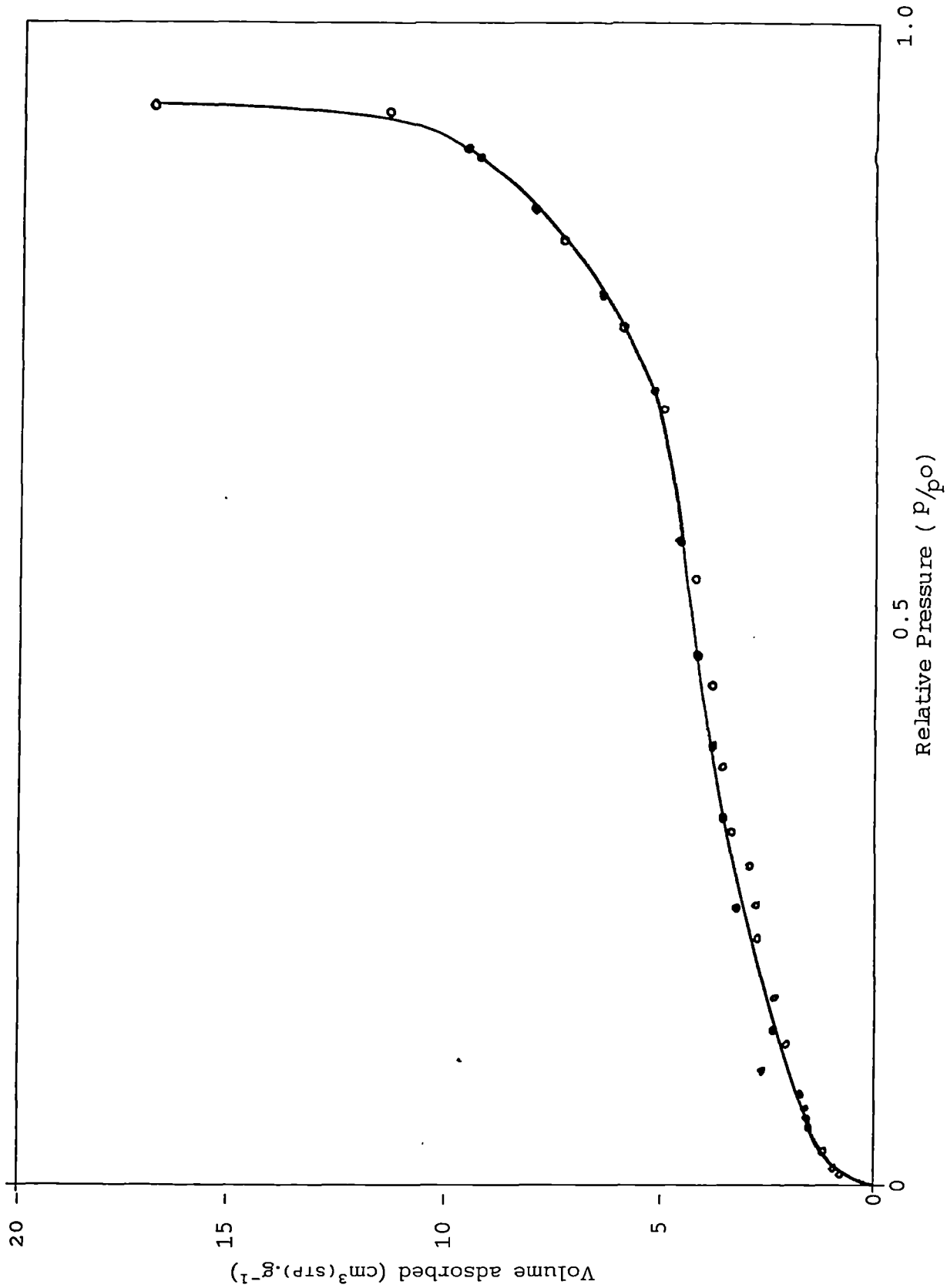

Figure 6.4 Nitrogen adsorption isotherm at 77K for sample 51.

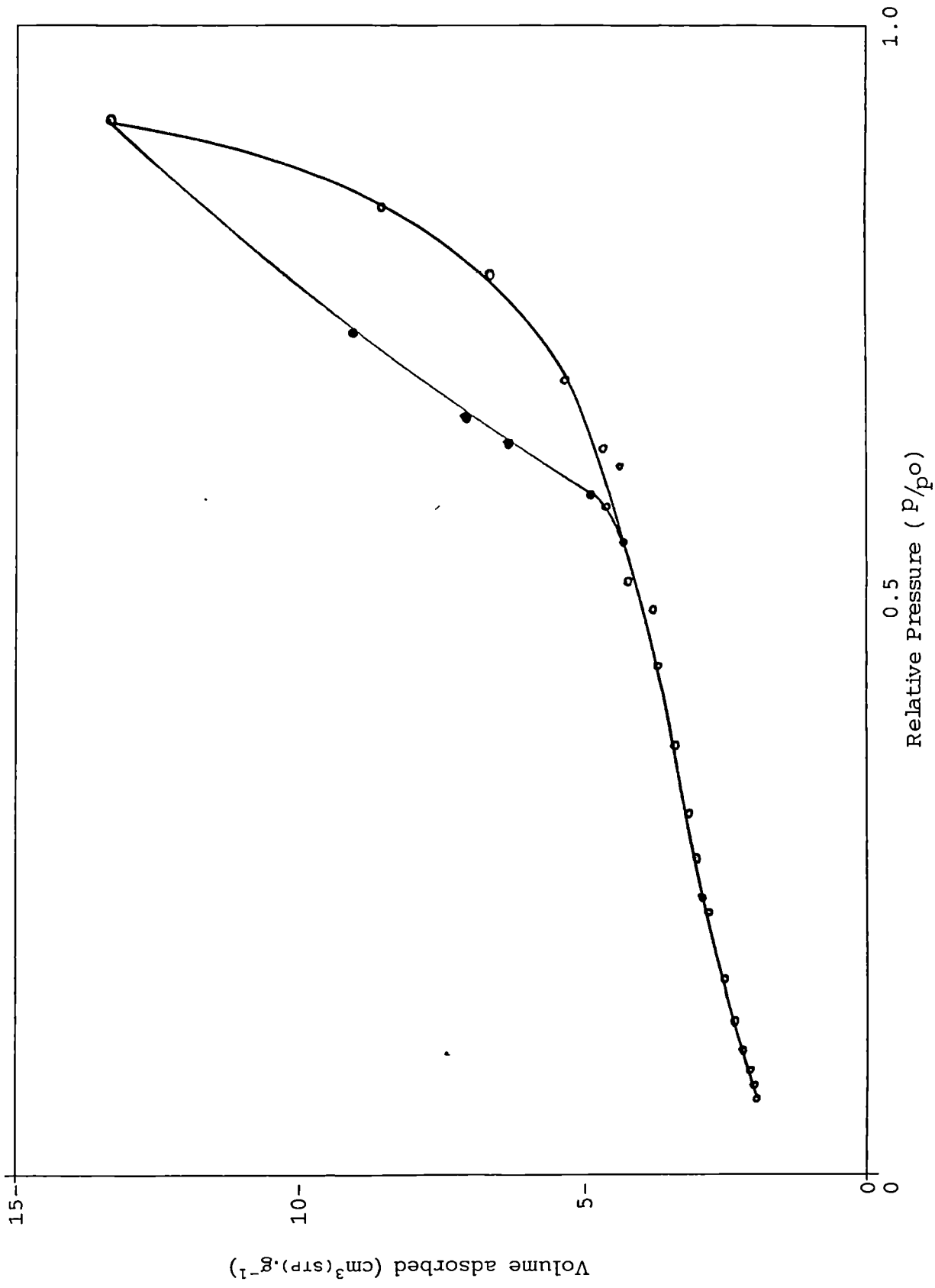

Figure 6.5 Nitrogen adsorption isotherm at 77K for sample 67.

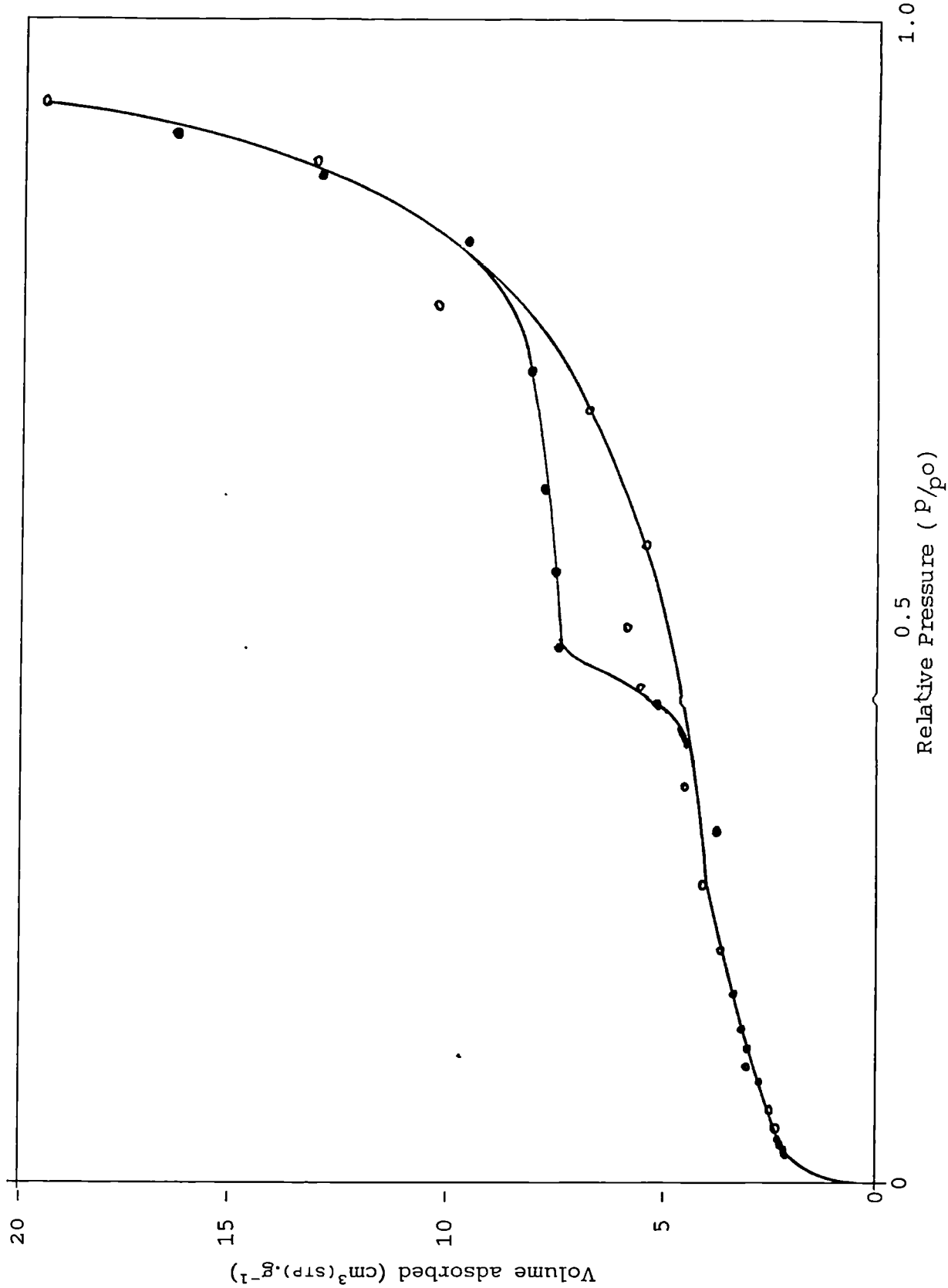

Figure 6.6 Nitrogen adsorption isotherm at 77K for sample 68.

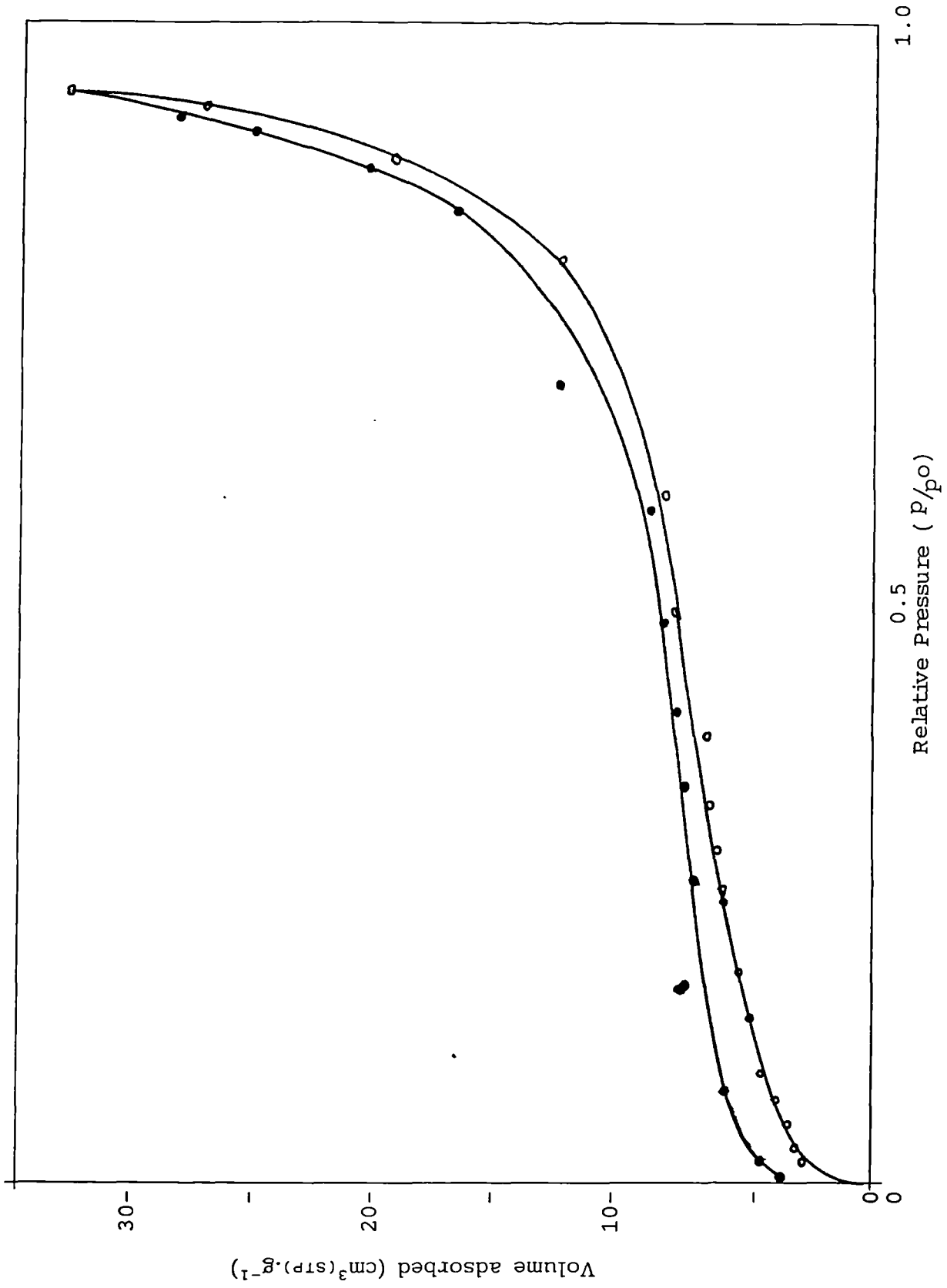

Figure 6.7 Nitrogen adsorption isotherm at 77K for sample 69.

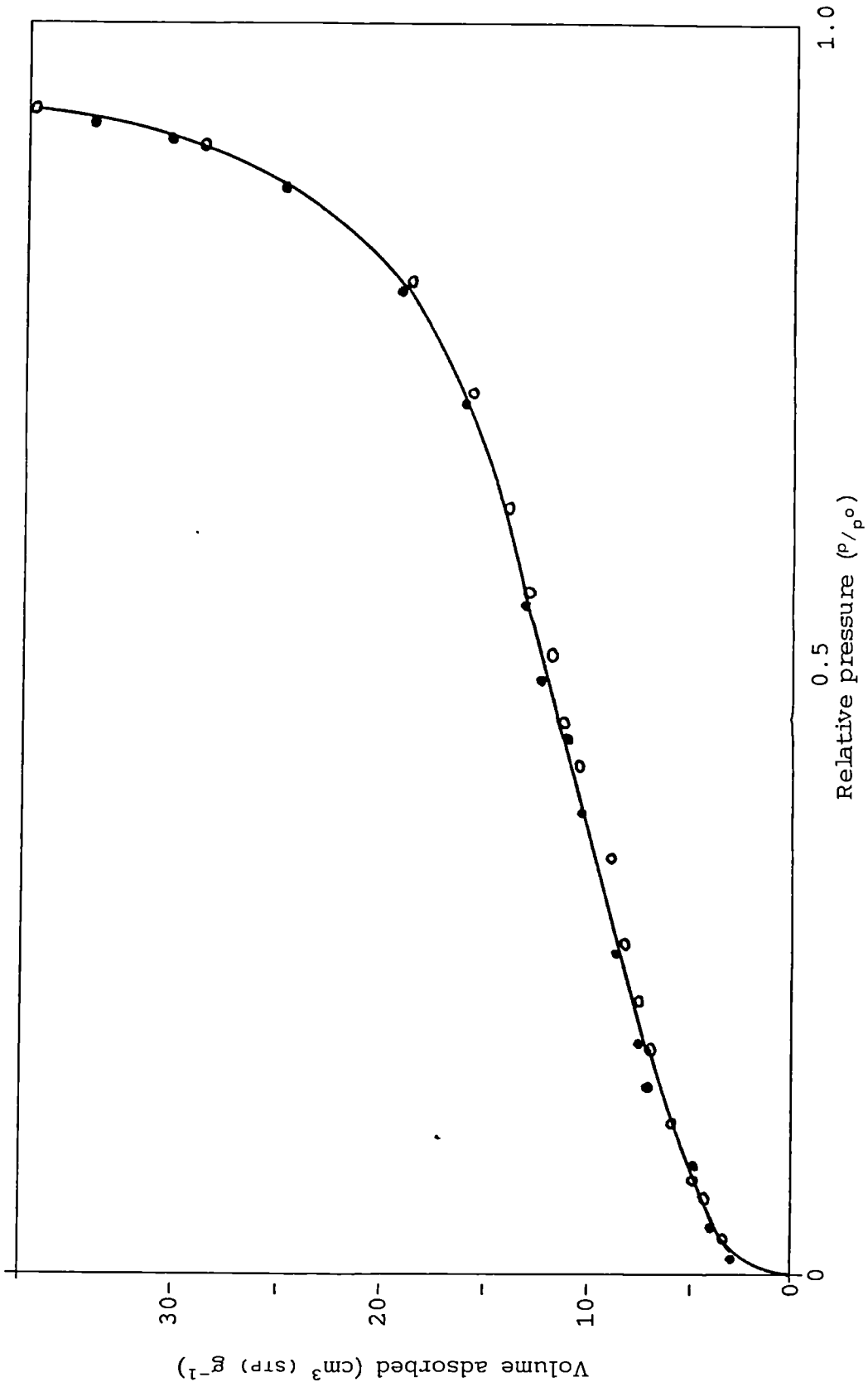

Figure 6.8 Nitrogen adsorption isotherm at 77K for sample 80.

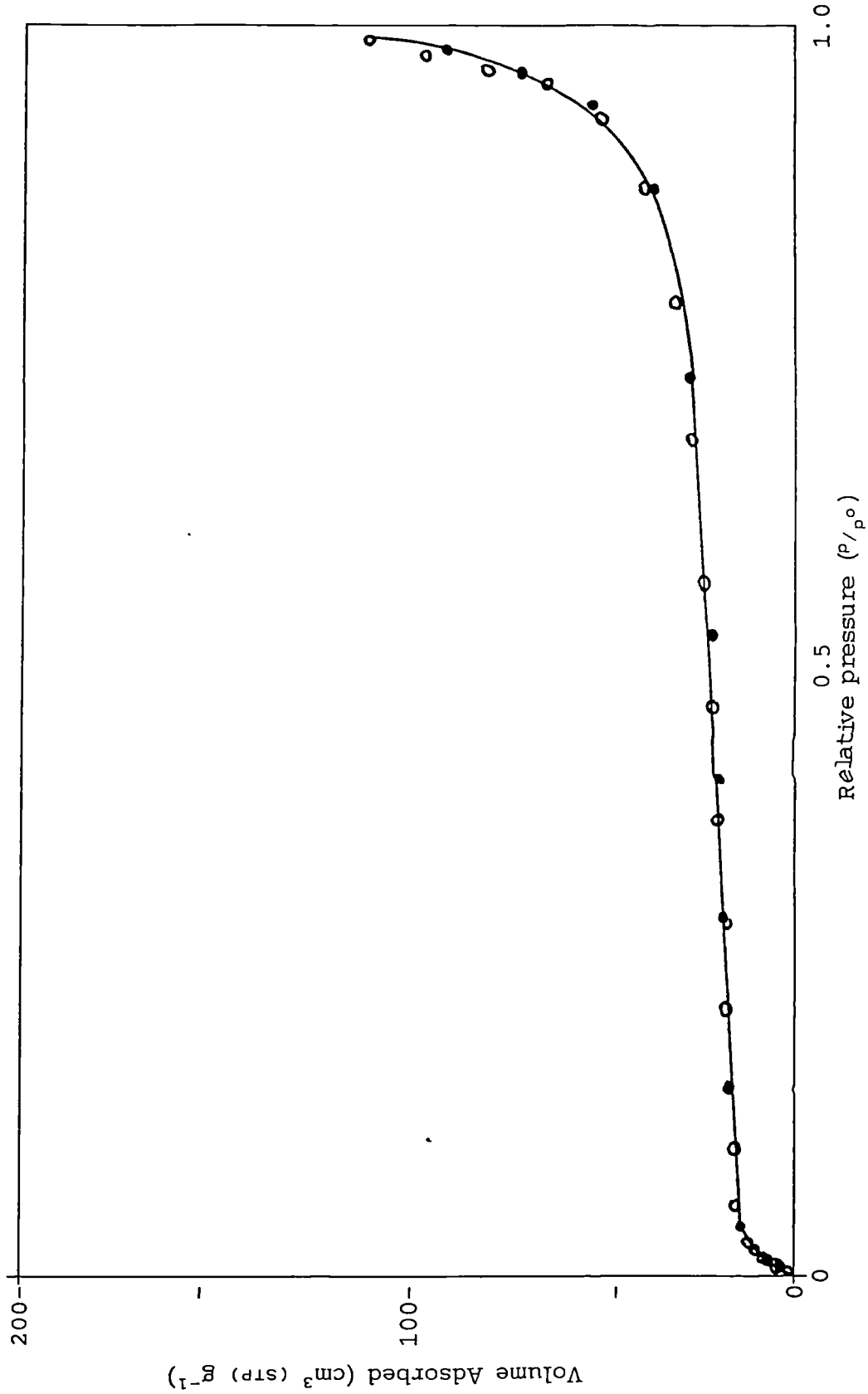

Figure 6.9 Successive nitrogen isotherm at 77K for sample 69

indicative of some mesoporosity. Sample 69, shown in Plate 11 B, exhibits a Type II isotherm with non-closing hysteresis, shown in Figure 6.7, which is typical of a plate-like material. It can therefore be postulated that the Type II isotherms with hysteresis loops exhibited by samples 67 and 68, are not due to mesoporosity, but due to aggregation of the plate-like crystals, as shown in Plate 11 A, forming voids of mesopore dimensions (width ca. 2 - 50 nm). Pure mesoporosity is indicated by the isotherm exhibiting a plateau at high p/p_o, Type IV isotherm, and an H1 type hysteresis loop.

Sample 19, shown in Plate 9 A, exhibits a Type VI isotherm, shown in Figure 6.2, which is indicative of a homogeneous surface. A sub-step is evident in the first riser of the isotherm, at relative pressure $p/p_o \sim 0.01 - 0.04$, which may be the result of a phase transition within the adsorbed film. Detailed investigation of a number of step-like isotherms produced with zeolites by Rouquerol [103-105], Thomy and Duval [106] and by others [107,108] has led to this phenomenon being interpreted as a two-dimensional phase change in the first molecular layer.

Sample 40, shown in Plate 5 A, exhibits an isotherm having Type V character, shown in Figure 6.3. The small step over the relative pressure range $p/p_o \sim 0 - 0.2$ is indicative of a weak adsorbent - adsorbate force, but once a molecule has become adsorbed, the adsorbate - adsorbate forces may promote the adsorption of further molecules, a co-operative process, so that the isotherm will become convex to the pressure axis. A plateau will then be formed in the multilayer region of the isotherm, as can be seen in Figure 6.3. The final upward sweep near saturation pressure is attributable to adsorption in coarse mesopores and macropores, and which is confirmed by the hysteresis which occurs on desorption.

6.1.2 Frenkel-Halsey-Hill (FHH) Plots

The FHH exponents of vermiculite and the calcium hydroxide materials vary from 0.99 for vermiculite to 2.83 for sample 69 and the FHH plots for vermiculite and samples 19, 40, 51, 67, 68 and 69 are shown in Figures 6.10 - 6.17 respectively. Due to the low surface areas of the samples, the values of the FHH exponents must be viewed with caution when using them as comparisons between samples. Comparisons of the changing values of the exponents of each sample, through the varying of the adsorption pre-treatments, will be more meaningful.

The low value of the FHH exponent r for vermiculite, from a linear plot over the range $p/p^o \sim 0.75 - 0.92$, shown in Figure 6.10, is probably due to vermiculite having a low surface energy. Sample 19, shown to be non-porous and have a homogeneous surface by nitrogen adsorption isotherm, has an exponent r value of 2.55 from a linear plot over the range $p/p^o \sim 0.86 - 0.98$, shown in Figure 6.11, which is a smaller value of r than that obtained with sample 40 of 2.74, over the linear range of $p/p^o \sim 0.88 - 0.97$ shown in Figure 6.12, even though there is a considerable similarity in the morphologies of the two samples, *cf* Plates 5 A and 9 A. This increase in the value of r from 2.55 - 2.74 is probably due to a combination of, an increase in surface energy resulting from the use of calcium acetate in the precipitation rather than calcium chloride in the precipitation process, and to there being adsorption in coarse mesopores and macropores as were shown to be present by analysis of the nitrogen adsorption isotherm.

FHH plots of samples 51, 67, 68 and 69, shown in Figures 6.13 - 6.16, exhibit linearity over a large range of relative pressures, $p/p^o \sim 0.3 - 0.9$, $\sim 0.2 - 0.8$, $\sim 0.1 - 0.9$ and $\sim 0.1 - 0.8$ respectively, and have respective r values of 2.50, 2.32, 2.26 and 2.83. The FHH plot for sample 51 exhibits a downward deviation from linearity at low p/p^o which is indicative of micropore filling. But the nitrogen isotherm for sample 51 is a completely reversible Type II, indicating a non-porous surface. The downward deviation is perhaps therefore due to aggregates of the material giving rise to fine,

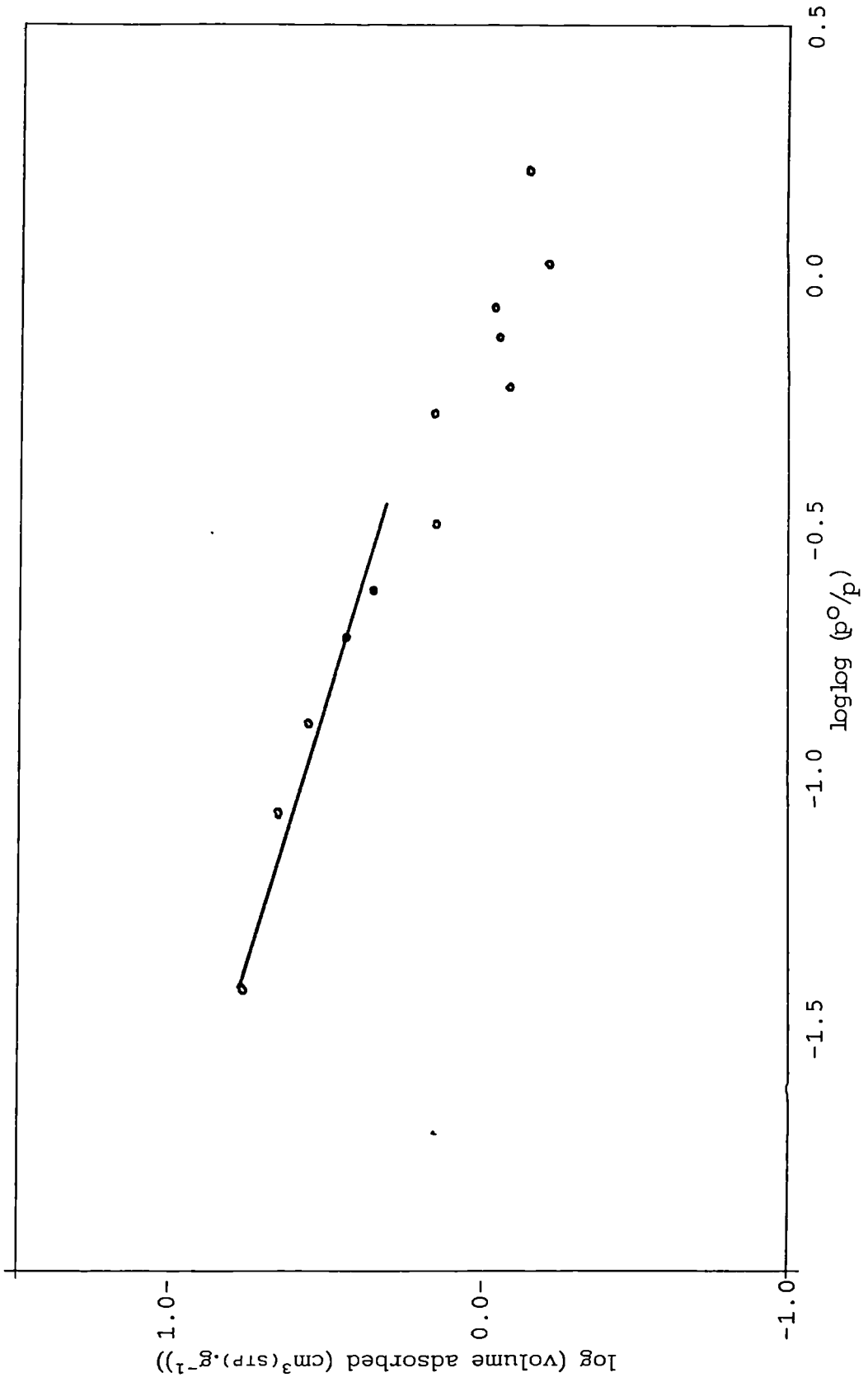

Figure 6.10 Frenkel-Halsey-Hill (FHH) plot for vermiculite.

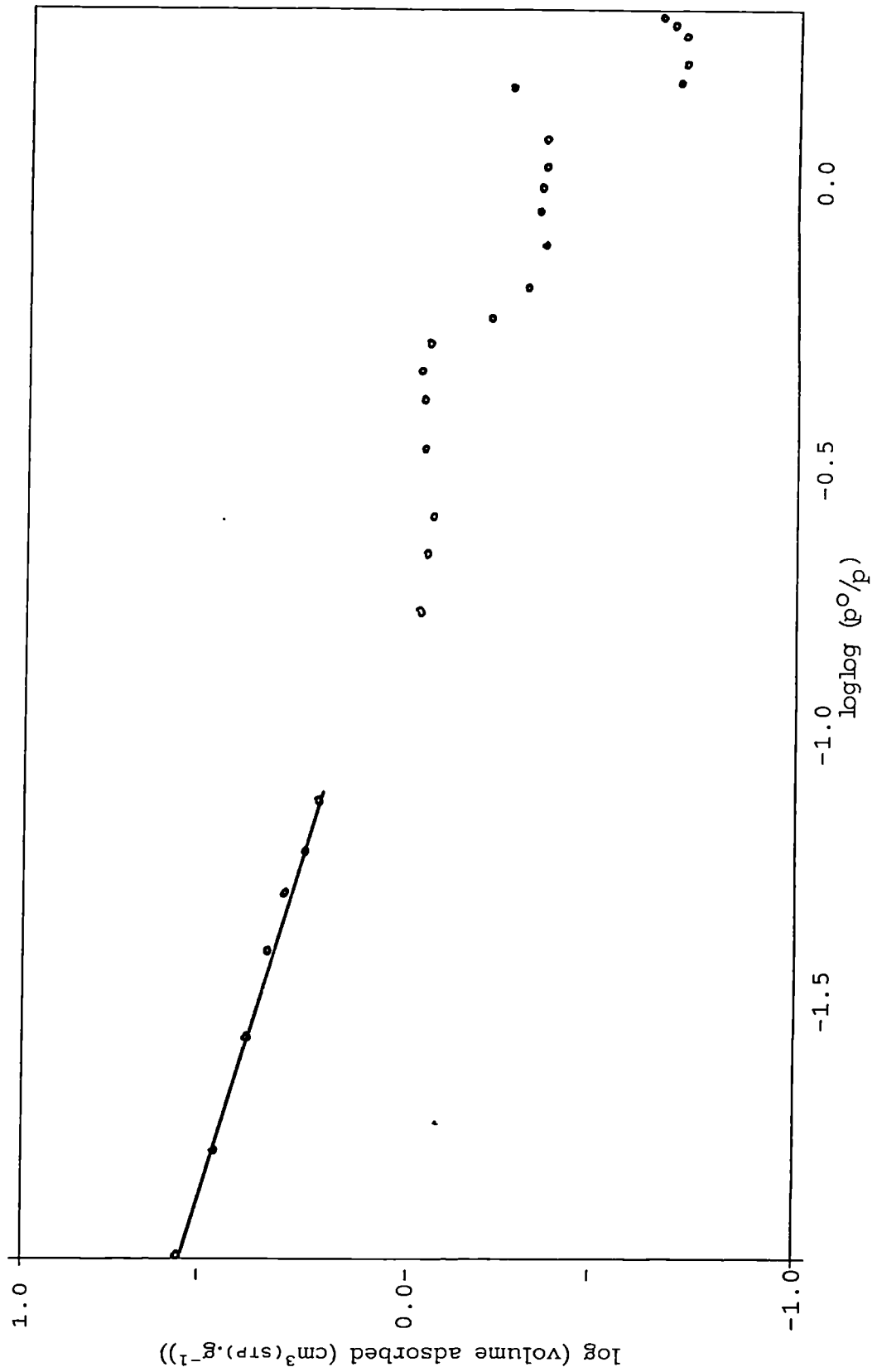

Figure 6.11 Frenkel-Halsey-Hill (FHH) plot for sample 19.

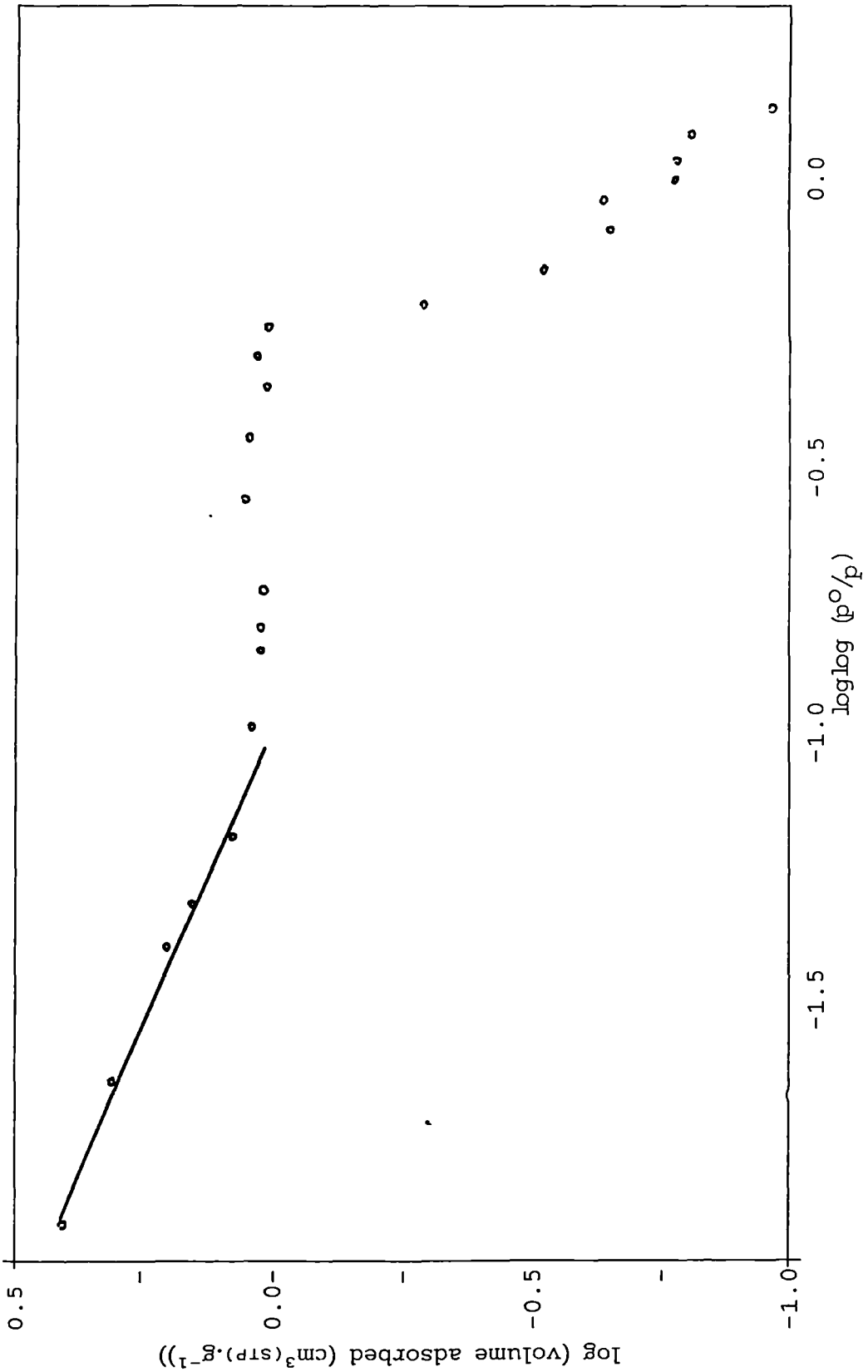

Figure 6.12 Frenkel-Halsey-Hill (FHH) plot for sample 40.

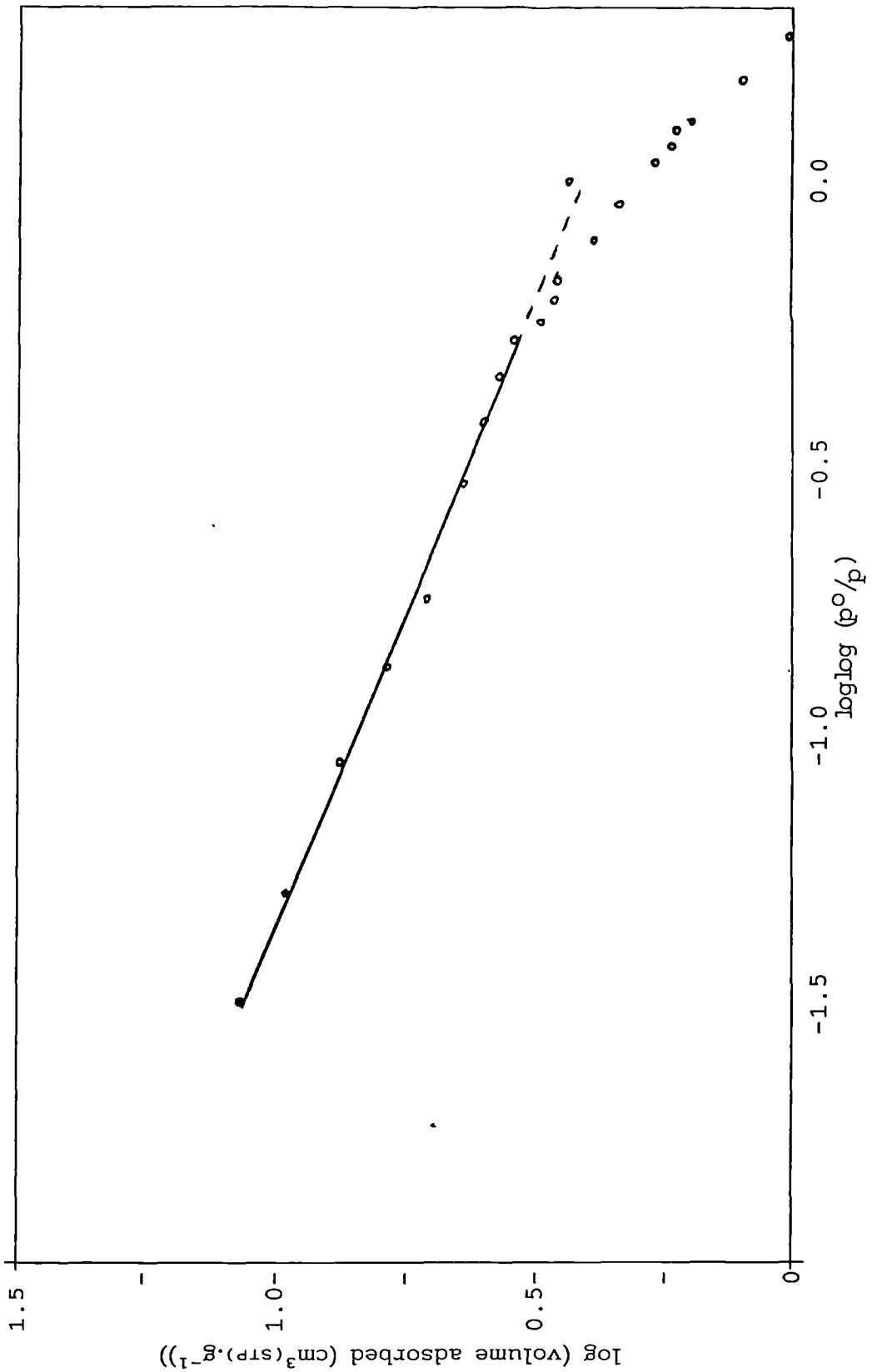

Figure 6.13 Frenkel-Halsey-Hill (FHH) plot for sample 51.

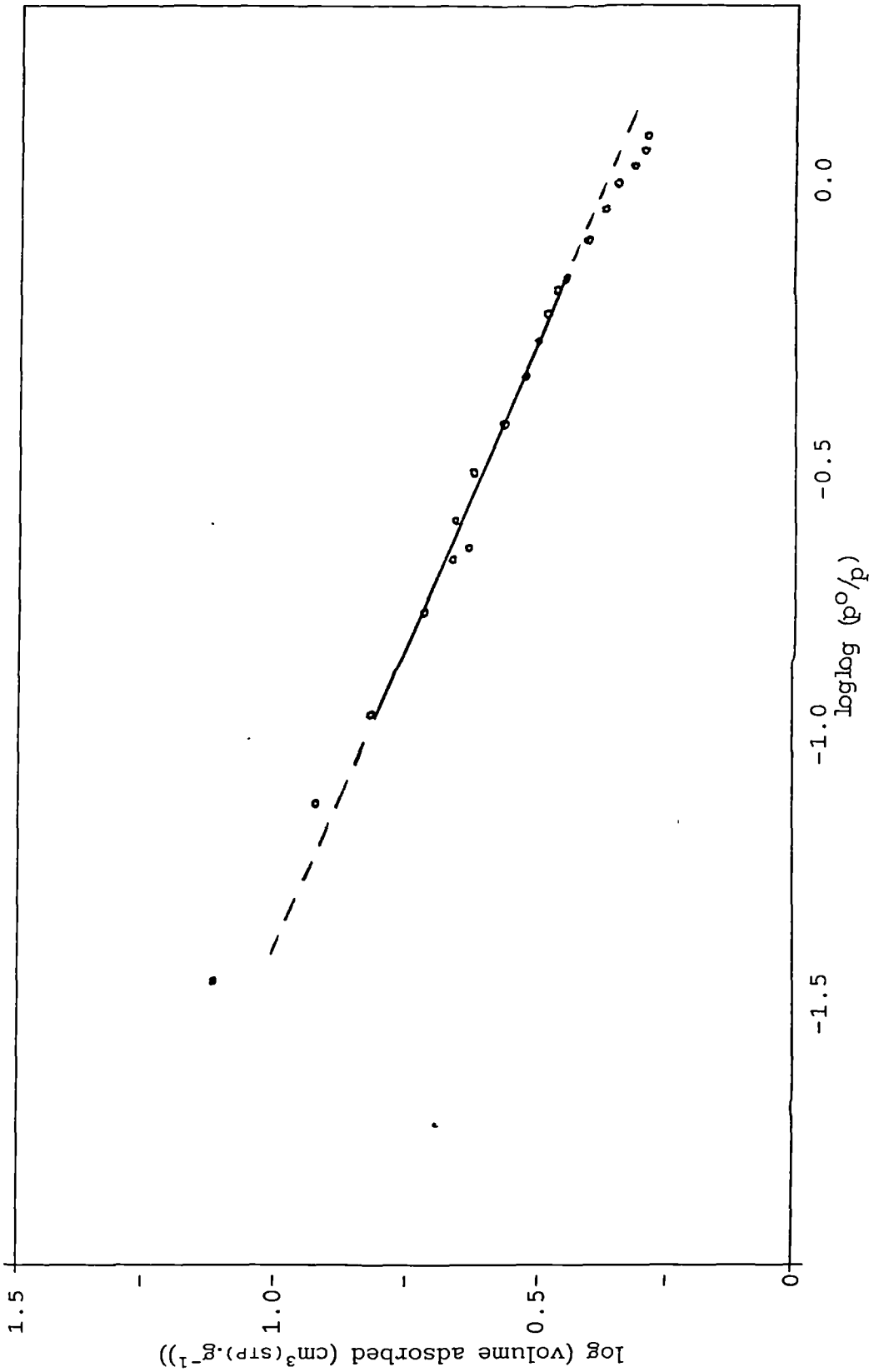

Figure 6.14 Frenkel-Halsey-Hill (FHH) plot for sample 67.

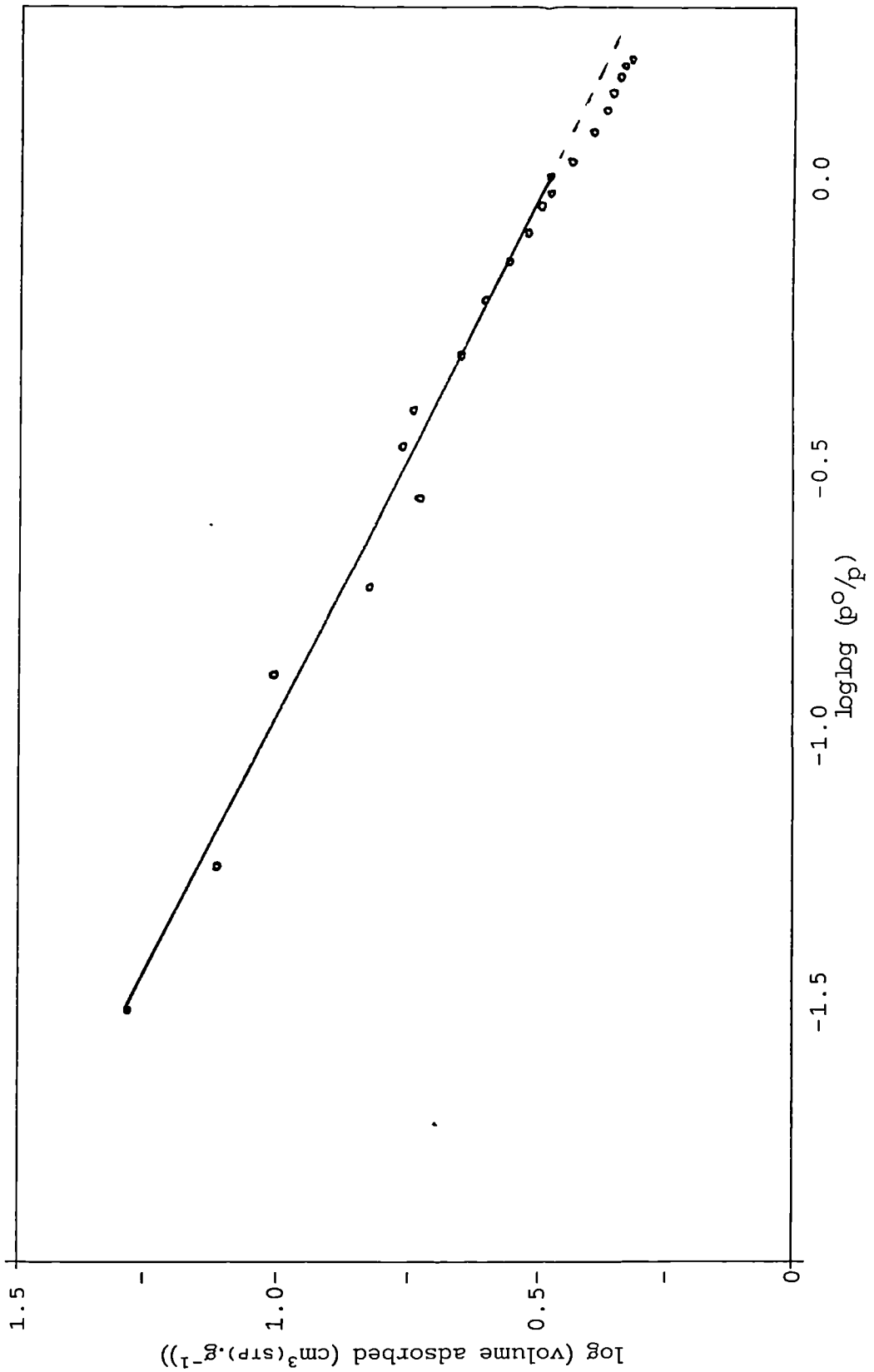

Figure 6.15 Frenkel-Halsey-Hill (FHH) plot for sample 68.

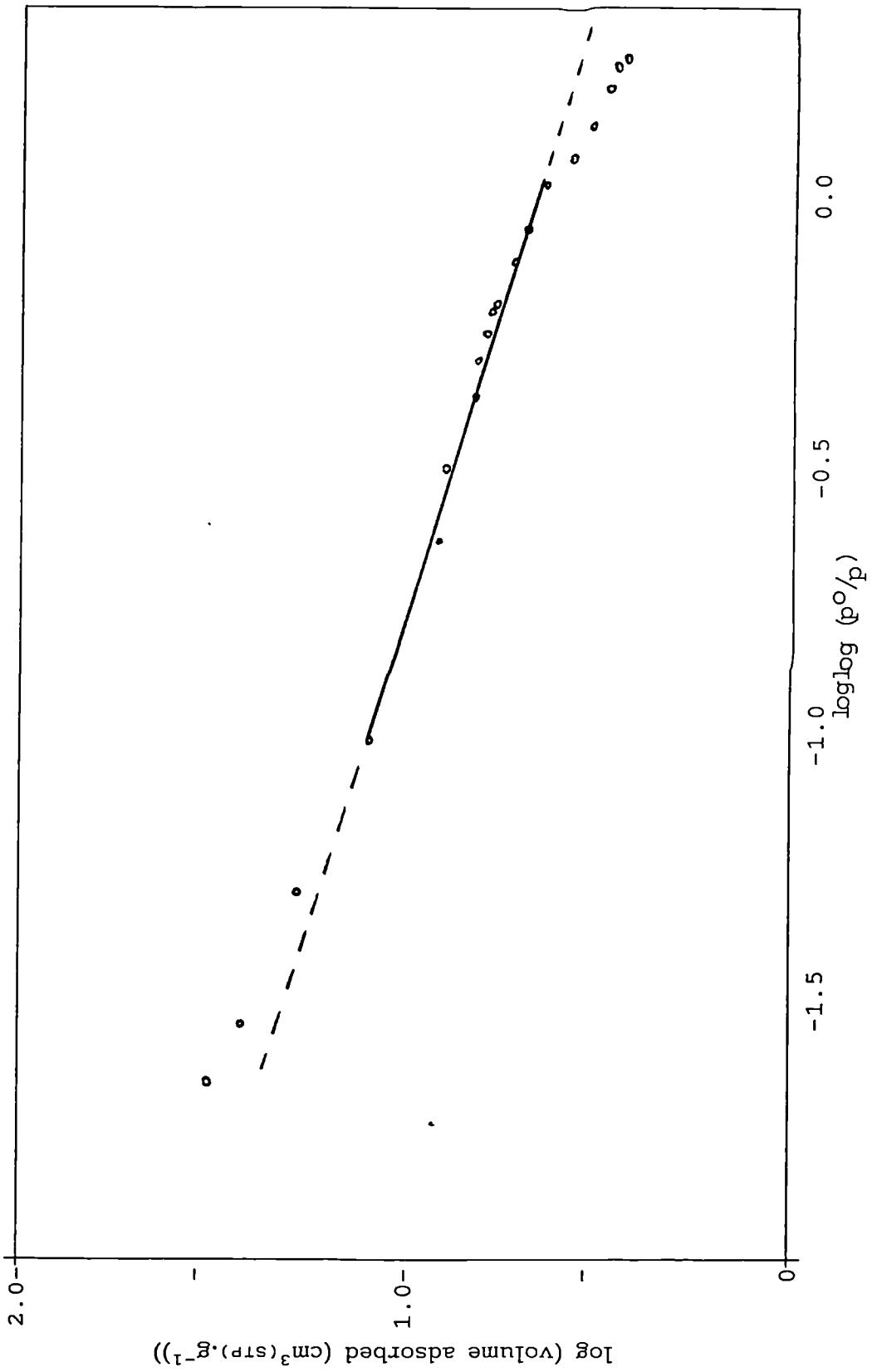

Figure 6.16 Frenkel-Halsey-Hill (FHH) plot for sample 69.

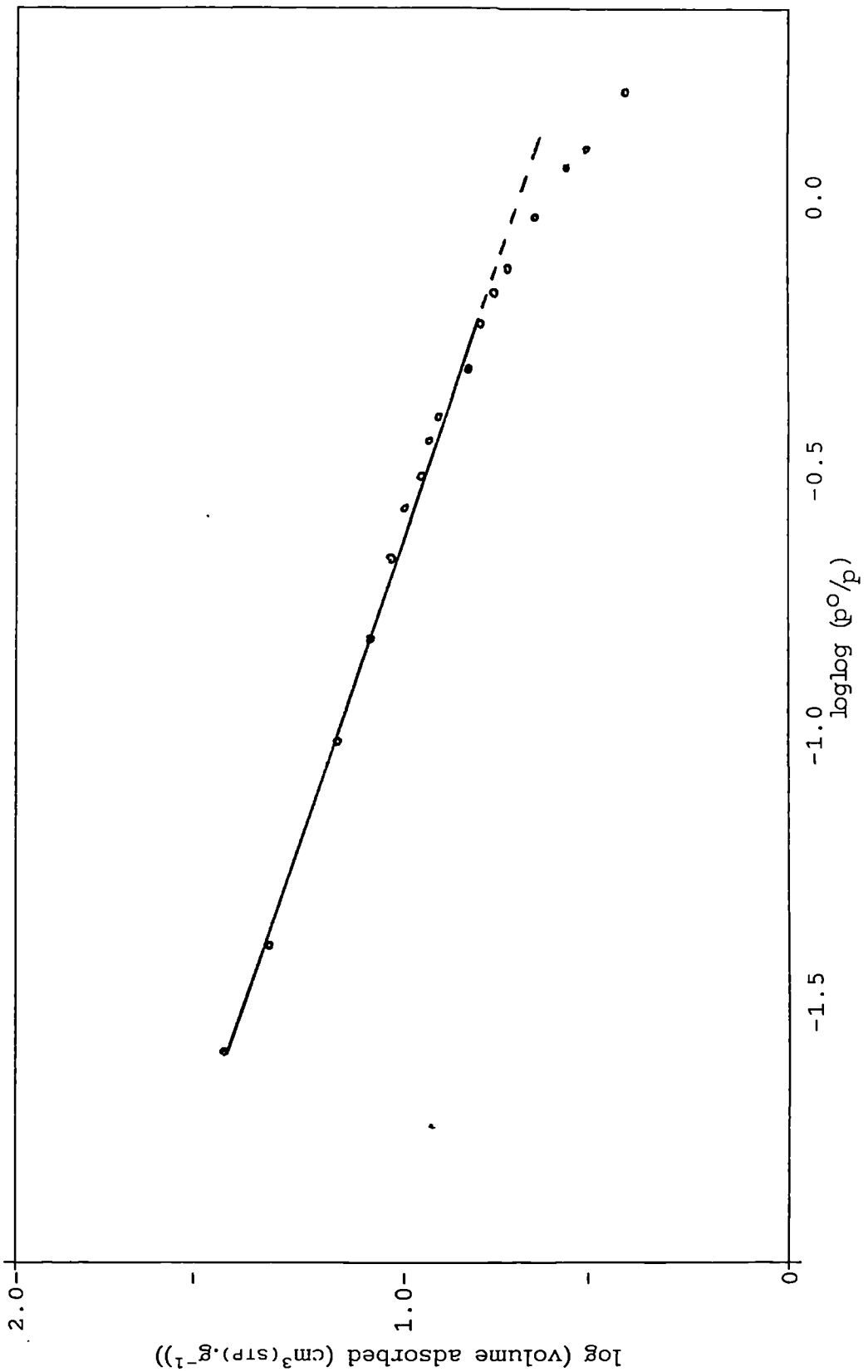

Figure 6.17 Frenkel-Halsey-Hill (FHH) plot from consecutive isotherm for sample 69.

pore-type openings. Similar downward deviation from linearity at low p/p_o is exhibited by samples 67, 68 and 69, but to a lesser extent. This decrease in downward deviation may be as a result of the sheet-like crystals of samples 67, 68 and 69 forming aggregates containing many more capillaries than pore-type openings. FHH plots for samples 67 and 69 exhibiting upward deviation from linearity at high relative pressures, onset of deviation at $p/p_o \sim 0.8$, support the assumption that the samples form aggregates containing capillaries. These observations imply that the suggestion that the cause of the increase in r is possibly correct.

A reduction in the value of r from 2.50 for sample 51 to 2.32 for sample 67 is unlikely to be due to a change in surface energy, but due to there being two different pore size distributions in sample 67, as the chemical nature of the two samples is the same, only the morphologies are different.

Samples 68 and 69 were prepared by the same precipitation process in which the precipitate was divided in to two portions. The first portion was washed in ethanol and designated sample 68 and the second portion was washed in acetone and designated sample 69. Sample 68, shown in Plate 11 A, exhibits an FHH plot, shown in Figure 6.15, exhibiting only downward deviation at low p/p_o and an r value of 2.26. Sample 69, shown in Plate 11 B, exhibits an FHH plot, shown in Figure 6.16, exhibiting both downward deviation at low p/p_o and upward deviation at high p/p_o, and an r value of 2.83. The observed increase in the value of r for sample 69 is most likely to be due to the formation of capillaries in the crystal structure resulting in capillary condensation producing an increased r value. This is a result of sample 69 consisting of large, thin plate-like crystals, shown in Plate 11 B, and samples 67 and 68 consisting of continuous, curled sheets, shown in Plates 10 A and B and 11 A respectively, hence the lower r values observed for samples 67 and 68. This result can be explained by Zettlemoyer's observation [109] that lower values of r (~2.1) are obtained for nitrogen on low-energy surfaces. It has been found [110] that aged copper phthalocyanine pigments (with discrete crystals in the acicular form) give r ~2.5. Lower r values (1.8-2.1) were

obtained with aggregates of less well-defined copper phthalocyanine crystals. In such cases, the decrease in the value of r appears to be the direct result of interparticle capillary condensation which may begin at p/p^o ~0.3 and thus change the course of the isotherm over the whole of the useful range of the FHH plot.

The suggestion that capillary condensation is the cause of the increase in the r value for sample 69 has been shown to be correct. From the FHH plots produced from the adsorption data of two consecutive nitrogen adsorption-desorption runs, shown in Figures 6.16 and 6.17 respectively for the first and second consecutive runs, on sample 69, it is evident that there is no upward deviation from linearity at high p/p^o in the plot from the second adsorption-desorption run, shown in Figure 6.17 (*cf.* Figure 6.16). Elimination of the upward deviation observed in the first adsorption-desorption run is probably due to the capillary condensed nitrogen, on desorption, forcing apart the plate-like crystals and making the surface more readily accessible to the nitrogen molecules on the second adsorption-desorption run.

6.1.3 Dubinin-Radushkevitch-Kaganer (DRK) Plot

The DRK surface areas obtained for vermiculite and samples 19, 40, 51, 67,68 and 69 are shown in Table 6.1. It can be seen that there is a rough correlation between the BET surface areas and the DRK surface areas, but in general such a comparison produces a confused picture [111-115]. In a number of investigations linear DRK plots have been obtained over restricted ranges of the isotherm, and in some cases reasonable agreement has been reported between the DRK and BET values. Kiselev and his co-workers [116] have pointed out, however, that since the DR and the DRK equations do not reduce to Henry's Law (n = const x p) as $n \rightarrow 0$, they are not readily susceptible of statistical-thermodynamic treatment. Moreover, it is not easy to see how exactly the same form of equation can apply to two quite diverse processes involving entirely different mechanisms. Thus it would be prudent to conclude that the significance of the DRK plot is obscure, and its validity for surface area estimation very doubtful.

6.1.4 Nitrogen BET Surface Areas

Nitrogen BET surface areas for vermiculite and samples 19, 40, 51, 67, 68 and 69, obtained from the nitrogen adsorption isotherms are shown in Table 6.1, and the nitrogen BET surface areas for samples 68, 69, 74, 80, 81 and 82 that were heat treated over the range of temperatures 293- 701K, determined using a Carlo Erba Sorpty 1750 single point nitrogen adsorption rig, are shown in Table 6.2.

Not surprisingly, the surface areas of the prepared calcium hydroxide materials increase as the morphology changes from large crystals of S_{BET} ~1, *eg.* Plate 9 A, to hexagonal tablets of S_{BET} ~10, *eg.* Plate 7 A, to thin, sheet-like crystals of S_{BET} ~22, *eg.* Plate 11 B, as can be seen from Table 6.1.

S_{SP} results shown in Table 6.2 are much more interesting. The samples can be classified into two distinct categories: (a) samples that exhibit a significant increase in S_{SP} as the temperature of the heat treatment increases, followed by a marked fall in S_{SP} at treatment temperatures of 601K or higher; and (b) samples which exhibit a slight increase in SSP on heat treating at 473K, thereafter the S_{SP} remains effectively constant over the range of temperatures up to 623K.

Samples 68 and 69, which are non-silylated, are category (a) materials. The TGA plot for non-silylated materials, shown in Figure 8.30 exhibits a weight loss with onset in the region of 673K which is due to the loss of water as the hydroxide is decomposed. As the water is driven off as vapour, it would be expected that the material would suffer fracturing together with formation of pore-type features. Such a mechanism would explain the marked increase of S_{SP} with increasing temperature. The recorded drop in S_{SP} for sample 69 at 603K could be due to carbonation as the samples were heated in air prior to S_{SP} measurement, whereby some of the pore-type features generated during the

decomposition of the hydroxide are blocked by the formation of surface carbonate moieties.

Samples 74, 80, 81 and 82 do not exhibit a similar marked increase in S_{SP}. They have all undergone a silylation reaction, which has apparently stabilised the calcium hydroxide, as can be seen from the TGA plot of a silylated sample, shown in Figure 8.31. Evidence of the stability imparted by silylation can be seen by comparing the S_{SP} results of sample 82 heated in air prior to S_{SP} measurement, to the S_{SP} results of sample 82 heated under vacuum prior to S_{SP} measurement. The S_{SP} measurements are identical for all temperatures up to 553K, but at 623K the S_{SP} increases from 28 m^2g^{-1} to 48 m^2g^{-1} for the sample heated under vacuum.

7. RESULTS AND DISCUSSION III

WATER ADSORPTION

7.1 Introduction

In this chapter the water isotherms are presented. The BET surface areas, DR plots and FHH exponents will be discussed. The results are summarised in Table 7.1 and the raw data have been collected in Appendix C.

7.1.1 Water Adsorption Isotherms

The water isotherms of samples 69, 74, 79, 80 and 82 carried out at 304K are shown in Figures 7.1 - 7.11 (solid symbols represent desorption branch). A series of water isotherms were performed on each sample without removal from the adsorption apparatus, wherein prior to running each isotherm the sample was either outgassed at a temperature from ambient to 773K, or heated in air at 423 - 773K prior to outgassing at 423K.

Sample 69, a non-silylated material, when outgassed under vacuum either at room temperature or at 473K exhibits isotherms of similar shape. Each isotherm in Figures 7.1 and 7.2 has pronounced hysteresis which extends to very low p/p^o and the initial part of the adsorption branch (at $p/p^o < 0.3$) is characteristic of a low affinity for water similar to that shown by dehydroxylated silicas [117-119]. It is already known that slow rehydroxylation takes place when dehydroxylated silicas are exposed to water vapour [117,120]. When a partially dehydroxylated silica is exposed to water vapour it undergoes slow rehydroxylation. This process will occur during the course of an isotherm determination, and because of its limited rate , will produce low-pressure hysteresis. Rehydroxylation probably commences with physical adsorption, initiated by hydrogen bonding of water molecules to any remaining hydroxyl groups in the surface, followed by the growth of clusters of molecules. When an adsorbed molecule is sufficiently close to a surface oxygen, chemical interaction resulting in two hydroxyl

Table 7.1 Summary of Results Obtained from Water Adsorption

Sample	Pre-treatment Temperature	Outgassing Temperature	BET Water Surface Area	"c" value	DR Water Surface Area	FHH Exponent	Morphology
69	-	298K	12	12	14	0.89	Hexagonal plates
69	-	473K	21	11	17	1.11	"
69	-	550K	798	27	1121	7.44	"
74	-	298K	37	30	18	1.24	Continuous sheets
74	-	473K	12	14	14	0.97	"
74	-	550K	600	-251	879	8.00	"
79	-	298K	14	28	16	1.27	Hexagonal plates
79	420K	420K	14	7	7	0.69	"
79	620K	420K	9	16	6	0.89	"
79	770K	420K	368	-738	543	6.45	"
80	-	298K	29	14	25	1.37	Hexagonal plates
80	470K	420K	29	5	11	0.98	"
80	770K	420K	474	11	606	4.06	"
82	-	298K	31	29	29	3.49	Irreg. hexagonal plates
82	470K	420K	5	2	8	0.57	"
82	620K	420K	19	2	22	1.11	"

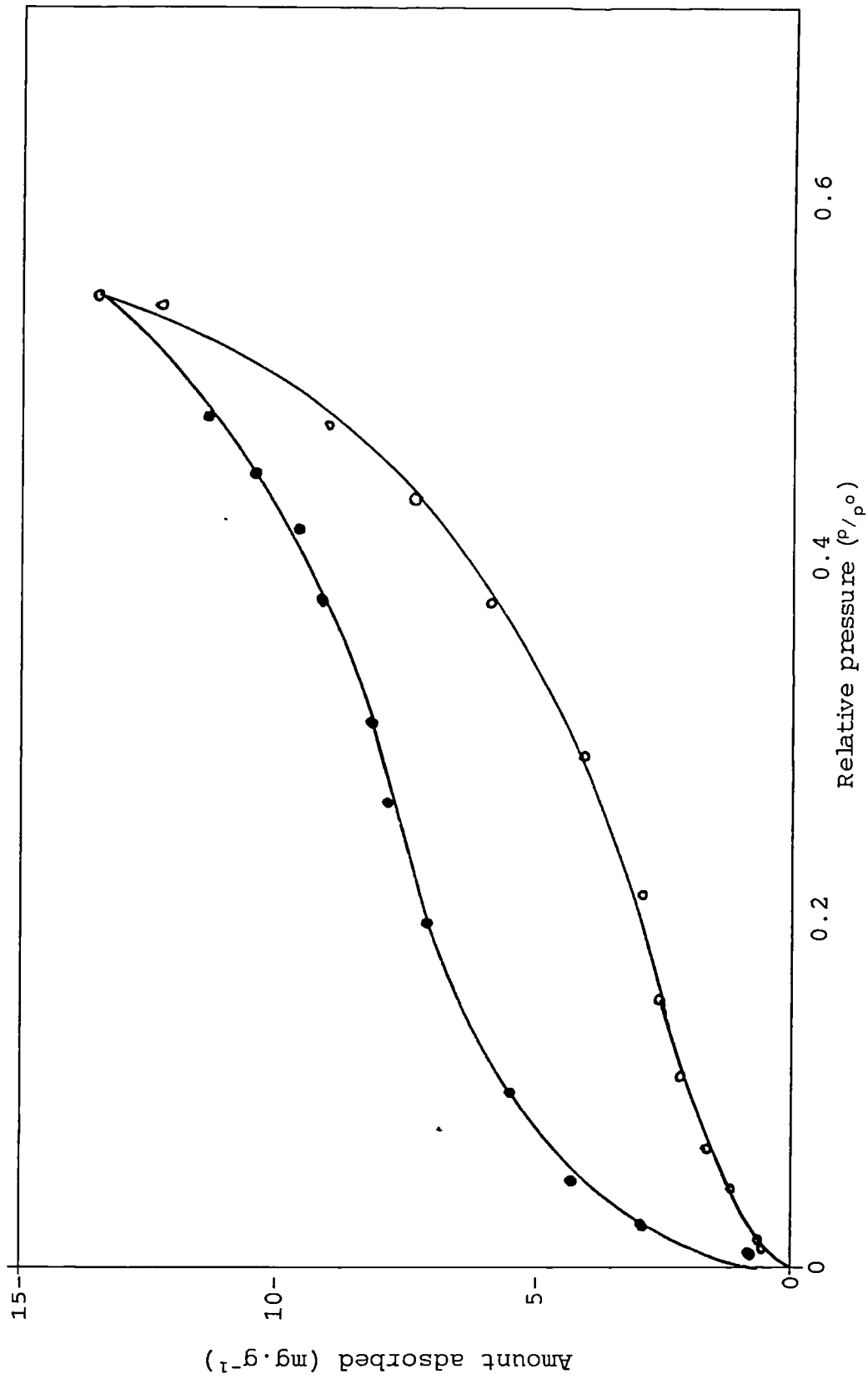

Figure 7.1 Water adsorption isotherm at 305K for sample 69 outgassed at 298K.

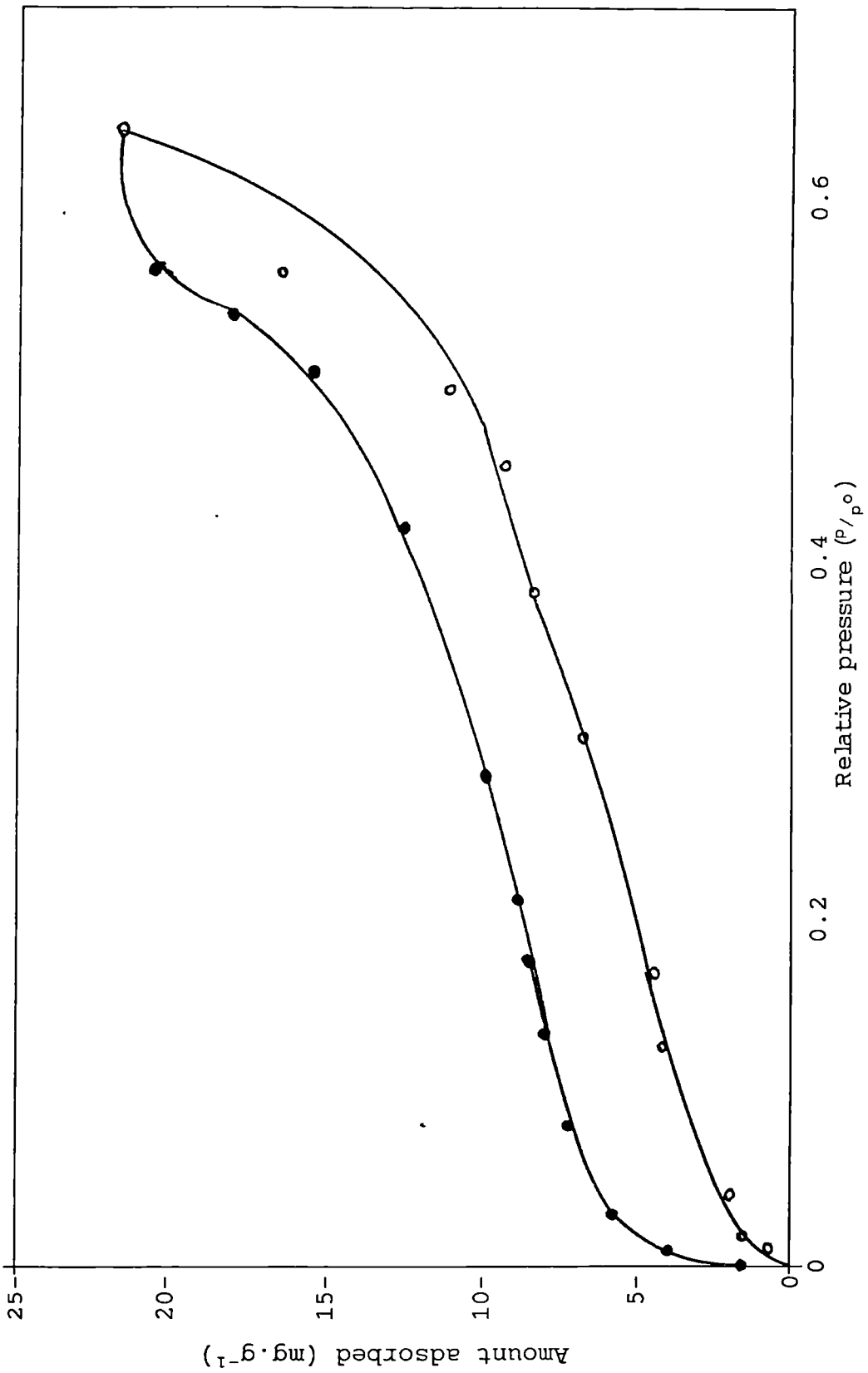

Figure 7.2 Water adsorption isotherm at 305K for sample 69 outgassed at 473KK.

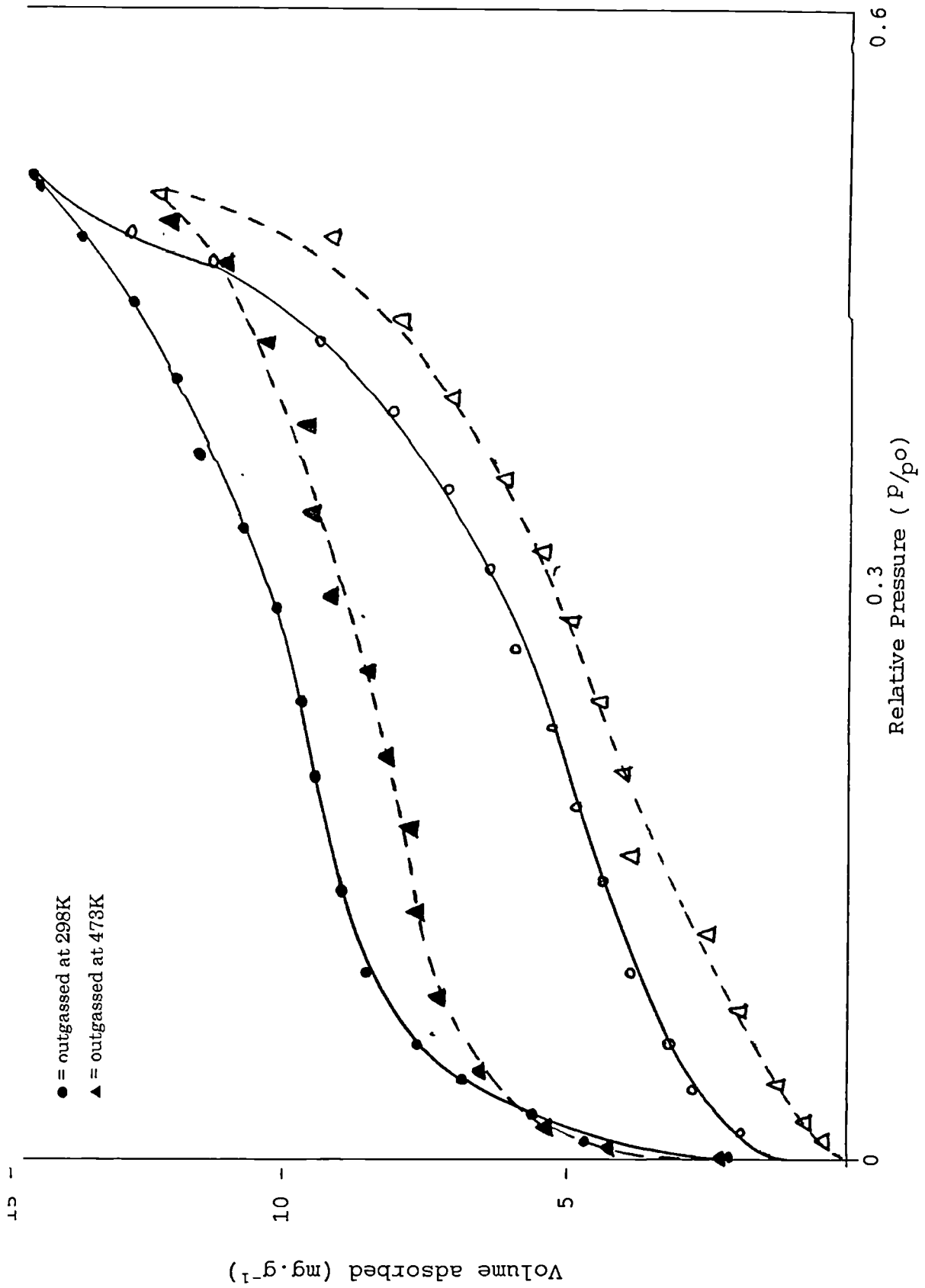

Figure 7.3 Water adsorption isotherms at 305K for sample 74 outgassed at 298K & 473K.

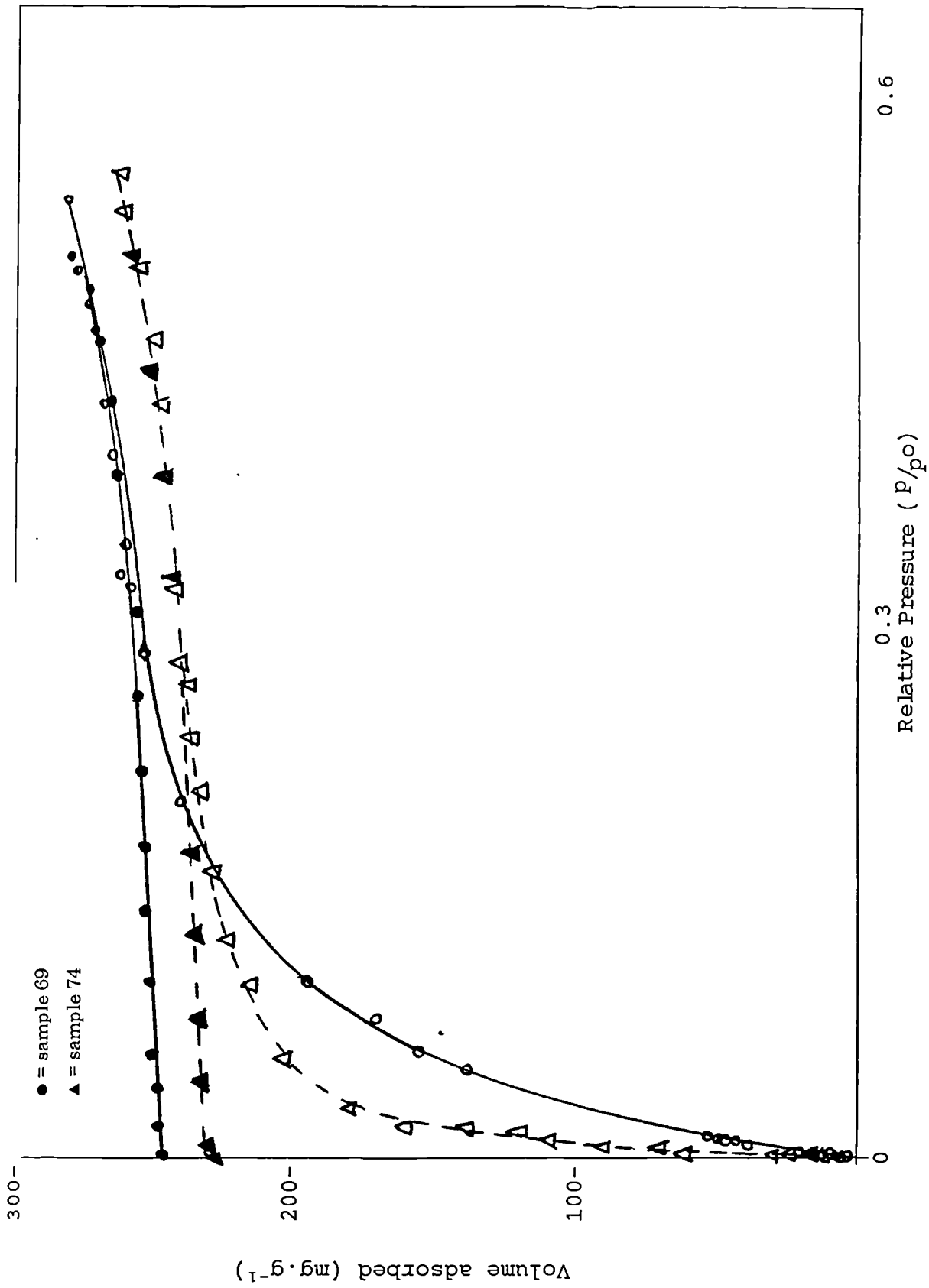

Figure 7.4 Water adsorption isotherms at 305K for samples 69 & 74 outgassed at 550K.

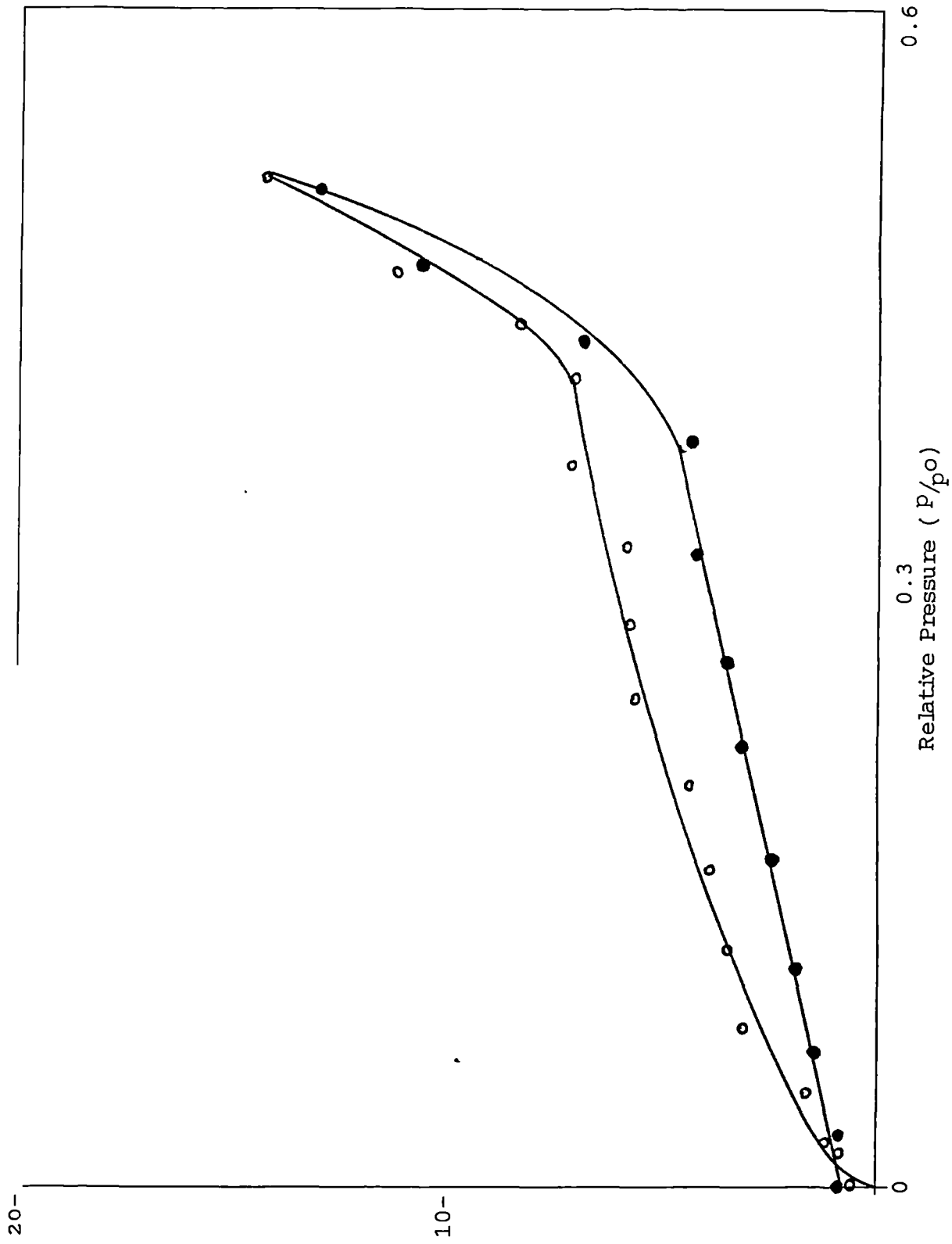

Figure 7.5 Water adsorption isotherm at 305K for sample 79 outgassed at 298K.

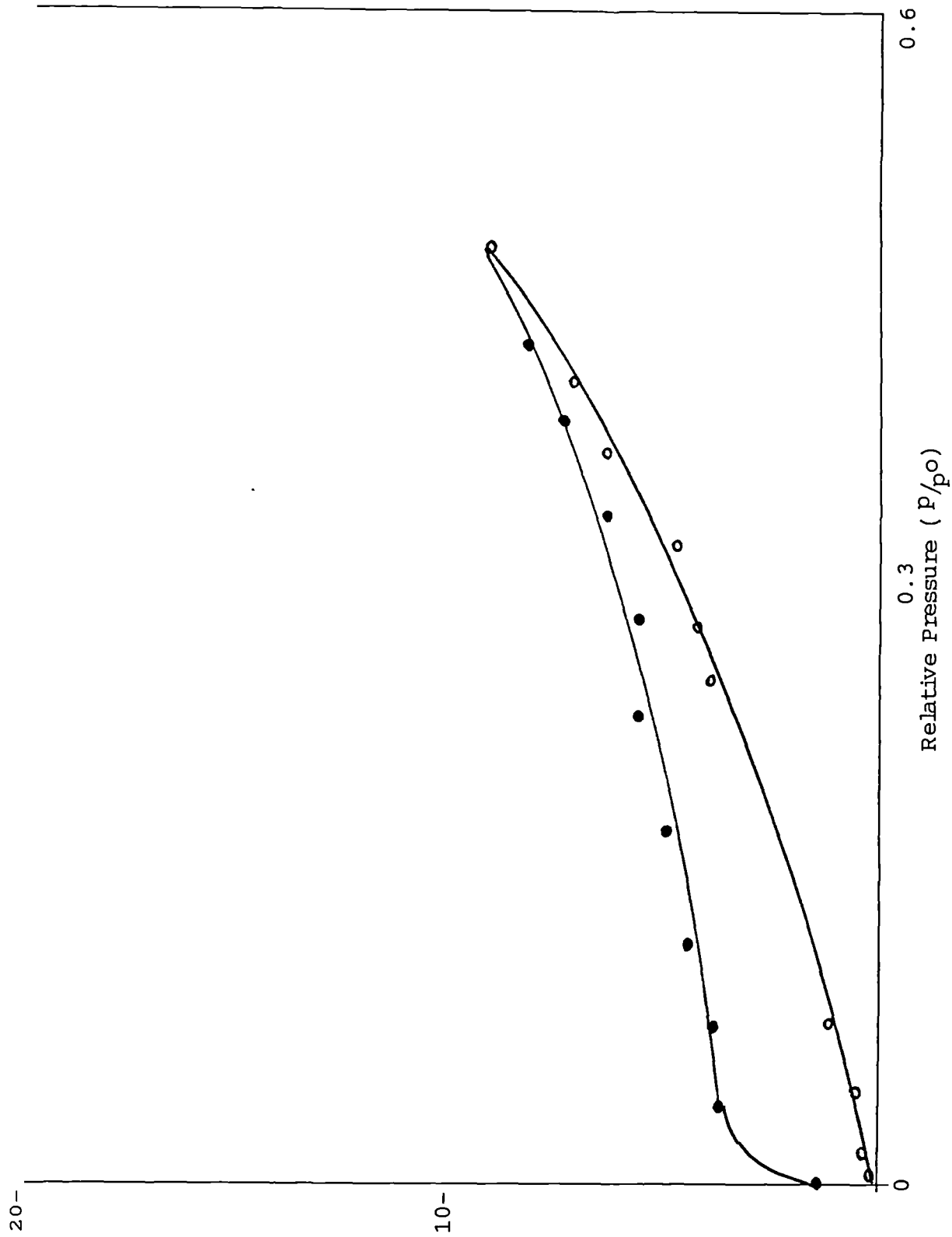

Figure 7.6 Water adsorption isotherm at 305K for sample 79 heated in air at 420K for 24 hours prior to outgassing at 420K.

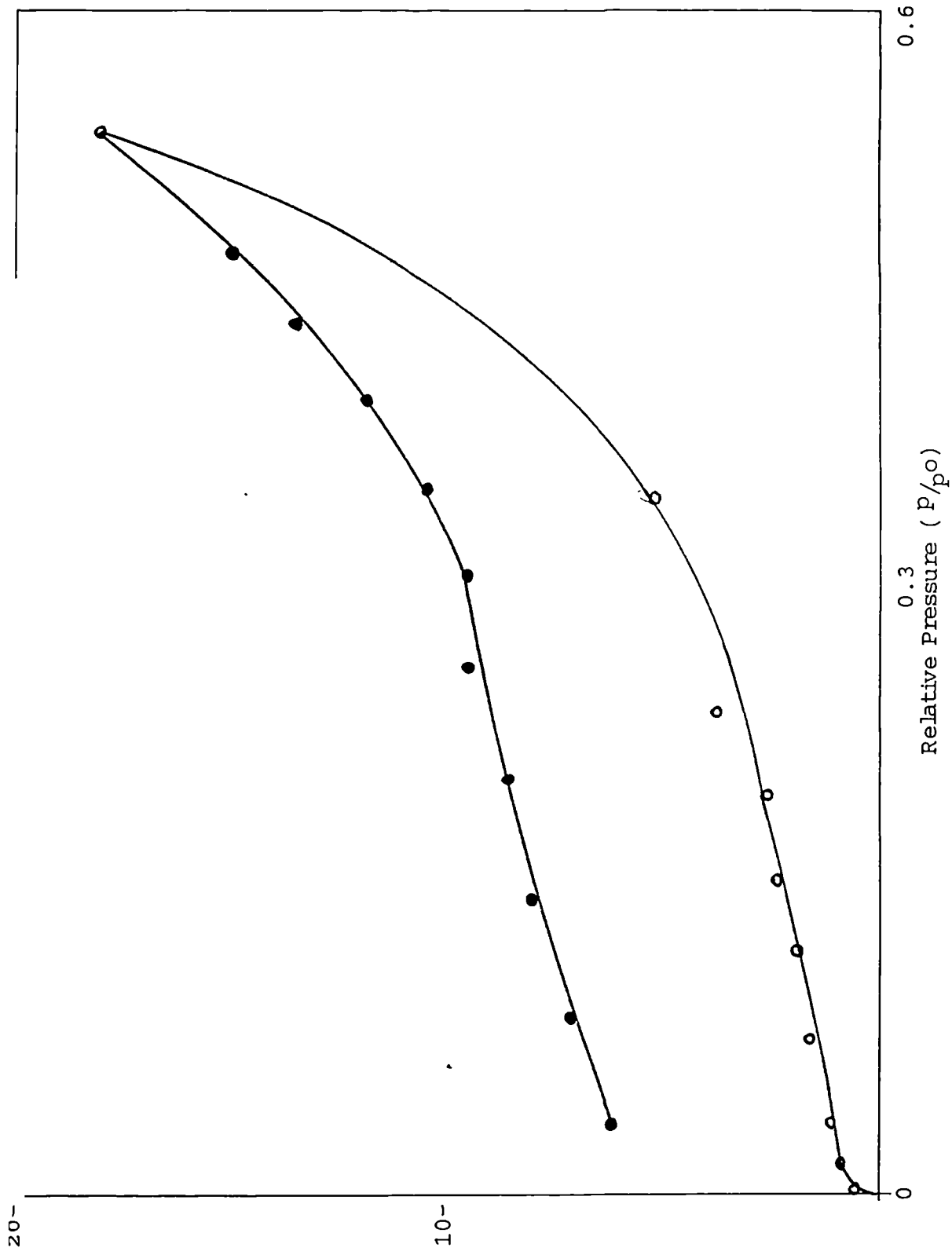

Figure 7.7 Water adsorption isotherm at 305K for sample 79 heated in air at 620K for 24 hourss prior to outgassing at 420K.

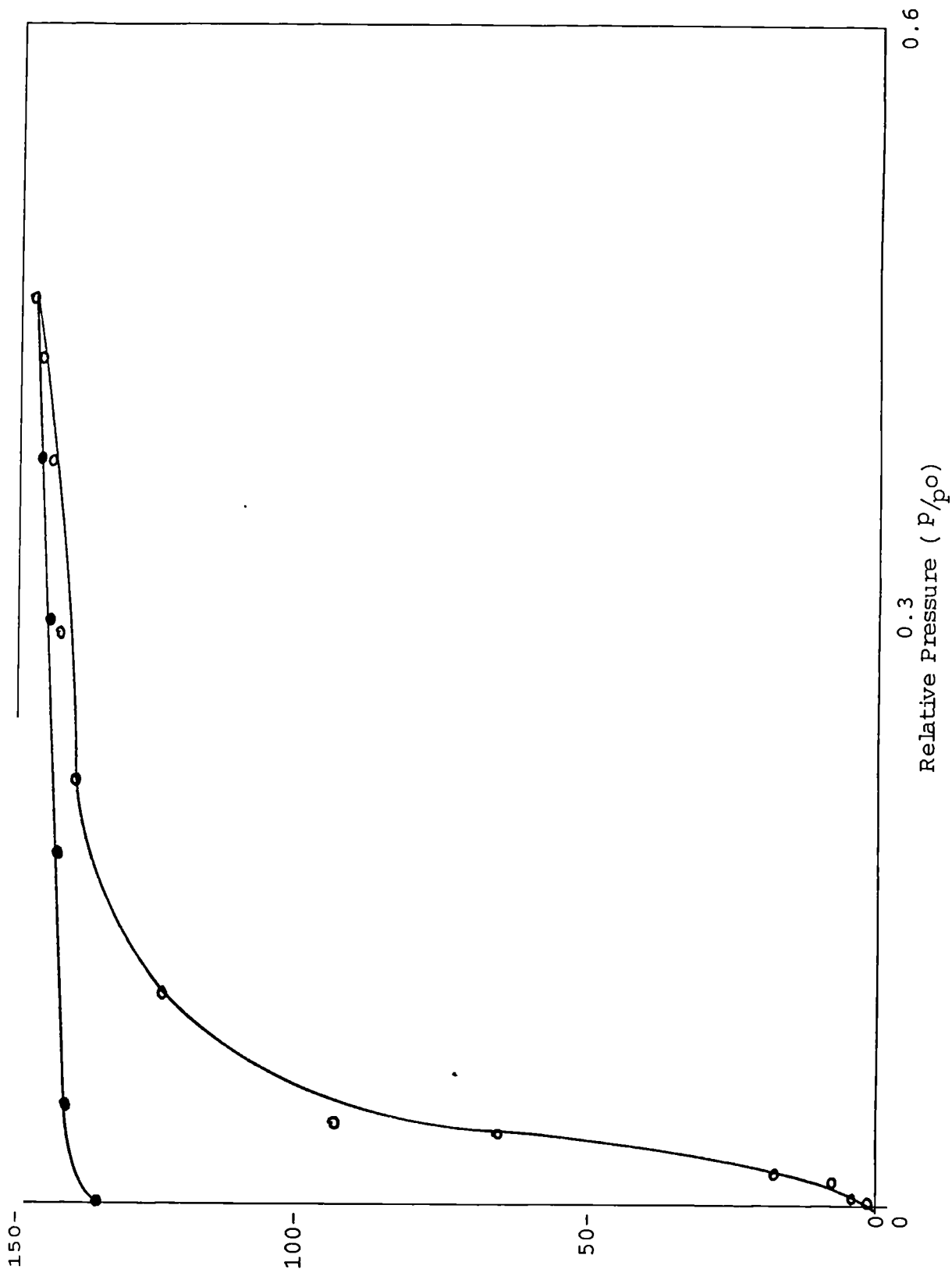

Figure 7.8 Water adsorption isotherm at 305K for sample 79 heated in air at 770K for 24 hours prior to outgassing at 420K.

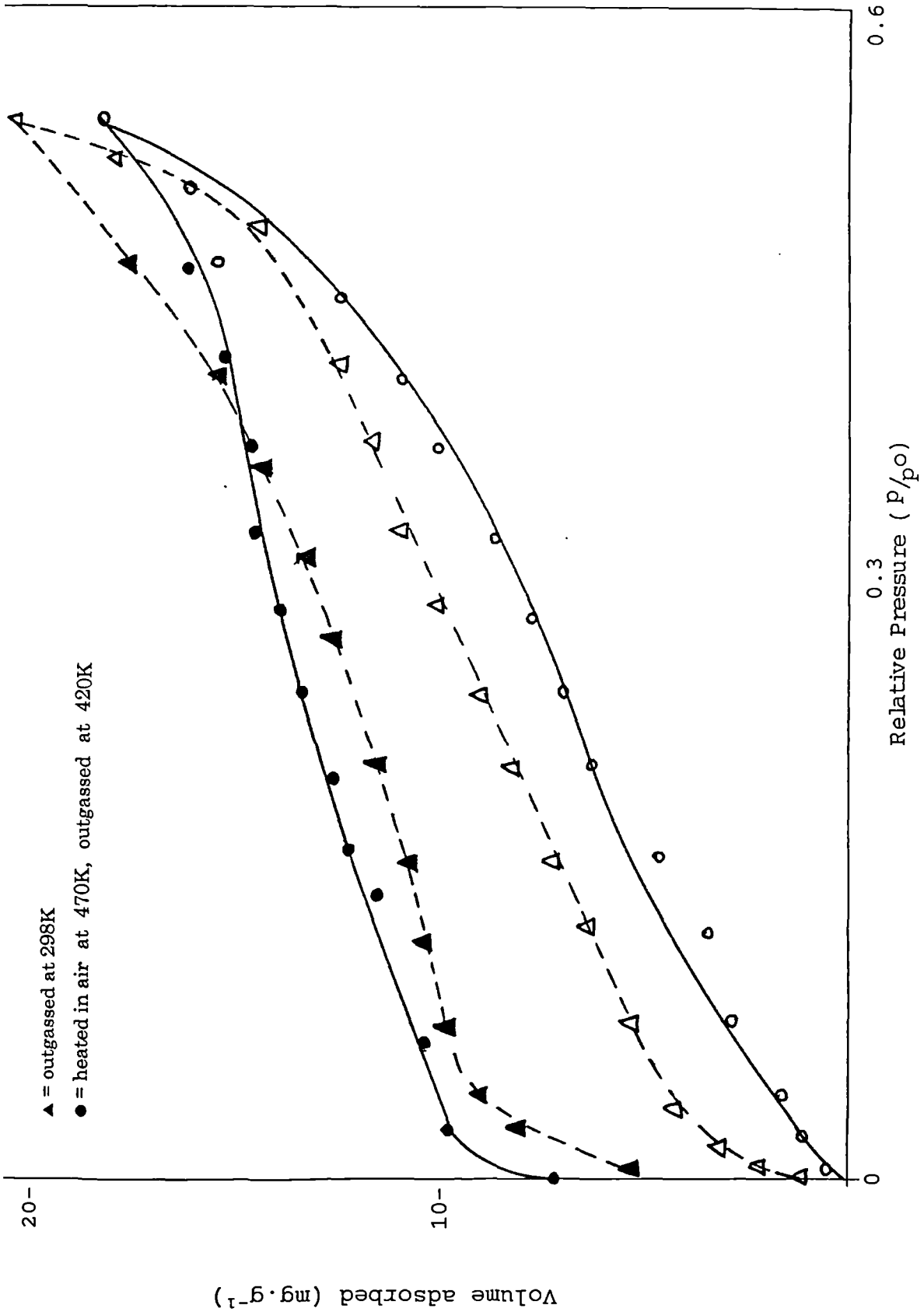

Figure 7.9 Water adsorption isotherms at 305K for sample 80 outgassed at 298K and after heating in air at 470K for 24 hours prior to outgassing at 420K.

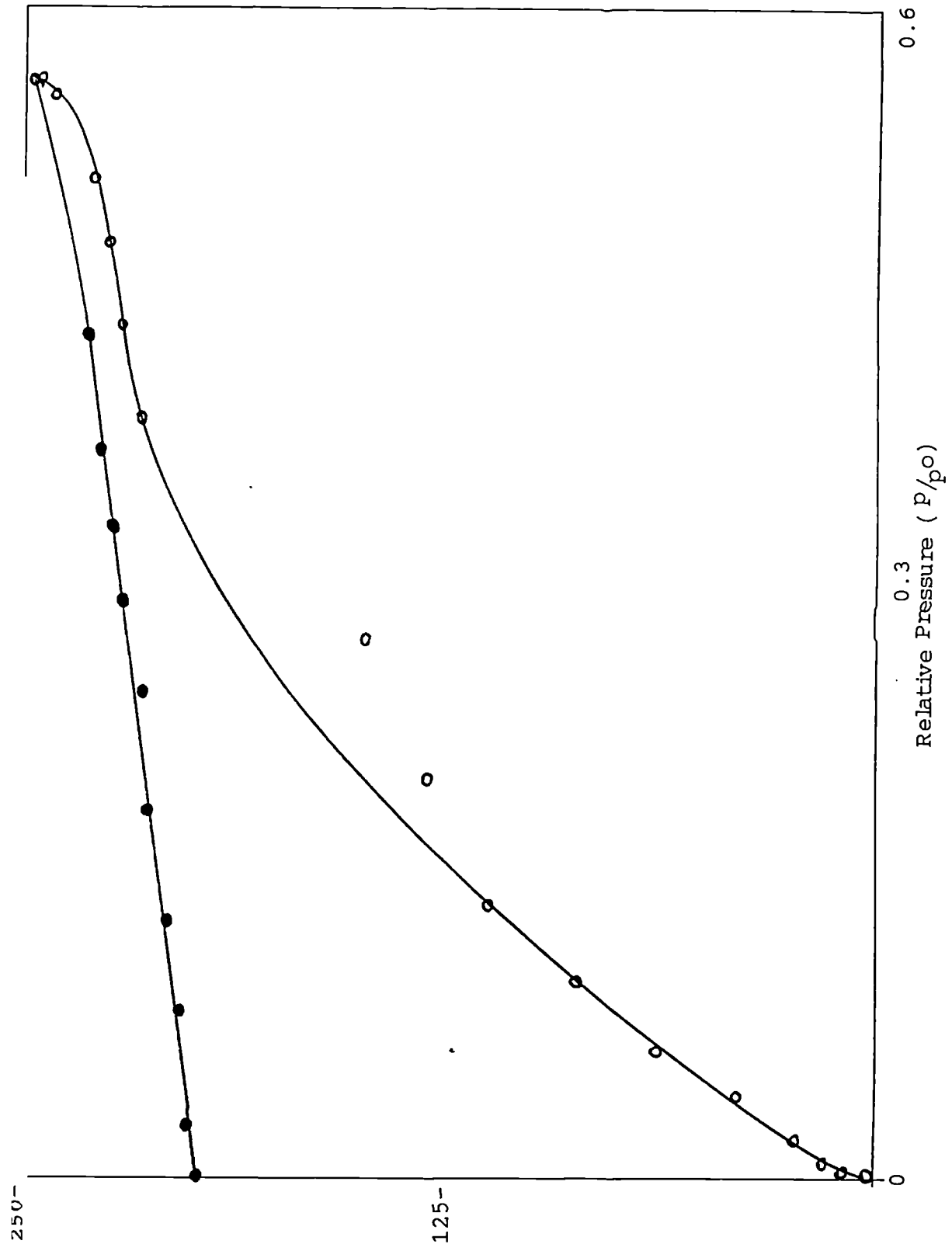

Figure 7.10 Water adsorption isotherm at 305K for sample 80 heated in air at 770K for 24 hours prior to outgassing at 420K.

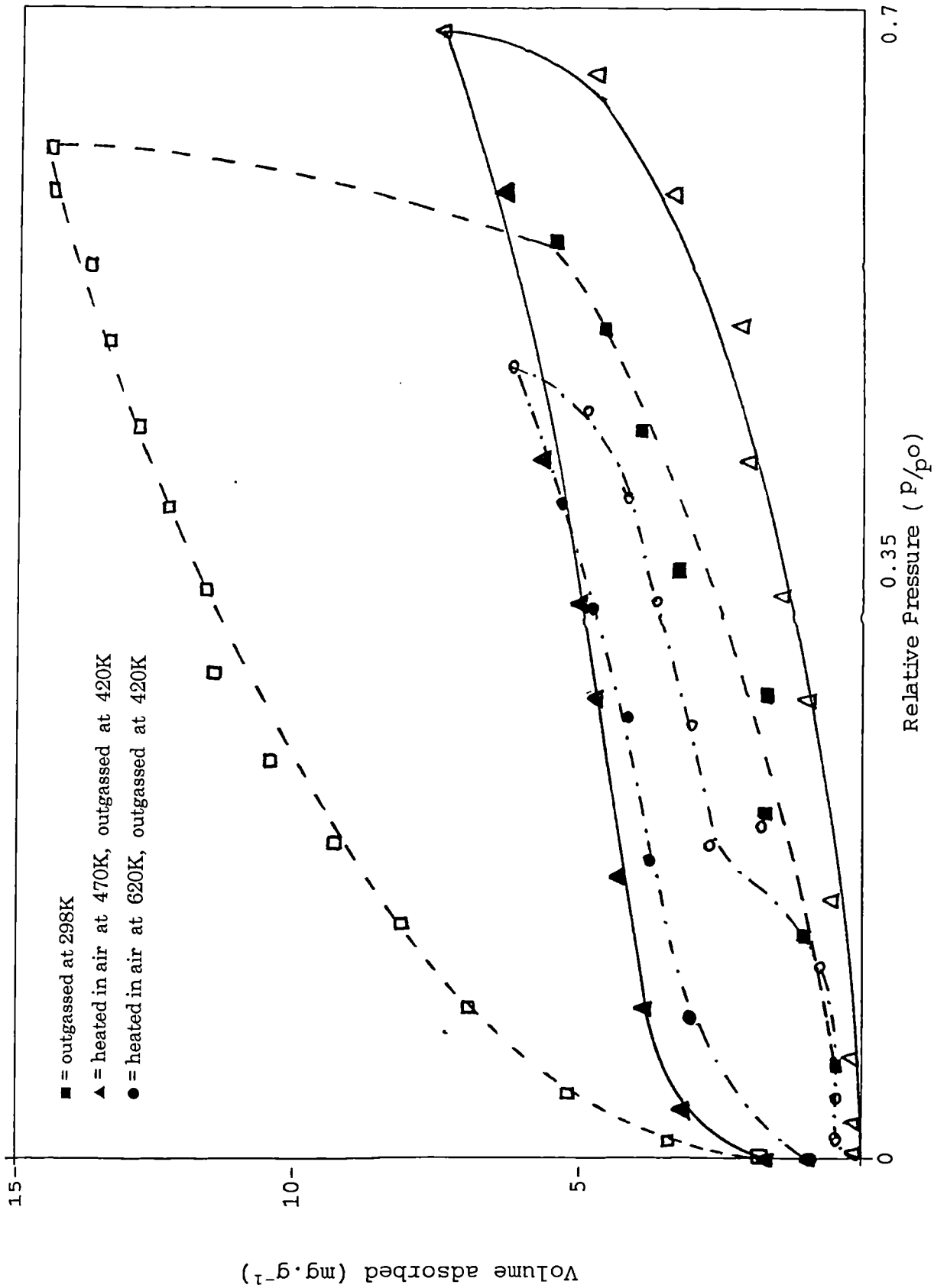

Figure 7.11 Water adsorption isotherms at 305K for sample 82 outgassed at 298K and heated in air at 470K & 620K for 24 hours prior to outgassing at 420K.

groups can occur; but since this rehydroxylation demands some rearrangement of surface atoms it will be an activated process and will therefore be slow. Owing to their superior ability to promote cluster formation, paired groups will lead to a more rapid hydroxylation than will isolated groups, and low-pressure hysteresis will be correspondingly less. Therefore the similarity between the calcium hydroxide material isotherms and previously published isotherms for hydroxylated silicas strongly indicates that the adsorption mechanism is the same in both cases. The shape of the isotherm for the sample outgassed at 473K, shown in Figure 7.2, is very similar to that observed when the sample is outgassed at room temperature (Figure 7.1), but the total amount of water vapour adsorbed is greater following outgassing at 473K. This is likely to be due to outgassing at the higher temperature resulting in not only surface dehydroxylation, but in removal of "trapped" water molecules from within the narrow channels and interstices within the aggregate. Such a view is consistent with the nitrogen adsorption data which showed the existence of aggregates.

Outgassing sample 69 at 553K results in a different type of isotherm, shown in Figure 7.4, which is indicative of chemisorption. The very steep initial part of the adsorption branch (at $p/p_o < 0.15$) is characteristic of a very great affinity for water. Rehydroxylation occurs rapidly, and irreversibly as is evident from the almost plateau-like desorption branch. The most likely explanation for this considerable change in isotherm shape is that the calcium hydroxide is decomposed, forming the oxide. Taking the intercept of the desorption branch with the ordinate to obtain the amount of water chemisorbed, and calculating the stoichiometric amount of water that would be required to slake the calcium oxide produced on outgassing, it is found that the two quantities of water are identical, being 24.3% by weight. Thus the assertion that the isotherm of the sample outgassed at 553K is decomposed is correct.

Sample 74, a silylated material having a sheet-like morphology, shown in Plate 12 A, exhibits isotherms, shown in Figure 7.3, of a similar shape to those obtained with the non-silylated material, shown in Figures 7.1 & 7.2, therefore indicating the existence of

a rehydration/rehydroxylation process. The amount of water adsorbed per gramme of sample 74 is higher following room temperature outgassing than the amount of water adsorbed following outgassing at 473K. This indicates a reduction in the number of sites available for hydroxylation, which in turn indicates an increase in hydrophobicity. Sample 69, the non-silylated material, in contrast exhibited an increase in the amount of water adsorbed following outgassing at 473K, indicating an increase in hydrophilicity. It has been postulated in the case of sample 69 that the increase in water adsorption following outgassing at 473K was due to the removal of water from within the narrow pores and interstices of aggregates, which increases the number of sites available for rehydration. The same mechanism may also be responsible for the apparent increase in hydrophobicity of sample 74 when outgassed at 473K. Sample 74 contains surface $Si(CH_3)_3$ groups which are hydrophobic and would be expected to reduce the amount of water that would be adsorbed irrespective of outgassing temperature. But here, an increase in hydrophobicity occurs. This is mostly likely due to water molecules "trapped" within the narrow pores and interstices of aggregates being forced out during outgassing; thereafter on exposure to water vapour, the water molecules are unable to either rehydrate the surfaces of the narrow pores and interstices of the aggregates or undergo capillary condensation as a direct result of the $Si(CH_3)_3$ surface groups. Furthermore, comparison of the isotherms for samples 69 and 74 reveals that the low-pressure hysteresis is larger for sample 74 than for 69, which confirms the greater hydrophobicity of sample 74 in that the rehydration/rehydroxylation of sample 74 is a much slower process than for sample 69.

Outgassing sample 74 at 473K greatly increases the amount of water adsorbed as can be seen from the isotherm, shown in Figure 7.4. The shape of the isotherm is identical to that obtained with sample 69 when outgassed at 553K, and is therefore likely to be produced by the same mechanism, namely decomposition to the oxide. Comparison of the two isotherms shows that the amount of water required to slake decomposed sample 74 is less than that required for decomposed sample 69. Calculating the stoichiometric quantity of water required to rehydroxylate sample 74 as pure calcium

oxide, the figure arrived at is 24.3% by weight, whereas the experimental amount is 22.9% by weight. This discrepancy can be explained by considering that the sample was silylated. The $Si(CH_3)_3$ groups are attached to the calcium hydroxide substrate via Ca—O bonds, which results in a reduction of the number of hydroxyl groups in the sample, and hence resulting in a reduction in the amount of calcium oxide produced on decomposition.

Sample 79, a silylated material comprising plate-like crystals, shown in Plate 12 B, when outgassed at room temperature produces a Type II isotherm exhibiting negative hysteresis, shown in Figure 7.5, and where the amount of water adsorbed at saturation is similar to that of sample 69, the non-silylated sample, but only half that of sample 74, a silylated sample.

The presence of negative hysteresis appears to be the direct result of aging [121], which occurs on exposure to water vapour. Thus, it has been found [122] that when an active solid (*e.g.* hydrous oxide) is left in contact with an aqueous medium or adsorbed water it generally undergoes irreversible structural and textural changes. With such systems three distinct aging processes have been identified [123]:

(i) Condensation polymerisation;
(ii) Aggregation - cementation; and
(iii) Recrystallisation.

Processes (i) and (ii) lead to a decrease in surface area, whereas process (iii) may involve fracture of particles or aggregates and as a consequence results in an increase in surface area.

A Type III isotherm is produced, shown in Figure 7.6, when sample 79 is heated in air at 423K for 24 hours prior to outgassing at 423K. The Type III isotherm is characteristic of weak gas-solid interactions [123] and of a non-porous or macroporous solid. It can be

seen from the adsorption branch of the isotherm that the uptake of water vapour at low relative pressures ($P/P_o < 0.3$) is about 50% of that of sample 79 when outgassed at room temperature. There are two possible explanations for this phenomenon. Firstly, the heating of the sample in air prior to outgassing may have caused some modification to the surface, such as migration of $Si(CH_3)_3$ groups to the surface, resulting in an increase in hydrophobicity; secondly, the preceding adsorption of water which resulted in the isotherm exhibiting negative hysteresis, shown in Figure 7.5, has resulted in the fracture of particles and aggregates, thus removing sites (narrow pores and interstices) available for possible capillary condensation. Furthermore, outgassing at room temperature may not have been sufficient to remove water trapped within the narrow pores and interstices of aggregates, hence the opportunity for adsorbate-adsorbate interactions (strong forces) would result in an enhanced adsorbate uptake and a Type II isotherm. Comparing the isotherm produced by sample 69 (non-silylated) outgassed at 473K, shown in Figure 7.2, to that of sample 79 (silylated) heated in air and outgassed at 423K, shown in Figure 7.6, it is readily apparent that some mechanism has caused a conversion from a Type II to a Type III isotherm. Kiselev [124] in a detailed study, treated a hydroxylated silica with trimethylchlorosilane so as to replace hydroxyl groups by the non-polar $Si(CH_3)_3$ groups; this had the effect of weakening both the dispersion and the polar interactions. As the surface concentration of the $Si(CH_3)_3$ groups increased the isotherm gradually lost its Type II character until with the completely converted surface, it was of Type III. Therefore in the case of sample 79, the conversion of the Type II isotherm in Figure 7.5 to the Type III isotherm in Figure 7.6 is probably due to the fracture of particles and aggregates by the first adsorption process with subsequent removal of "trapped" water molecules to leave a surface having a considerable concentration of $Si(CH_3)_3$ groups.

Heating sample 79 in air at 623K for 24 hours, prior to outgassing at 423K, results in the sample exhibiting a Type II isotherm with a broad hysteresis loop, shown in Figure 7.7. The low water uptake at low relative pressures ($P/P_o < 0.3$) and the plateau at P/P_o ~0.05 - 0.25 are indicative of a homogeneous, non-porous surface; whereas the

rapid increase in water uptake at $P/P_o \sim 0.35$ together with the large hysteresis loop, indicate capillary condensation. This is a considerable change from the Type III isotherm shown in Figure 7.6. Therefore a chemical and/or physical change has occurred to the surface of the sample. The magnitude and shape of the isotherm in Figure 7.7 is similar to that obtained by the non-silylated sample, shown in Figure 7.2, thus the surface of the sample must have been affected by heating at 623K in air. The most probable affect is carbonation of the surface of the sample, which may also result in some cementation of particles leading to formation of narrow pores and interstices. This hypothesis is corroborated by the infra-red spectroscopic studies (*ante*). The lower total water uptake by the carbonated silylated sample compared to the non-silylated sample is most probably due to the $Si(CH_3)_3$ groups being heat stable and preventing carbonation in their region of the surface.

Heating sample 79 at 773K for 24 hours, prior to outgassing at 423K, produces a marked change in the isotherm to a Type I, shown in Figure 7.8. The rapid water uptake at very low relative pressures ($P/P_o < 0.05$), and the desorption branch intercepting the ordinate at 135 mg g^{-1}, is indicative of chemisorption. If the calcium hydroxide crystals were decomposed to form the oxide the amount of water required to slake the oxide would be ~240 mg g^{-1}. In this case the amount of water irreversibly absorbed is only 135 mg g^{-1}. Therefore ~55% of the hydroxyl groups were converted to the oxide, and thus the remaining hydroxyl groups must have been carbonated or replaced by $Si(CH_3)_3$ groups.

Sample 80, having a plate-like morphology as can be seen from Plate 13 A, exhibits Type II isotherms with very broad hysteresis loops, shown in Figure 7.9, when outgassed at room temperature and when heated in air at 473K for 24 hours prior to outgassing at 423K. These isotherms are very similar in shape to those obtained with sample 74, shown in Figure 7.3, which is expected as the samples were precipitated using the same proportions of precipitants. The only significant difference in the precipitation reaction is that, for sample 80 the amount of silylating agent present was

considerably larger than was present for sample 74. Comparing the isotherms for sample 80, it is seen that the hysteresis associated with the isotherm of the room temperature outgassed sample is not as broad as that associated with the isotherm of the sample heated to 473K prior to outgassing at 423K, but the total amount of water adsorbed by the heated sample is lower than the amount adsorbed by the room temperature outgassed sample. These results could indicate that when sample 80 is outgassed at room temperature, water molecules trapped within aggregates, and associated narrow, pore-like features and interstices, are not removed. This would result in the presence of sites at which water molecules could easily be adsorbed onto and desorbed from. Alternatively the surface propionate groups, shown to be present by reflectance FTIR spectroscopy (Figure 8.17) may be the source of hydrophilic sites upon which the water vapour could adsorb rapidly. Upon heating the sample at 473K and outgassing at 423K, the hysteresis loop is considerably broadened and is non-closing, indicating the water adsorbed is strongly bound. This effect could be due to the heat treatment causing removal of water molecules from narrow, pore-like openings and interstices within aggregates, thus the water molecules re-enter the "pores" and interstices slowly, as is confirmed by the shape of the adsorption branch. On desorption only 60% of the adsorbed water is removed. Heating the sample prior to running the isotherm may also have caused decomposition of some or all of the surface propionate groups, rendering the surface more hydrophobic, thus once water molecules have been forced into the matrices of the aggregates they may be entrapped by the $Si(CH_3)_3$ groups.

Sample 80 heated in air at 773K for 24 hours prior to outgassing at 423K gives rise to a Type II isotherm with non-closing hysteresis, shown in Figure 7.10. As with samples 69, 74 and 79 the isotherm is indicative of chemisorption of water in terms of rehydroxylation of the oxide formed through the decomposition of the calcium hydroxide material. Comparison of the adsorption branches of samples 69, 74, 79, shown in Figures 7.4 and 7.8, and 80, shown in Figure 7.10, at $p/p^o < 0.2$ reveals a considerable difference in the extent of rehydroxylation of sample 80 compared to those

of samples 69, 74 and 79. Calculating the amount of water irreversibly chemisorbed by the sample, using the amount sorbed per gramme determined from the isotherm desorption branch where it intersects the ordinate, it is found that only 85% of the stoichiometric amount of water required to slake the sample, calculated as pure oxide, is irreversibly sorbed. Therefore the heat treatment prior to outgassing has induced a significant change to the surface properties of sample 80 compared to samples 69, 74 and 79. There are two possible explanations for this change, of which neither are likely to be sole affects, but most probably act in concert: **(a)** migration of $Si(CH_3)_3$ groups to the surface, resulting in an increase in hydrophobicity; and **(b)** carbonation of the surface through the action of atmospheric CO_2, which results in formation of a microporous calcium carbonate layer.

Sample 82, a silylated calcium hydroxide material consisting of small hexagonal platelets (< 1μm diam.) shown in Plate 13 B, exhibits Type I, II and III isotherms, shown in Figure 7.11, similar to the isotherms obtained for sample 74 (*cf.* Figures 7.5 - 7.7 with Figure 7.11).

A Type I isotherm is obtained following outgassing at room temperature. The isotherm exhibits a very broad negative hysteresis indicative of recrystallisation occurring through the presence of adsorbed water, which may involve fracture of particles or aggregates and as a consequence results in an increase in surface area and breakdown of narrow, pore-like openings and interstices where capillary condensation may occur (as described for sample 74 *post*). The rapid desorbing of water molecules over the relative pressure range $P/P_o \sim 0.55 - 0.60$ indicates the breaking down of aggregates allowing rapid removal of capillary condensed water.

Heating sample 82 in air at 473K for 24 hours prior to outgassing at 423K, results in the conversion of the Type I isotherm to a Type III isotherm. The water uptake over a large range of relative pressure (P/P_o 0 - 0.5) is very small with no real upswing in the adsorption branch until $P/P_o \sim 0.65$. Such a shape indicates a hydrophobic surface,

considerably more hydrophobic than sample 79 treated under the same conditions, shown in Figure 7.6. This difference in hydrophobicity must be due to the nature of the surface groups. Sample 79 was precipitated using sodium hydroxide solution and a mixture of solutions of calcium chloride and calcium propionate (in a molar ratio of 10:1 respectively) in the presence of silylating agent, thus the surface of the calcium hydroxide material would contain propionate groups together with $Si(CH_3)_3$ groups; whereas sample 82 was precipitated using sodium hydroxide and calcium chloride solutions in stoichiometric quantities, in the presence of a silylating agent, thus the surface would contain $Si(CH_3)_3$ groups, residual OH groups and some chloride ions. It would therefore be expected that the propionate groups would act as sites for the adsorption of water, thus explaining the difference in adsorptivity between samples 79 and 82. The broad hysteresis loop exhibited indicates rehydration, which is probably associated with residual hydroxyl groups remaining on the surface following silylation. As can be seen from the adsorption branch, Figure 7.11, the water is only adsorbed close to the saturation pressure, therefore the hydrophilic sites are shielded by the bulky $Si(CH_3)_3$ groups. On reduction of the relative pressure there is no significant desorption of water until $P/_{P^o} < 0.1$ evidenced by the plateau-like desorption branch. Perhaps the $Si(CH_3)_3$ groups act in an "umbrella-like" fashion preventing loss of adsorbed water molecules.

Heating sample 82 in air at 623K for 24 hours prior to outgassing at 423K gives rise to an isotherm having a stepped adsorption branch, shown in Figure 7.11, of Type VI in character. Stepped isotherms are generally indicative of non-porous, homogeneous surfaces, but the sample also exhibits a broad hysteresis loop. The conversion of a Type III isotherm to a Type VI isotherm must involve modification of the surface of the sample. Carbonation of the surface is the most likely explanation. The first small step of the adsorption branch will be due to water adsorbing onto the carbonate moieties amongst the $Si(CH_3)_3$ groups; the second step being larger due to the stronger adsorbate-adsorbate interactions as water molecules adsorb to the water molecules adsorbed onto the carbonate moieties. The broad hysteresis loop observed may again be

due to the "umbrella-like" action of the $Si(CH_3)_3$ groups in preventing the desorption of water molecules until the relative pressure is considerably reduced (to $p/p^o < 0.05$).

7.1.2 Frenkel-Halsey-Hill (FHH) Plots

The FHH exponents of the calcium hydroxide materials vary from 0.57 for sample 82, heated in air at 473K prior to outgassing at 423K, to 8.00 for sample 74, outgassed at 523K. The FHH plots for samples 69, 74, 79, 80 and 82 are shown in Figures 7.12 - 7.27.

7.1.2.1 Samples Outgassed at Room Temperature

FHH plots for samples 69, 74, 79, 80 and 82, shown in Figures 7.12, 7.15, 7.18, 7.22 and 7.25 respectively, exhibit linearity over a large range of relative pressures, $p/p^o \sim 0.005 - 0.54$, ~0.026 - 0.60, ~0.034 - 0.445, ~0.037 - 0.494 and ~0.299 - 0.622 respectively, and exhibit r values of 0.89, 1.24, 1.27, 1.37 and 3.49 respectively. It is evident that the r value increases as the respective range of linearity decreases.

The FHH plot for sample 69 (the only non-silylated sample) is linear for the whole range of relative pressures, and the r value of 0.89 is the lowest of all the room temperature outgassed samples. This indicates the absence of micropore filling and/or capillary condensation. Thus it can be tentatively suggested that the r value for sample 69 outgassed at room temperature could be used as a "yardstick" for comparing silylated samples and judging whether there has been an increase or decrease in hydrophobicity with respect to a "standard calcium hydroxide material". The totally reversible nitrogen isotherm, shown in Figure 6.9, adds weight to this possibility.

Sample 74 exhibits downward deviation from linearity at low p/p^o which is indicative of micropore filling or, most probably, filling of fine, pore-like openings formed by agglomeration of the material, hence the increase in the r value to 1.24.

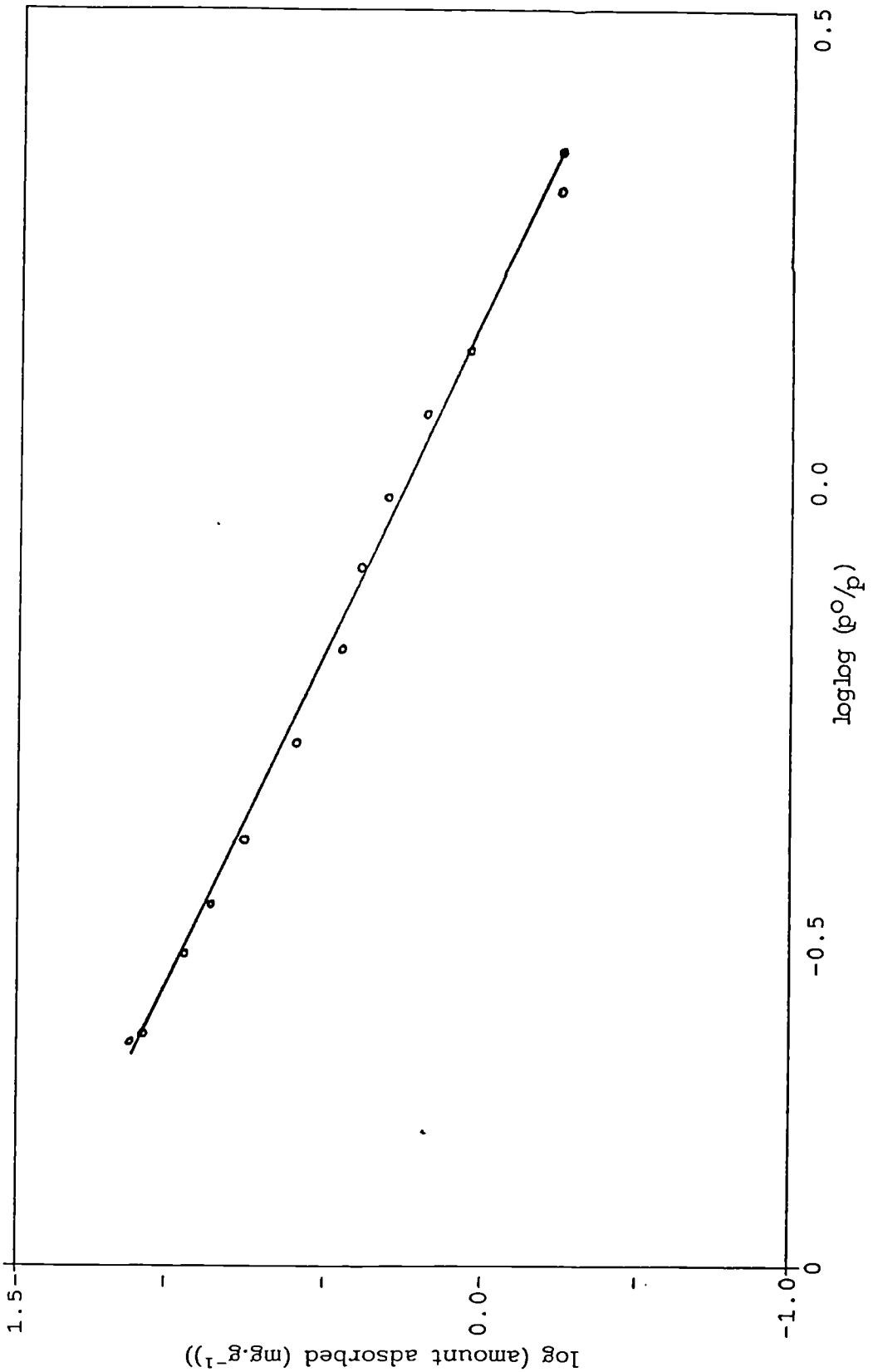

Figure 7.12 Frenkel-Halsey-Hill (FHH) plot for water adsorption at 305K for sample 69 outgassed at 298K.

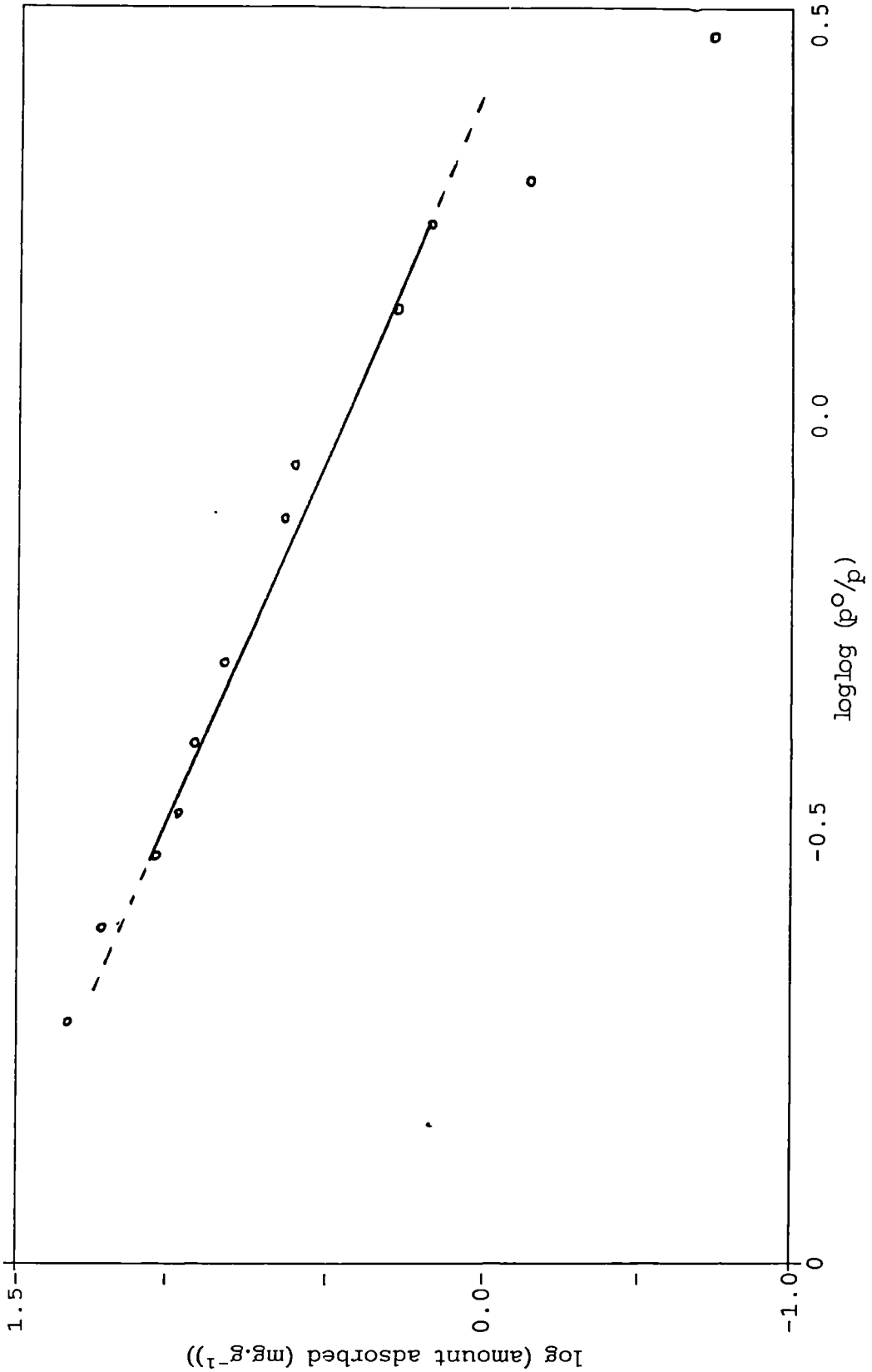

Figure 7.13 Frenkel-Halsey-Hill (FHH) plot for water adsorption at 305K for sample 69 outgassed at 470K.

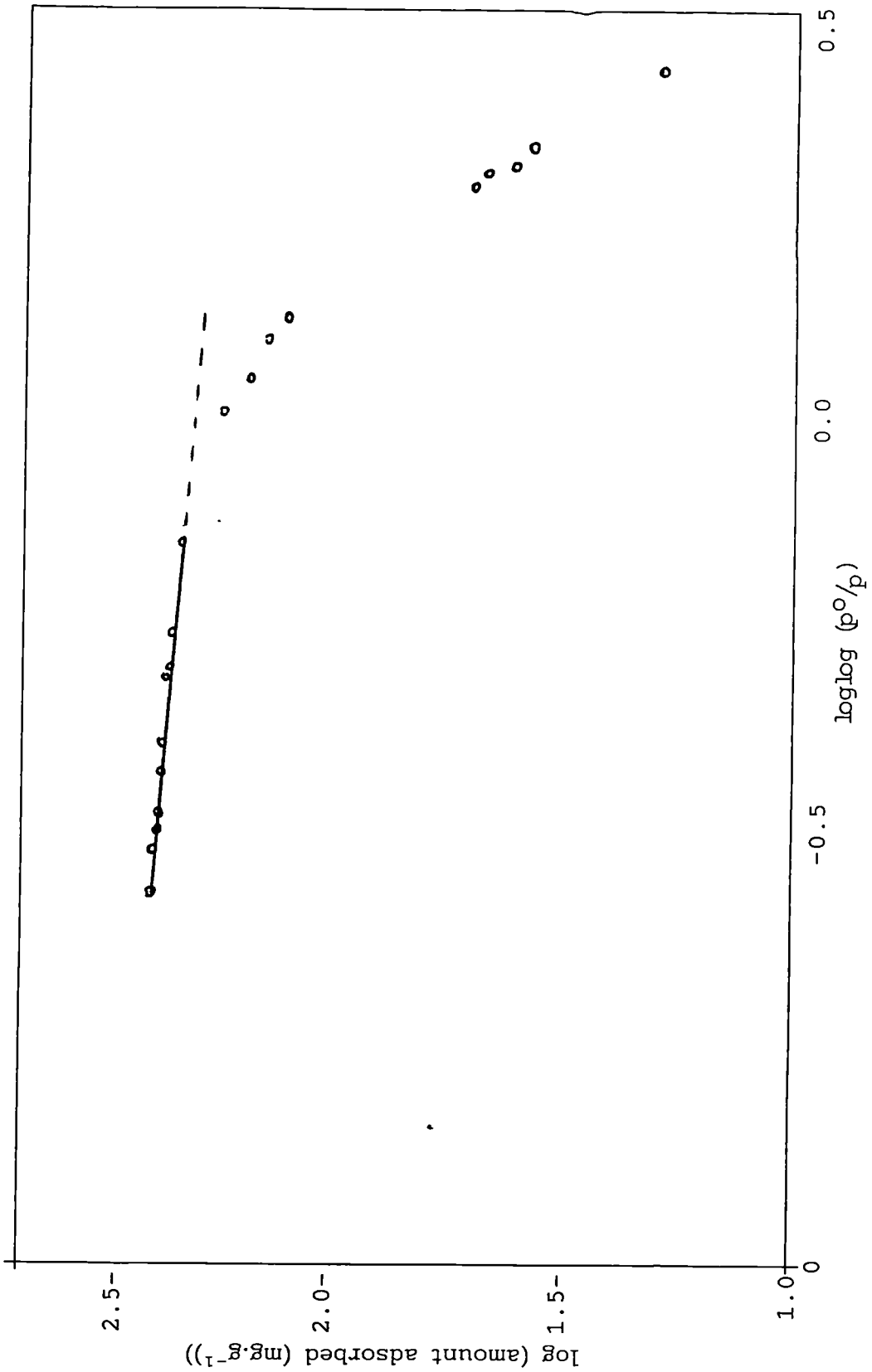

Figure 7.14 Frenkel-Halsey-Hill (FHH) plot for water adsorption at 305K for sample 69 outgassed at 550K.

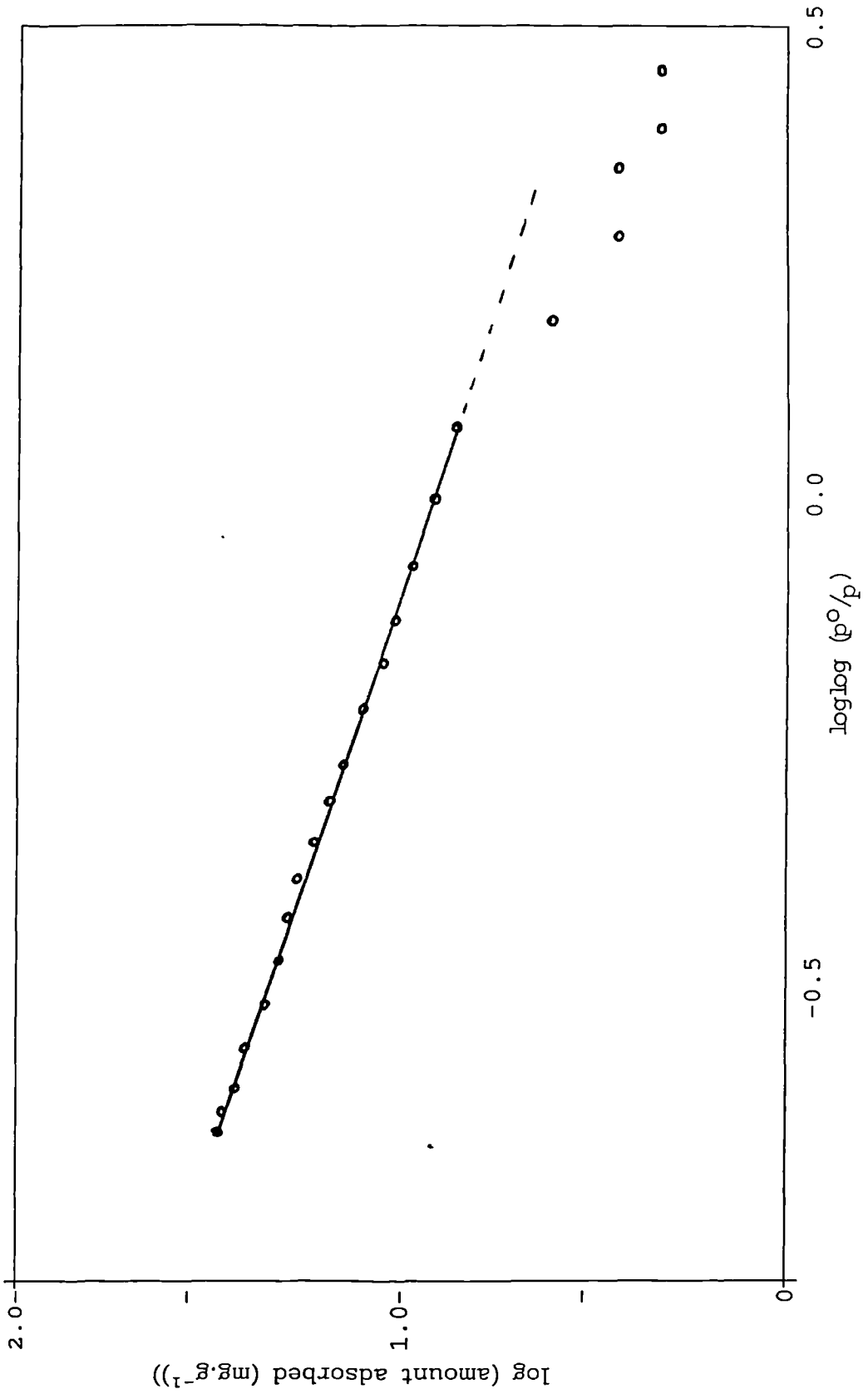

Figure 7.15 Frenkel-Halsey-Hill (FHH) plot for water adsorption at 305K for sample 74 outgassed at 298K.

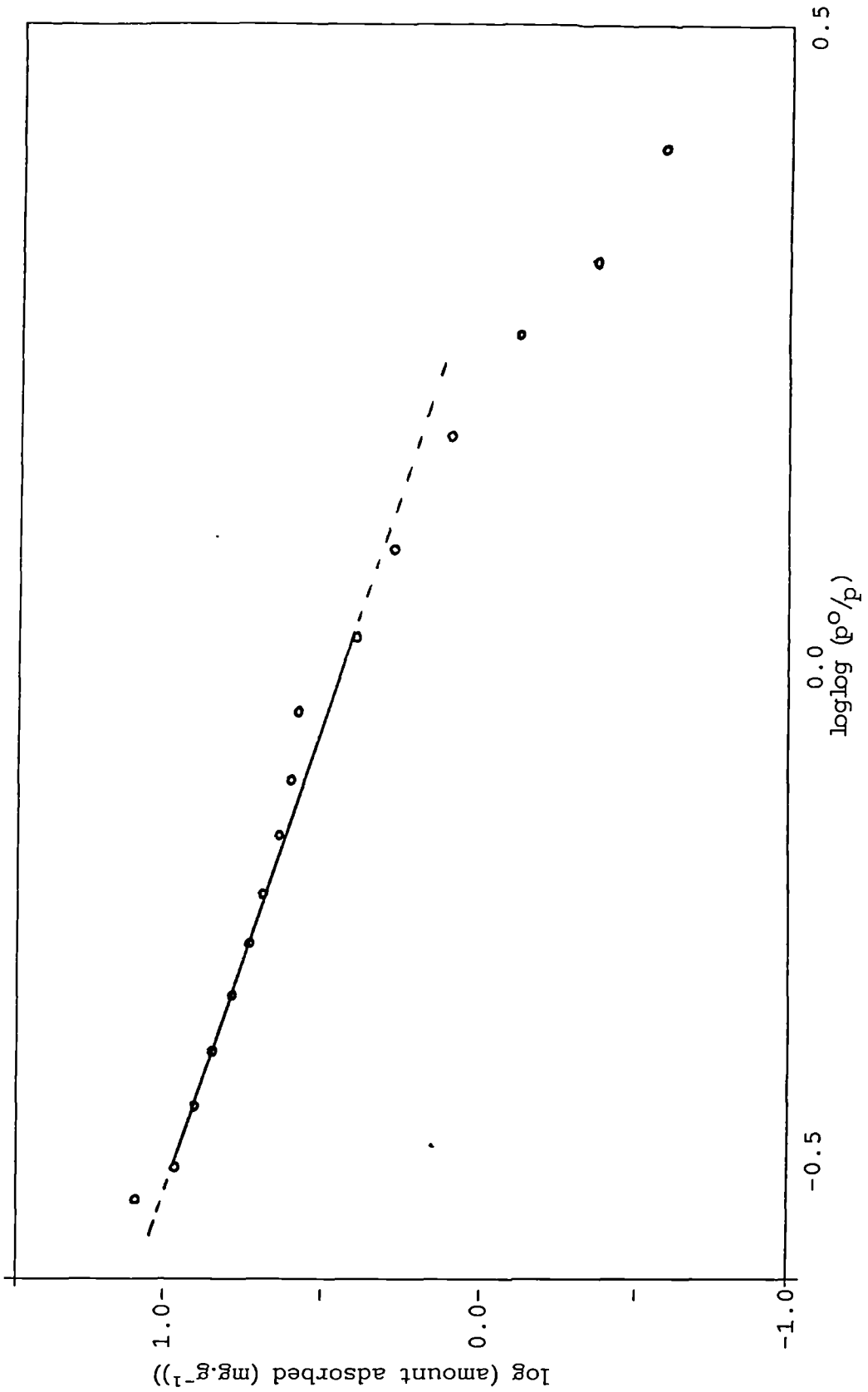

Figure 7.16 Frenkel-Halsey-Hill (FHH) plot for water adsorption at 305K for sample 74 outgassed at 470K.

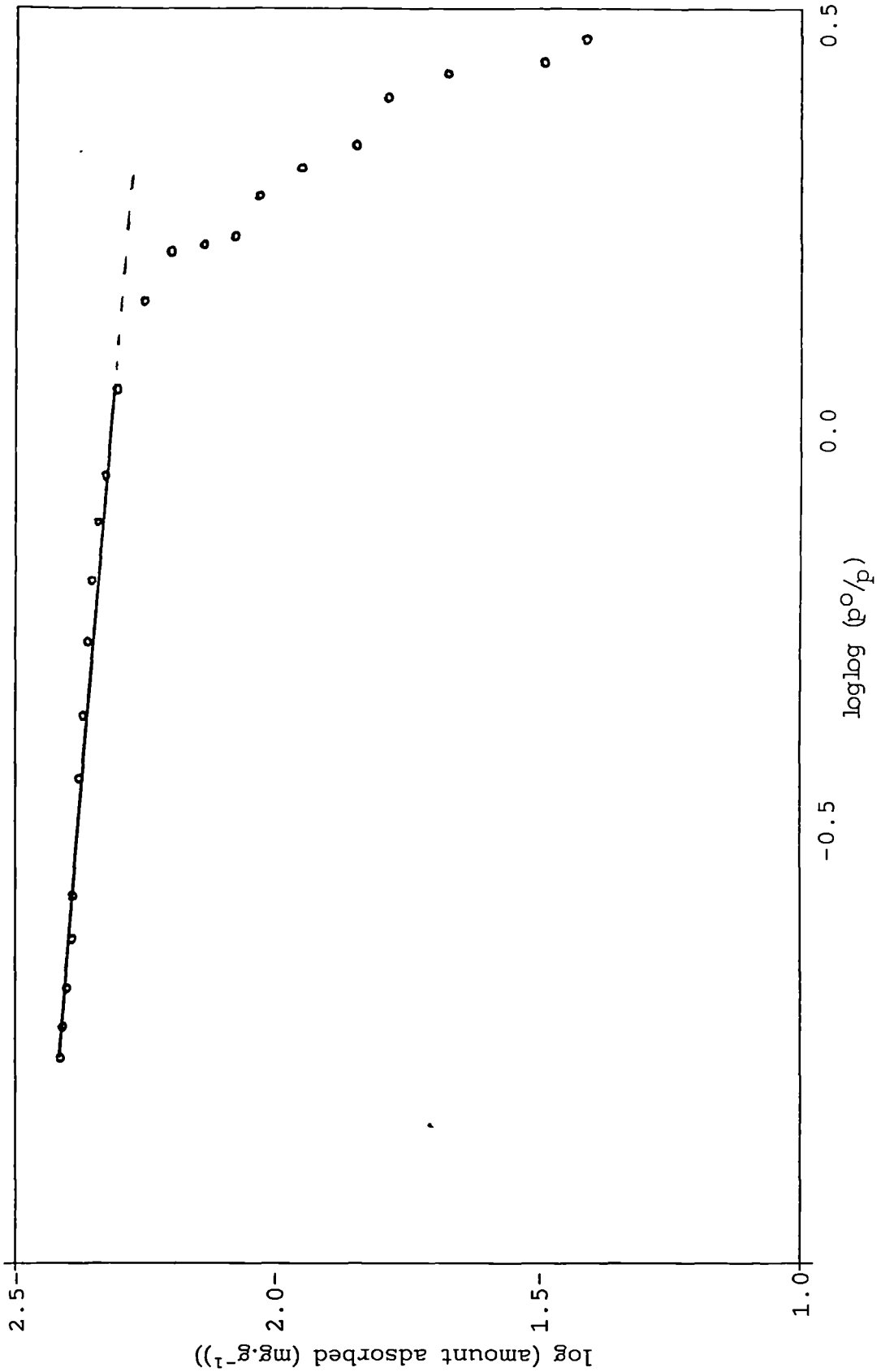

Figure 7.17 Frenkel-Halsey-Hill (FHH) plot for water adsorption at 305K for sample 74 outgassed at 550K.

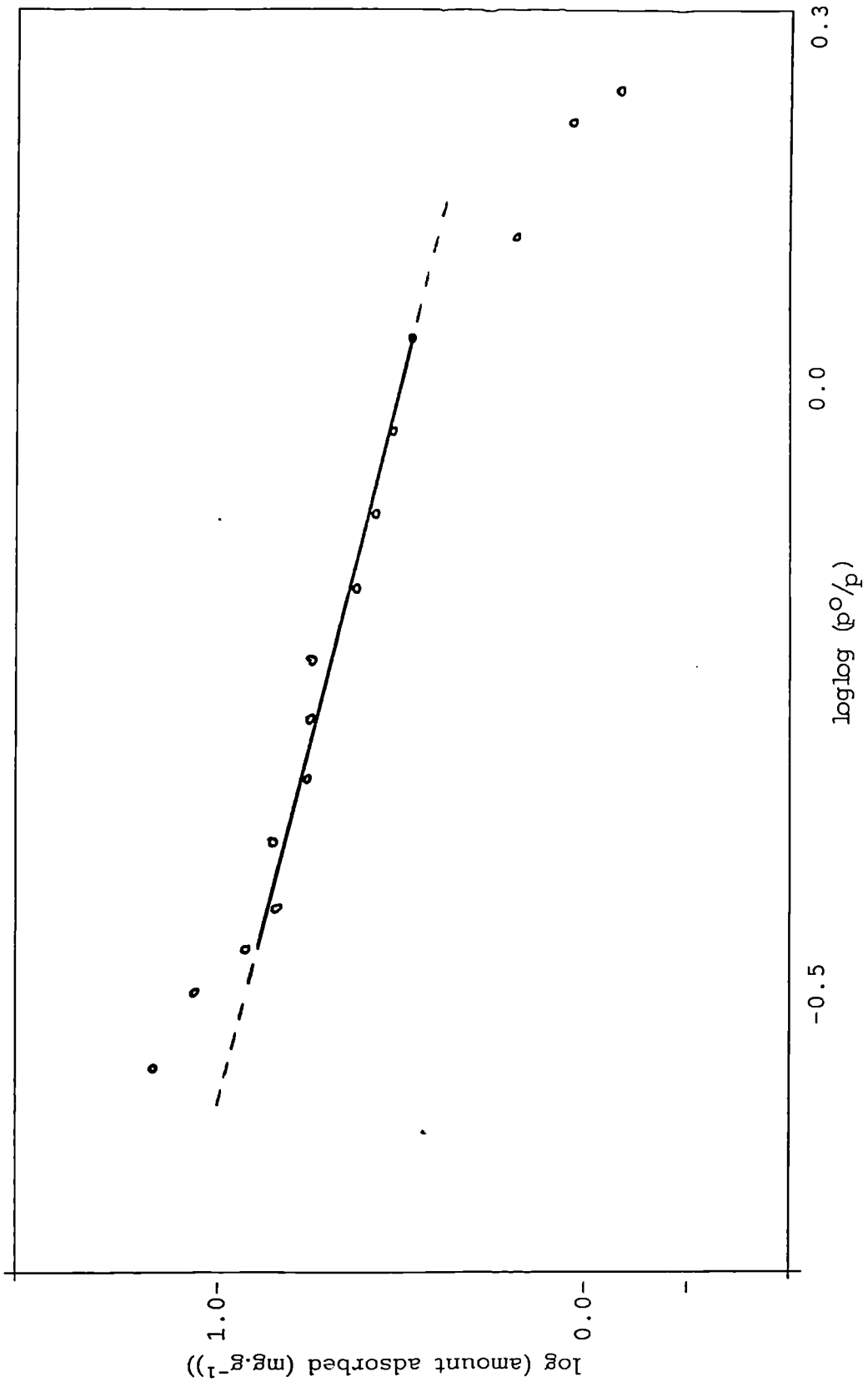

Figure 7.18 Frenkel-Halsey-Hill (FHH) plot for water adsorption at 305K for sample 79 outgassed at 298K.

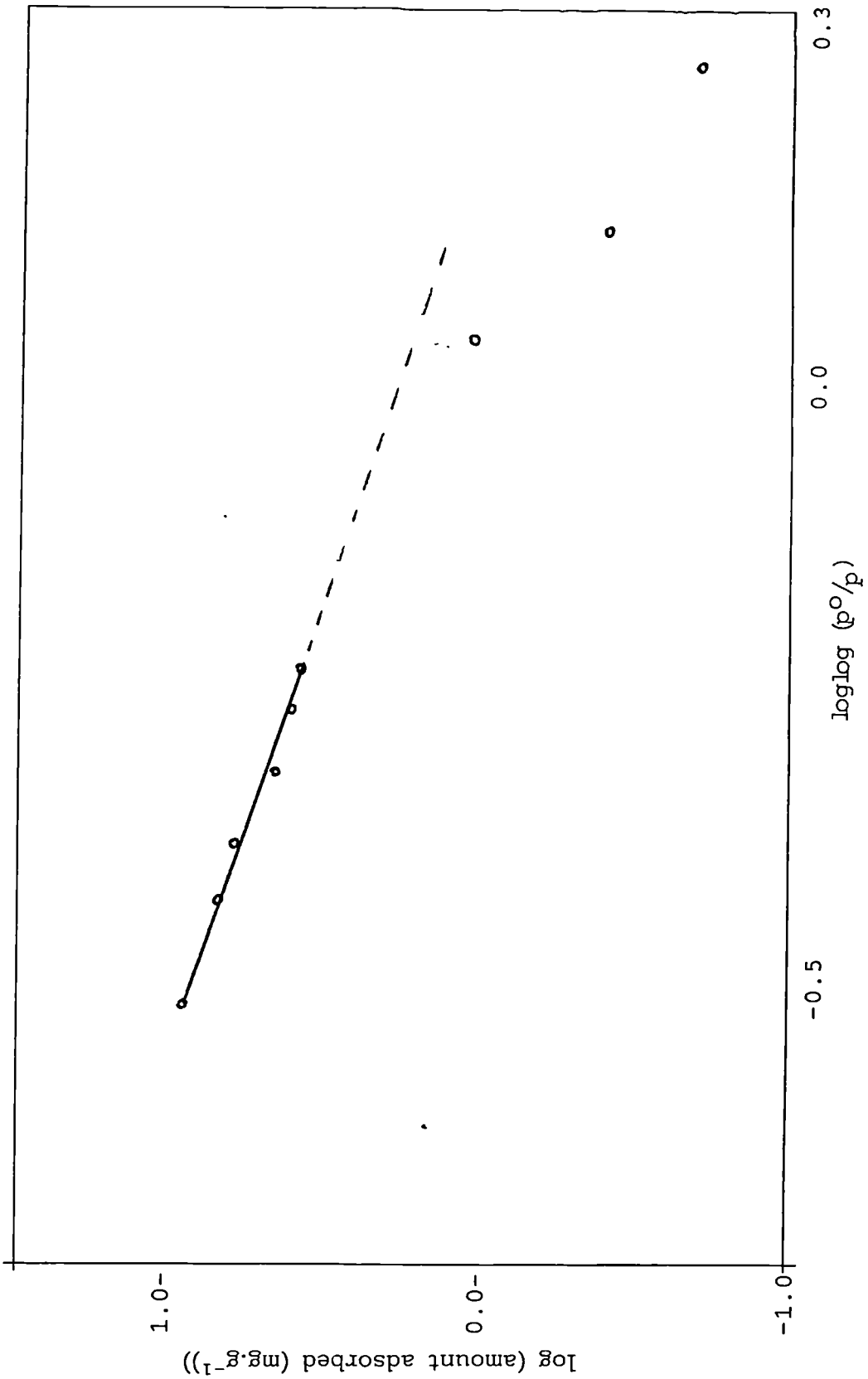

Figure 7.19 Frenkel-Halsey-Hill (FHH) plot for water adsorption at 305K for sample 79 heated in air at 420K for 24 hours prior to outgassing at 420K.

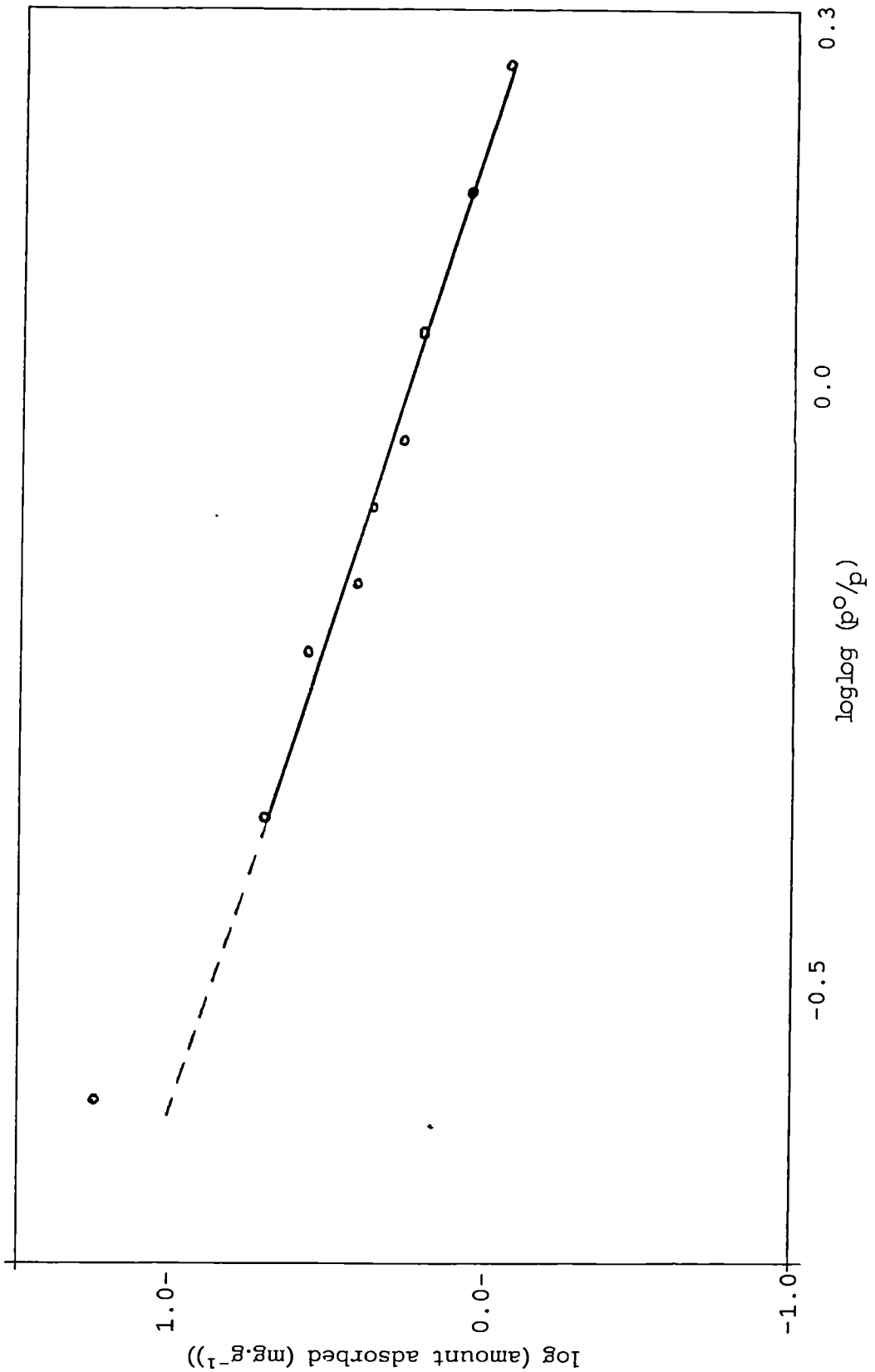

Figure 7.20 Frenkel-Halsey-Hill (FHH) plot for water adsorption at 305K for sample 79 heated in air at 620K for 24 hours prior to outgassing at 420K.

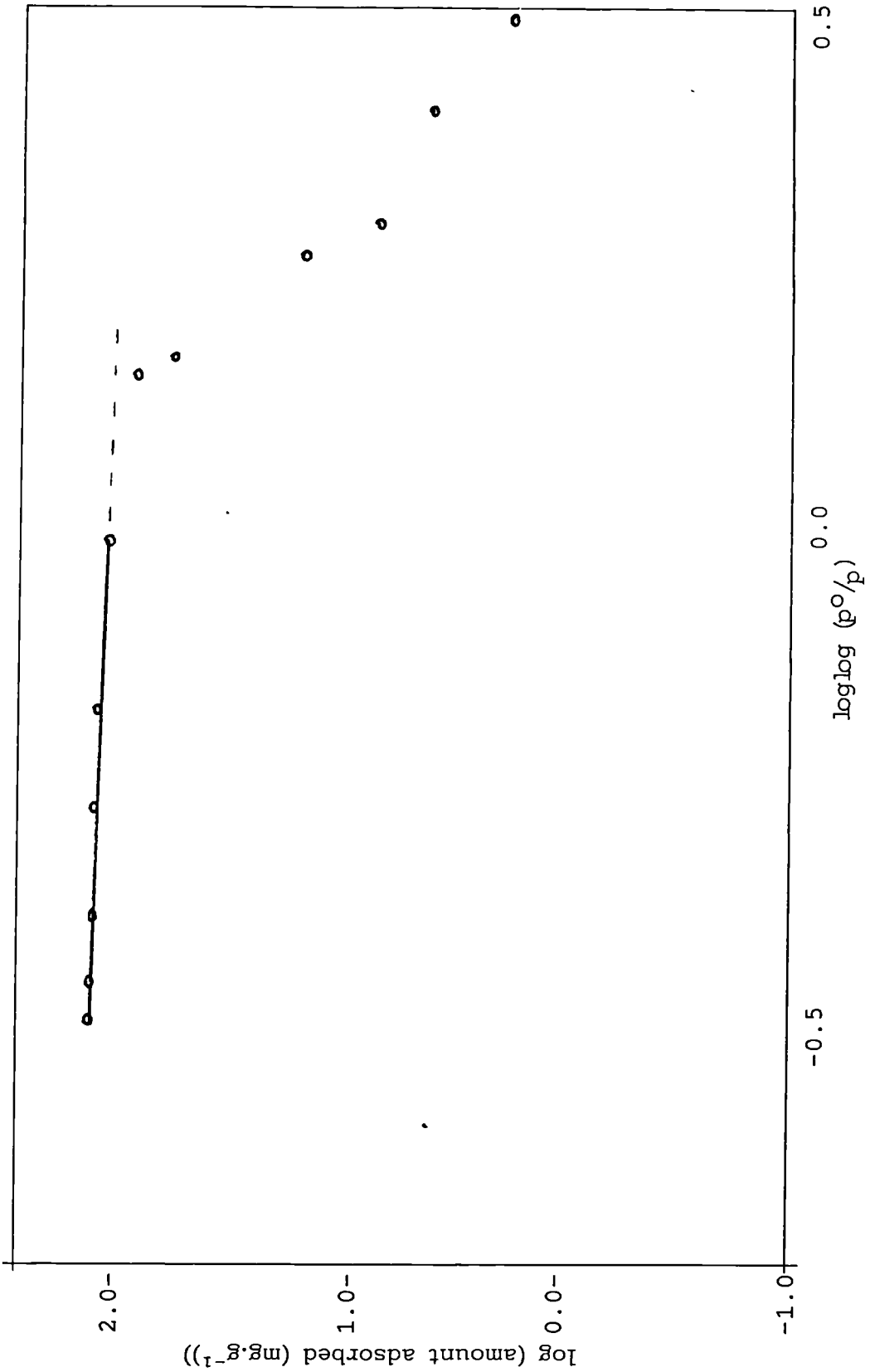

Figure 7.21 Frenkel-Halsey-Hill (FHH) plot for water adsorption at 305K for sample 79 heated in air at 770K for 24 hours prior to outgassing at 420K.

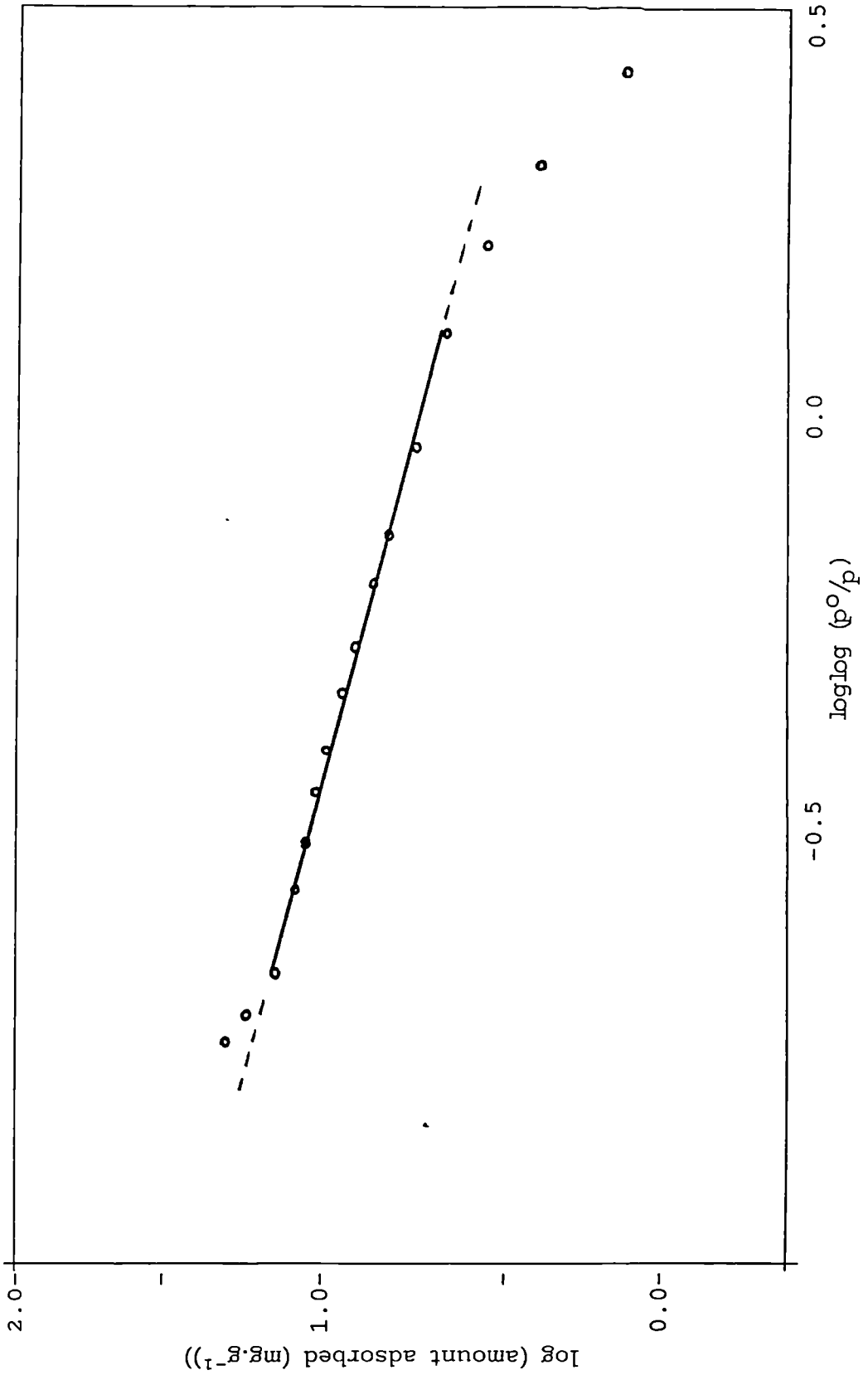

Figure 7.22 Frenkel-Halsey-Hill (FHH) plot for water adsorption at 305K for sample 80 outgassed at 298K.

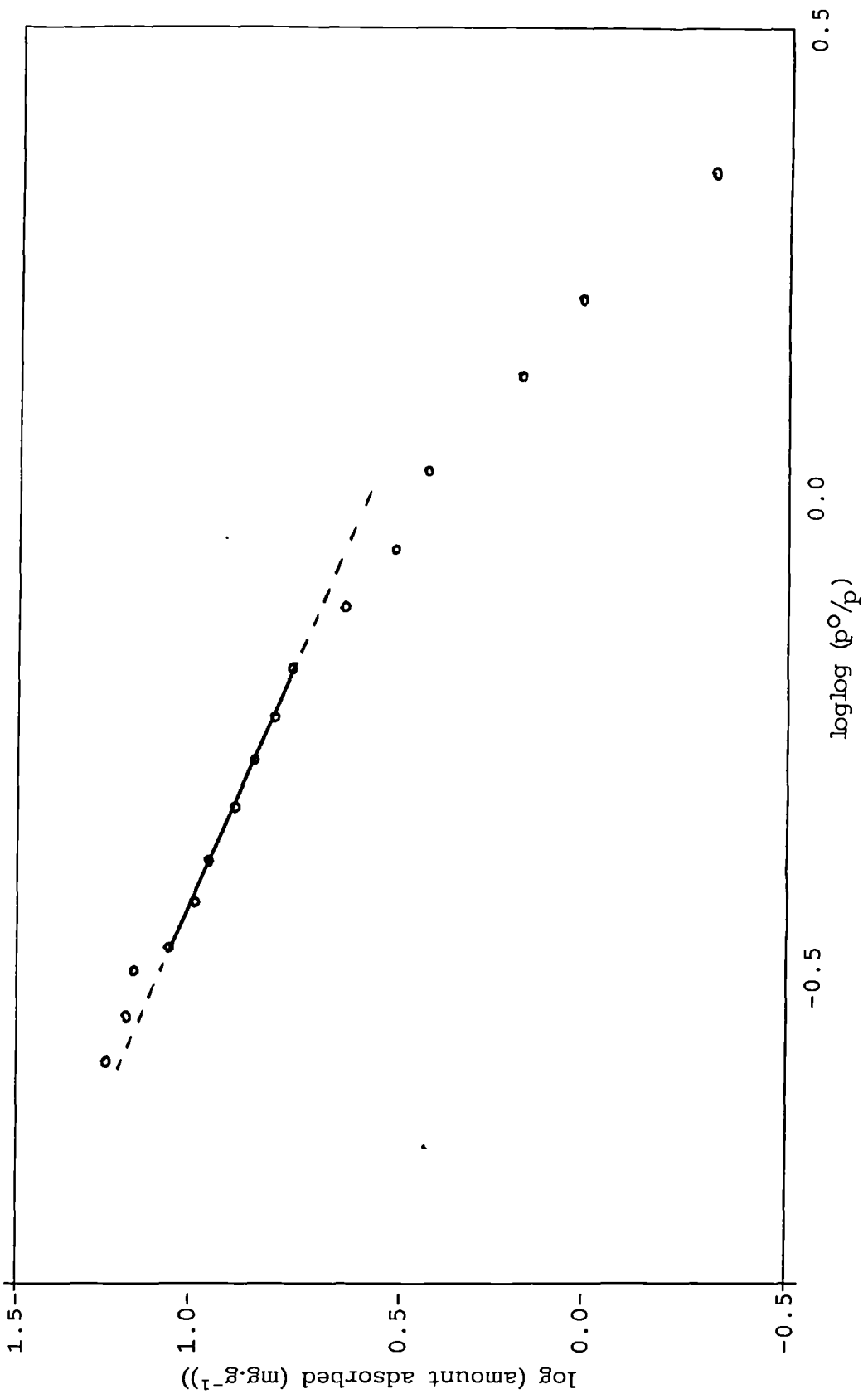

Figure 7.23 Frenkel-Halsey-Hill (FHH) plot for water adsorption at 305K for sample 80 heated in air at 470K for 24 hours prior to outgassing at 420K.

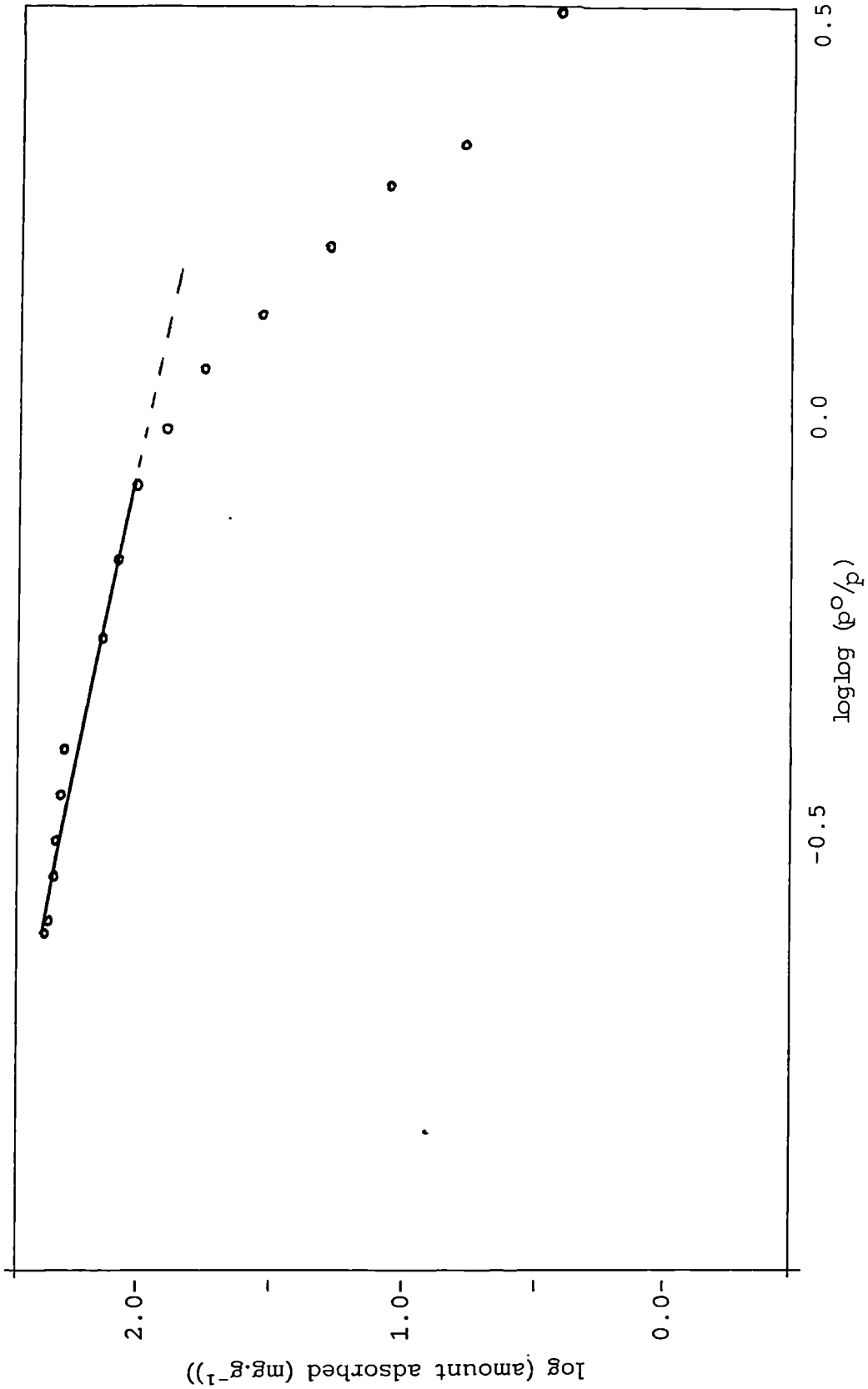

Figure 7.24 Frenkel-Halsey-Hill (FHH) plot for water adsorption at 305K for sample 80 heated in air at 770K for 24 hours prior to outgassing at 420K.

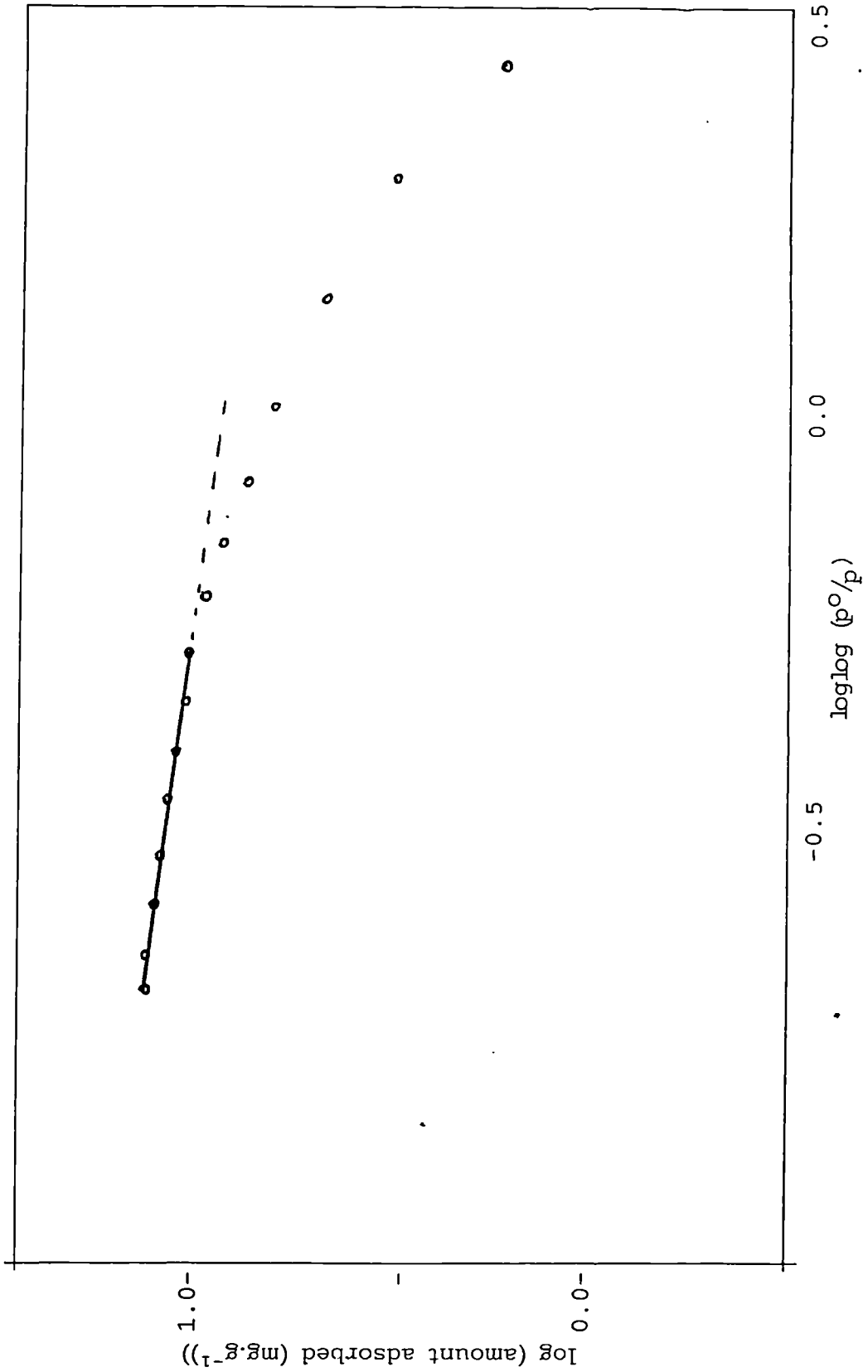

Figure 7.25 Frenkel-Halsey-Hill (FHH) plot for water adsorption at 305K for sample 82 outgassed at 298K.

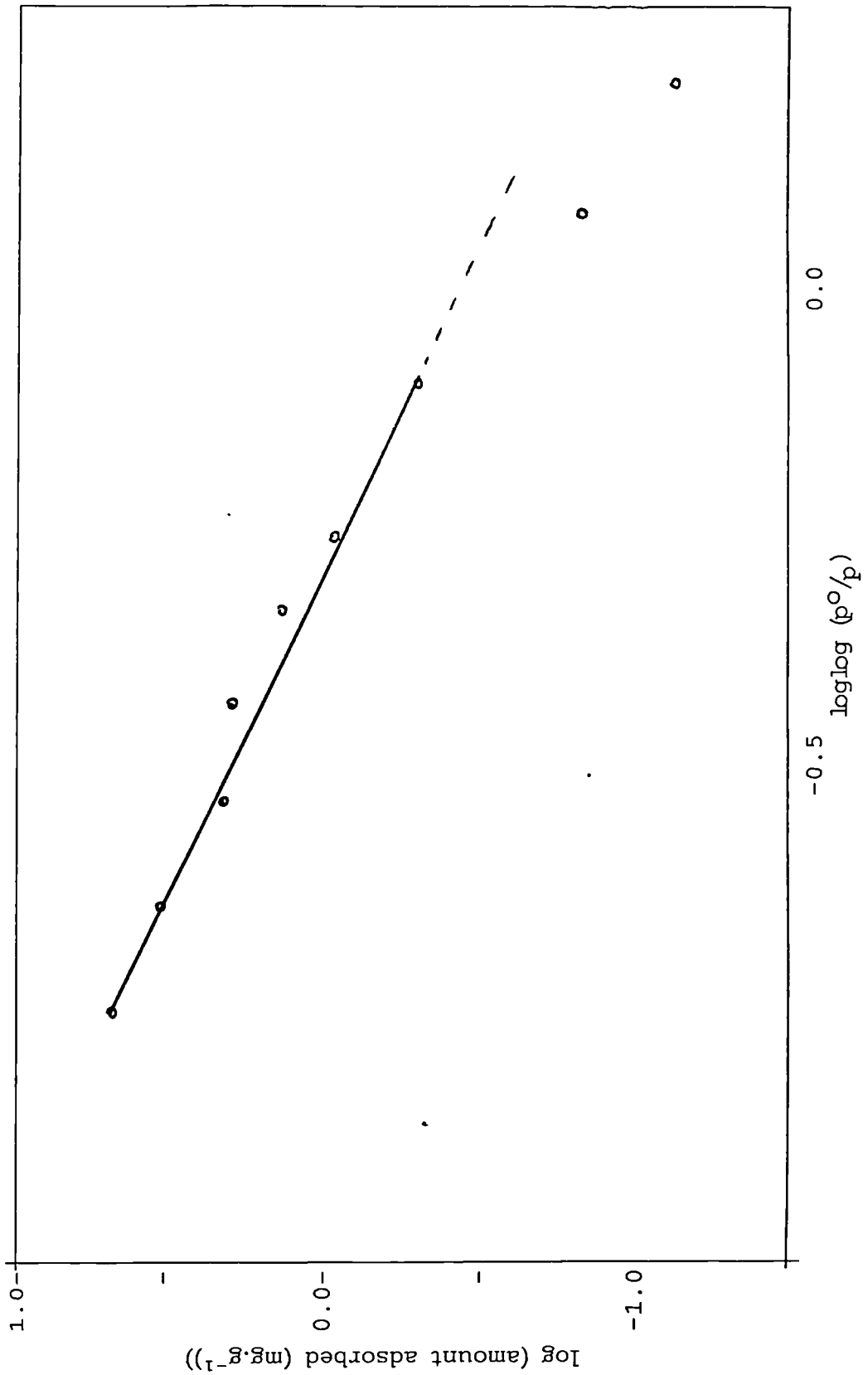

Figure 7.26 Frenkel-Halsey-Hill (FHH) plot for water adsorption at 305K for sample 82 heated in air at 470K for 24 hours prior to outgassing at 420K.

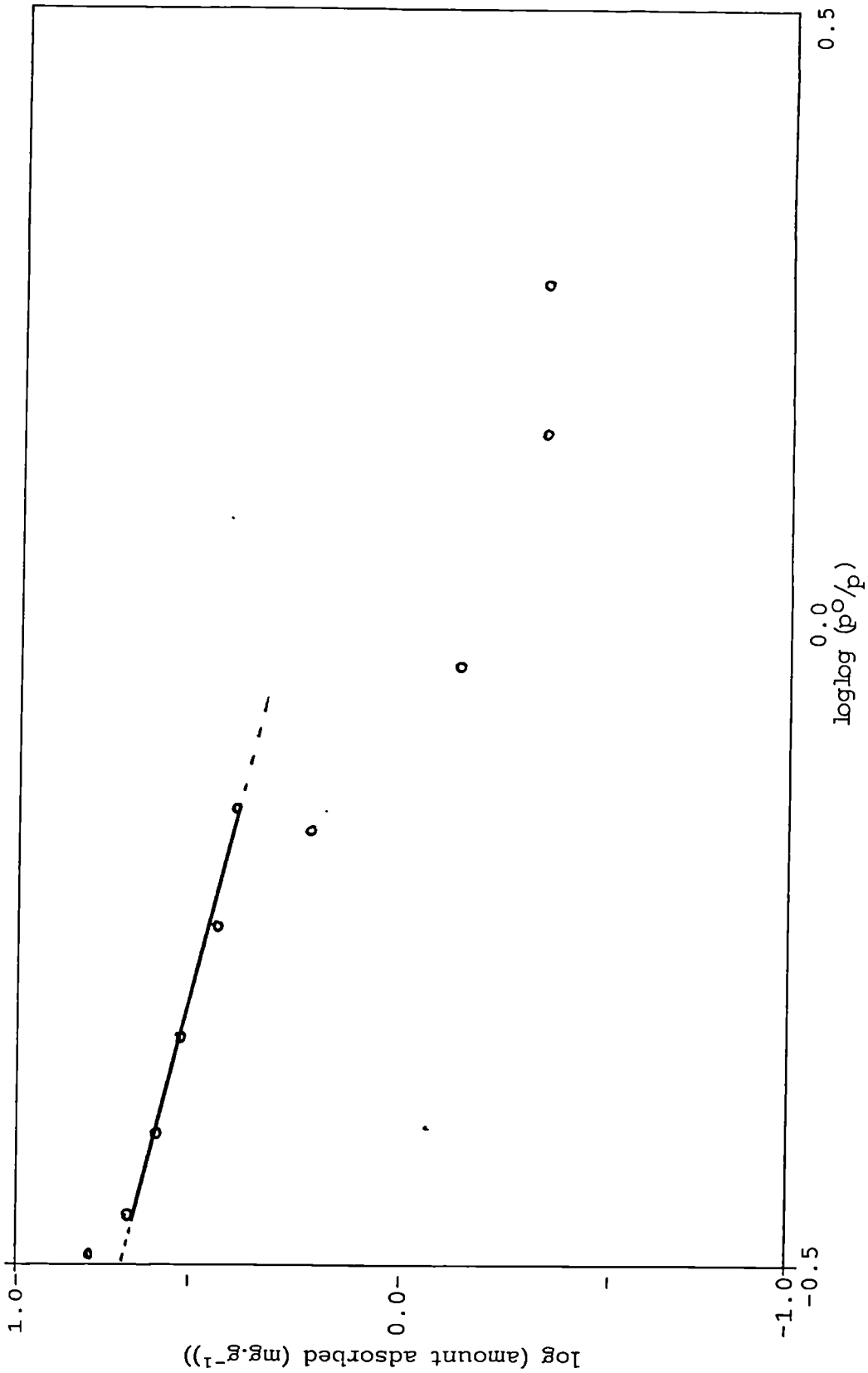

Figure 7.27 Frenkel-Halsey-Hill (FHH) plot for water adsorption at 305K for sample 69 heated in air at 620K for 24 hours prior to outgassing at 420K.

Sample 79 exhibits both downward deviation from linearity at low P/P_o and upward deviation from linearity at high P/P_o, indicating not only the presence of aggregates containing fine, pore-like openings, but also the presence of aggregates containing capillaries, which explains the increase of the r value (as discussed in 6.1.2 *post*) to 1.27.

Similarly, sample 80 exhibits both upward deviation and downward deviation from linearity. An increase in the r value to 1.37 is indicative of an increase in microporosity or degree of agglomeration, of which the latter is the most probable cause due to a decrease in particle size as can be seen by comparing Plates 12 A, 12 B and 13 A

The FHH plot for sample 82 exhibits considerable downward deviation from linearity at low relative pressures ($P/P_o < 0.2$) and a correspondingly high r value of 3.49. Plate 13 B shows that sample 82 comprises aggregates of tablet-like crystals <1μm in diameter, which indicates that the high r value is due to the effect of filling of narrow, pore-like openings at low relative pressures. Consequently the course of the isotherm over the whole of the useful range of the FHH plot is changed, resulting in an increased r value. This effect is somewhat similar to the increase in the value of r produced as a result of micropore filling observed by Carrott *et al* [125]. The absence of any deviation at high relative pressures implies no capillary condensation occurred.

The most likely explanation for these results is that pore entrances were partially blocked by the introduction of $Si(CH_3)_3$ groups, whilst narrow channels and interstices within the calcium hydroxide material structure remained available for water vapour adsorption. Such an explanation is consistent with the electron micrographic evidence that some precipitated calcium hydroxide materials contains an assemblage of small crystals bonded together in the form of aggregates (e.g. Plate 13 B). Hydroxyl groups, water molecules and, possibly, ethanol molecules remain trapped within the very fine pores and interstices which constitute the microstructure of aggregates. This microstructure was able to accommodate a high proportion of the adsorbed water, even

after the silylation had effectively coated the external surface. According to this picture the external surface of the calcium hydroxide materials was essentially hydrophobic whilst the internal surface remained hydrophilic.

7.1.2.2 Samples Outgassed at Elevated Temperature

FHH plots for samples 69, 74, 79, 80 and 82, shown in Figures 7.13, 7.16, 7.19, 7.23 and 7.26 respectively, exhibit linearity over the range of relative pressures, p/p^o ~ 0.017 - 0.64, ~0.078 - 0.48, ~0.083 - 0.483, ~0.165 - 0.549 and ~0.040 - 0.622 respectively, and exhibit r values of 1.11, 0.97, 0.69, 0.98 and 0.57 respectively. It is clearly evident that there has been a marked change in the r values resulting from heating the samples.

Sample 69 was outgassed at 473K for 16 hours. The FHH plot has linearity over a large range of relative pressures, but also exhibits a marked downward deviation from linearity at low relative pressures unlike when outgassed at room temperature (*cf.* Figure 7.12). The most likely explanation for these results is that by outgassing at elevated temperature, water molecules and , possibly, ethanol molecules trapped within the interstices between the crystals will be removed, together with some surface hydroxyl groups. On rehydration the interstices will be refilled giving rise to the observed downward deviation from linearity, and rehydration of active surface sites (Ca^{2+} ions exposed by dehydroxylation) will occur. This latter effect will result in the observed increase in the r value, which indicates an increase in hydrophilicity.

The FHH plot for sample 69 outgassed for 16 hours at 553K, shown in Figure 7.14, exhibits marked downward deviation from linearity at low relative pressures (p/p^o < ~ 0.18) and has a very large r value of 7.44. The magnitude of the downward deviation is greater than would be expected for micropore filling and therefore must be due to chemisorption (*i.e.* rehydroxylation of the formed oxide). Similarly the large

r value, indicating an extremely hydrophilic material, is due to the calcium hydroxide material being converted into calcium oxide and subsequently being rehydroxylated.

Sample 74 exhibits a marked downward deviation from linearity at low relative pressures ($P/P_o < 0.12$) and an upward deviation from linearity only at the highest relative pressure. The latter effect was not observed with the room temperature outgassed sample (*cf.* Figure 7.15). Electron microscopy has shown sample 74 to consist of folded sheets of the calcium hydroxide material (see Plate 12 A) which are likely to contain many narrow openings and interstices. On outgassing at elevated temperature, water molecules trapped within the openings and interstices are removed leaving narrow, pore-like openings available for subsequent rehydration. On exposure to water vapour the rehydration proceeds at a slower rate than for the room temperature outgassed sample as can be seen from the adsorption isotherms, shown in Figure 7.3, and from the FHH plots, shown in Figures 7.15 and 7.16, where the plot becomes linear at $P/P_o \sim 0.026$ for the room temperature outgassed sample and at $P/P_o \sim 0.12$ for the sample outgassed at 473K. These observations can be explained by considering that the removal of all water molecules from the interstitial spaces by outgassing at 473K will leave the sample denuded of active sites (trapped water molecules), and for rehydration of the interstices to occur the water molecules will need to be forced past the hydrophobic, surface $Si(CH_3)_3$ groups. Therefore the reduction in the r value is a direct result of the increase in hydrophobicity of the sample caused by the removal of interstitial water molecules. Although there is an indication of upward deviation from linearity at $P/P_o \sim 0.51$ implying the presence of some capillary condensation, which would in turn cause a decrease in the r value, the indication is not significant when compared to the information obtained from the adsorption isotherm shown in Figure 7.3.

Outgassing sample 74 at 553K for 16 hours results in an FHH plot, shown in Figure 7.17, is similar to that obtained for sample 69 (see Figure 7.14), with a similarly large r value of 8.00 which can be explained by the conversion of the calcium hydroxide

material to calcium oxide by the outgassing conditions. For sample 74 the downward deviation from linearity occurs at very low relative pressures ($p/p^o < \sim 0.005$), therefore the chemisorption process (*i.e.* rehydroxylation of the calcium oxide) occurs more rapidly than for sample 69. A factor in the rate of chemisorption of the water vapour must be the precipitate morphology. Sample 74 comprises a folded, sheet-like material, shown in Plate 12 A, which has an S_{SP} of 68 m^2g^{-1}, whereas sample 69 comprises a close-packed, hexagonal plate-like material, shown in Plate 11 B, which has an S_{SP} of 27 m^2g^{-1}. Therefore the accessibility of the surface to the water vapour is considerably greater for sample 74, which may explain the difference in rate of rehydration.

Heating sample 79 at 473K in air prior to outgassing at 423K does not result in any significant change in the degree of downward deviation from linearity at low relative pressures ($p/p^o < 0.05$), but the upward deviation from linearity at high relative pressures exhibited by the room temperature outgassed sample, shown in Figure 7.18, is not present in the FHH plot for the heated sample, shown in Figure 7.19, and there is a significant decrease in the r value from 1.27 to 0.69. These results indicate that the fine structure within the precipitate is not altered by the heating process and that the water molecules trapped within the narrow, pore-like openings and interstices are easily desorbed, thus the water molecules can only be weakly bonded to the surface. Furthermore, this indicates that sample 79 has a hydrophobic surface, which implies the surface has a significant number of $Si(CH_3)_3$ groups present. The elimination of upward deviation from linearity at high relative pressures results from a loss of capillary-sized pores. Bye et al [126] have suggested that exposure to water vapour causes structural and textural changes (see 7.1.1 *ante*); one of which is cementation. Cementation would have the effect of drawing the precipitate particles, shown in Plate 12 B, together and causing a conversion of capillaries into pore-like openings. This loss of capillary condensation may also be responsible for the significant reduction in the r value, rather than by any increase in hydrophobicity through a surface chemical effect caused by the heating process.

Heating sample 79 in air for 24 hours at 623K prior to outgassing at 423K for 16 hours results in a linear FHH plot (the final point is displaced above the line of linearity as a result of overnight equilibration). The elimination of downward deviation from linearity at low relative pressures indicates that either narrow, pore-like openings have been blocked or the previous exposure to water vapour has resulted in recrystallisation involving fracture of particles or aggregates causing a significant reduction in the number of narrow, pore-like openings. Of these two possibilities the former is most probable. On heating at 473K sample 79 exhibited a Type III isotherm, but when heated at 623K the sample exhibited a Type II isotherm. This change in isotherm type was also accompanied by a decrease in $S_{H_2O.BET}$ from 14 m^2g^{-1} to 9 m^2g^{-1} and a decrease in S_{DR} of 7 m^2g^{-1} to 6 m^2g^{-1} respectively. Thus we apparently have a contradiction whereby there is an increase in hydrophilicity evidenced by the change from a Type III to a Type II isotherm and by an increase in the FHH plot r value from 0.69 to 0.89, yet there is a decrease in $S_{H_2O.BET}$ and S_{DR}. The most probable explanation for these results is that there has been a surface chemical change which causes a blocking of narrow, pore-like openings while increasing the hydrophilicity of the surface. This chemical process is probably carbonation, as is indicated by infra-red spectroscopic studies.

The FHH plot for sample 79 heated at 773K in air for 24 hours prior to outgassing at 423K for 16 hours, shown in Figure 7.21, exhibits the marked downward deviation from linearity that indicates chemisorption rather than microporosity as has been described for samples 69 and 74 above. As has been indicated by the adsorption isotherm, shown in Figure 7.8, the calcium hydroxide material has been converted to the oxide, hence the considerable increase in the FHH plot r value from 0.89 when heated at 623K to 6.45 when heated at 773K.

Sample 80 follows a similar pattern to sample 79. The FHH plot, shown in Figure 7.23, exhibits a downward deviation from linearity at low relative pressures ($p/p^o < 0.215$) which is larger than exhibited by the room temperature outgassed sample, shown in

Figure 7.22. Upward deviation from linearity exhibited by the room temperature outgassed sample is not present in the FHH plot for the heated sample (points 14-16 appear above the linear portion of the plot as a result of equilibration over 3 days). These results are consistent with the explanation of particle cementation occurring as a result of exposure to water vapour, with resultant loss of capillary condensation and consequent reduction of the r value.

Heating sample 80 at 773K in air for 24 hours prior to outgassing at 423K for 16 hours results in an FHH plot, shown in Figure 7.24, typical of that obtained as a result of decomposition of the calcium hydroxide material to calcium oxide (*cf.* samples 69 and 74). The marked downward deviation from linearity at low relative pressures ($P/P^o < \sim 0.15$) is again evidence of chemisorption in terms of rehydration of the resultant oxide, but unlike the other samples the r value is markedly lower at 4.06. This indicates that although the calcium hydroxide material has been converted to the oxide the surface still retains considerable hydrophobicity, which is also indicated by the adsorption isotherm, shown in Figure 7.10 (*cf.* with Figures 7.4 and 7.8). These results are possibly explained by a combined effect of the formation of a microporous carbonate layer and the presence of surface $Si(CH_3)_3$ groups.

The FHH plot for sample 82 heated at 473K in air prior to outgassing at 423K, shown in Figure 7.26, is markedly different to that obtained for the room temperature outgassed sample, shown in Figure 7.25. Downward deviation from linearity only occurs below $P/P^o \sim 0.06$ for the heated sample, whereas for the room temperature outgassed sample the downward deviation occurs below $P/P^o \sim 0.24$. No evidence of any upward deviation from linearity in either plot implies that the small, precipitated crystals, shown in Plate 13 B, are tightly packed in aggregates which only contain narrow, pore-like openings. A considerable difference in the r values is very evident, being 3.49 for the room temperature outgassed sample and 0.57 for the heated sample. These results taken together with the water adsorption isotherms, shown in Figure 7.11, clearly indicate that recrystallisation of the sample on exposure to water vapour involving fracture of

particles or aggregates, and consequently resulting in an increase in surface area, has occurred. The absence of capillary condensation means that the r values are directly related to the hydrophobicity of the samples, and considering that the surface area of the sample will have increased without any increase in the amount of water adsorbed, implies that there is a high surface coverage of $Si(CH_3)_3$ groups.

Heating sample 82 at 623K for 24 hours prior to outgassing at 423K for 16 hours results in a marked change in the FHH plot, shown in Figure 7.27. The plot exhibits both downward and upward deviations from linearity. In this case the downward deviation is not indicative of micropores or narrow, pore-like openings, but is a result of the sample having a non-porous surface as is evident from the stepped adsorption isotherm, shown in Figure 7.11, and as a result the points in the region $P/P_o < \sim 0.19$ are related to monolayer formation. The upward deviation though will be related to capillary condensation. There was no evidence of capillary condensation for either the room temperature outgassed sample or the sample heated at 473K prior to outgassing, therefore some mechanism must be operating to create capillaries or to allow water molecules to enter previously inaccessible capillaries. A possible mechanism may be through carbonation of the surface, as shown by infra-red studies, reducing the hydrophobicity related to the surface $Si(CH_3)_3$ groups by creating sufficient hydrophilic surface moieties to permit the water molecules to "percolate" into the narrow, pore-like openings and interstices within the aggregates of the sample.

7.1.3 Dubinin-Radushkevitch-Kaganer (DRK) Plot

The DRK surface areas obtained for samples 69, 74, 79, 80, and 82 are shown in Table 7.1. It can be seen that for most cases there is a good correlation between the BET surface areas and the DRK surface areas, but there are two exceptions. Samples 79 and 80 heated at 473K in air prior to outgassing at 423K have S_{DR} approximately one half

that of the S_{BET}. These results can be explained by deviations in the DR plot which are due to several possible factors:

(1) Change in the adsorption mechanism with pore size;

(2) Change in adsorption potential with pore size;

(3) Active surface groups (heterogeneity); and

(4) Constrictions in the micropores.

When such deviations occur the linearity of the DR plot is obtained only at $P/p^o < 0.01$ and if the micropore size distribution is wide the linear range may be restricted to $P/p^o < 0.005$.

But in general such a comparison produces a confused picture as in the case described for nitrogen adsorption (see 6.1.3), thus it would again be prudent to conclude that the significance of the DRK plot is obscure, and its validity for surface area estimation very doubtful.

7.1.4 Water BET surface Areas

The $S_{H_2O.BET}$ for samples 69, 74, 79, 80 and 82 are summarised in Table 7.1.

Clear trends in the data become evident on comparing the results for each sample to one another. The surface area measurements for the non-silylated sample (no. 69) increase with respect to an increase in treatment temperature, whereas the surface area measurements for the silylated samples (nos. 74, 79, 80 & 82) with respect to increasing treatment temperature either initially decrease or remain constant, followed by a sharp increase in surface area. These results can be explained in two possible ways: (i) adsorbed water causes either recrystallisation of the sample resulting in a decrease of surface area or fracture of aggregates resulting in an increase of surface area; and (ii) heating of the sample causes removal of water molecules trapped within the voids and interstices of the sample aggregates which when present would act as "sites" for water adsorption, resulting in a decrease in hydrophilicity for the samples possessing

surface $Si(CH_3)_3$ groups, and an increase in water surface area with respect to the non-silylated sample. The latter is the most probable mechanism when the previously discussed water and nitrogen isotherms are taken into account.

The large values for surface areas obtained after heating the samples at either 773K in air or 553K under vacuum are due to chemisorption rather than to surface coverage or multilayer formation.

8. RESULTS AND DISCUSSION IV

INSTRUMENTAL TECHNIQUES

8.1 Introduction

In this chapter the results of spectroscopic studies, thermogravimetric analysis, electron diffraction, X-ray photoelectron spectroscopy, and chemical analysis by atomic absorption and electron scanning for chemical analysis (ESCA) are presented. The infra-red spectrum of calcium hydroxide is characterised in Appendix D, the spectra of the precipitated and surface reacted samples are shown in Figures 8.1 - 8.28, the X-ray photoelectron spectra of a silylated sample and the organic composite are shown in Figure 8.29, the thermogravimetric analysis plots of silylated and non-silylated samples are shown in Figures 8.30 - 8.31 and the differential thermal analysis plot for the organic composite is shown in Figure 8.32.

8.1.1 Infra-red Spectroscopy

The reflectance and transmission spectra of laboratory grade calcium hydroxide are shown in Appendix E . It is evident from the characterisation of the spectra that carbonate is a major contaminant, formed as a result of reaction with atmospheric CO_2.

Carbonation to varying degrees is a feature of all of the precipitated calcium hydroxide samples and is evidenced by the absorption bands at 2515cm^{-1}, 1626cm^{-1} and 872cm^{-1}. The presence of carbonate formed through the action of atmospheric CO_2 is confirmed by the affect of heating sample 82 in air at 773K (sample 82 had been shown to be stable to thermal decomposition up to ~ 913K by TGA), where the transmittance FTIR spectrum, shown in Figure 8.24, exhibits absorption peaks at 2876cm^{-1}, 2512cm^{-1}, 1796cm^{-1} and 1410cm^{-1} which are indicative of carbonate. Comparison of this spectrum with the reflectance FTIR spectrum of sample 82, shown in Figure 8.23, prior to heating in air brings the effects of carbonation into stark relief.

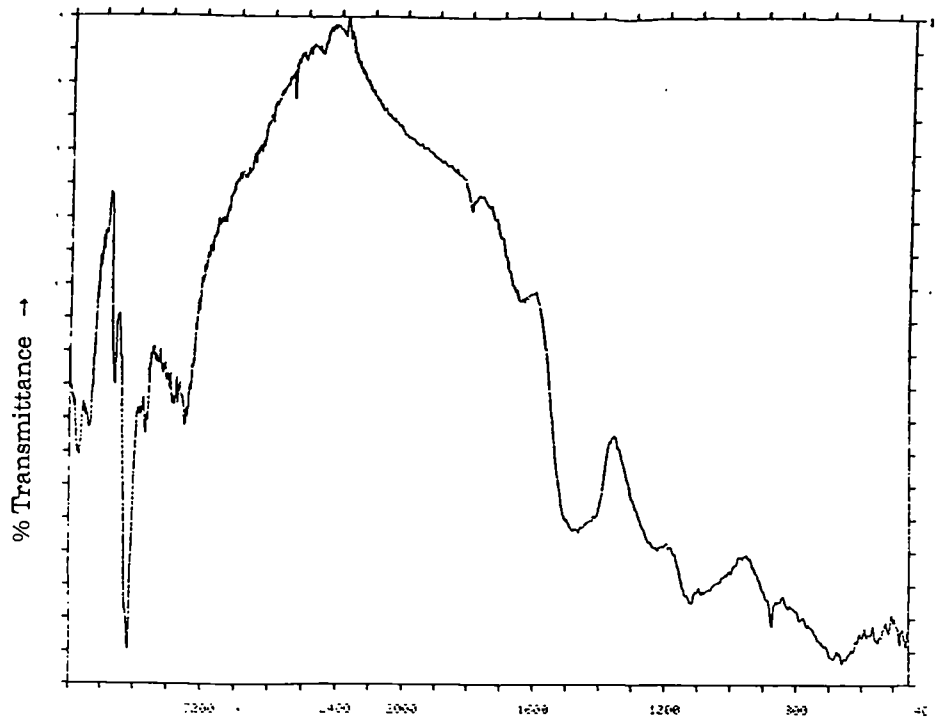

Figure 8.1 Reflectance FTIR Spectrum of Sample 9.

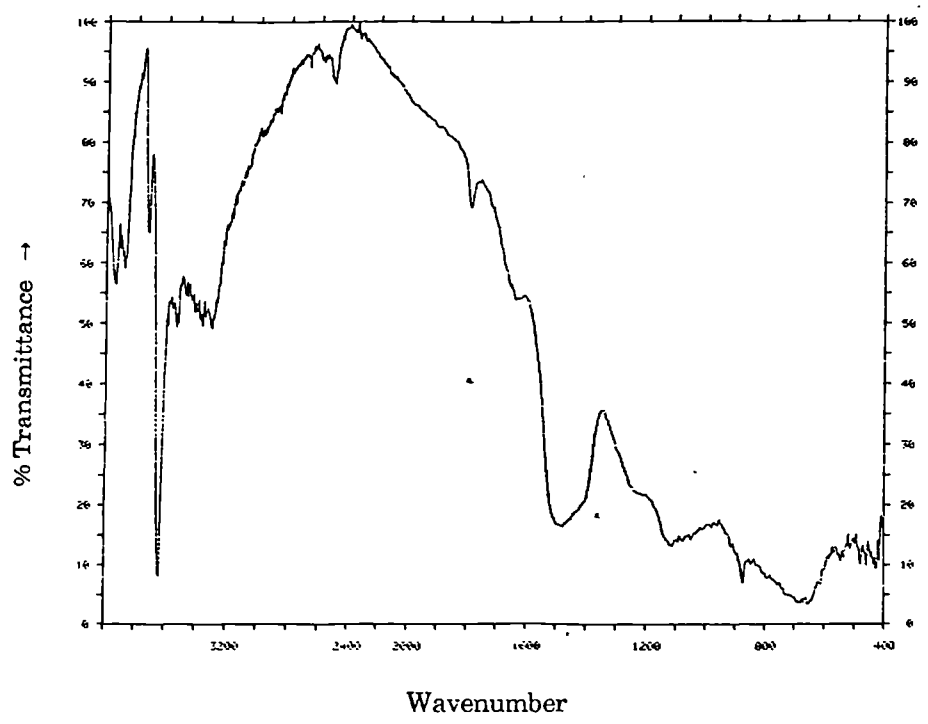

Figure 8.2 Reflectance FTIR Spectrum of Sample 19.

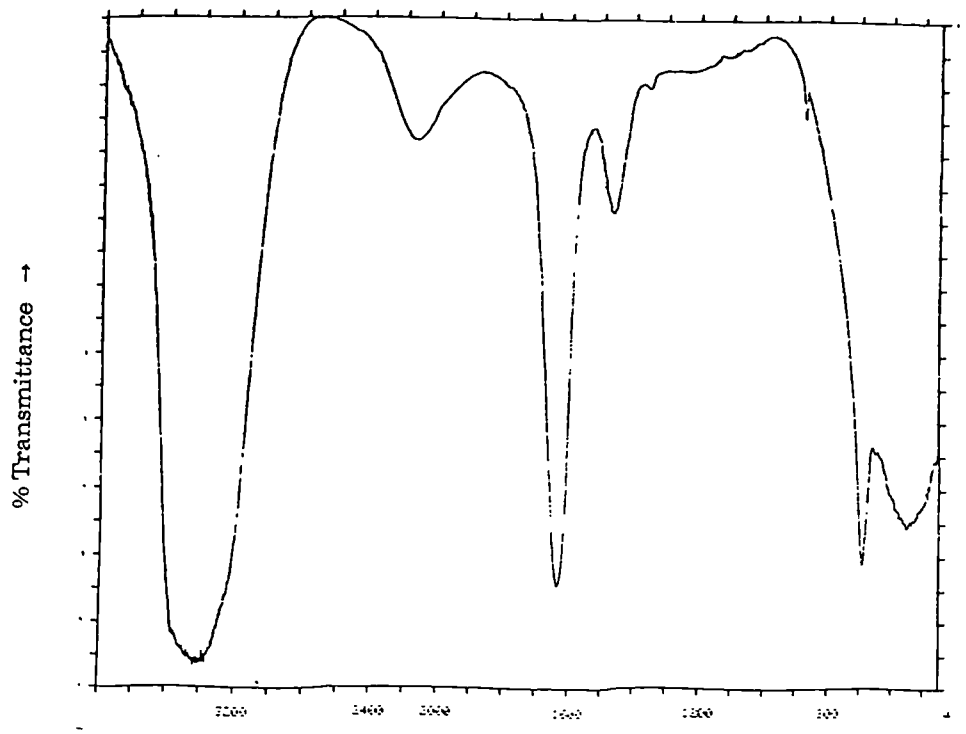

Figure 8.3 Transmission FTIR Spectrum of Sample 35.

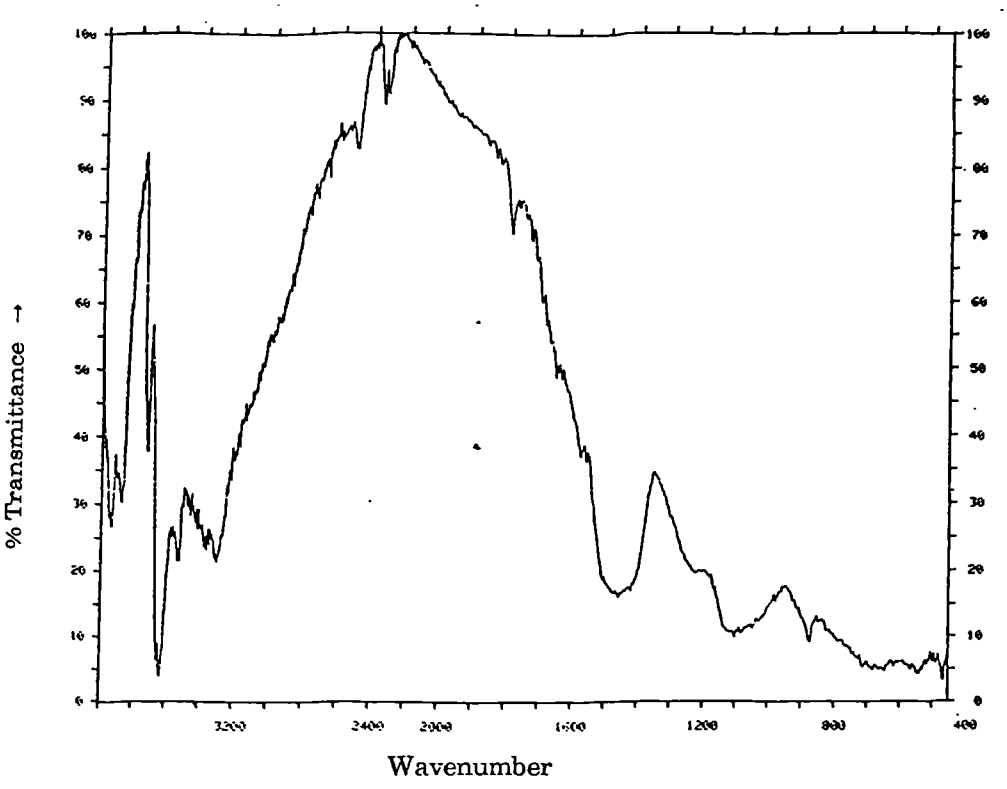

Figure 8.4 Reflectance FTIR Spectrum of Sample 39.

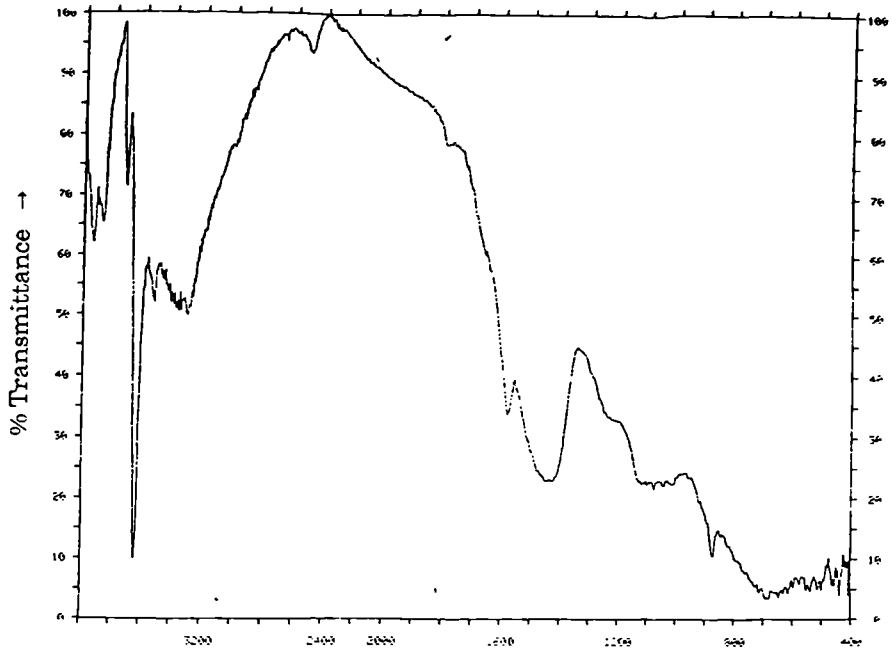

Figure 8.5 Reflectance FTIR Spectrum of Sample 40.

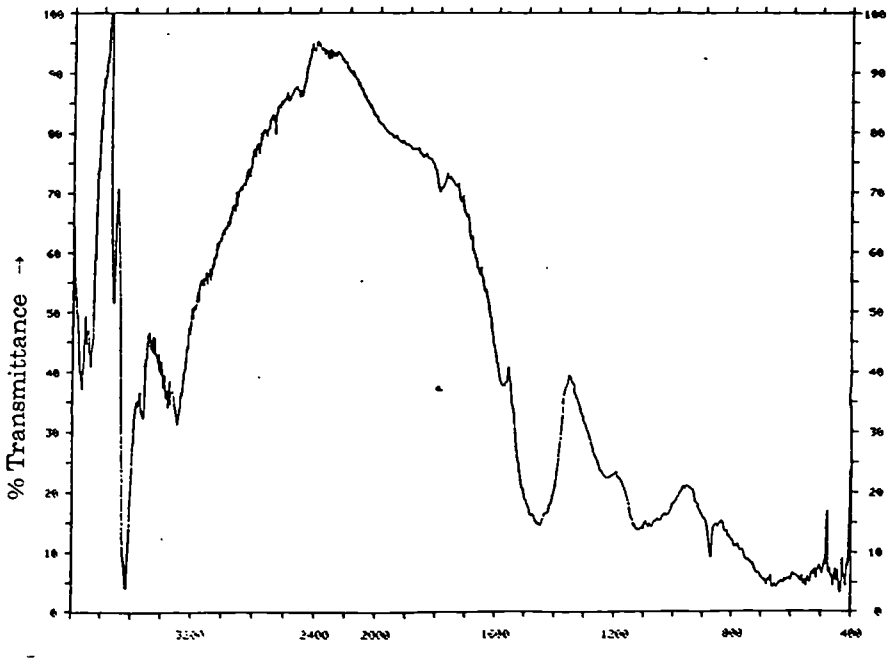

Figure 8.6 Reflectance FTIR Spectrum of Sample 44.

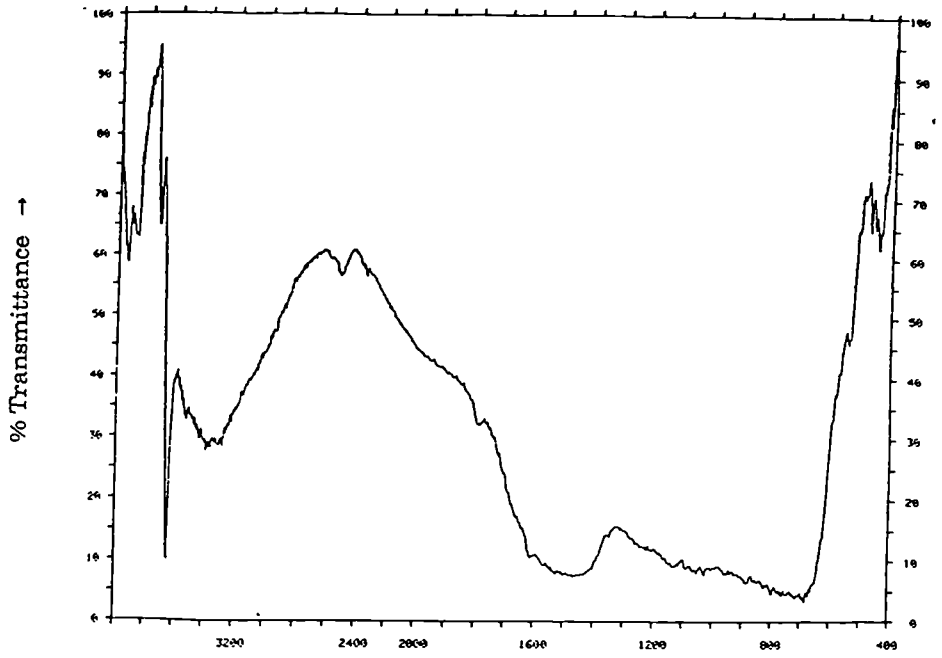

Figure 8.7 Reflectance FTIR Spectrum of Sample 49.

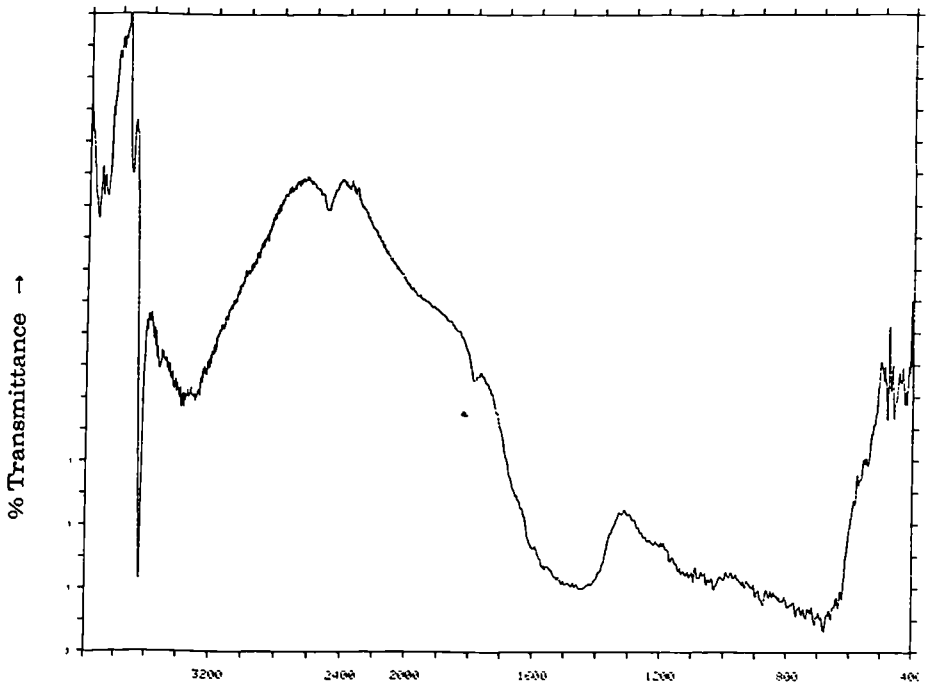

Figure 8.8 Reflectance FTIR Spectrum of Sample 50.

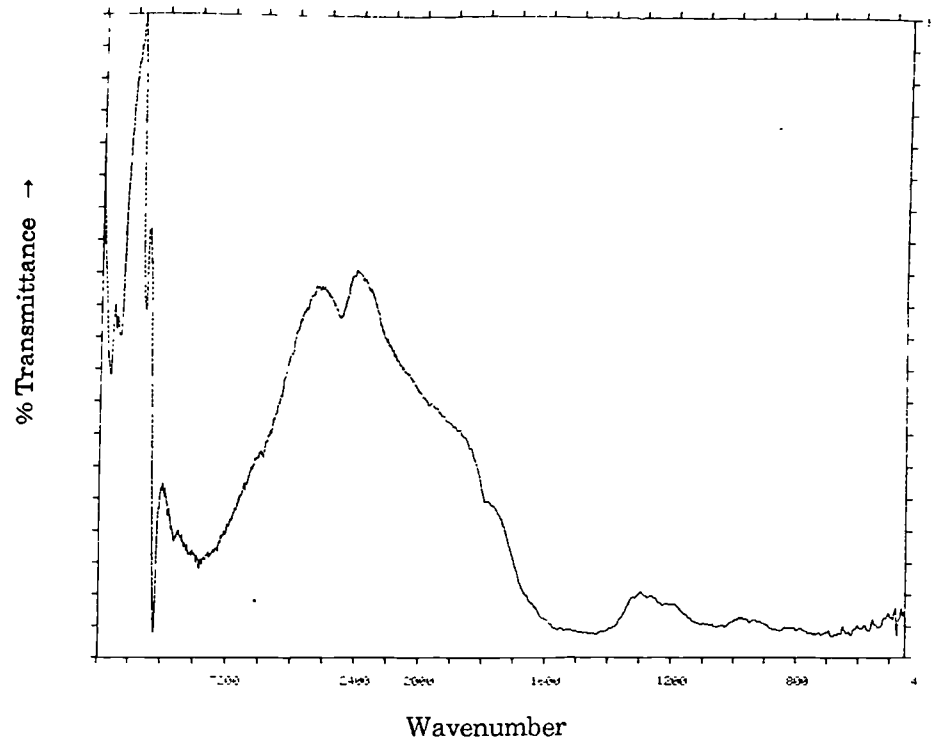

Figure 8.9 Reflectance FTIR Spectrum of Sample 51.

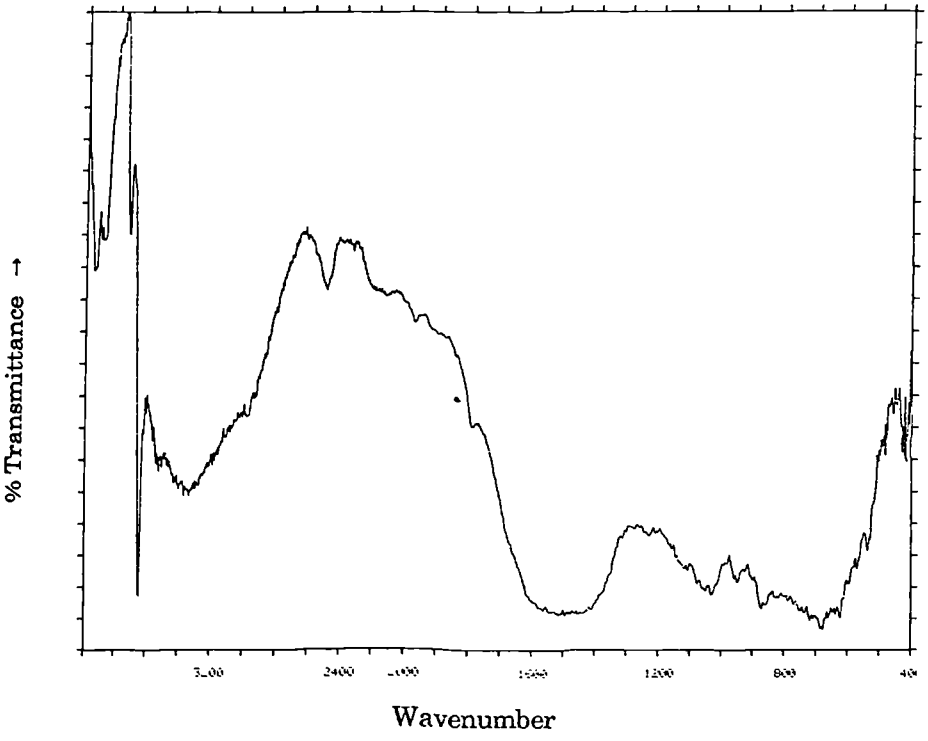

Figure 8.10 Reflectance FTIR Spectrum of Sample 52.

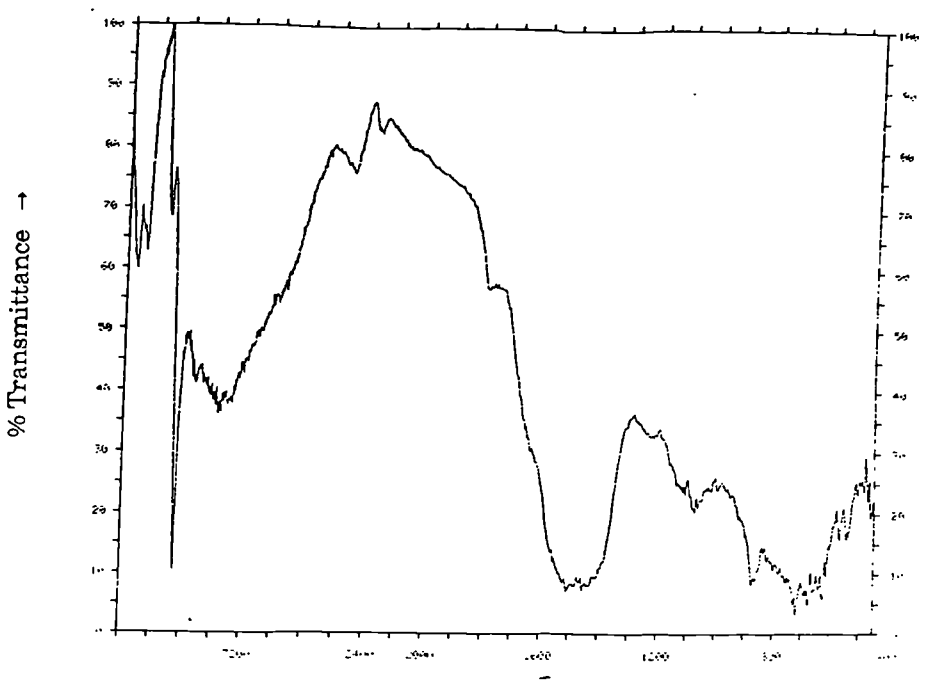

Figure 8.11 Reflectance FTIR Spectrum of Sample 55.

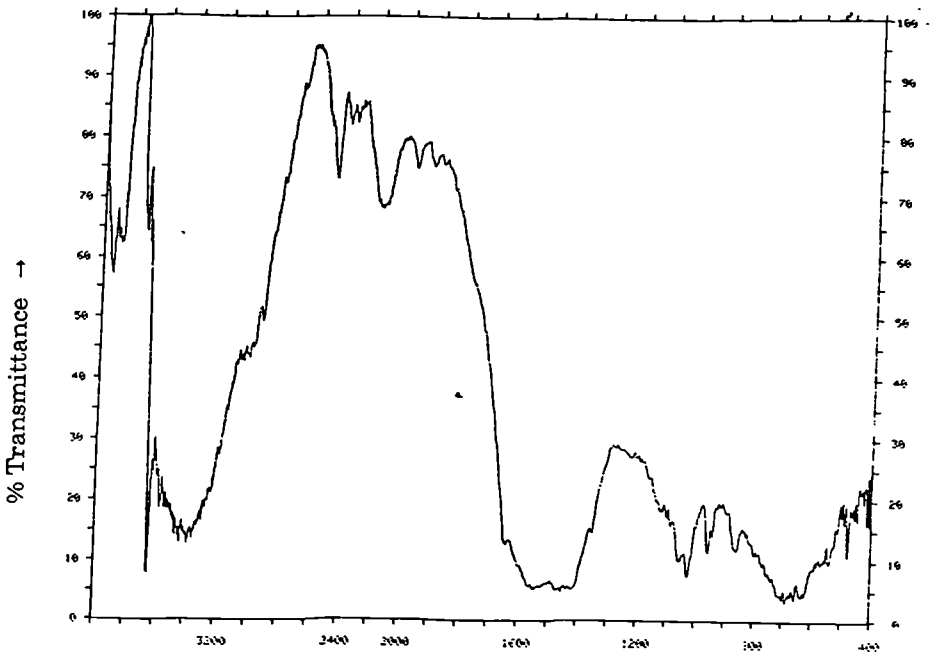

Figure 8.12 Reflectance FTIR Spectrum of Sample 58.

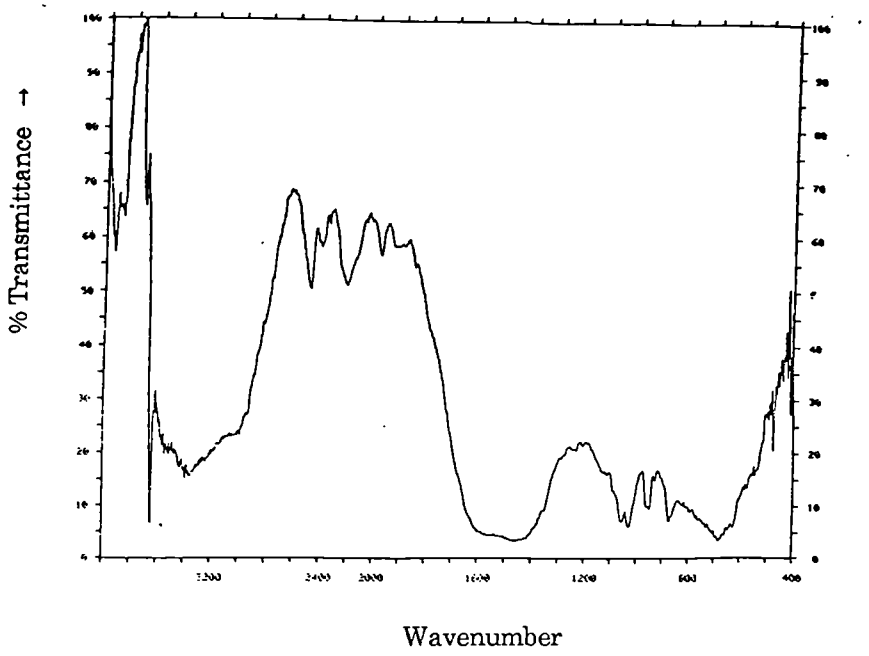

Figure 8.13 Reflectance FTIR Spectrum of Sample 60.

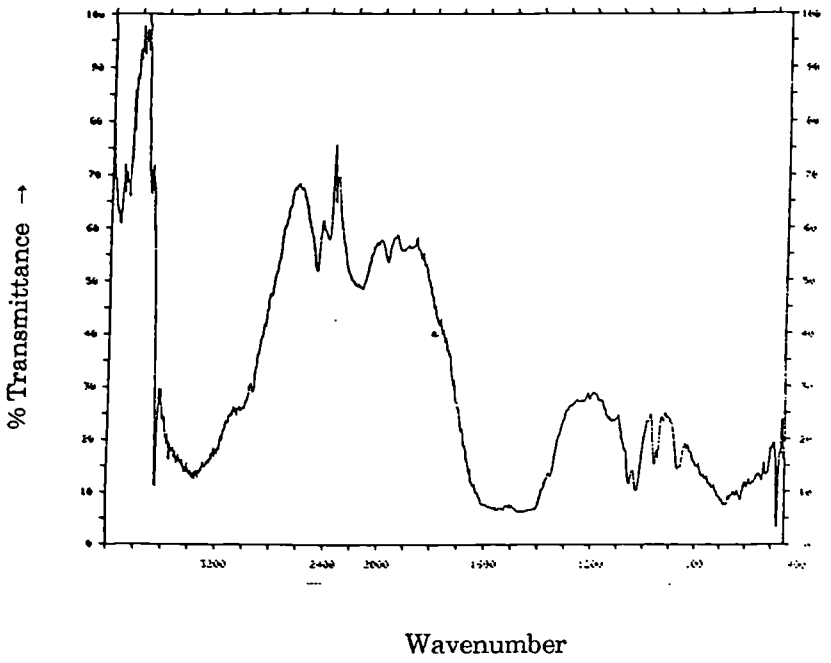

Figure 8.14 Reflectance FTIR Spectrum of Sample 67.

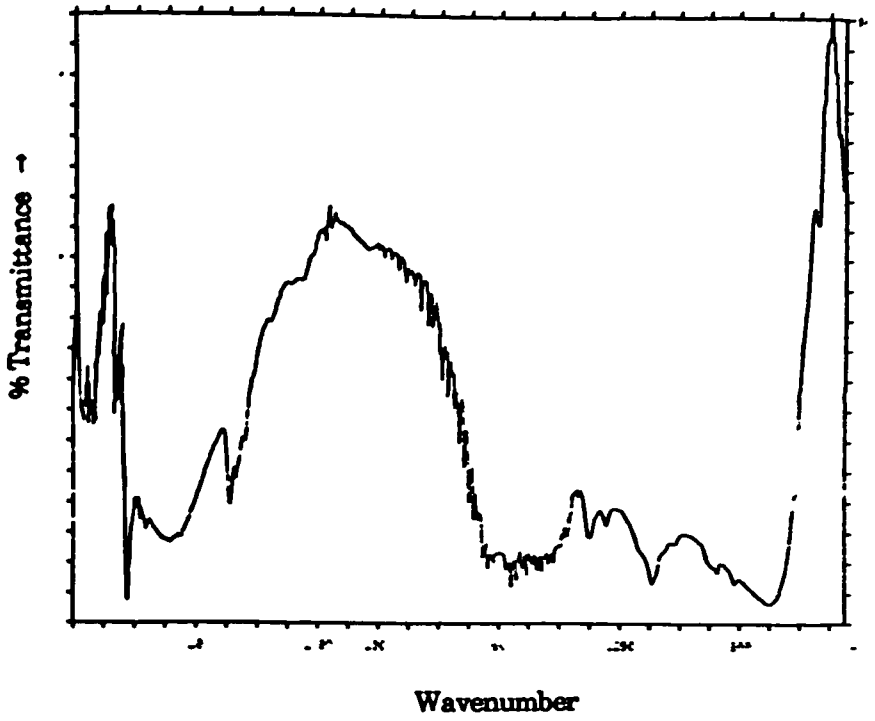

Figure 8.15 Reflectance FTIR Spectrum of Sample 68.

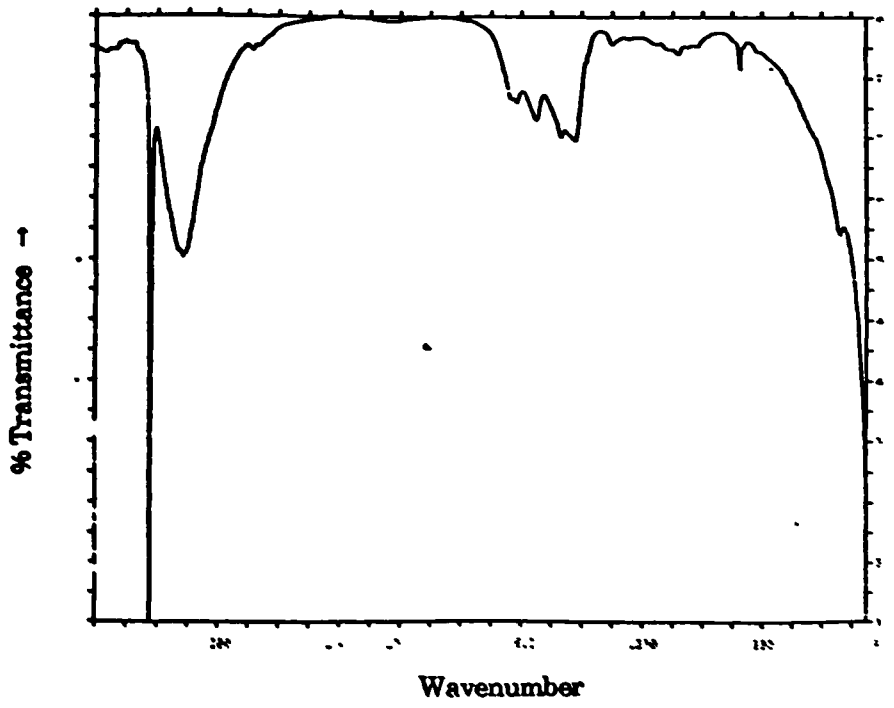

Figure 8.16 Transmission FTIR Spectrum of Sample 68.

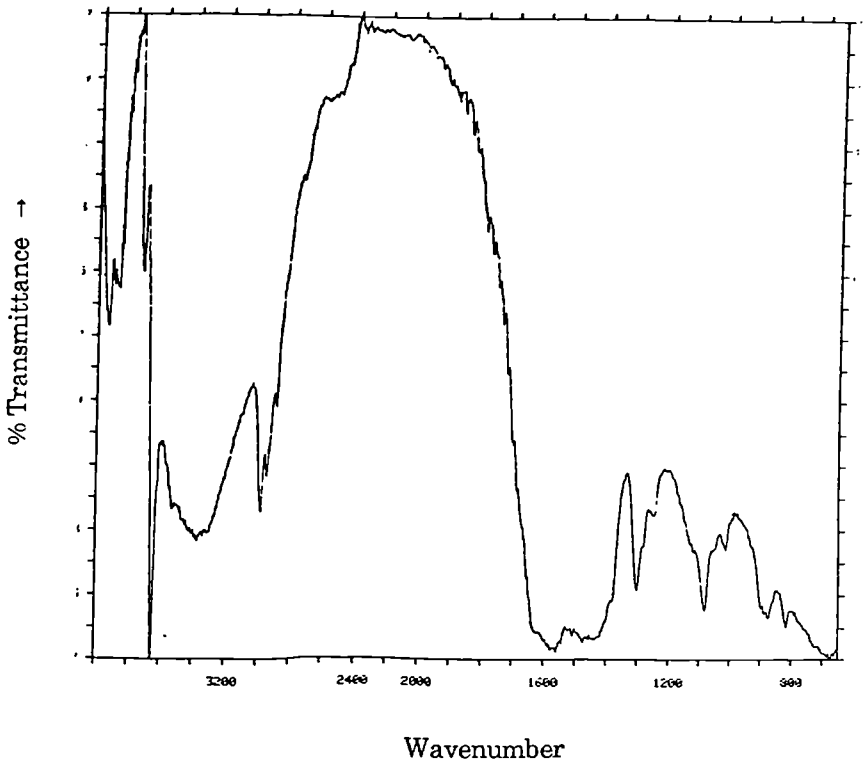

Figure 8.17 Reflectance FTIR Spectrum of Sample 69.

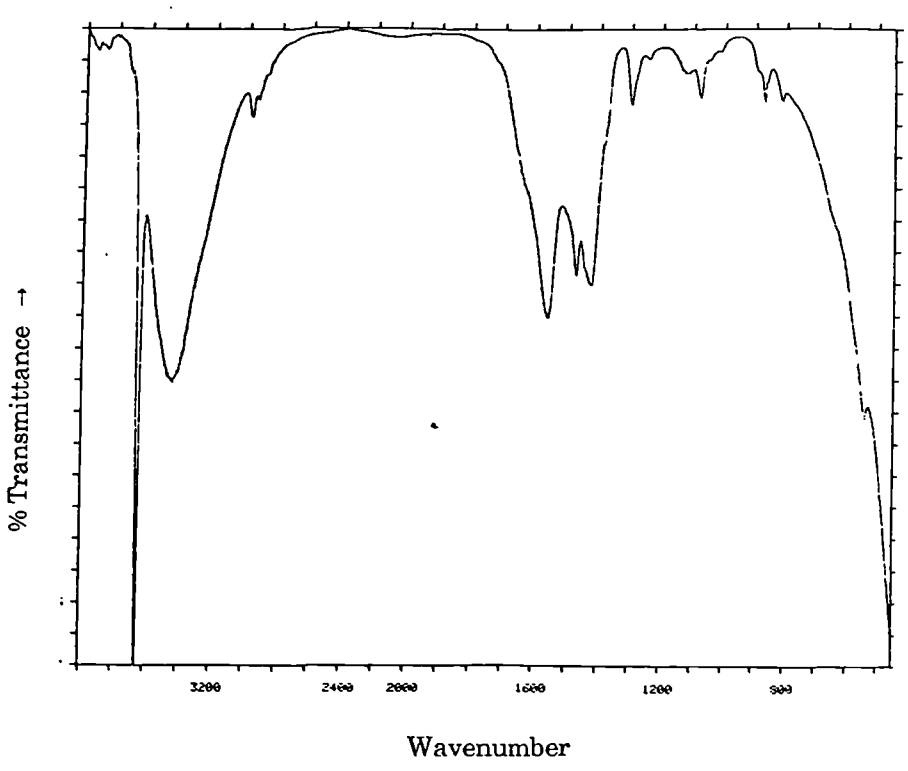

Figure 8.18 Transmission FTIR Spectrum of Sample 69.

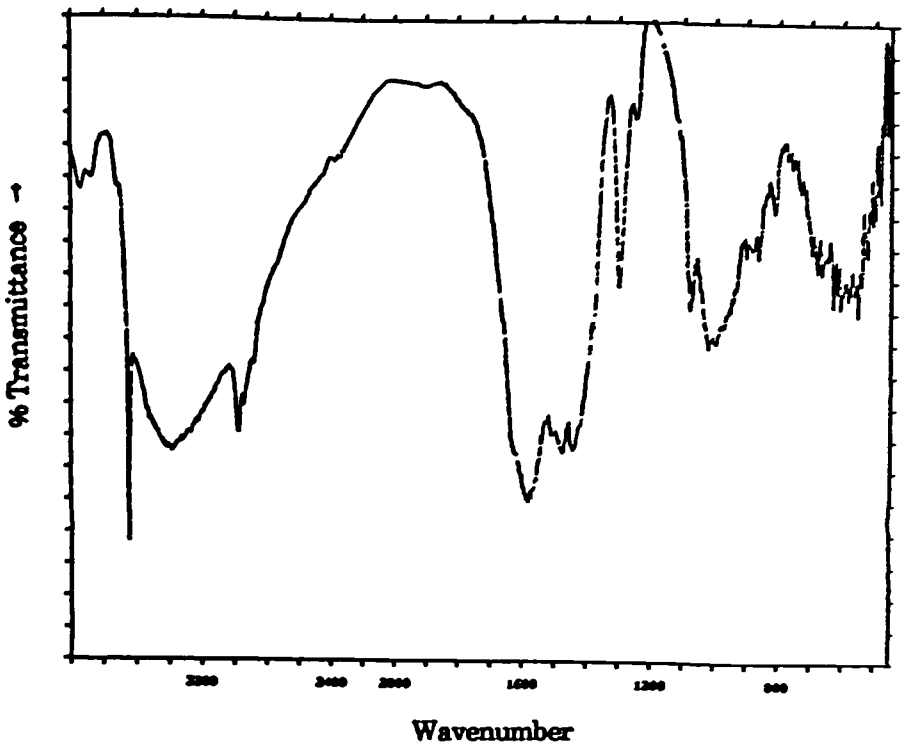

Figure 8.19 Reflectance FTIR Spectrum of Sample 74.

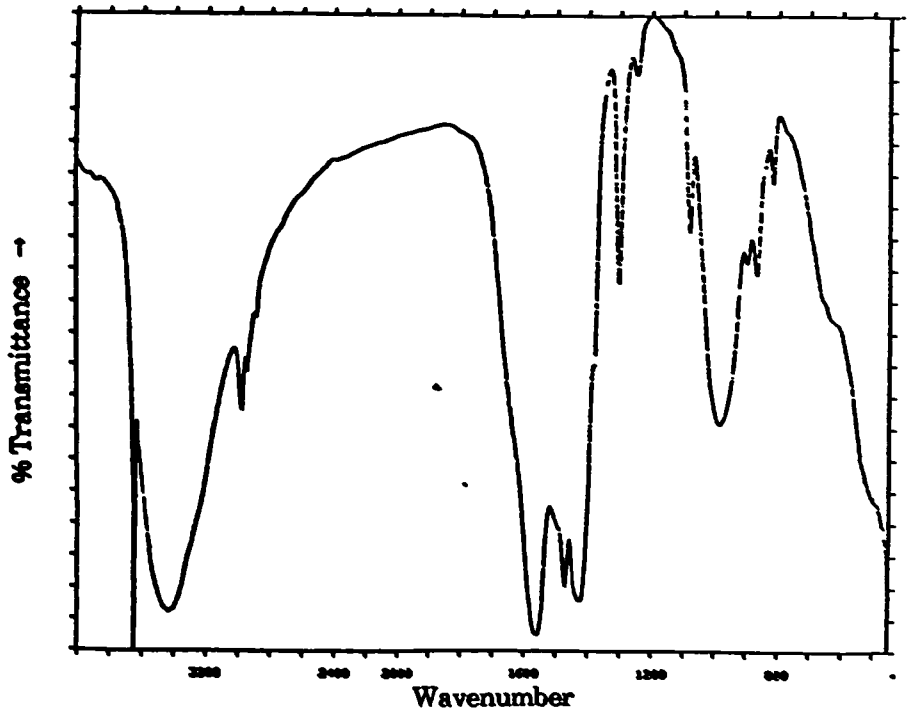

Figure 8.20 Transmission FTIR Spectrum of Sample 74.

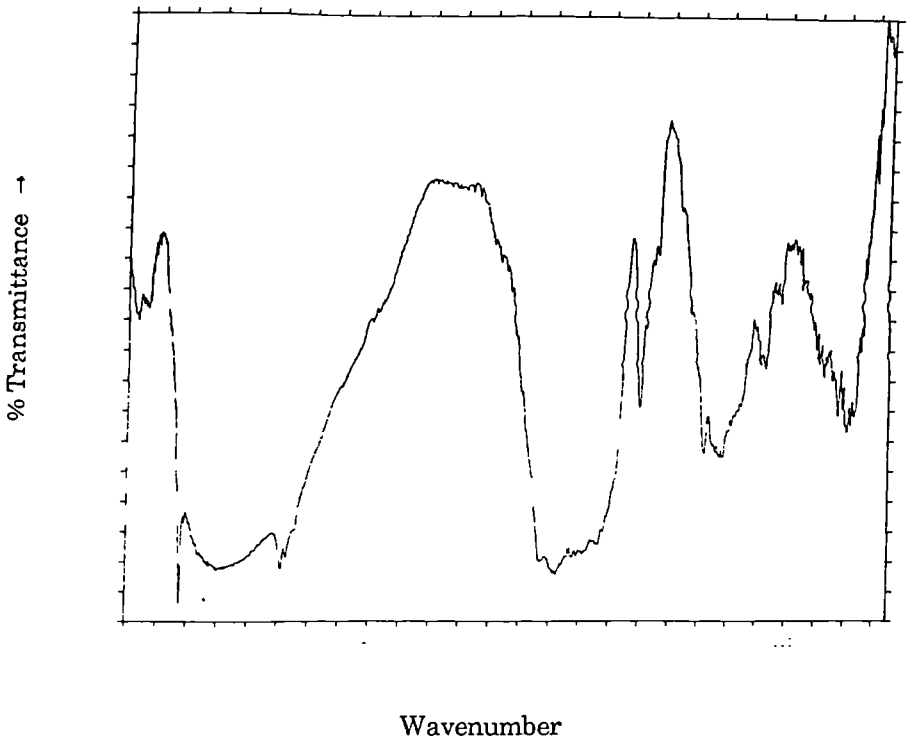

Figure 8.21 Reflectance FTIR Spectrum of Sample 80.

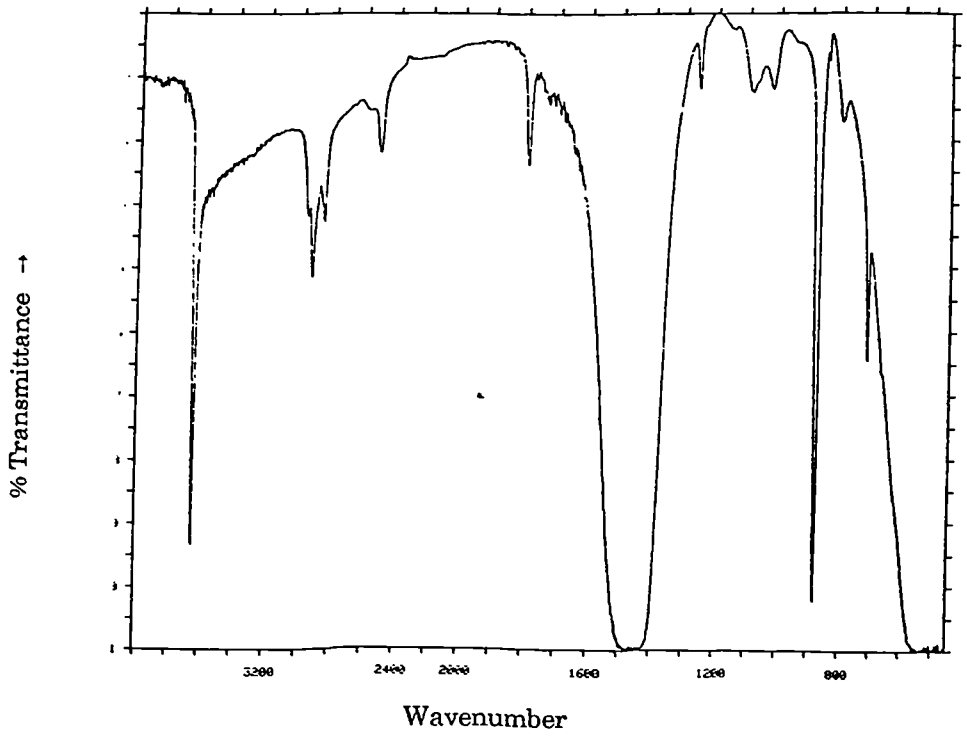

Figure 8.22 Transmission FTIR Spectrum of Sample 80.

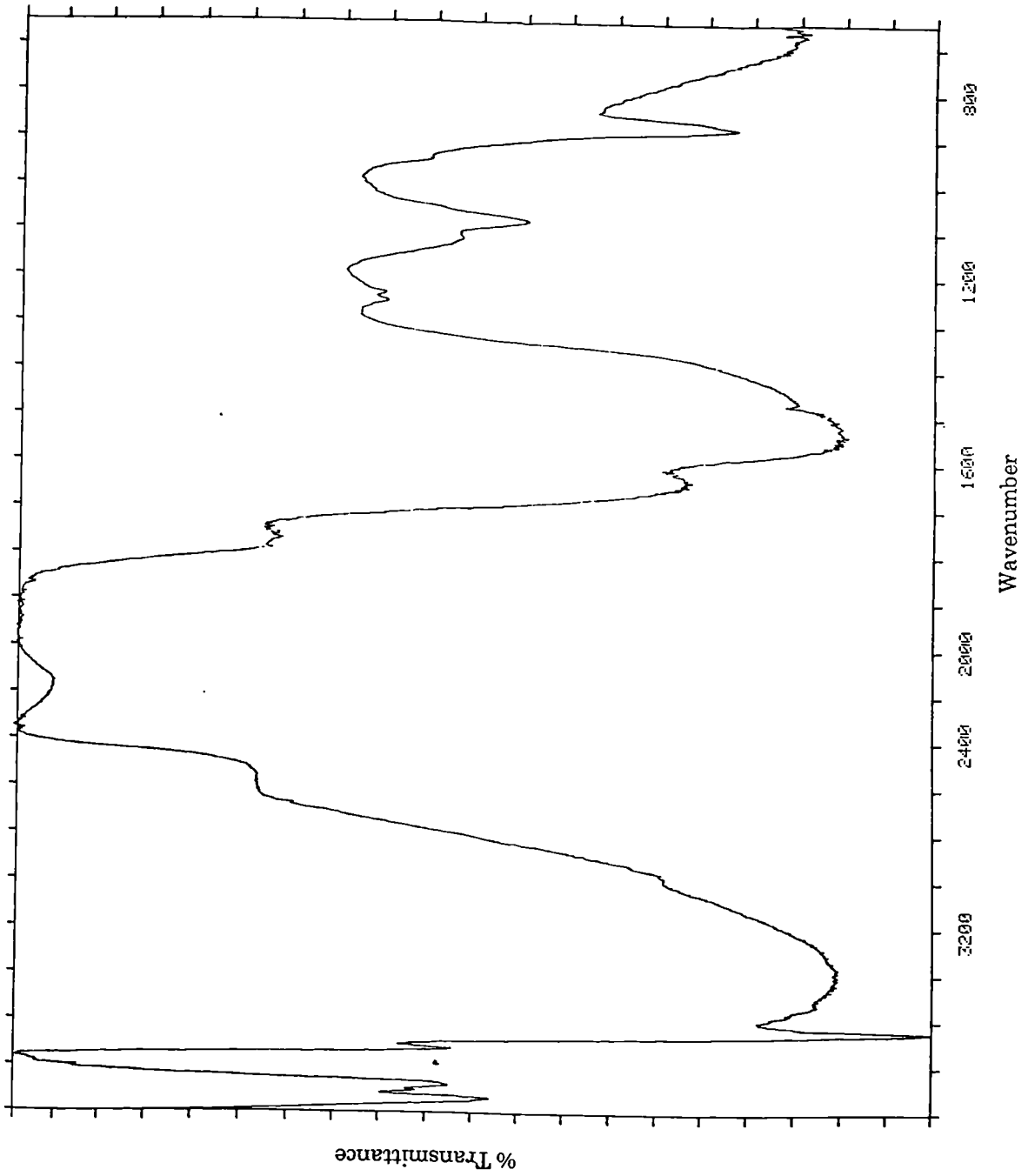

Figure 8.23 Reflectance FTIR Spectrum of Sample 82.

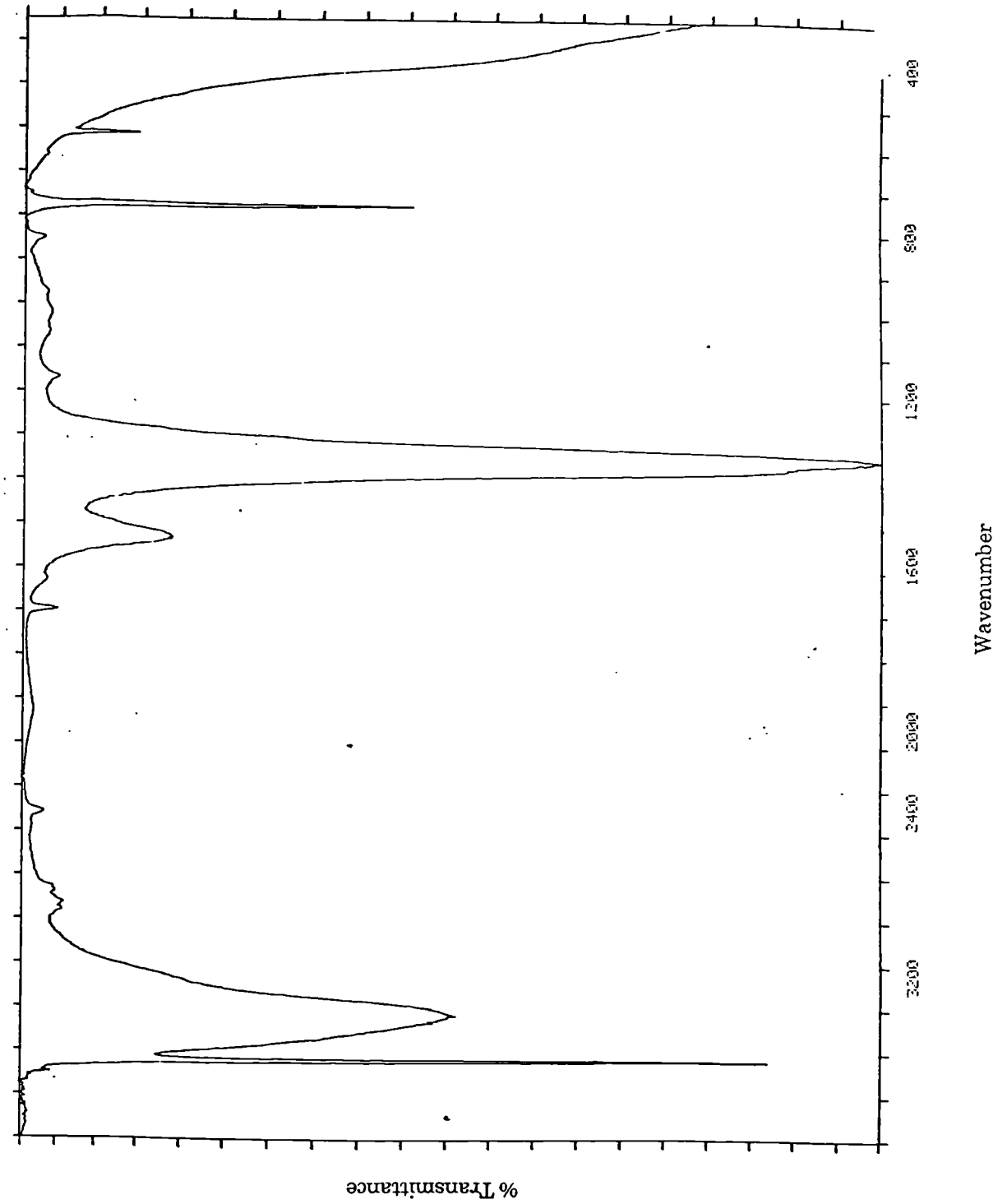

Figure 8.24 Transmission FTIR Spectrum of Sample 82.

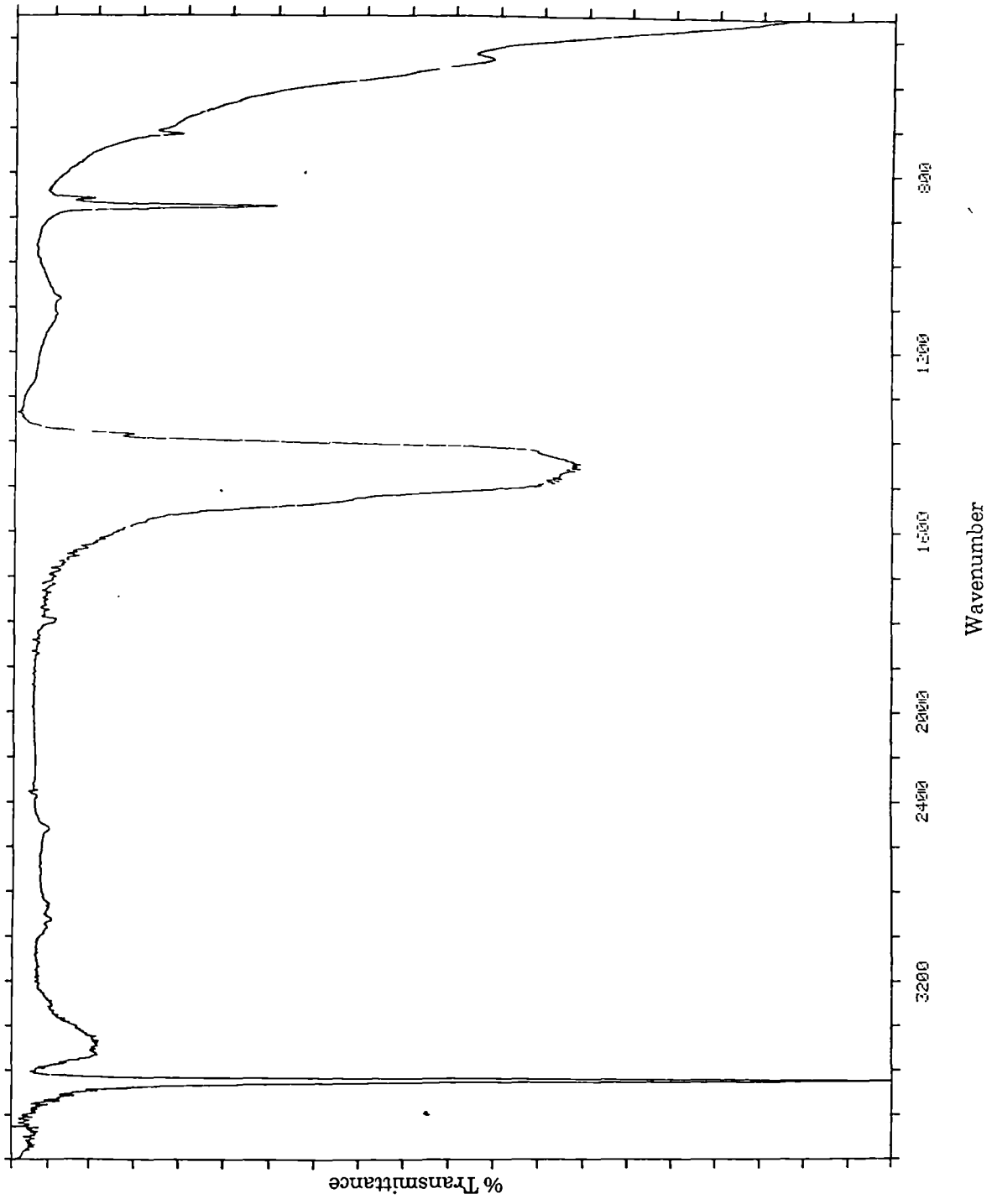

Figure 8.25 Transmission FTIR Spectrum of Sample 82 heated to 620K.

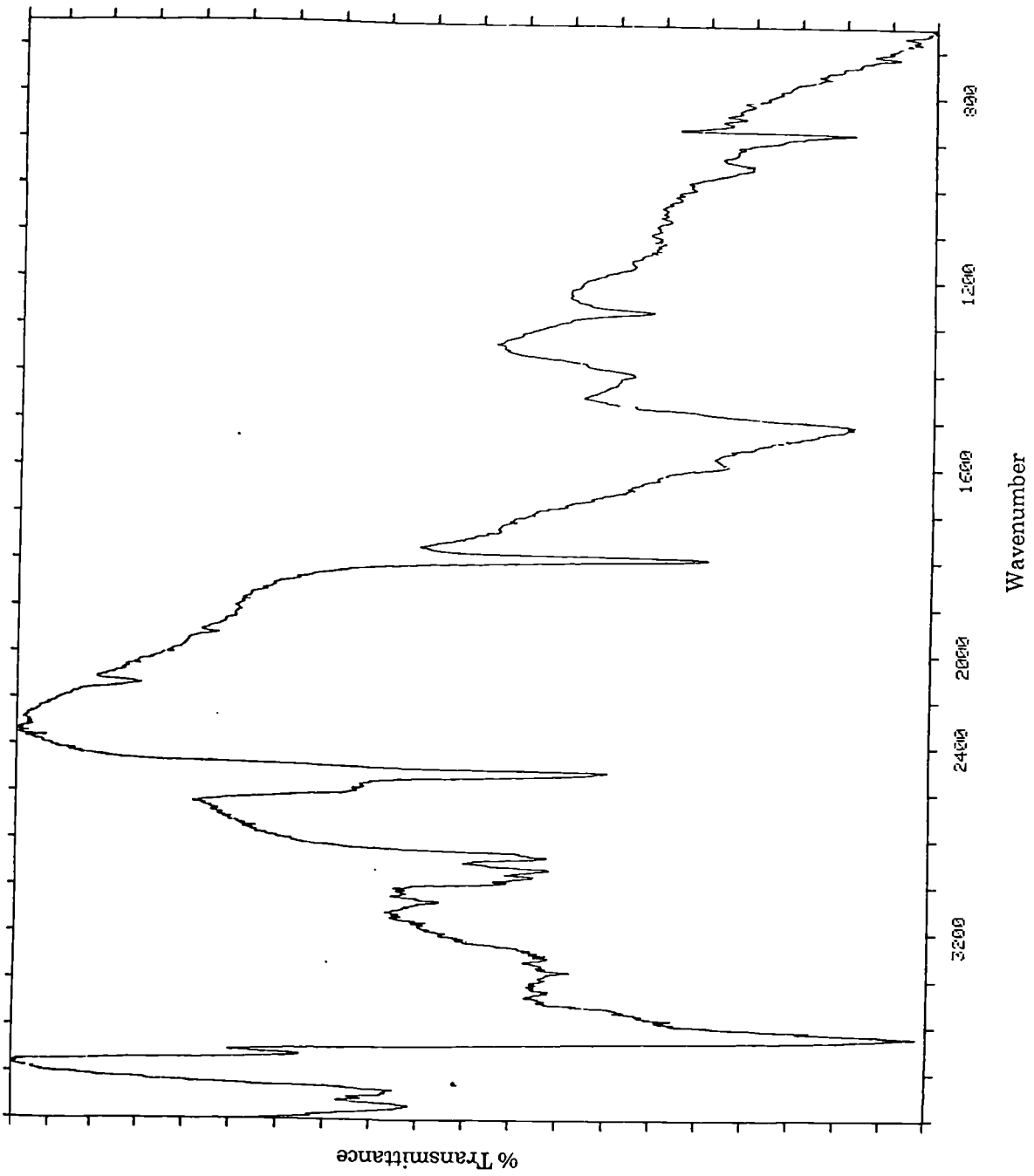

Figure 8.26 Reflectance FTIR Spectrum of Sample 82 heated to 770K.

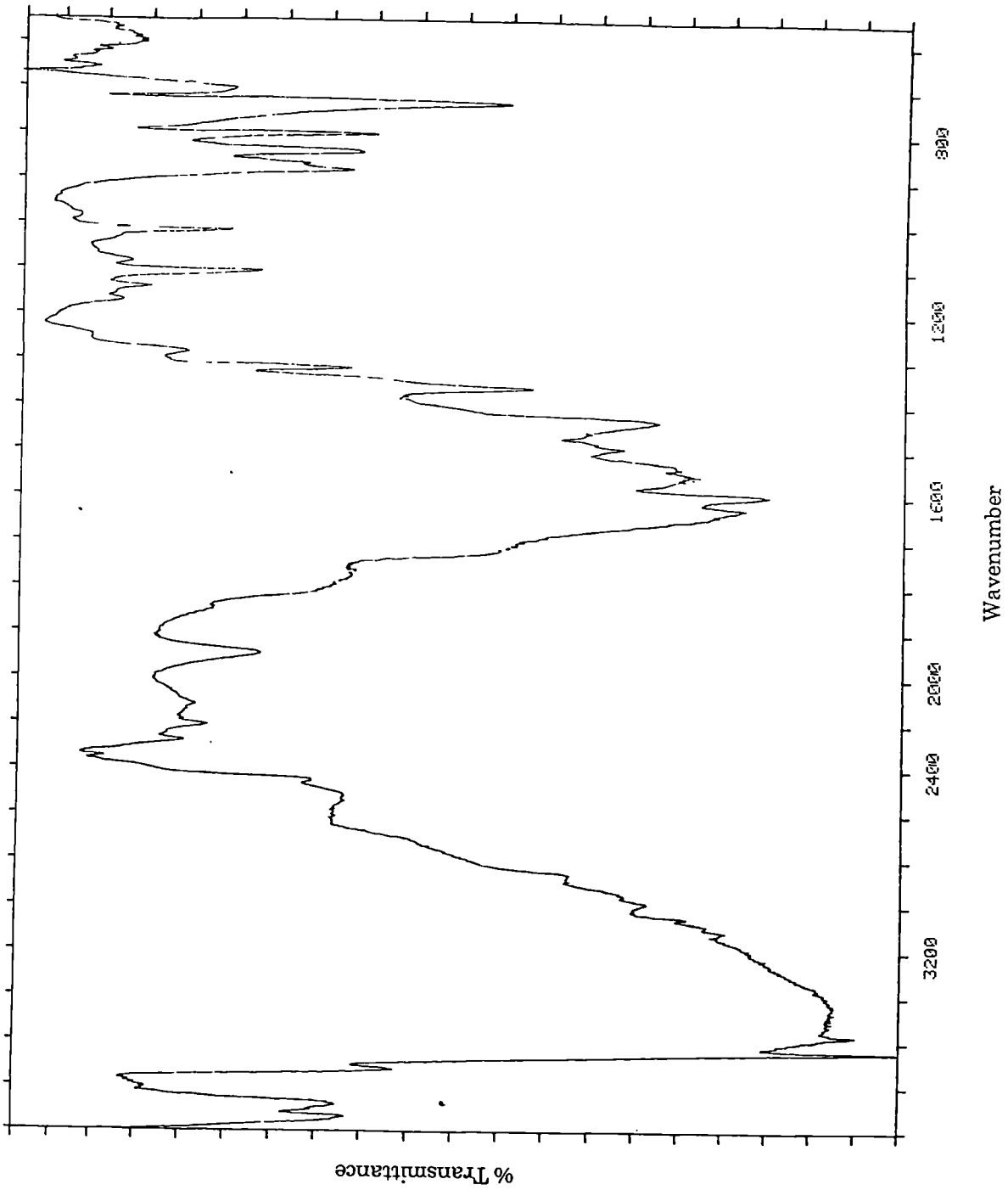

Figure 8.27 Reflectance FTIR Spectrum of Sample 82X.

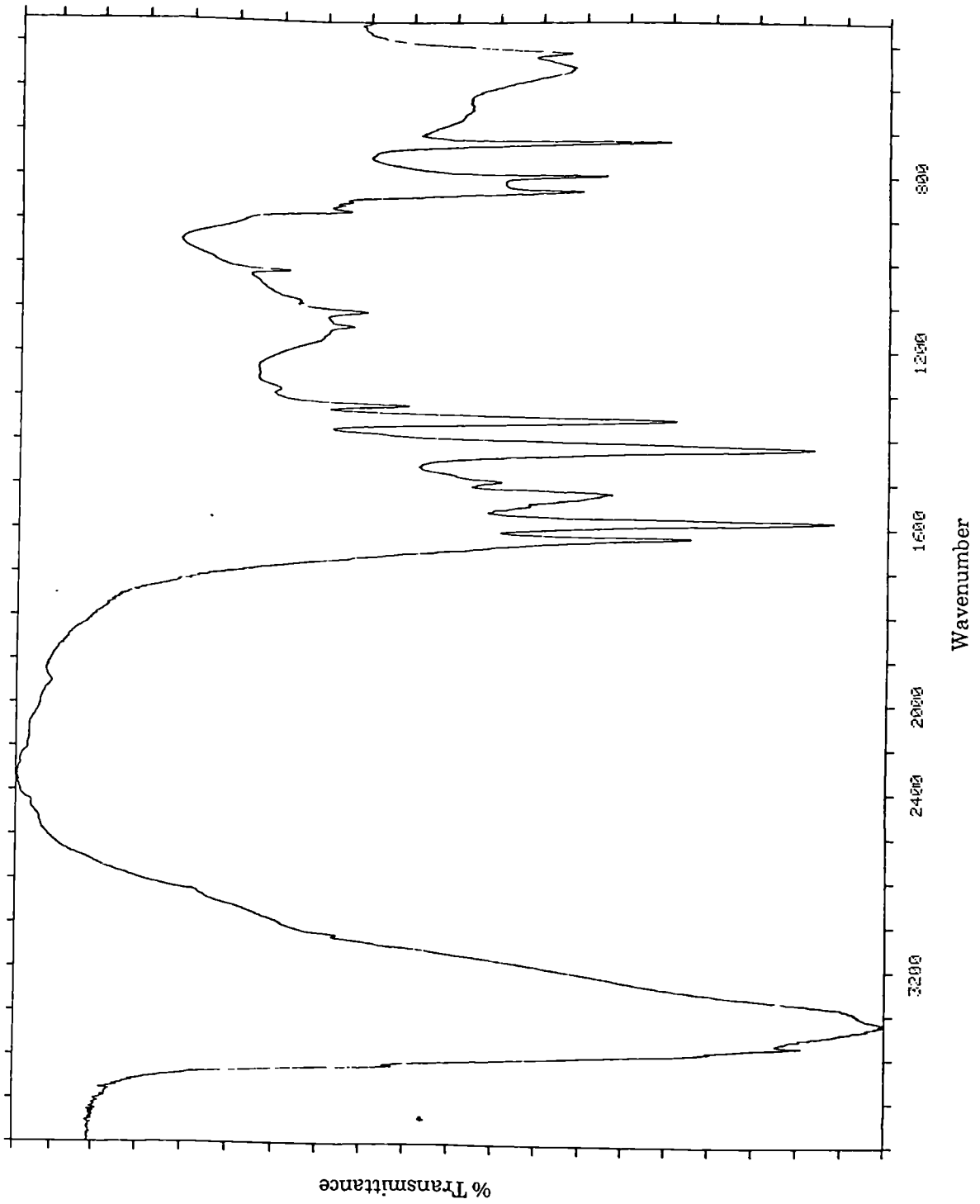

Figure 8.28 Transmission FTIR Spectrum of 82X.

The broad absorption band at 3400cm^{-1} is removed by heating, this band is due to adsorbed H-bonded water molecules, and its suppression reveals the small sharp band at 3530cm^{-1} due to bulk OH groups.

Some of the FTIR spectra of the precipitated calcium hydroxide samples exhibit a broad peak at 3368cm^{-1}, while others do not. The 3368cm^{-1} peak is associated with water, thus some of the samples contain a lower amount of water than others. A trend becomes apparent on matching the spectra to the electron micrographs. Samples 9, 19, 39, 40, and 44, shown in Plates 1 B, 9 A, 3 B, 5 A, and 4 A & B respectively, are formed of large crystals of size ~ 2mm or greater, whereas samples 12, 17, 47, 49, 50, 51, 52, 55, 58, 60, 67, 68, 69, 74, 79, 80 and 82, shown in Plates 2 A, 2 B, 5 B, 6 A, 6 B, 7 A, 7 B, 8 A, 8 B, 9 B, 10 A & B, 11 A, 11 B, 12 A, 12 B, 13 A and 13 B respectively, consist of platelets or sheet-like crystals. Therefore whether water is incorporated into the sample depends upon morphology. An increase in water content is associated with plate-like and sheet-like morphologies; the likely explanation for this is that water is held within the voids and interstices of the aggregates, and the mild drying conditions used following precipitation are not sufficient to remove the trapped water molecules.

Sample 35 produces a FTIR spectrum, shown in Figure 8.3, that is totally different from the other samples, in that it is the spectrum of a carbonate. There are no bands assignable to calcium hydroxide. Sample 35 was prepared in a non-aqueous medium; all of the precipitants were dissolved in absolute ethanol. Carbon dioxide has a much higher solubility in ethanol than in water, thus the sample must be carbonated as it is precipitated, as all other conditions are identical for each sample.

The reflectance FTIR spectra of samples 39, 40 and 44, shown in Figures 8.4 - 8.6, exhibit a sharp peak at 1580cm^{-1} which is absent from the other spectra. The 1580cm^{-1} peak appears in the reflectance FTIR spectrum of calcium acetate, a precipitant used in the preparation of samples 39, 40 and 44, and also in the preparation of samples 49, 50, 51, 52, 55, 58 and 60. This latter group of samples do not exhibit the 1580cm^{-1} peak in

their FTIR spectra, but the peak at 1455cm^{-1} is much broader than for samples 39, 40 and 44. As has been discussed above, the presence of trapped water molecules in the plate-like samples caused broadening of the peak at 3400cm^{-1}, likewise the broadening of the peak at 1455cm^{-1} is likely to be due to the same effect. Therefore, the broadening of the 1455cm^{-1} peak must mask the acetate peak at 1580cm^{-1}. The presence of acetate in samples 49, 50, 51, 52, 55, 58 and 60, spectra shown in Figures 8.7 - 8.13, is confirmed by the presence of characteristic acetate peaks in the reflectance spectra at 2500cm^{-1}, 2378cm^{-1}, 2345cm^{-1}, 2216cm^{-1}, 1980cm^{-1}, 1917cm^{-1}, 1900cm^{-1} and 1839cm^{-1}. These peaks are variable in intensity, the intensity appears to increase on progression from sample 49 to sample 60. This coincides with the changes in morphology. As the crystal changes from a hexagonal tablet ~ 30nm thick (sample 60, Plate 9 B) the acetate peaks in the range 2500 - 1839cm^{-1} become stronger. This result implies the surface concentration of acetate increases as the platelet thickness decreases, hence the change in precipitation conditions results in a change in the surface acetate concentration. Samples 58 and 60 exhibit the most intense acetate peaks, and they are both precipitated by rapid mixing of the precipitants in aqueous ethanolic media. The precipitants comprised an equimolar mixture of calcium chloride and calcium acetate, which was added to sodium hydroxide solution, where the calcium salts in total concentration exceed the stoichiometric requirement of the reaction. It has been shown in chapter 5, that the rate of addition of the precipitants is an important factor in obtaining thin, plate-like crystals; it was also shown that the presence of acetate was also related to platelet formation. Thus, from the FTIR evidence it can be deduced that the increasing surface concentration of acetate is directly related to the decrease in platelet thickness. This implies that calcium chloride reacts preferentially with the sodium hydroxide, leaving the calcium acetate to poison the large (0001) faces preventing crystal growth in that direction. Slow addition of the calcium salts to sodium hydroxide would allow time for the calcium acetate to react, thus reducing the amount available for poisoning.

Samples 67, 68 and 69 exhibit peaks in the reflectance FTIR spectra, shown in Figures 8.14 - 8.18, not assignable to calcium hydroxide, at 2975cm^{-1}, 2947cm^{-1},

2875cm^{-1}, 1470cm^{-1}, 1303cm^{-1}, 1172cm^{-1} and 805cm^{-1}. These peaks coincide with those exhibited by laboratory grade calcium propionate. The presence of bands in the spectra due to propionate groups confirms that the same mechanism occurs during the precipitation process incorporating calcium propionate as a co-precipitant, as occurs when using calcium acetate as a co-precipitant. Confirmation that the propionate groups are concentrated on the surface of the precipitated calcium hydroxide is obtained by comparison of the reflectance and transmission FTIR spectra of samples 68 or 69, shown in Figures 8.15 & 8.16, and Figures 8.17 & 8.18 respectively. The intensity of the propionate bands is evidently stronger in the reflectance spectra than in the transmission spectra.

The reflectance and transmission FTIR spectra, shown in Figures 8.19 & 8.20, of sample 74, produced by silylation of precipitated calcium hydroxide poisoned by propionate moieties, exhibit absorption bands characteristic of calcium hydroxide and propionate groups together with a strong peak at 819cm^{-1}, associated with $Si(CH_3)_3$ groups, which is stronger in the reflectance spectrum than in the transmission spectrum. This result is strongly indicative that the $Si(CH_3)_3$ moieties are on the surface.

Similarly, the presence of $Si(CH_3)_3$ groups on the surface of sample 80 is confirmed by the FTIR spectra, shown in Figures 8.21 & 8.22, although the transmission spectrum shows considerable evidence of carbonation.

The FTIR spectra of sample 82 give a clearer picture than the other silylated samples because no "poison" was present during the precipitation and silylation reactions. A group of very weak bands in the region 2960 - 2880cm^{-1} are visible in the reflectance FTIR spectra, shown in Figures 8.23, giving evidence of the presence of a small number of aliphatic moieties; this together with the peak at 874cm^{-1} shows the presence of $Si(CH_3)_3$ moieties.

Heating sample 82 at 823K in air results in the appearance of additional peaks in the spectrum, shown in Figure 8.26, at 3936cm^{-1}, 3856cm^{-1}, 3843cm^{-1}, 3823cm^{-1}, 3753cm^{-1}, 3738cm^{-1}, 2875cm^{-1}, 2512cm^{-1}, 2139cm^{-1}, 1796cm^{-1}, 1081cm^{-1}, 953cm^{-1} and 714cm^{-1} which are all assignable to carbonate, and loss of the broad peaks at 3500cm^{-1} and at 1636cm^{-1} which are assignable to water. Removal of most of the water, by heating at 623K, reveals a sharp band at 3531cm^{-1} which is due to bulk OH groups (the peak at 3645cm^{-1} is due to OH groups at or near the surface) in the transmission spectrum (Figure 8.25).

Upon reaction of sample 82 with 3-aminopropyltriethoxysilane and subsequent formation of the nitrobenzamide, the OH band at 3645cm^{-1} collapses (cf. Figures 8.28 & 8.24), indicating that reaction is primarily taking place with the surface OH groups. The band at 3545cm^{-1} in the spectrum of the reaction product (Figure 8.28) corresponds with the bulk OH groups, while the broad band at 3436cm^{-1} can be assigned to the amide group. Assignments have been confirmed by comparison with the spectrum of calcium hydroxide exposed to D_2O. The reduction in intensity for the bands associated with the presence of water, is consistent with a modification of the surface to render it less hydrophilic, by introducing organic groups. The bands at 1620cm^{-1} and 724cm^{-1} corresponds to an amide, the bands at 1520cm^{-1} and 1356cm^{-1} correspond to R-NO_2 moieties and the bands at 1140cm^{-1}, 1107cm^{-1}, 1015cm^{-1} and 856cm^{-1} correspond to a 1,4-disubstituted benzene ring. It can therefore be suggested that a molecular composite has been synthesised from the stabilised calcium hydroxide material.

8.1.2 Ultra-violet Spectroscopy

Reflectance UV spectroscopy was carried out for sample 82 and the reaction product of sample 82 with 3-aminopropyltriethoxysilane and with *para*-nitrobenzoyl chloride (designated 82X). The reflectance UV spectrum showed sample 82 to be largely transparent in the wavelength region 250 - 700 nm, but the reaction product shows a

strong adsorption band at 320 nm, which is what is expected for a nitrobenzamide moiety, such as that present in the 82X.

This result is a further indication that the introduction of nitrobenzamide moieties to the surface of sample 82 has occurred.

8.1.3 X-ray Photoelectron Spectroscopy (XPS)

A complete wide scan was collected for sample 74. The elements detected were C (32.5 atom%), O (48.0 atom%), Si (3.0 atom%), Ca (15.3 atom%) and Cl (1.5 atom%). Deconvolution of the C1s envelope suggests the presence of at least 3 states of carbon:

C (1) B. Energy 285.0 eV C-C, C=C, C-H 18.5 atom%

C (2) B. Energy 287.0 eV C-O 2.8 atom%

c (3) B. Energy 289.4 eV carbonate 11.2 atom%

These results support the hypothesis that the $Si(CH_3)_3$ groups are indeed bonded to the calcium atoms through the hydroxyl oxygen atom to produce a surface comprising —Ca-O-$Si(CH_3)_3$ moieties dispersed among —Ca-OH moieties. The chlorine detected is probably due to unreacted calcium chloride starting material, and the large carbonate presence will be due to the sample standing under atmospheric conditions for a considerable time prior to running the spectrum.

The spectra for samples 82 and 82X, shown in Figure 8.29, exhibit a single peak in the silicon binding energy region at 104.9 eV, whereas 82X exhibits multiple peaks in the binding energy region 99.4 - 106.3 eV which indicates a number of different environments inhabited by the silicon atoms. These different environments are most likely to be associated with $Si(CH_3)_3$ groups of the starting material, unreacted 3-aminopropyltriethoxysilane, unreacted intermediate aminopropyldiethoxysilyl groups and 82X.

Careful inspection of the C1s peak produced by 82X reveals at least five shoulders, suggesting the presence of at least 6 states of carbon. This number of states would be consistent with a composite containing not only the proposed nitrobenzamide moiety, but also the $Si(CH_3)_3$ moiety present in the starting material. Chemical analysis of 82X gave 10.65% C, 2.40% H, and 1.51% N. The H:C ratio was thus higher than that required for the proposed nitrobenzamide product. This is probably due to the presence of $Si(CH_3)_3$ groups from reaction with hexamethyl disilazane, or to the presence of small amounts of water adsorbed on the surface. The N:C ratio, however, was that expected for the nitrobenzamide composite.

8.1.4 Atomic Absorption

Atomic absorption was carried out on precipitated calcium hydroxides that had been reacted with a silylating agent under differing conditions. The results summarised in Table 8.1 clearly show that silylation effectively only occurs when the silylating agent is present in the precipitation medium during the precipitation reaction.

8.1.5 Thermal Analysis

Thermal analysis was carried out on a typical non-silylated sample (no.70), a typical silylated sample (no.74, containing 3.4 wt% Si), and the organic composite (82X) and its silylated starting material (no.82).

The thermogravimetric analysis (TGA) plot of the non-silylated sample in air, shown in Figure 8.30, clearly exhibits a major weight loss in the range 638 - 713K relating to decomposition of $Ca(OH)_2$ to CaO, with a further significant weight loss in the range 999 - 1196K relating to decomposition of carbonate. In comparison the TGA plot for the silylated sample, shown in Figure 8.31, exhibits a first major weight loss in the range 801 - 971K relating to decomposition to CaO, with a further significant weight loss in the range 1025 - 1183K relating to decomposition of carbonate. It is therefore

evident that the surface silylation of calcium hydroxide crystals results in stabilisation, in terms of temperature at which decomposition to CaO occurs. The temperature range over which carbonate is decomposed is unaffected. Sample 82 decomposed at 907 - 918K, typical for a silylated calcium hydroxide material, and 82X produced from sample 82 decomposed at 1013K, but this was preceded by the exothermic decomposition of the organic component at 533K. In a nitrogen atmosphere, the differential thermal analysis (DTA) plot, shown in Figure 8.32, shows decomposition of the organic component in 82X taking place at a markedly higher temperature, but decomposition to CaO occurring at a slightly lower temperature. Exothermic decomposition of the organic component occurred at 679K, albeit with a lower evolution of heat, and decomposition to CaO occurred at 971K. This result can be explained by considering the decomposition of the organic component. In air, combustion of the organic component would result in the carbonising of the surface, which together with some surface carbonation would protect the underlying OH groups, resulting in an increase in decomposition temperature. When heated in nitrogen, the organic component would require a higher temperature to initiate decomposition, which in the absence of oxygen, would carbonise the surface to a lesser extent. The absence of oxygen would also inhibit the carbonation of the surface, which, together with the reduced degree of carbonisation of the surface, would leave the crystals more susceptible to decomposition to CaO.

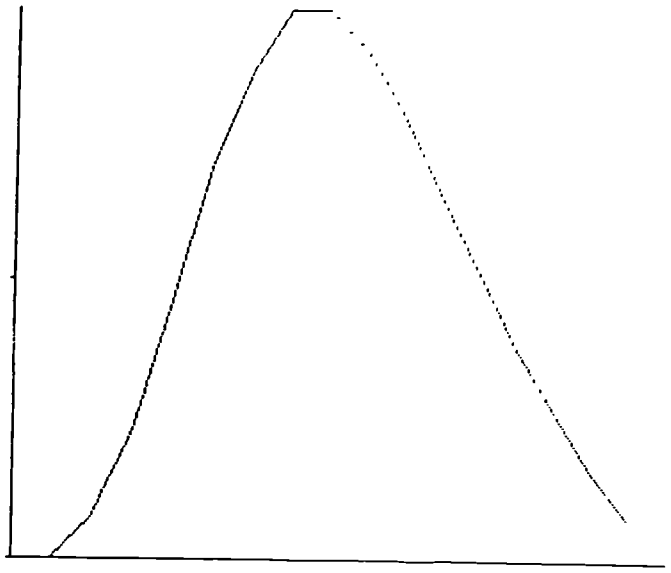

XPS Spectrum of Sample 82.

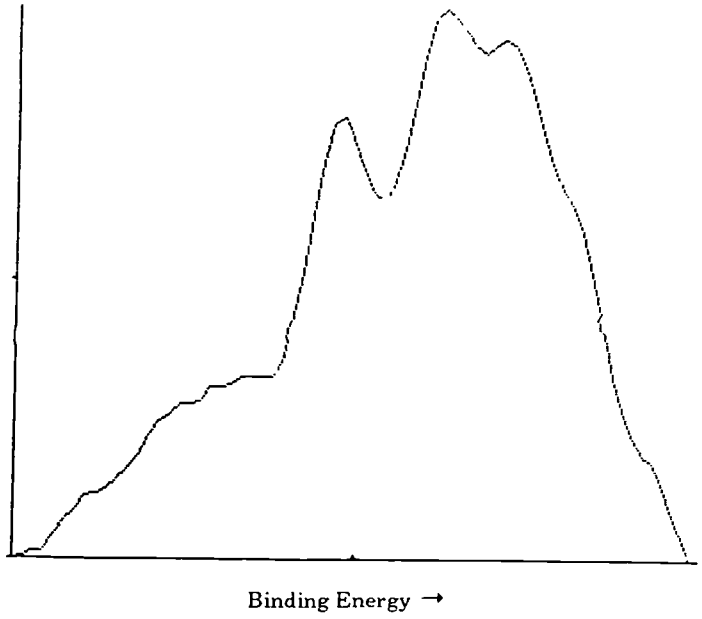

XPS Spectrum of the Organic Composite.

Figure 8.29 XPS Spectra of Sample 82 and of the Organic Composite Prepared from Sample 82.

Figure 8.30 TGA for a non-silanated sample (no.67).

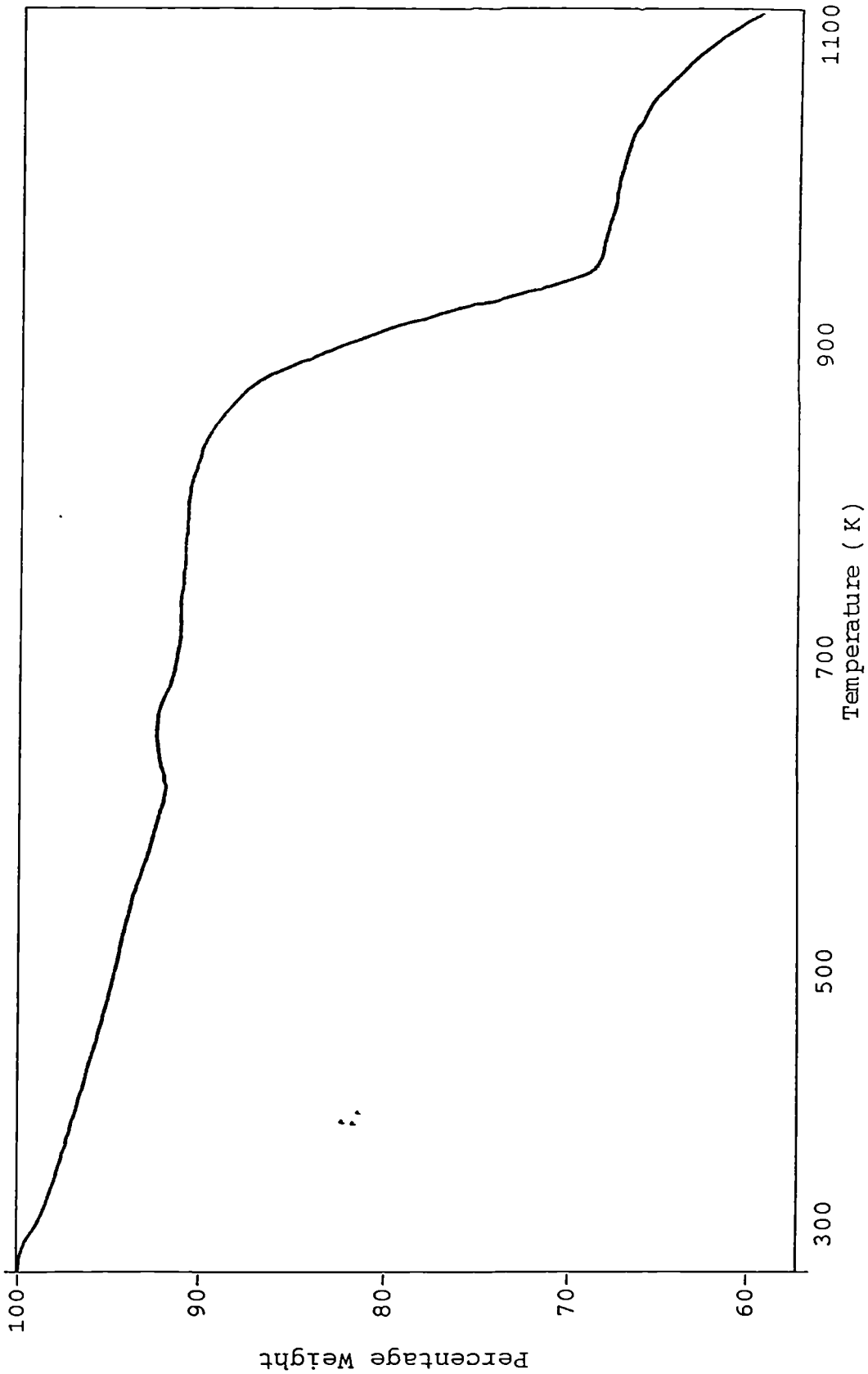

Figure 8.31 TGA for a silanated sample (no. 74).

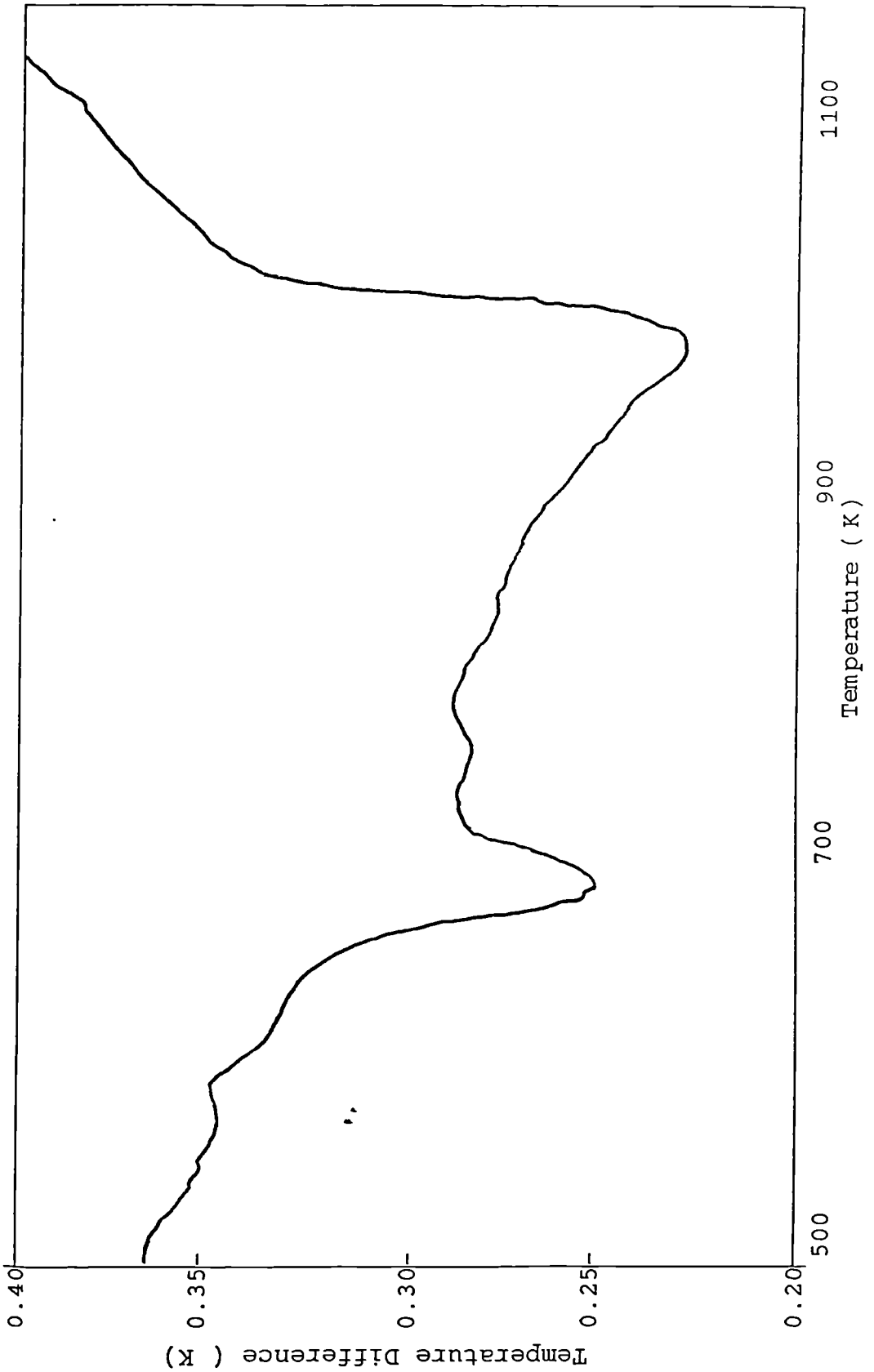

Figure 8.32 DTA for the organic composite (no. 82X).

Silylation Process	Silylating Agent	% Si w/w Introduced
Pre-precipitated $Ca(OH)_2$ obtained from NaOH and $CaCl_2$, suspended in acetone/silylating agent mixture for 2 hours.	Hexamethyldisiloxane	0.021
Pre-precipitated $Ca(OH)_2$ obtained from NaOH and $CaCl_2$ suspended in acetone/silylating agent mixture for 2 hours.	Hexamethyldisilazane	0.024
Pre-precipitated $Ca(OH)_2$ obtained from NaOH and a mixture of $CaCl_2$ and $Ca(OOCC_2H_5)_2$, suspended in acetone/silylating agent mixture for 2 hours.	Hexamethyldisilazane	0.020
$Ca(OH)_2$ precipitated from NaOH and a mixture of $CaCl_2$, $Ca(OOCC_2H_5)_2$, and silylating agent.	Hexamethyldisilazane	3.4
$Ca(OH)_2$ precipitated from NaOH and a mixture of $CaCl_2$, $Ca(OOCC_2H_5)_2$, and silylating agent.	Tetraethyl silicate	none detectable

Table 8.1 Quantities of Silicon Introduced by silylation

9. CONCLUSIONS

Scanning electron microscopy has clearly shown the variety of morphologies of calcium hydroxide that can be obtained by varying the precipitation conditions. The mechanisms operating in the precipitation liquor leading to the observed morphologies have been elucidated. An excess of hydroxyl ions present during precipitation has been shown to produce octahedral crystals, whereas an excess of chloride ions produces hexagonal prisms. Precipitation in ethanolic medium produces hexagonal platelets, and with the addition of carboxylate ions to the precipitation mixture large, sheet-like crystals are produced. Poisoning of the (0001) faces of the crystallites by carboxylate moieties has been shown to be the mechanism by which plate-like and sheet-like crystals are formed. FTIR spectroscopy has confirmed that the carboxylate moieties are predominantly on the surface and that the greater the length of the carbon chain of the moiety, the greater was the "sheeting" effect. Experimental work has shown that for a range of carboxylate group concentrations, the "sheeting" effect is similar, supporting the postulate that poisoning of the (0001) faces is occurring. TEM in the diffraction mode confirmed that poisoning occurs on the (0001) faces.

It was found that the surface of the platelets and sheet-like crystals can be stabilised by silylation reactions. The introduction of $Si(CH_3)_3$ groups into the surface resulted from precipitation of calcium hydroxide in the presence of 1,1,1,3,3,3 - hexamethyl-disilazane. FTIR spectroscopy and XPS confirmed the presence of surface $Si(CH_3)_3$ groups.

The greater stability of the silylated calcium hydroxide was demonstrated using thermogravimetric analysis, where non-silylated calcium hydroxide decomposed at ~ 693K compared to ~ 713K for the silylated samples.

A novel calcium hydroxide composite has been prepared from a stabilised calcium hydroxide by reaction with 3 - aminoproyltriethoxy silane, followed by reaction with

4 - nitrobenzamide. The presence of the large organic moiety on the surface of the sample was confirmed by UV, FTIR, XPS, TGA and by chemical analysis for C, H and N.

Nitrogen adsorption has shown the crystals to be non-porous. Large crystals of calcium hydroxide gave Type VI isotherms, indicating homogeneous surfaces, whereas the plate-like samples gave reversible Type II isotherms, and the sheet-like samples gave Type II isotherms exhibiting various degrees of hysteresis, indicating presence of porosity. Repeating the measurements eliminated the hysteresis loops, thus the effect was shown to be due to capillary condensation in the voids and interstices of agglomerates.

Water isotherms of the non-silylated samples were of Type II character with very broad hysteresis loops which have been shown to be due to rehydration and capillary condensation. Outgassing or heating the sample to above its decomposition temperature results in a Type I isotherm typical of a chemisorption process related to rehydroxylation. Silylated samples, after heating at 423K or higher, but below the decomposition temperature, exhibited Type II adsorption isotherms with considerably reduced water uptake, or Type III adsorption isotherms indicating an increase in hydrophobicity which can be related to the introduction of hydrophobic $Si(CH_3)_3$ groups onto the surface.

To summarise, it has been found that the morphology of calcium hydroxide crystal precipitates can be modified by variation of the precipitation conditions, and the sheet-like forms can be stabilised by silylation of the surface. The increased thermal and chemical stability of the sheet-like materials permit the preparation of calcium hydroxide organic composites by reaction of the surface OH groups with acidic organic groups.

REFERENCES

1. Bunn, C. W., et al. ,Proc. Roy Soc. (London) A 151,141 (1935)
2. Harrington, E. A., Am J Sci 13,467 (1927)
3. Levi, G. R., Giorn. chim.ind.ed.appl., 333 (1924)
4. Natta, G., Gazz. chim. Ital., 58, 344 (1928)
5. Natta, G., et al. Gazz. chim. Ital., 58, 597 (1928)
6. Petch, H. E., et al., J Opt. Soc. Am., 44, 744 (1954)
7. Petch, H. E., Phys. Rev., 99, 1635 (1955)
8. Petch, H. E., Can J Phys., 35, 983 (1957)
9. Petch, H. E., Acta Cryst., 10, 779 (1957)
10. Petch, H. E., Acta Cryst., 14, 950 (1961)
11. Rejna, A., Atti accad. Lincei (6), 5, 1008 (1927)
12. Rumpf, E., Ann Physik., 87, 595 (1928)
13. Tilley,C. E., Mineral. Mag., 23, 419 (1933)
14. Busing, W. R., et al., J Chem. Phys., 26, 563 (1957)
15. Glemser, O., Z. anorg. u. allgem. Chem.,283,111 (1956)
16. Hartert, E., et al., Naturwissenschaften, 40, 199 (1953)
17. v. Glasenapp, M., Kolloid-Z., 31, 195 (1922)
18. Nogareda, C., Rev. acad cienc. exact. fis-quim. y.nat. Madrid, 26, 315 (1931)
19. Selivanoff, F., J Russ. Phys. Chem. Soc., 44, 1797 (1912)
20. Yasuę T., Kojima Y., and Arai Y., Gypsum & Lime, 206 (1987)
21. Hedrin, R., Svenska Forskningst. Cement Betong Vid Kgl. Tek. Hogskol Stockholm Handl. No.33 (1962)
22. Tadros, M. E., et al., J Colloid Interface Sci., 55,20 (1976)
23. Tomazic, B., et al., J Cryst. Growth, 75, 329 (1986)
24. Tomazic, B., et al., J Cryst. Growth, 75, 339 (1986)
25. Ballard, D. G. H., et al., J Mat. Sci., 18, 545 (1983)
26. Taylor, H. F. W., Chem. Ind., 620 (1981)
27. Birchall, J. D., et al., Proc. Brit. Ceram. Soc., 67, 48 (1984)
28. Gimblett, F. G. R., et al., VII Congress, Chemistry of Cement, Paris, II-225 (1980)
29. Qu Wu, Z., et al., J Amer. Ceram. Soc., *35, 305 (1984)*
30. Jackson K.A., Liquid metals and Solidification, Am. Soc. for Metals (1958)
31. Tempkin D.E., Crystallisation process, Consultant Bureau, New York (1964)
32. Davey R.J., Industrial Crystallisation 78, North-Holland, Amsterdam (1979)
33. Davey R.J., Current Topics in Material Science, 8, 429 (1982)
34. Human H.J., et al., Paperat ICCG 6, Moscow (1980)
35. Bourne J.R., et al., J Cryst. Growth, 34, 221 (1976)
36. Bourne J.R., J Cryst. Growth, 34, 230 (1976)
37. Bourne J.R., et al., J Cryst. Growth, 39, 267 (1977)
38. Ohara M, et al., Modelling Crystal Growth Rates from Solution, Prentice - Hall Inc. (1973)
39. Hillig W.B., Acta Met, 14, 1968 (1966)
40. Frank F.C., Disc. Faraday. Soc., 5, 48 (1949)
41. Burton W.K., et al., Phil. Trans. Roy. Soc., 243, 299 (1951)
42. Bennema P., et al., Crystal Growth an Introduction, North - Holland, Amsterdam (1973)
43. Jagannathan R, et al., J Cryst. Growth, 51, 601 (1981)
44. Jagannathan R, et al., Photogr. Sci. Eng., 25, 61 (1982)
45. Janssen van Rosmalen R., et al., J Cryst. Growth, 29, 342 (1975)
46. Tomazic B., Mohanty R., Tadros M. and Estrin J., J. Cryst. Growth, 75,339 - 347 (1986)
47. Berglund K.A. and Larson M.A., Growth of Contact Nuclei of Citric Acid Monohydrate, Proceedings IV (1981) 72)
48. Tomazic B., Mohanty R., Tadros M. and Estrin J., J. Cryst. Growth, 75,339 - 347 (1986)
49. Shinnar R., J. Fluid Mech., 10, 259 (1961)
50. Harris M.R. & Sing K.S.W., J. Appl. Chem. 5, 223(1955)
51. Baker F.S., Ph.D Thesis, Brunel University (1974)

52. Carrott P.J.M., Ph.D. Thesis, Brunel University (1979)
53. Gregg S.J. and Sing K.S.W., "Adsorption Surface Area and Porosity", Academic Press (1967)
54. McLeod A I , Ph.D. Thesis, Brunel University (1979)
55. McBain J.W. and Bakr A.M., J. Am. Chem. Soc., 48, 690 (1926)
56. Handbook of Chemistry and Physics, Ed. R C Weast, CRC Press, 57th Edition (1976)
57. Sing K.S.W., Everett D.H., Haul R.A.W., Moscou L., Pierotti R.A., Roquerol J., and Siemieniewska T., Pure & Appl. Chem. 57, 603 (1985)
58. London F., Z. Physik, 63, 245 (1930)
59. Barrer R.M., J. Coll. Interface Sci., 1, 3 (1967)
60. Sing K.S.W., " Colloid Science", Chem. Soc. Spec. Per. Rep., 1, 1 (1973)
61. Brunauer L.S., Deming L.S., Deming W.S. and Teller E., J. Am. Chem. Soc., 62, 1723 (1940)
62. Langmuir, I., J. Am. Chem. Soc. , 38, 2221 (1916)
63. Langmuir, I.,J. Am. Chem. Soc., 40, 1361 (1918)
64. Dubinin M. M. and Zaverina E.D., Zhur. Fiz. Khim., 23, 1129 (1949)
65. Gregg S.J. and Sing K.S.W., " Surface and Colloid Science", Matijevic E. (Ed.), John Wiley & Sons, London (1976)
67. Freeman J.J. and McLeod A I , Fuel., 72, 619 (1983)
68. Branauer S., Emmett P.H., and Teller E., J. Am. Chem. Soc., 60, 309 (1938)
69. Cook M. A., J. Am. Chem. Soc., 70, 2925 (1948)
70. Singleton J.H. and Halsey G.D., Can. J. Chem., 33, 184 (1955)
71. Robens E., "Surface Area Determination", Everett D.H. and Ottewill R.H. (Eds.) Butterworths, London (1970)
72. Roquerol J., Roquerol F., Peres C., Grillet Y., Boudellal M., "Characterisation of Porous Solids" Soc. Chem. Ind., London, p. 107 (1979)
73. Lord Kelvin, Phil. Mag., 42, 448 (1871)
74. Defay R., Prigogine I, Bellemans A.,Everett D.H., "Surface Tension and Adsorption", Longmans, London (1966)
75. Harris M. R., *Chem. Ind., 26, 9 (1965)*
76. Frenkel J.,"Kinetic Theory of Gases", Oxford University Press (1946)
77. Halsey G., J. Chem. Phys., *16, 931 (1948)*
78. Hill T. L.,"Advances in Catalysis", IV, Academic Press, New York (1952)
79. Pierce C., J. Phys. Chem., 63, 1076 (1959)
80. idem 64, 1184 (1960)
81. Payne D. A., and Sing K. S. W., Chem. & Ind., 918 (1969)
82. Carrott P. J. M. McLeod A., Sing K. S. W., "Adsorption at the Gas - Solid and *Liquid - Solid* Interface", Rouquerol J. and Sing K. S. W. (Eds), Elsevier, Amsterdam (1982)
83. Zettlemoyer A. C., J. Coll. Interface Sci., 28, 343 (1968)
84. Young D. M. & Crowell A. D., "Physical Adsorption of Gases", Butterworth, London (1962)
85. Sing K. S. W. in "Surface Area Determination",Eds. Everett D. H. & Ottewill R. H., Butterworths, London (1970) p.25
86. Sing K. S. W., Chem. Ind., 829 (1967), 1520 (1968)
87. Carruthers J. D., et al., Chem. Ind. 1772 (1968)
88. Bhambhani M. R., Cutting P. A., Sing K. S. W. & Turk D. H., J. Coll. Interface Sci., 38, 109 (1972)
89. Carruthers J. D., Payne D. A., Sing K. S. W. and Stryker L. J., J. Coll. Interface Sci., 36, 205 (1971)
90. Mikhail R. Sh., Brunauer S. & Bodor E. E., J. Coll. Interface Sci., 26, 45 (1968), 26, 54 (1968)
91. Parfitt G. D., Sing K. S. W. & Urwin D., J. Coll. Interface Sci., 53, 187 (1975)
92. Brown C. E. & Hall P. G., Trans. Faraday Soc., 67, 3558 (1971)
93. Gregg S. J., J. Chem. Soc., Chem. Comm., 699 (1975)
94. Dubinin M. M., Chem. Rev., 60, 235 (1960)
95. Polanyi M., "The Adsorption of Gases on Solids", Disc. Faraday Soc. 316 (1932)
96. Dubinin M. M., Astakhov V. A., Adv. Chem. Ser., 102, 69 (1971)

97. Dubinin M. M., "Chemistry and Physics of Carbon", Walker P. L., (Ed), Arnold, London, 2, 51 (1966)
98. Marsh H., Rand B., J. Coll. Interface Sci., 33, 1 (1970)
99. Dandy A. J., J. Phys. Chem., 72,334 (1968)
100. Kaganer M. G., Zh. Fiz. Khim., 33, 2202 (1959)
101. Krishnan, K., and Ferraro, R., "Techniques Used in Fourier Transform Infrared Spectroscopy
102. Brunauer, S., Deming, L. S., Deming, W. S., and Teller, E., J. Am. Chem. Soc., 62, 1723 (1940)
103. Rouquerol j., Partyka, S., and Rouquerol, F.,J. Chem Soc., Faraday Trans. I, 73, 306 (1977)
104. Rouquerol, J., Rouquerol, F., Pérès, C., Grillet, Y., and Boudellal, M., in "Characterisation of Porous Solids", Proc. Int. Symp. 1978 (eds. Gregg, S. J., Sing K. S. W., and Stoeckli, H. F.), p. 107, Soc. Chem. Ind., London (1979)
105. Grillet, Y., Rouquerol, F., and Rouquerol, J., J. Colloid Interface Sci., 70, 239 (1979)
106. Thomy, A. and Duval, X., J. Chim. Phys., 67,1101 (1970)
107. Nicholson, D., and Sing, K. S. W., in "Colloid Science" (ed. Everett, D. H.), Vol. 3, p. 6, Specialist Periodical Report, Chemical Society, London (1979)
108. Shaw, C. G. and Fain, S. C., Surface Sci., 83, 1 (1979)
109. Zettlemoyer, A.C., J. Colloid Interface Sci. 75, 13 (1980)
110. Dean, C.R.S., Mather, R.R., Segal, D.L. and Sing, K.S.W., in S.J. Gregg, K.S.W. Sing and F.W. Stoeckli (Eds.), Proc. Symp. Characterisation of Porous solids, Neuchatel, July 9-12, 1978, Soc. Chem. Ind., London 1979, pp.359-367
111. Klemperer, D. F., in "Surface Area Determination", p.55, Butterworths, London (1970)
112. Gottwald, B. A., in "Surface Area Determination", p.59, Butterworths, London (1970)
113. Granville, A., Hall, P. G. and Hope, C. J., Chem. and Ind., p.435 (1970)
114. Walker, P. L. and Patel, R. L., Fuel, 49, 91 (1970)
115. Pomeshchikov, V. D. and Pozdeev, V. V., Kinetika i Kataliz., 12, 794 (1971)
116. Avgul, N. N., Bezus, A. G., Dobrova, E. S. and Kiselev, A. V., J. Colloid Interface Sci., 42, 486 (1973)
117. Kiselev, A. V., in "The Structure and Properties of Porous Materials", (D. H. Everett and F. S. Stone, Eds.), p.195 Butterworths, London, 1958
118. Young, G. J., J. Colloid Sci., 13, 67 (1958)
119. Baker, F. S. and Sing, K. S. W., J. Colloid and Interface Sci., 55, 3 (1976)
120. Dzhigit, O. M., Kiselev, A. V., and Muttik, G. G., Kolloid Zh., 23, 461 (1961)
121. Rahman, A. A. and Sing, K. S. W., Thermochimica Acta, 277, (1979)
122. Bye, G. C. and Sing, K. S. W., in "Particle Growth in Suspension", SCI, monograph no. 38, p. 29, Ed. A. L. Smith, Academic Press (1973)
123. Kiselev, A. V., J. Colloid Interface Sci., 28, 430 (1968)
124. Kiselev, A. V., Quart. Rev. Chem. Soc., XV, 116 (1961)
125. Carrott, P. J. M., McLeod, A. I. and Sing, K. S. W., Stud. Surf. Sci. Catal., 10, 403 (1982)
126. Bye, G. C. and Sing, K. S. W., in "Particle Growth in Suspension", SCI, monograph no. 38, p. 29, Ed. A. L. Smith, Academic Press (1973)
.End Table R.

APPENDIX A Precipitation Data for all Samples

Sample	Sodium Hydroxide		Calcium Chloride		Calcium Acetate		Rate of addn of Ca salts ml/min	Vol. of water placed in reaction vessel /ml	Vol. of EtOH placed in reaction vessel /ml	Agitation
	Vol/ml	Concn/M	Vol/ml	Concn/M	Vol/ml	Concn/M				
1	25.0	0.75	25.0	0.75	-	-	1.0	25	-	N
2	25.0	0.75	25.0	0.75	-	-	1.0	25	-	Y
3	25.0	0.75	25.0	0.75	-	-	1.0	50	-	N
4	25.0	0.75	25.0	0.75	-	-	1.0	50	-	Y
5	25.0	0.75	25.0	0.75	-	-	1.0	75	-	N
6	25.0	0.75	25.0	0.75	-	-	1.0	75	-	Y
7	25.0	0.75	25.0	0.75	-	-	1.0	100	-	N
8	25.0	0.75	25.0	0.75	-	-	1.0	100	-	Y
9	25.0	0.75	25.0	0.75	-	-	6.0	100	-	Y
10	25.0	0.75	25.0	0.75	-	-	6.0	75	-	Y
11	25.0	0.75	25.0	0.75	-	-	6.0	50	-	Y
12	25.0	0.75	25.0	0.75	-	-	6.0	25	-	Y
13	25.0	0.75	25.0	0.75	-	-	6.0	-	-	Y
14	25.0	0.75	25.0	0.75	-	-	2.0	50	-	Y
15	25.0	0.75	25.0	0.75	-	-	0.25	50	-	Y
16	25.0	0.75	25.0	0.75	-	-	*500.0	50	-	Y
17	25.0	0.75	25.0	0.75	-	-	0.25	50	-	Y
18	25.0	0.75	25.0	0.75	-	-	0.25	-	50	Y

APPENDIX A (continued)

Sample	Sodium Hydroxide		Calcium Chloride		Calcium Acetate		Rate of addn of Ca salts ml/min	Vol. of water placed in reaction vessel /ml	Vol. of EtOH placed in reaction vessel /ml	Agitation
	Vol/ml	Concn/M	Vol/ml	Concn/M	Vol/ml	Concn/M				
19	25.0	1.5	25.0	0.75	-	-	6.0	100	-	Y
20	25.0	1.5	25.0	0.75	-	-	6.0	75	-	Y
21	25.0	1.5	25.0	0.75	-	-	6.0	50	-	Y
22	25.0	1.5	25.0	0.75	-	-	6.0	25	-	Y
23	25.0	1.5	25.0	0.75	-	-	6.0	-	-	Y
24	25.0	1.5	25.0	0.75	-	-	3.0	50	-	Y
25	25.0	1.5	25.0	0.75	-	-	2.0	50	-	Y
26	25.0	1.5	25.0	0.75	-	-	*500.0	50	-	Y
27	25.0	1.5	25.0	0.75	-	-	3.0	-	50	Y
28	25.0	1.5	25.0	0.75	-	-	6.0	-	50	N
29	25.0	1.5	25.0	0.75	-	-	6.0	-	-	N
30	25.0	1.5	25.0	0.75	-	-	6.0	25	-	N
31	25.0	1.5	25.0	0.75	-	-	6.0	50	-	N
32	25.0	1.5	25.0	0.75	-	-	6.0	75	-	N
33	25.0	1.5	25.0	0.75	-	-	6.0	100	-	N
x34	20.0	1.0	25.0	1.0	-	-	2.0	-	100	Y
x35	11.0	1.0	25.0	1.0	-	-	3.0	-	100	Y
x36	25.0	1.0	12.5	1.0	-	-	3.0	-	100	Y

APPENDIX A (continued)

Sample	Sodium Hydroxide Vol/ml	Sodium Hydroxide Concn/M	Calcium Chloride Vol/ml	Calcium Chloride Concn/M	Calcium Acetate Vol/ml	Calcium Acetate Concn/M	Rate of addn of Ca salts ml/min	Vol. of water placed in reaction vessel /ml	Vol. of EtOH placed in reaction vessel /ml	Agitation
x37	25.0	1.0	5.0	1.0	-	-	3.0	-	100	Y
x38	25.0	1.0	2.5	1.0	-	-	3.0	-	100	Y
39	25.0	1.0	-	-	25.0	1.0	6.0	100	-	Y
40	50.0	1.0	-	-	25.0	1.0	6.0	75	-	Y
41	50.0	1.0	-	-	10.0	1.0	6.0	90	-	Y
42	25.0	1.0	-	-	25.0	1.0	6.0	-	50	Y
43	25.0	1.0	12.5	1.0	12.5	1.0	6.0	100	-	Y
44	25.0	1.0	5.0	1.0	20.0	1.0	6.0	100	-	Y
45	25.0	1.0	20.0	1.0	5.0	1.0	6.0	100	-	Y
46	25.0	1.0	12.5	1.0	12.5	1.0	6.0	-	50	Y
47	25.0	1.0	5.0	1.0	20.0	1.0	6.0	-	50	Y
48	25.0	1.0	20.0	1.0	5.0	1.0	6.0	-	50	Y
49	25.0	1.0	12.5	1.0	12.5	1.0	6.0	45	5	Y
50	25.0	1.0	12.5	1.0	12.5	1.0	6.0	40	10	Y
51	25.0	1.0	12.5	1.0	12.5	1.0	6.0	30	20	Y
52	25.0	1.0	12.5	1.0	12.5	1.0	6.0	20	30	Y
53	25.0	1.0	12.5	1.0	12.5	1.0	6.0	10	40	Y
**54	25.0	1.0	12.5	1.0	12.5	1.0	6.0	-	50	Y
55	25.0	1.0	12.5	1.0	12.5	1.0	6.0	-	50	Y

APPENDIX A (continued)

Sample	Sodium Hydroxide Vol/ml	Sodium Hydroxide Concn/M	Calcium Chloride Vol/ml	Calcium Chloride Concn/M	Calcium Acetate Vol/ml	Calcium Acetate Concn/M	Rate of addn of Ca salts ml/min	Vol. of water placed in reaction vessel /ml	Vol. of EtOH placed in reaction vessel /ml	Agitation
56	25.0	1.0	12.5	1.0	12.5	1.0	1.0	-	50	Y
57	25.0	1.0	12.5	1.0	12.5	1.0	0.2	-	50	Y
58	25.0	1.0	12.5	1.0	12.5	1.0	53.0	-	50	Y
59	25.0	1.0	12.5	1.0	12.5	1.0	2.5	-	50	Y
60	25.0	1.0	12.5	1.0	12.5	1.0	xx53.0	-	50	Y
61	25.0	1.0	12.5	1.0	12.5	1.0	xx2.5	-	50	Y
62	25.0	1.0	12.5	1.0	12.5	1.0	xx0.2	-	50	Y
63	25.0	1.0	12.5	1.0	12.5	1.0	xx1.0	-	50	Y
64	25.0	1.0	12.5	1.0	12.5	1.0	*0.2	-	50	Y
65	25.0	1.0	12.5	1.0	12.5	1.0	*1.0	-	50	Y
66	25.0	1.0	12.5	1.0	12.5	1.0	*2.5	-	50	Y
67	25.0	1.0	12.5	1.0	12.5	1.0	*53.0	-	50	Y
68	250.0	1.0	125.0	1.0	+125.0	1.0	*500.0	-	250	Y
++69	250.0	1.0	125.0	1.0	+125.0	1.0	*500.0	-	250	Y

APPENDIX A (continued)

Sample	Sodium Hydroxide		Calcium Chloride		Calcium Acetate		Rate of addn of Ca salts ml/min	Vol. of water placed in reaction vessel /ml	Vol. of EtOH placed in reaction vessel /ml	Agitation
	Vol/ml	Concn/M	Vol/ml	Concn/M	Vol/ml	Concn/M				
70	50.0	1.0	25.0	1.0	-	-	*500.0	-	50	Y
71	50.0	1.0	25.0	1.0	25.0	1.0	*500.0	-	50	Y
72	50.0	1.0	25.0	1.0	-	-	*500.0	-	50	Y
73	50.0	1.0	25.0	1.0	-	-	*500.0	-	50	Y
74	50.0	1.0	25.0	1.0	25.0	1.0	*500.0	-	100	Y
79	100.0	1.0	50.0	1.0	+5.0	1.0	*500.0	-	100	Y
80	100.0	1.0	50.0	1.0	+50.0	1.0	*500.0	-	100	Y
81	100.0	1.0	50.0	1.0	25.0	1.0	*500.0	-	100	Y
82	100.0	1.0	50.0	1.0	-	-	*500.0	-	100	Y

= Prepared in the presence of a silylating agent

+ = Calcium propionate used in place of calcium acetate

++ = Precipitate acetone washed

* = Precipitants added simultaneously

** = Precipitate washed in water

x = Precipitants as absolute ethanol solutions

xx = NaOH added to the Ca salts

Water Adsorption Data for Sample 79, Heated at 423K then Outgassed at 423K

Adsorption			Desorption		
Dose	P/P^o	V_{ads}	Dose	P/P^o	V_{ads}
1	0.0050	0.0000	1	0.4320	8.2750
2	0.0160	0.1970	2	0.3930	7.3890
3	0.0470	0.3940	3	0.3440	6.4030
4	0.0830	1.0840	4	0.2910	5.6150
5	0.2600	3.9410	5	0.2400	5.6150
6	0.2870	4.2360	6	0.1810	4.9260
7	0.3290	4.7290	7	0.1230	4.4330
8	0.3770	6.4040	8	0.0800	3.7430
9	0.4140	7.1920	9	0.0390	3.5470
10	0.4830	9.1620	10	0.0004	1.2810

Water Adsorption Data for Sample 79, Heated at 623K then Outgassed at 423K

Adsorption			Desorption		
Dose	p/p^o	V_{ads}	Dose	p/p^o	V_{ads}
1	0.0040	0.5830	1	0.4840	15.0520
2	0.0160	0.8740	2	0.4470	13.5950
3	0.0380	1.1650	3	0.4070	11.9440
4	0.0810	1.6510	4	0.3620	10.5850
5	0.1260	1.9420	5	0.3180	9.6140
6	0.1620	2.4280	6	0.2700	9.6140
7	0.2050	2.7190	7	0.2140	8.6420
8	0.2480	3.8840	8	0.1520	8.1570
9	0.3580	5.3410	9	0.0910	7.1860
10	0.5450	18.0610	10	0.0370	6.2150

Water Adsorption Data for Sample 79, Heated at 773K then Outgassed at 423K

Adsorption			Desorption		
Dose	P/P^o	V_{ads}	Dose	P/P^o	V_{ads}
1	0.0008	1.9490	1	0.3840	147.0000
2	0.0030	4.5480	2	0.3010	145.0000
3	0.0110	7.7960	3	0.1810	143.0000
4	0.0150	17.6490	4	0.0500	141.0000
5	0.0350	66.0480	5	0.0008	135.0000
6	0.0400	94.5200			
7	0.1080	124.0000			
8	0.2180	140.0000			
9	0.2930	143.0000			
10	0.3820	145.0000			
11	0.4340	147.0000			
12	0.4650	149.0000			

Water Adsorption Data for Sample 80, Heated at 473K then Outgassed at 423K

Adsorption			Desorption		
Dose	p/p^o	V_{ads}	Dose	p/p^o	V_{ads}
1	0.0060	0.5040	1	0.4720	16.2130
2	0.0230	1.1080	2	0.4250	15.3070
3	0.0440	1.6110	3	0.3800	14.7030
4	0.0830	2.8200	4	0.3350	14.6020
5	0.1280	3.4240	5	0.2950	13.9970
6	0.1670	4.6320	6	0.2530	13.3940
7	0.2150	6.3440	7	0.2080	12.6880
8	0.2530	7.0490	8	0.1710	12.2860
9	0.2910	7.8550	9	0.1480	11.5810
10	0.3320	8.7610	10	0.0720	10.3720
11	0.3790	10.1710	11	0.0270	9.7680
12	0.4140	11.0770	12	0.0008	7.1500
13	0.4560	12.5880			
14	0.4750	15.5080			
15	0.5120	16.2130			
16	0.5490	18.3280			

Water Adsorption Data for Sample 80, Heated at 773K then Outgassed at 423K

Adsorption			Desorption		
Dose	p/p^o	V_{ads}	Dose	p/p^o	V_{ads}
1	0.0008	2.6970	1	0.4370	230.0000
2	0.0070	6.3590	2	0.3770	226.0000
3	0.0120	12.3320	3	0.3380	222.0000
4	0.0240	21.0030	4	0.2990	219.0000
5	0.0460	37.9590	5	0.2520	213.0000
6	0.0700	62.0460	6	0.1900	211.0000
7	0.1050	85.7460	7	0.1330	205.0000
8	0.1450	110.8000	8	0.0870	201.0000
9	0.2080	129.8000	9	0.0260	198.0000
10	0.2810	148.2000	10	0.0004	195.0000
11	0.3950	213.1000			
12	0.4420	219.5000			
13	0.4850	224.1000			
14	0.5190	229.1000			
15	0.5620	241.0000			
16	0.5690	246.0000			
17	0.5700	248.0000			

Water Adsorption Data for Sample 82, Outgassed at Room Temperature.

Adsorption			Desorption		
Dose	p/p^o	V_{ads}	Dose	p/p^o	V_{ads}
1	0.0020	1.7920	1	*0.5620*	*5.5250*
2	0.0110	3.4340	2	0.5100	*4.6290*
3	0.0400	5.2260	3	0.4470	3.9570
4	0.0920	7.0180	4	0.3620	3.2850
5	0.1440	8.2130	5	0.2850	1.7170
6	0.1940	9.4070	6	0.2110	1.7170
7	0.2440	10.5270	7	0.1350	1.0450
8	0.2990	11.4980	8	0.0580	0.4480
9	0.3500	11.6470			
10	*0.4010*	*12.3190*			
11	0.4500	*12.8420*			
12	0.5030	13.3640			
13	0.5490	13.7370			
14	0.5950	14.4090			
15	0.6220	14.4840			

Water Adsorption Data for Sample 82, Heated at 473K then Outgassed at 423K

Adsorption			Desorption		
Dose	p/p^o	V_{ads}	Dose	p/p^o	V_{ads}
1	0.0040	0.0740	1	0.5950	6.4030
2	0.0220	0.0740	2	0.4290	5.7330
3	0.0620	0.1490	3	0.3410	5.0630
4	0.1590	0.5210	4	0.2820	4.7650
5	0.2810	0.9680	5	0.1730	4.3180
6	0.3450	1.4150	6	0.0920	3.8720
7	0.4280	2.0100	7	0.0290	3.1270
8	0.5110	2.1590	8	0.0000	1.6380
9	0.5930	3.3510			
10	0.6670	4.7650			

Water Adsorption Data for Sample 82, Heated at 623K then Outgassed at 423K

Adsorption			Desorption		
Dose	p/p^o	V_{ads}	Dose	p/p^o	V_{ads}
1	0.0130	0.4440	1	0.4010	5.4070
2	0.0370	0.4440	2	0.3380	4.8160
3	0.1170	0.7410	3	0.2710	4.2220
4	0.2060	1.7780	4	0.1830	3.7780
5	0.1930	2.7410	5	0.0860	3.0370
6	0.2670	3.0370	6	0.0000	0.9620
7	0.3420	3.7040			
8	0.4060	4.2220			
9	0.4610	4.9630			
10	0.4870	6.2960			

APPENDIX D

Characterised Reflectance FTIR Spectra of Calcium Hydroxide

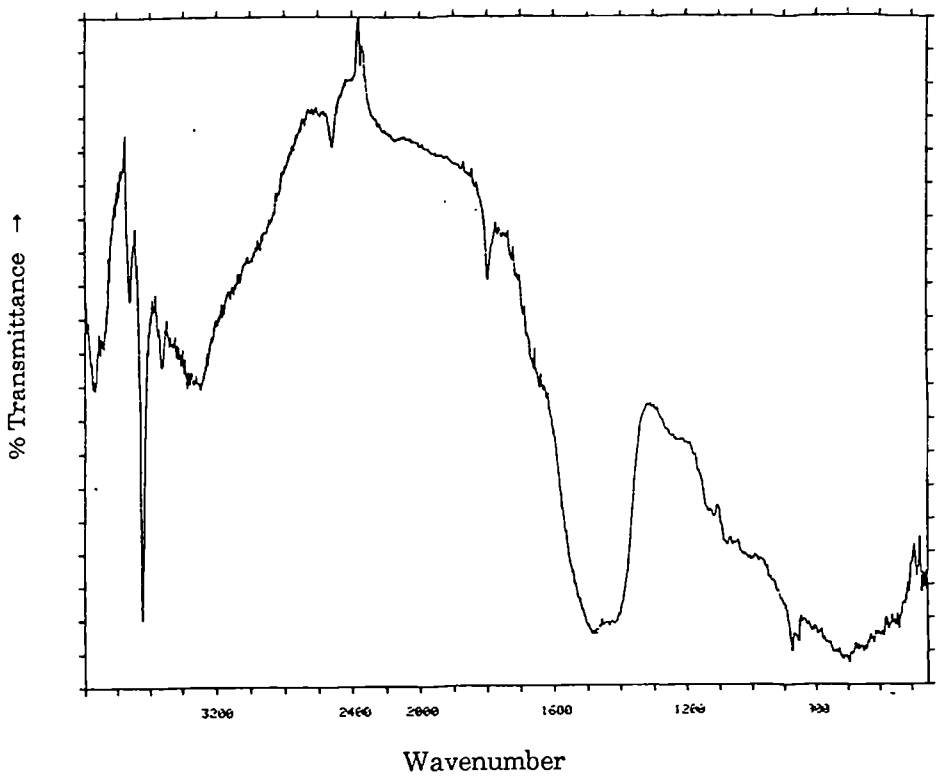

cm-1	Mode	cm-1	Mode
3645	O-H Stretch	1790	Carbonate
3520	Hydroxide	1490	CO_3^{2-} ν_3 & ν_4
3283	Water	876	CO_3^{2-} ν_2 (no ν_1)
2515	Carbonate	710	CO_3^{2-} ν_4
2350	Hydroxide	542	$Ca(OH)_2$

Characterised Transmission FTIR Spectra of Calcium Hydroxide

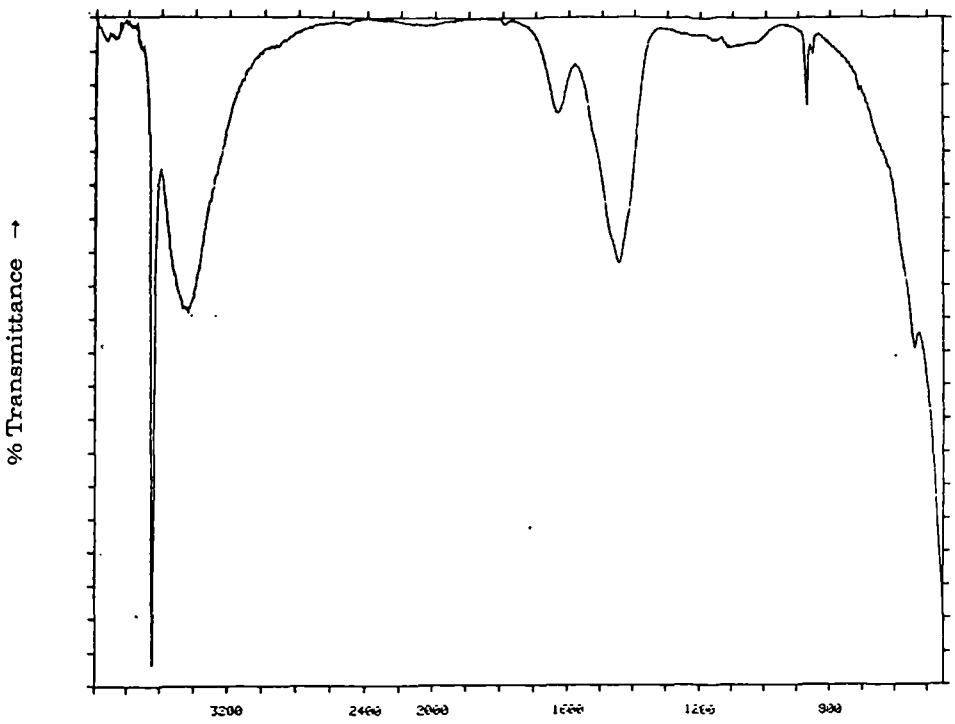

cm^{-1}	Mode
3645	O-H Stretch
3463	Water
1632	Carbonate
1457	CO_3^{2-} ν_3
867	Carbonate
841	Carbonate

APPENDIX E

Reaction Scheme for the Preparation of the Organic Composite

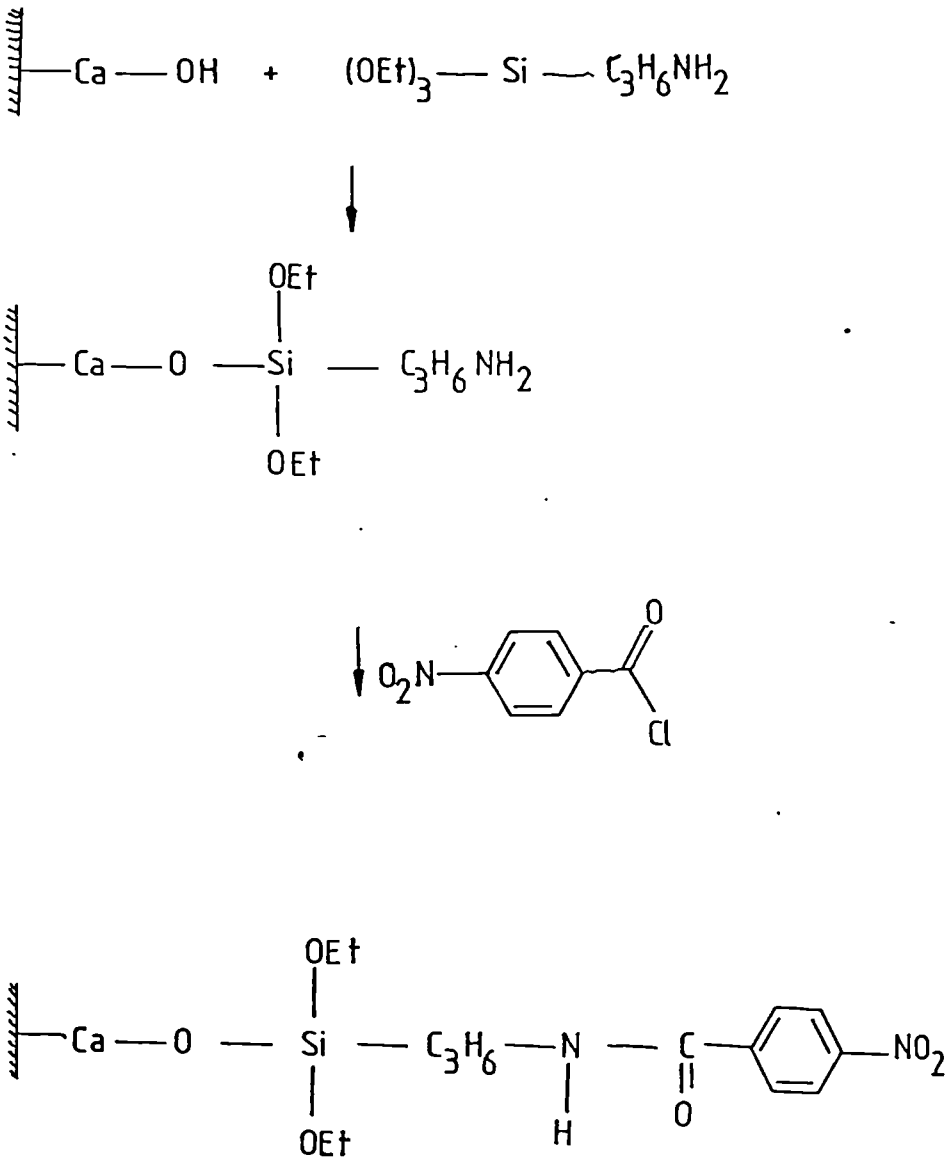

PLATE 1

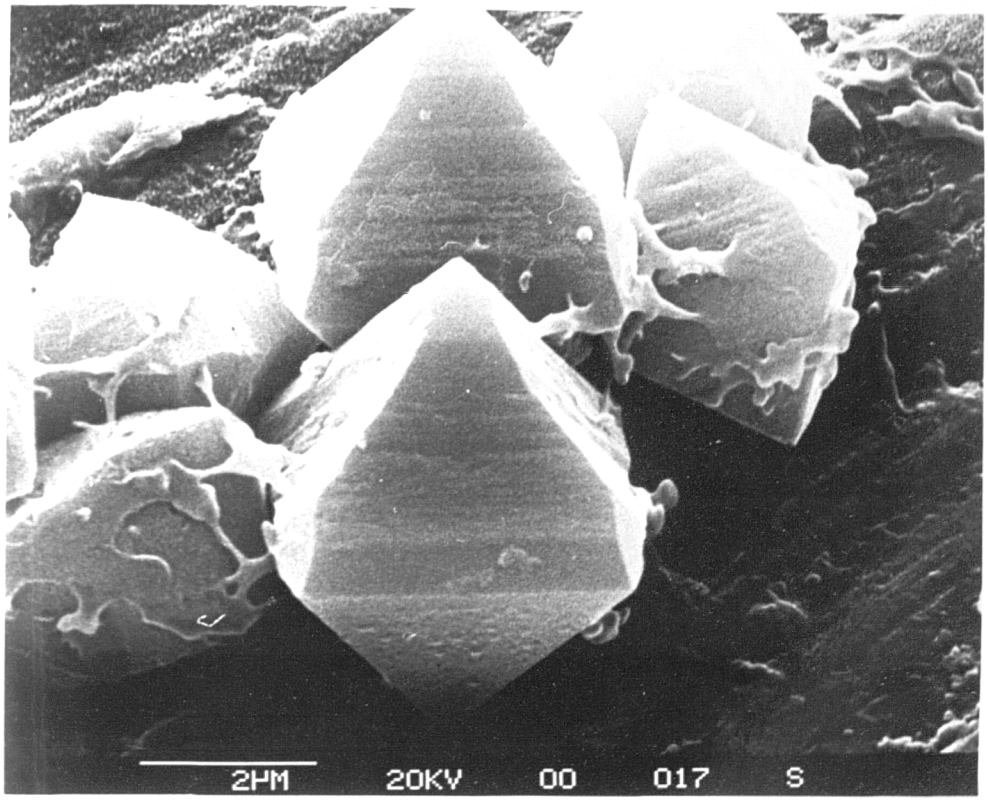

A

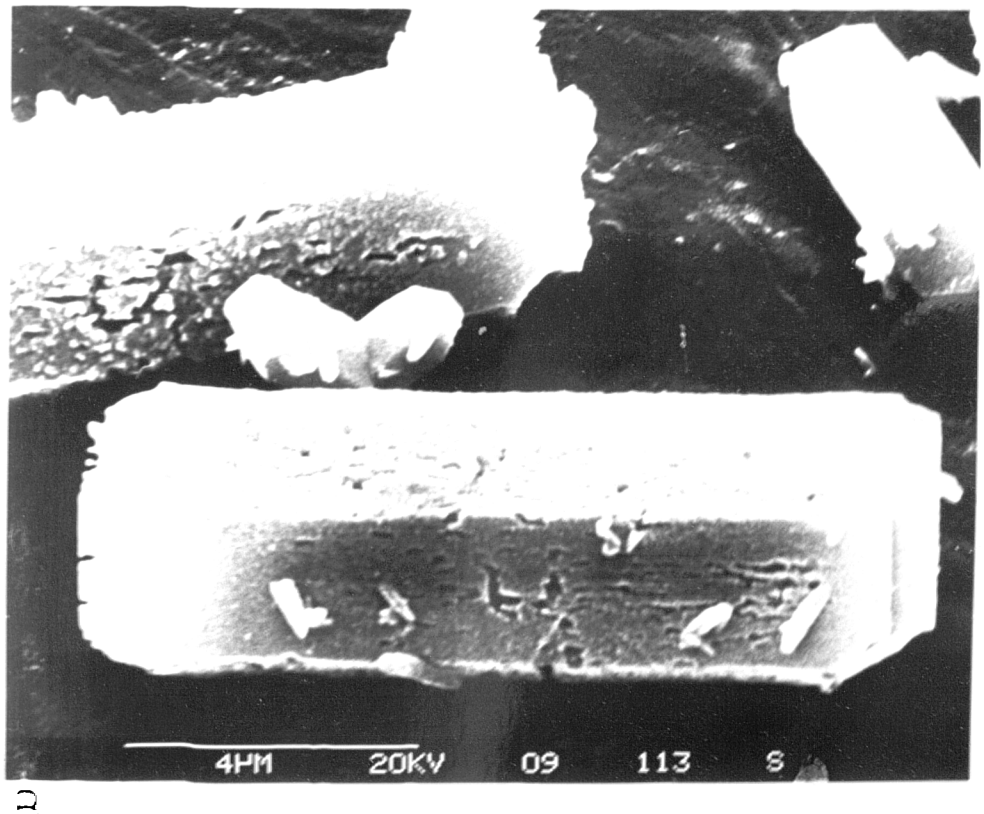

B

PLATE 2

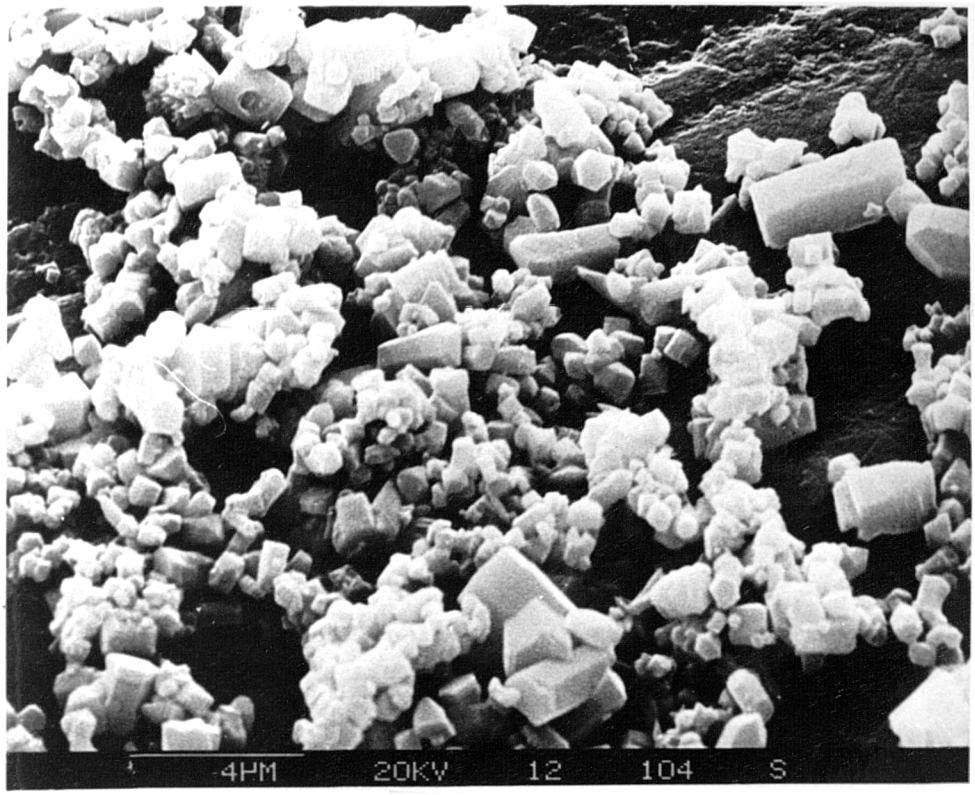

A

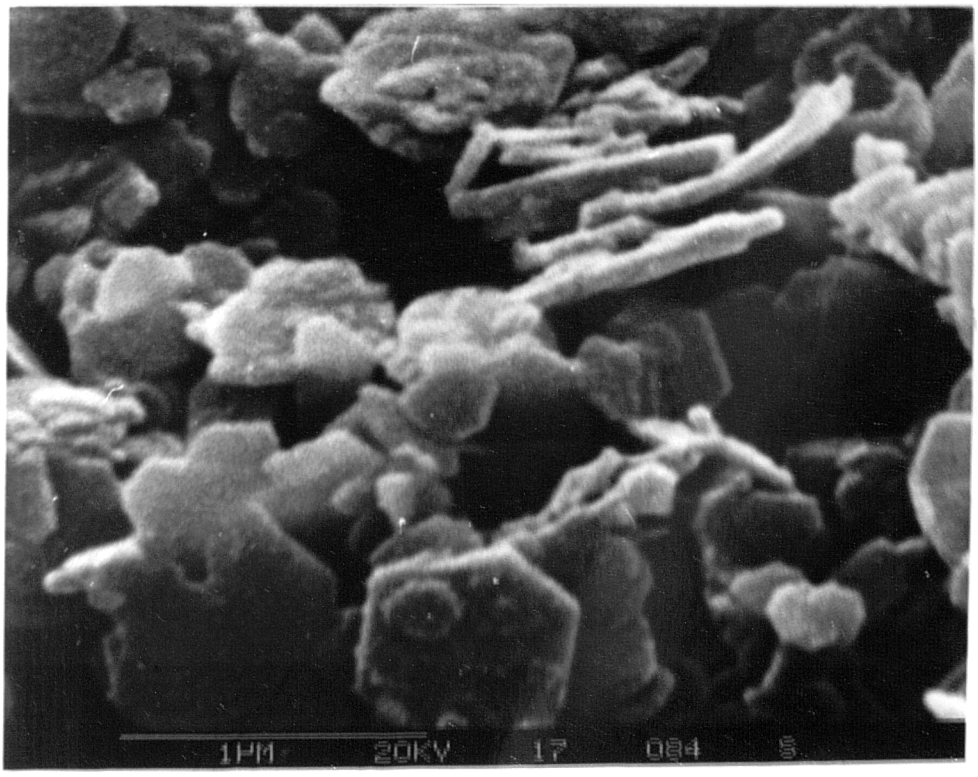

B

PLATE 3

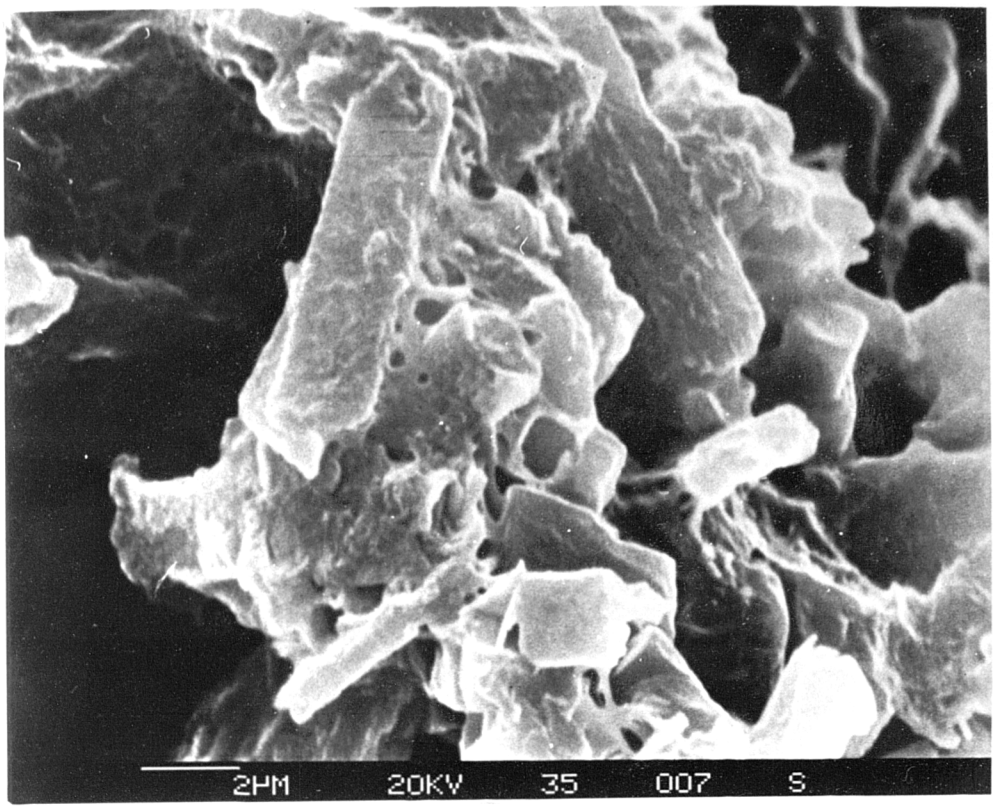

A

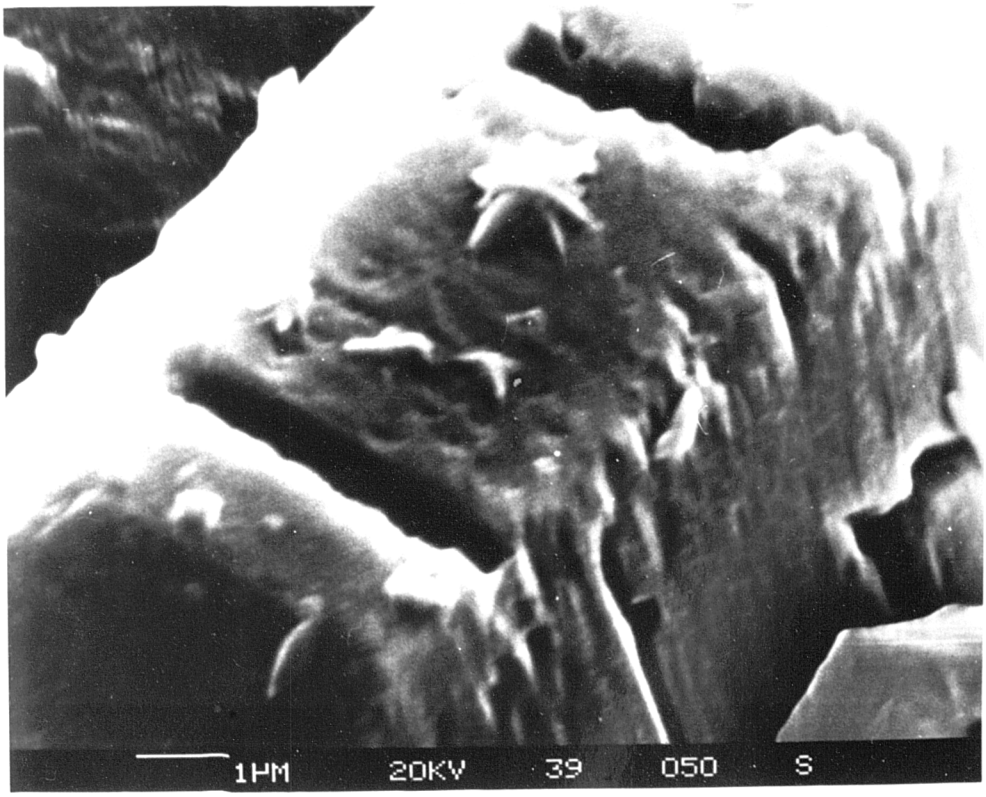

B

PLATE 4

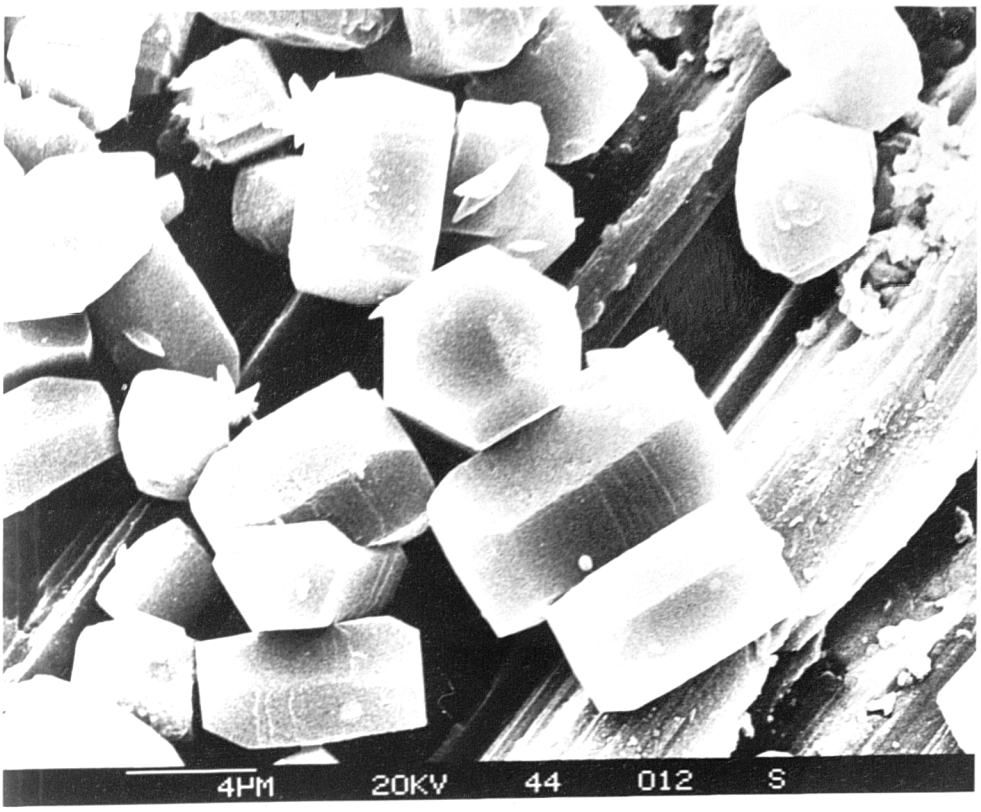

A

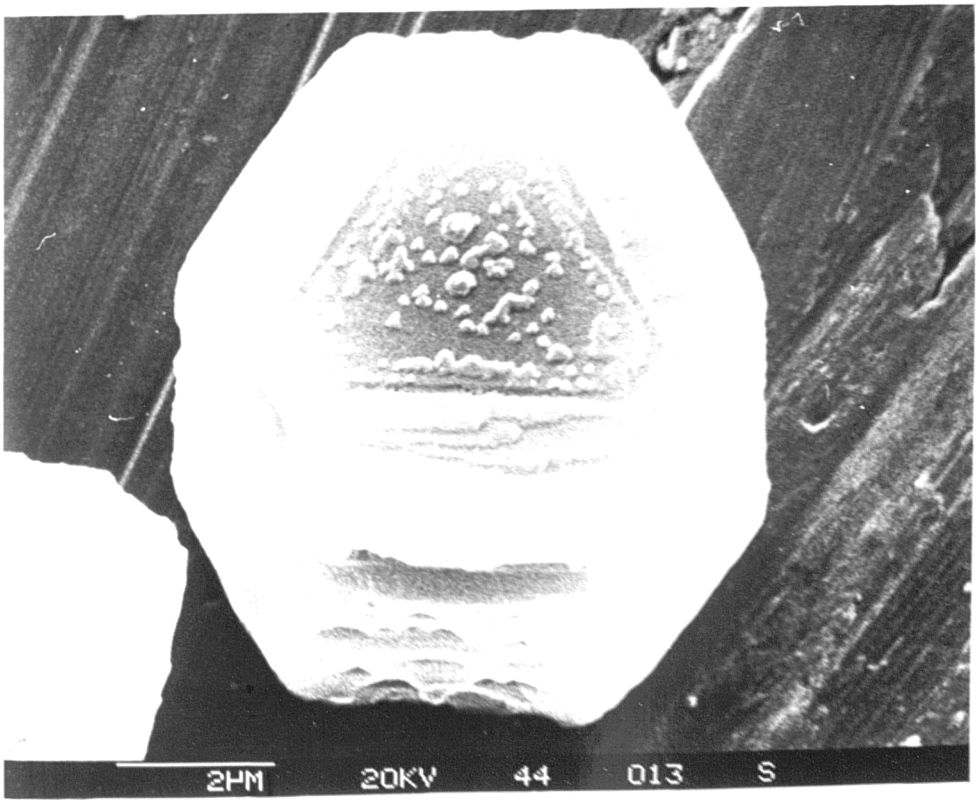

B

PLATE 5

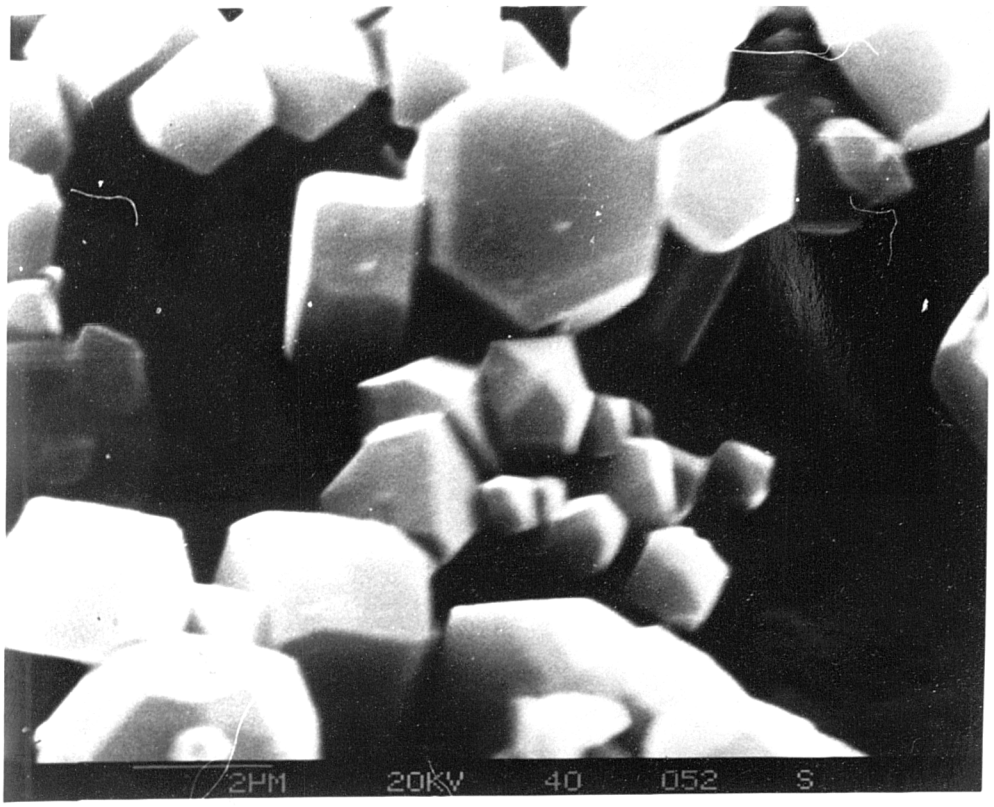

A

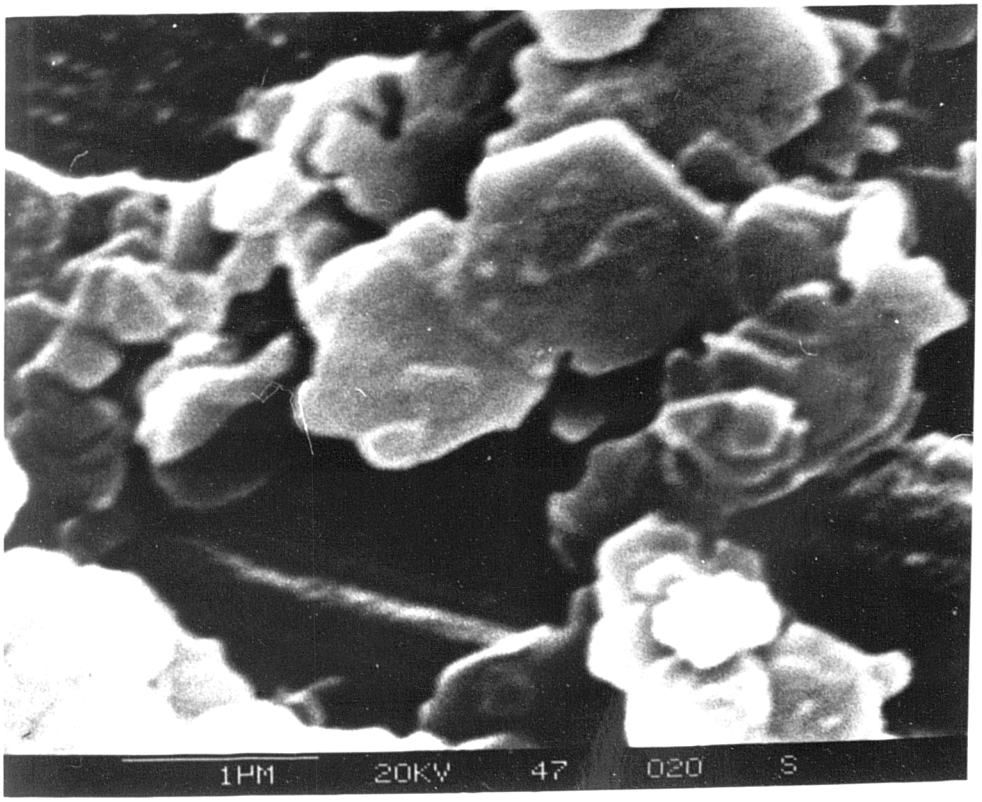

B

PLATE 6

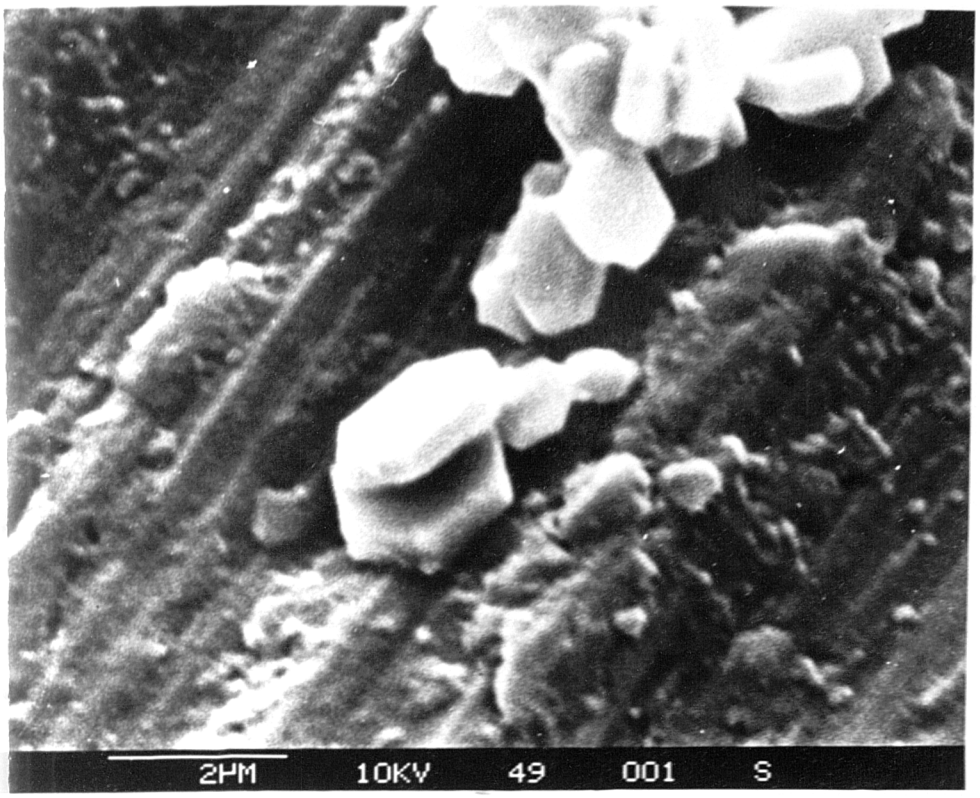

A

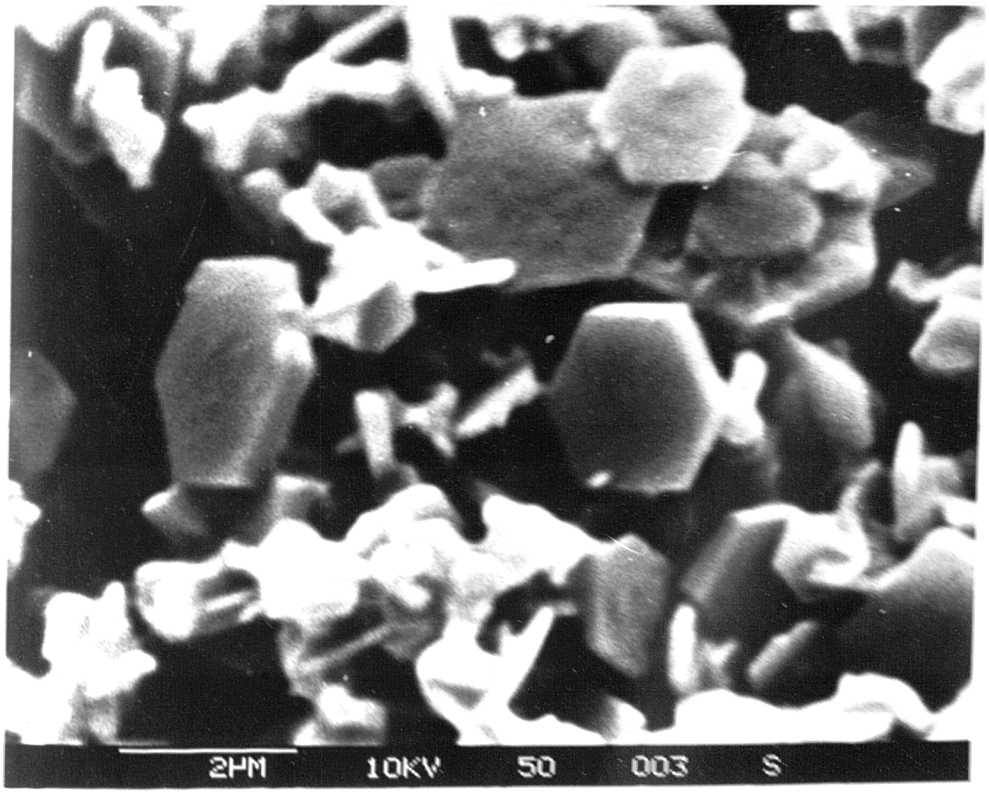

B

PLATE 7

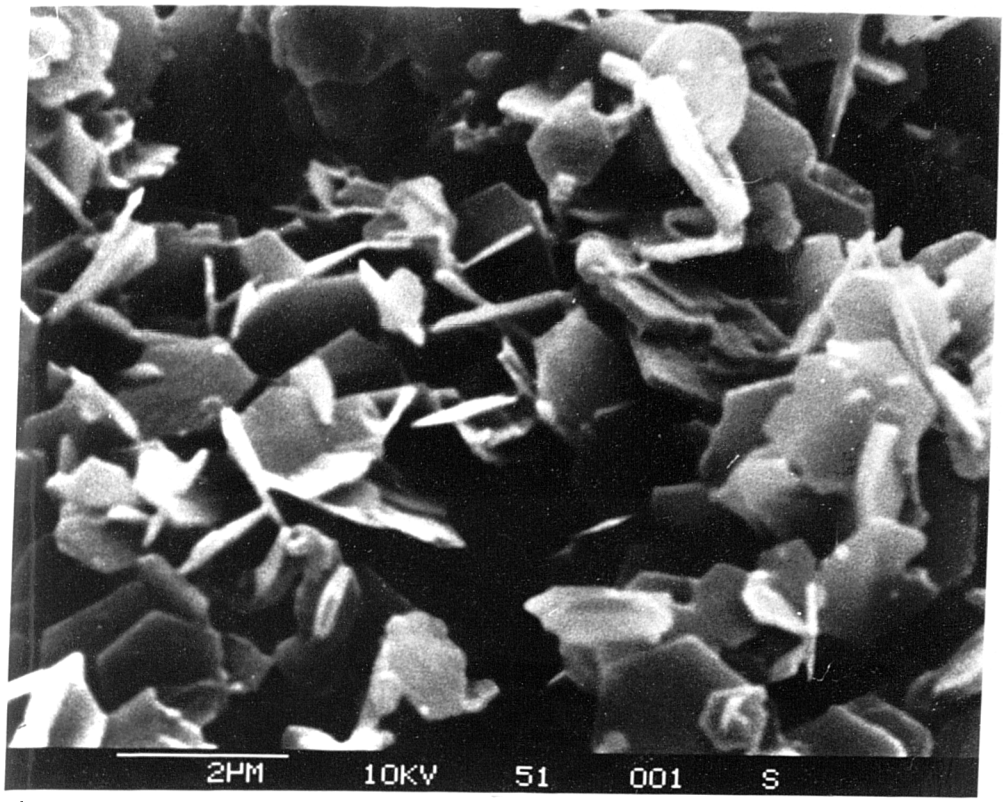

A

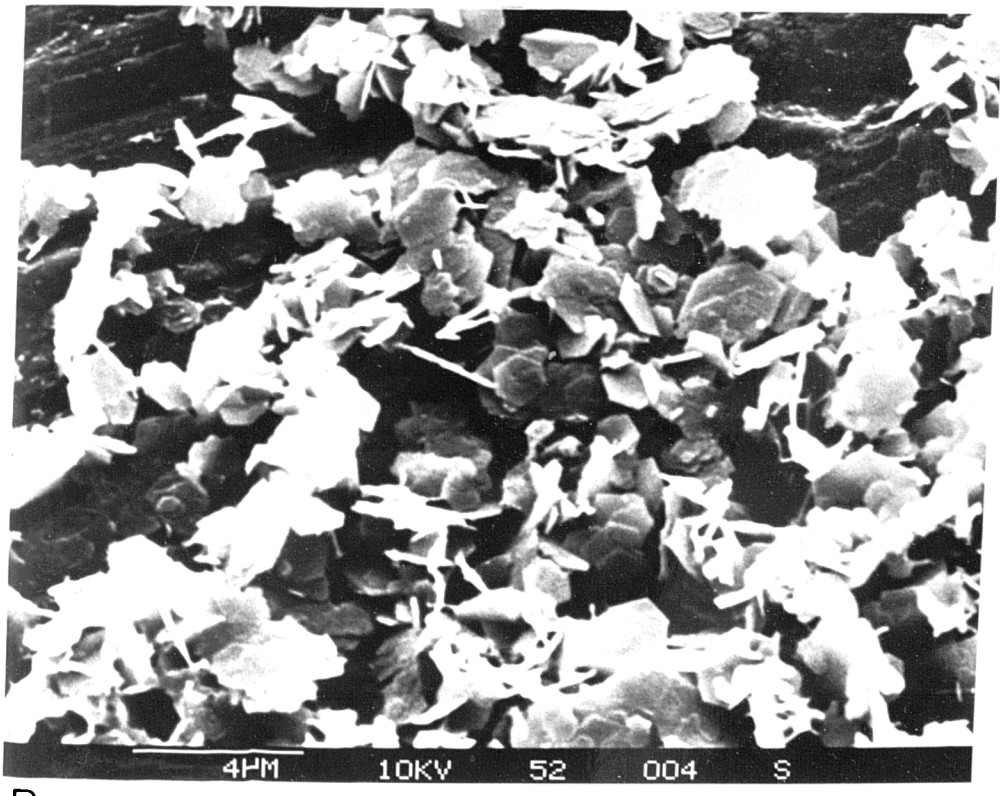

B

PLATE 8

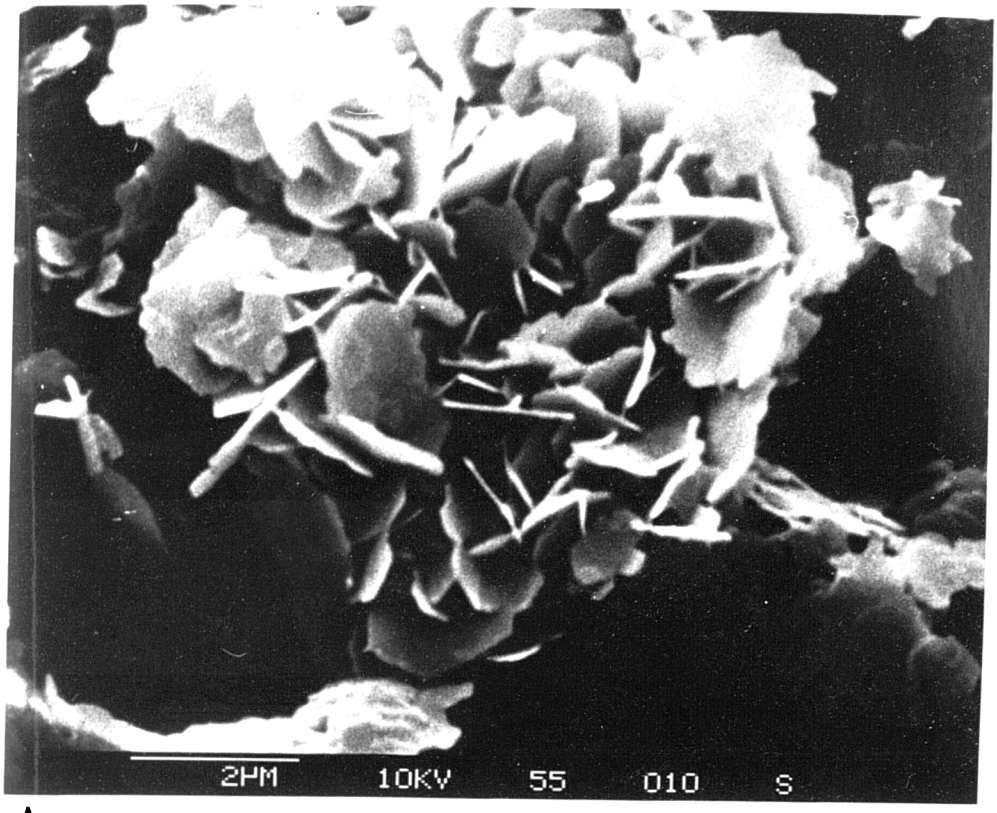

A

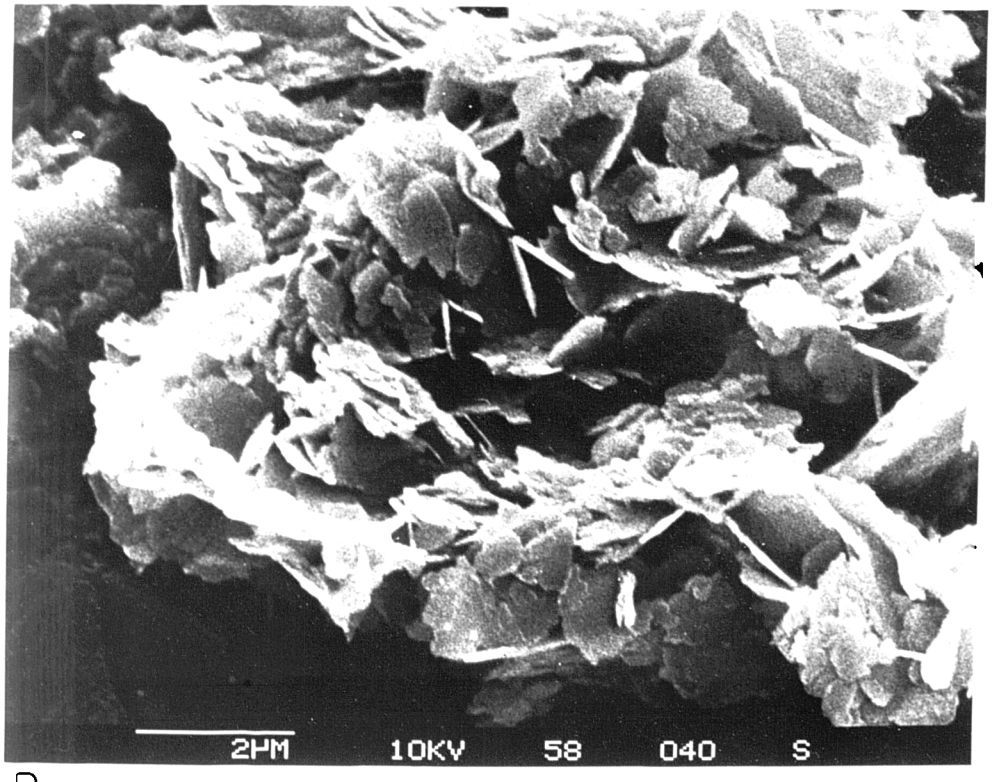

B

PLATE 9

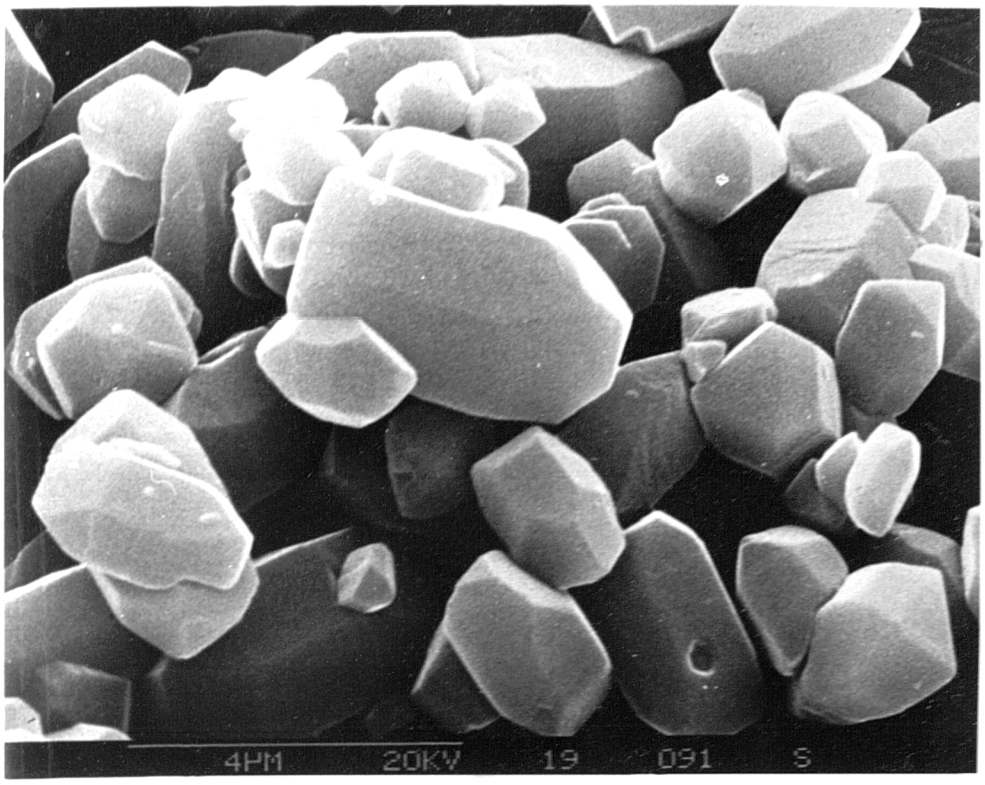

A

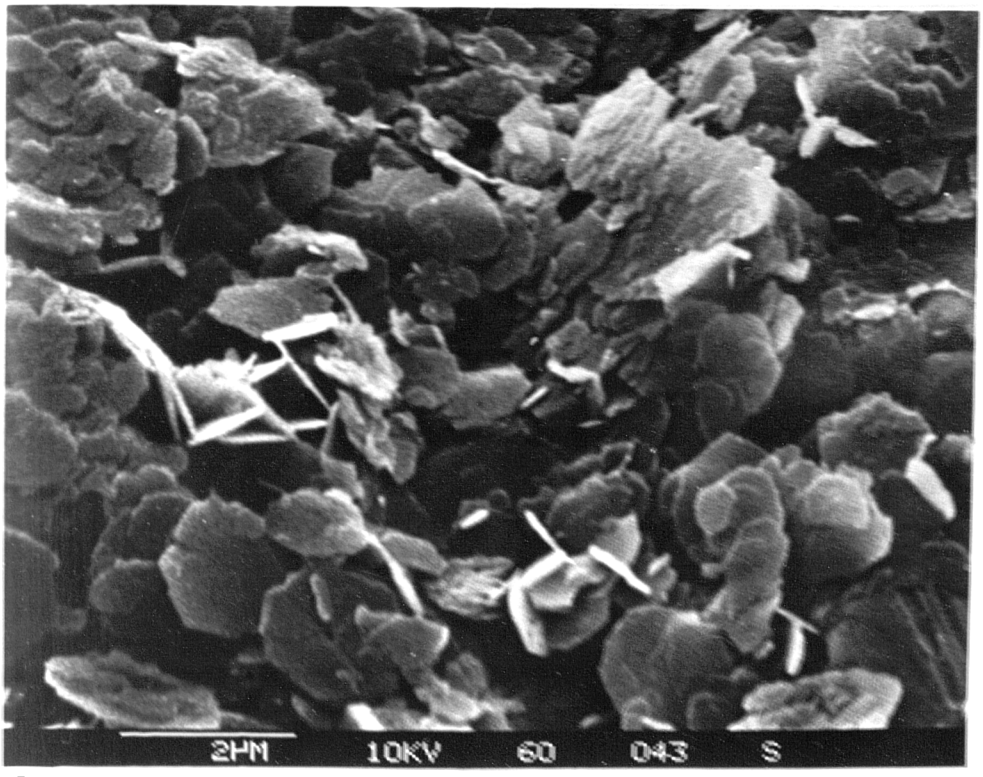

B

PLATE 10

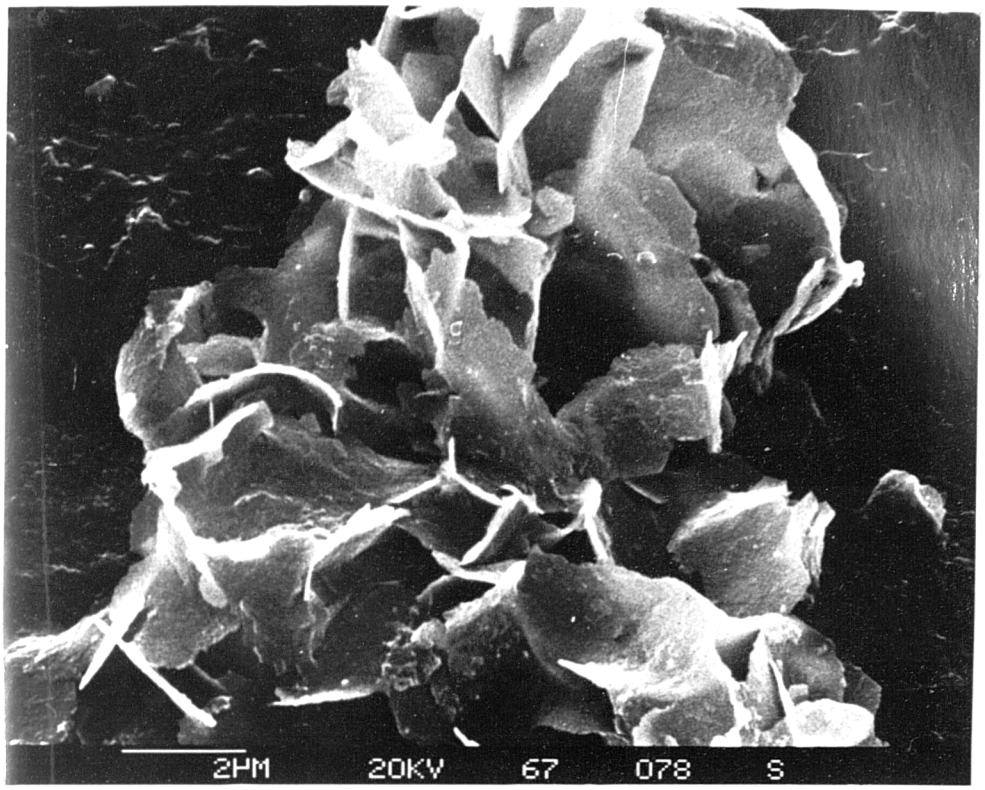

A

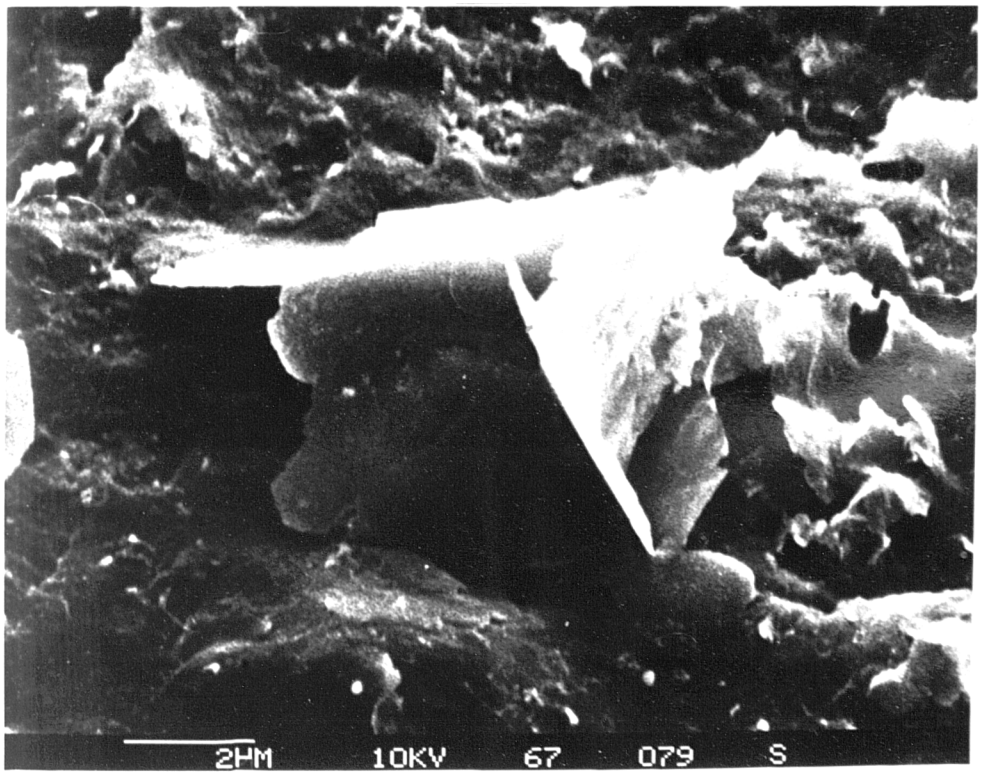

B

PLATE 11

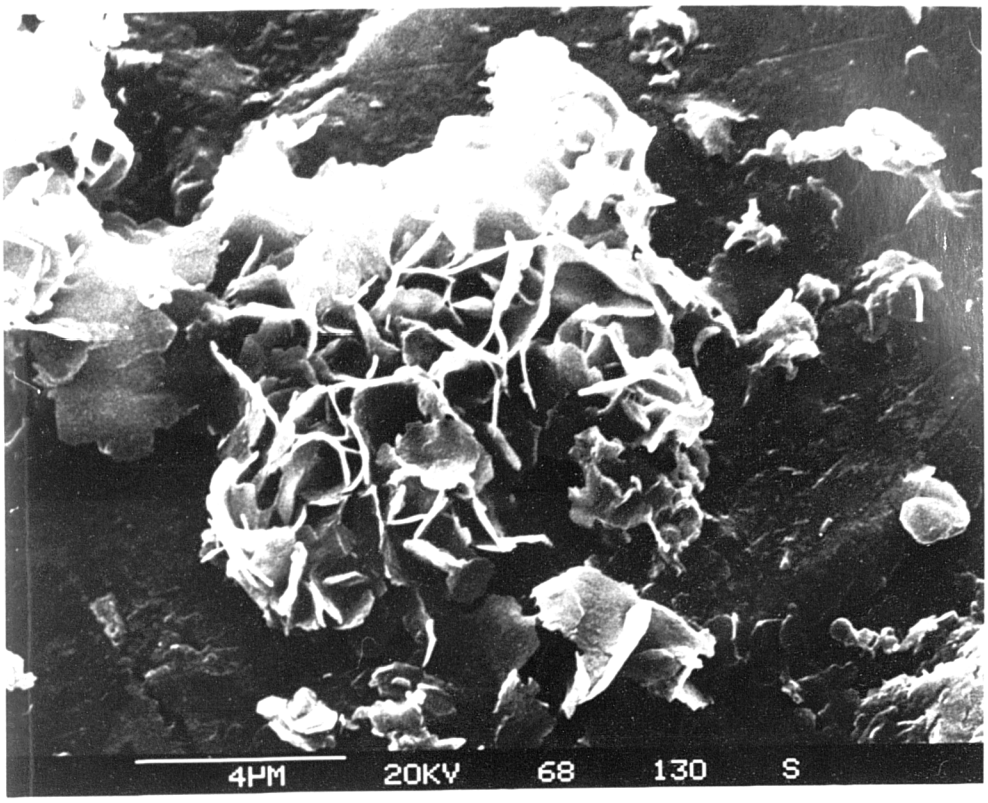

A

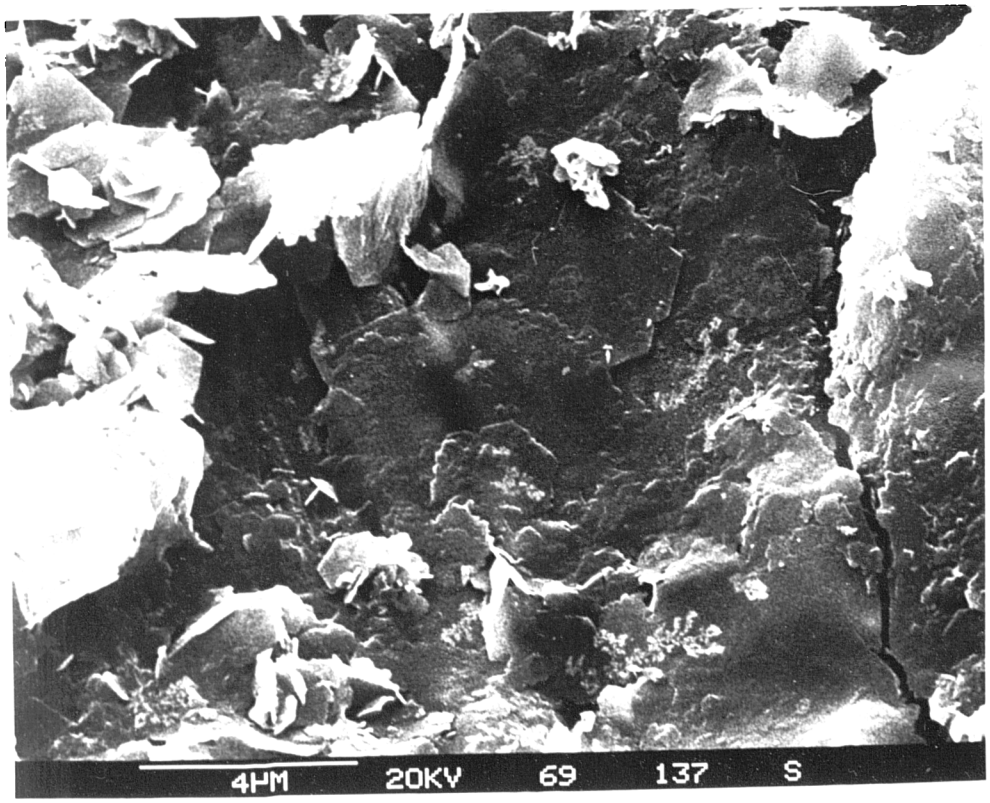

B

PLATE 12

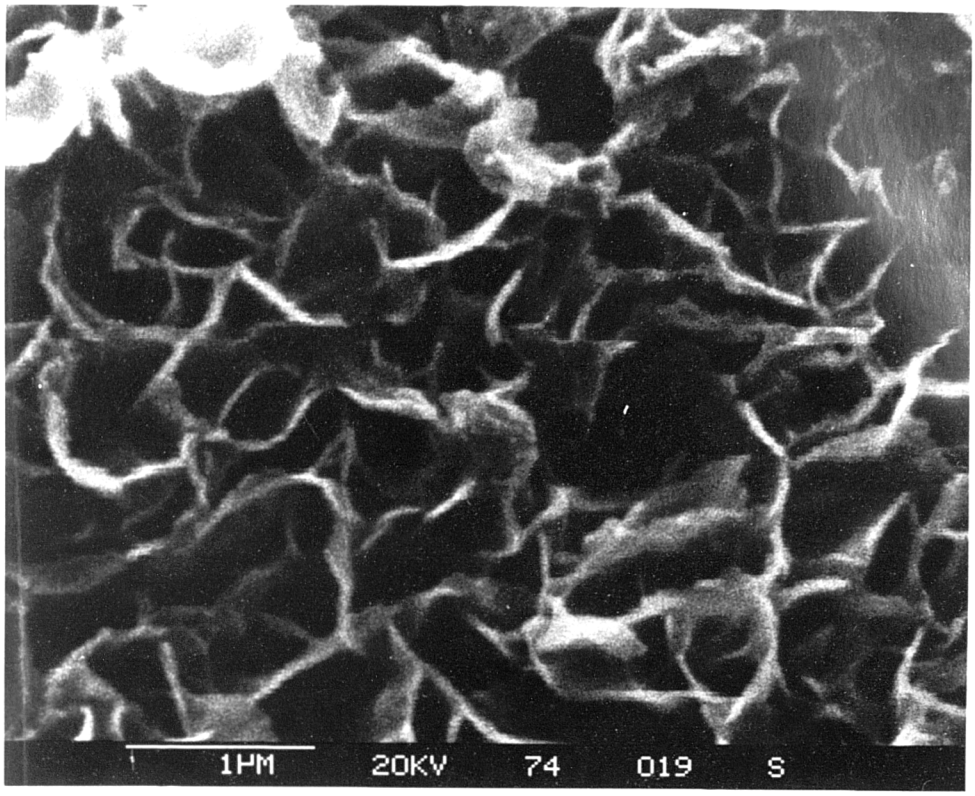

A

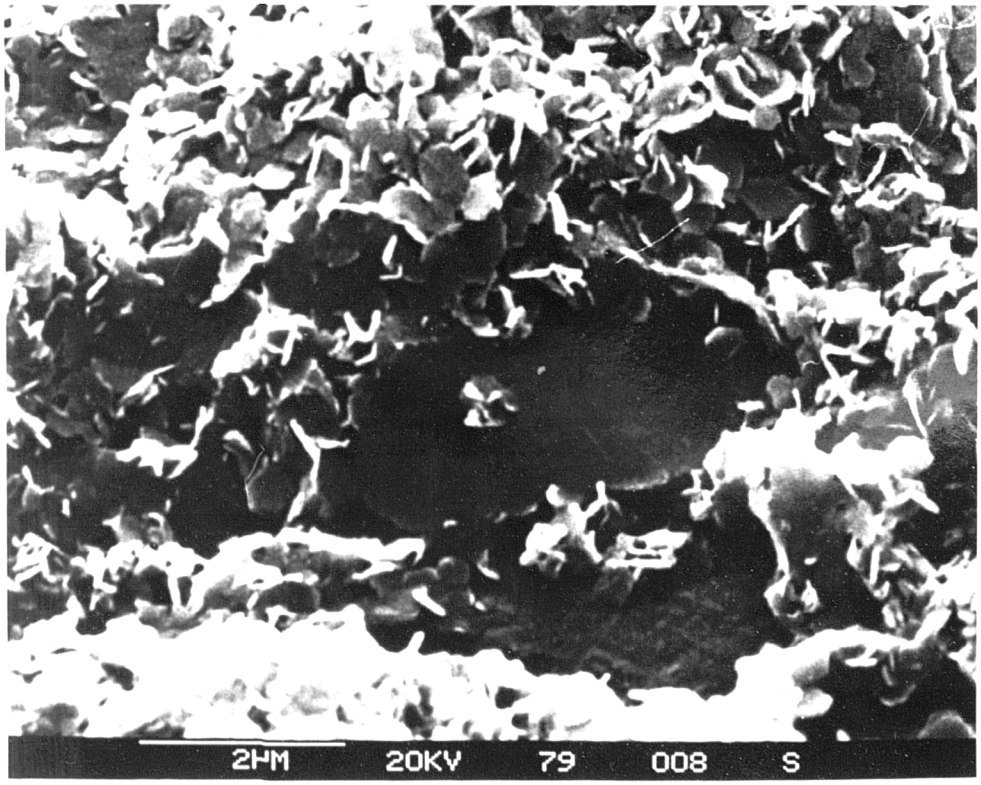

B

PLATE 13

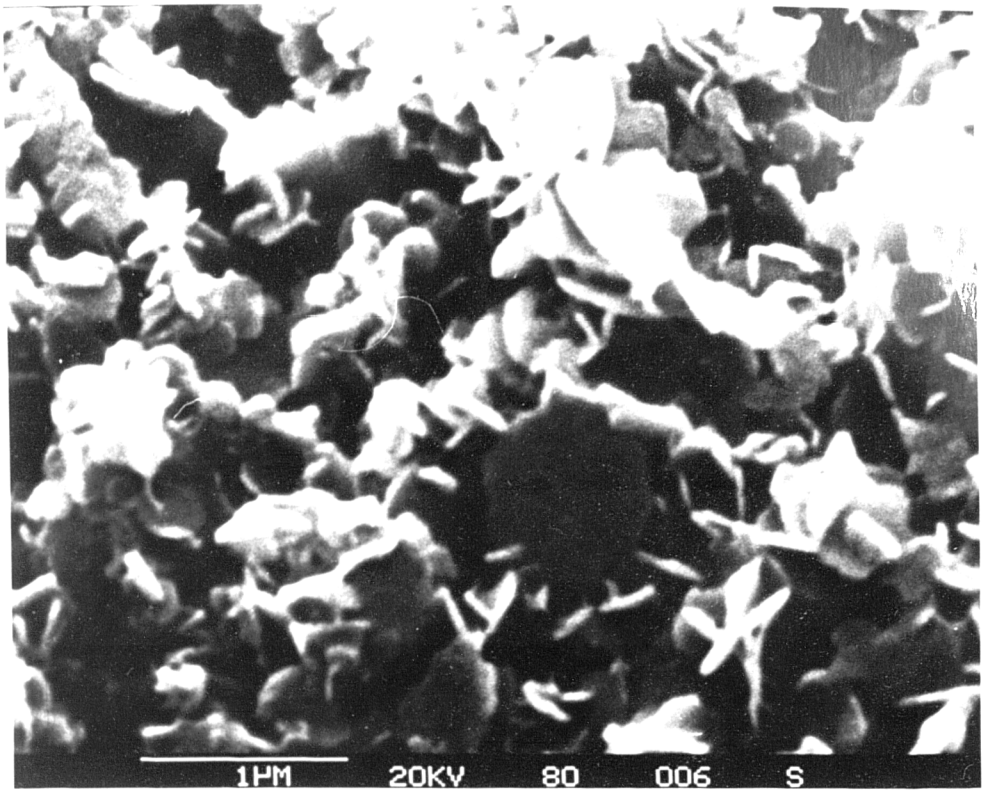

A

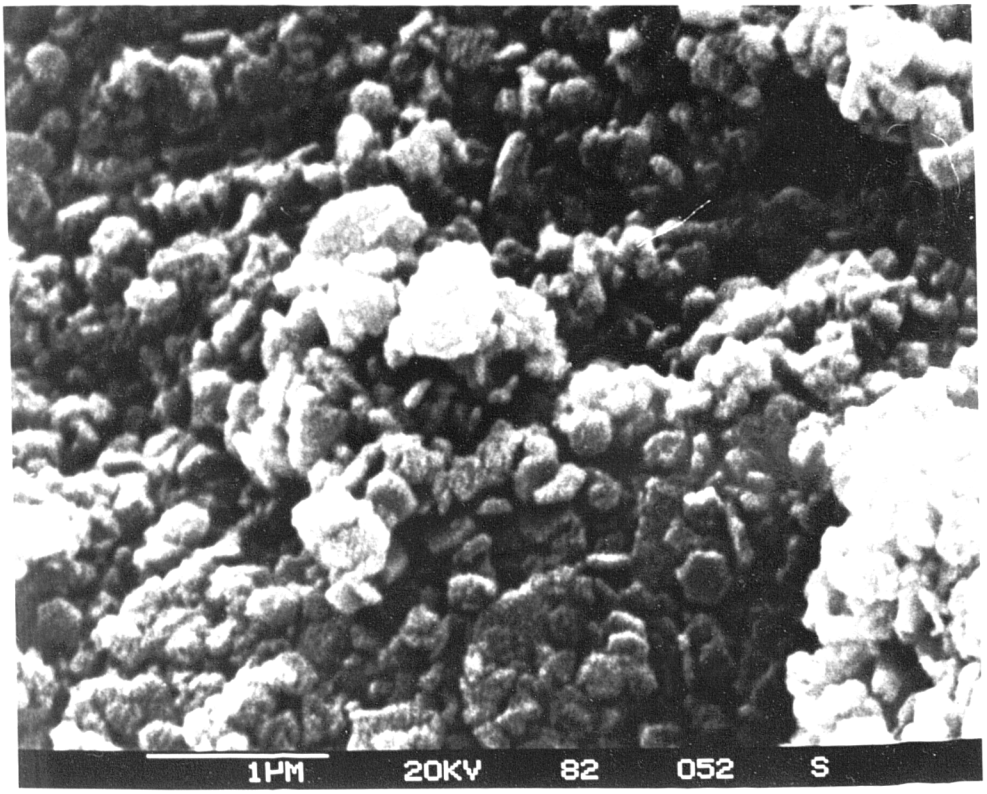

B

PLATE 14

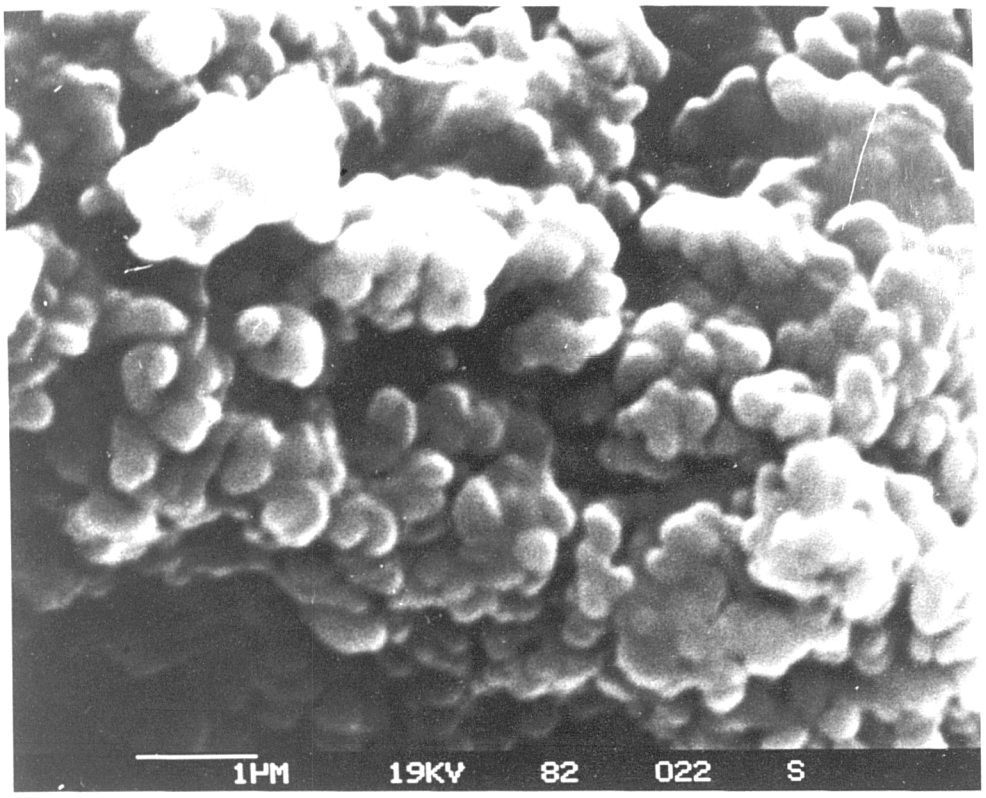

A